

**EFFECTS OF LATERAL BOUNDARIES AND
RESOLUTION ON FLOOD SIMULATION:
A CASE STUDY FOR ISTANBUL**

**MSc. Thesis by
Müge KÖMÜRCÜ, BSc.**

Department : Meteorological Engineering

Programme : Meteorological Engineering

JUNE 2005

**EFFECTS OF LATERAL BOUNDARIES AND
RESOLUTION ON FLOOD SIMULATION:
A CASE STUDY FOR ISTANBUL**

**M.Sc. Thesis by
Müge KÖMÜRCÜ, B.Sc.**

(511031103)

Date of submission : 9 May 2005

Date of defence examination: 1 June 2005

Supervisor (Chairman): Assoc. Prof. Dr. Yurdanur ÜNAL

Members of the Examining Committee Prof.Dr. Nüzhet DALFES (İ.T.Ü.)

Assoc. Prof.Dr. Sibel MENTEŞ

JUNE 2005

FOREWORD

Precipitation and flood prediction are important incidents with vulnerable impacts on people, societies, and economies. Therefore, many sensitivity studies have been done on flood prediction using modeling tools up to now in order to construct best modeling basis for the prediction of the future cases. Furthermore, recent flooding events in Istanbul revealed that due to the impacts of wrong urbanization, even with not very high amounts of rainfall it was possible to observe dangerous flood events. For these reasons, it is the aim of this study to find an approach for the prediction of precipitation in Istanbul considering the recent event of 16 August 2004.

First of all and most importantly, I would like to thank to Dr. Tayfun Kındap for working with me throughout this study, for all his guidance, continuous help, and for dedication of most of his very precious time to my study. Not all scientists like to share their whole knowledge; at this point Dr. Kındap not only shared his knowledge with me, but also helped me discover the problems, find my own solutions to them, and showed me once again with a live proof that a scientist must be in development all the time. I am therefore very happy and lucky to have the opportunity to work with this wonderful scientist and wonderful person.

Moreover, I would also like to thank to research assistants Mr. Ufuk Utku Turuncoglu (M.Sc.), and Miss. Yasemin Ezber (M.Sc.), for helping me solve the problems I encountered without time constrictions, for making my study period joyful, and for all their encouragement.

Besides, I would like to thank to Associate Professor Yurdanur Ünal for being my advisor and for inspiring me about studying atmospheric science since the second year of my undergraduate studies.

Furthermore, I would like to thank to, Professor Mehmet Karaca, for introducing me the world of atmospheric science with his classes, for helping me obtain a wide spectra of thinking, for being the best idol of all times, for understanding me and believing in me and my work and finally for giving me support and help whenever I needed.

In addition, I would like to thank to Dr. Ümit Anteplioğlu for his positive contributions to my study. I would also like to thank to my friend Mr. Hakkı Baltacı (B.Sc.) for all his contributions.

Finally, I would like to thank to Professor Mustafa Serdar Çelebi, for all his support, and help all through the stressful study period, and for solving my data storage problem.

May, 2005

Müge Kömürcü

TABLE OF CONTENTS

| | |
|--|-------------|
| ABBREVIATION | vi |
| LIST OF TABLES | vii |
| LIST OF FIGURES | viii |
| LIST OF SYMBOLS | xii |
| SUMMARY | xiii |
| ÖZET | xiv |
| 1. INTRODUCTION | 1 |
| 2. PREVIOUS STUDIES | 3 |
| 3. MM5 | 18 |
| 3.1. Model Vertical and Horizontal Grids | 18 |
| 3.2. Governing Equations and Numerical Algorithms | 19 |
| 3.2.1. Hydrostatic model equations | 19 |
| 3.2.1.1. Horizontal momentum equation | 20 |
| 3.2.1.2. Temperature | 20 |
| 3.2.1.3. Surface pressure | 21 |
| 3.2.2. Nonhydrostatic model equations | 21 |
| 3.2.2.1. Vertical coordinate | 22 |
| 3.2.2.2. Momentum | 22 |
| 3.2.2.3. Pressure | 22 |
| 3.2.2.4. Temperature | 23 |
| 3.3. Model Dynamics | 23 |
| 3.3.1. Finite differencing | 23 |
| 3.3.1.1. Spatial finite differencing | 23 |
| 3.3.1.2. Temporal finite differencing | 23 |
| 3.3.2. Time splitting | 25 |
| 3.3.2.1. Nonhydrostatic time splitting | 25 |
| 3.3.2.1. Hydrostatic time splitting | 26 |
| 3.3.3. Lateral boundary conditions | 26 |
| 3.3.4. Upper radiative boundary condition | 27 |
| 3.3.5. Mesh refinement scheme and feedback | 27 |
| 3.3.6. Map projection | 28 |
| 3.4. Model Physics | 28 |
| 3.4.1. Horizontal diffusion | 28 |
| 3.4.2. Dry convective adjustment | 28 |
| 3.4.3. Precipitation physics | 29 |
| 3.4.3.1. Simple ice moisture scheme | 29 |

| | |
|--|-----------|
| 3.4.3.2. Kain Fritsch 2 cumulus scheme | 30 |
| 3.4.4. Planetary boundary layer parameterizations | 30 |
| 3.4.4.1 MRF planetary boundary layer (PBL) | 31 |
| 3.4.5. Atmospheric radiation parameterization scheme | 31 |
| 3.4.5.1 Rapid radiative transfer model (RRTM) | 31 |
| 3.4.6. Surface scheme | 31 |
| 3.5. Model Components | 31 |
| 4. DATA | 33 |
| 4.1. Terrestrial Data | 33 |
| 4.1.1 Terrestrial height data | 33 |
| 4.1.2. Vegetation data | 34 |
| 4.2. Meteorological Data | 35 |
| 4.2.1 NCEP/NCAR Reanalysis data | 35 |
| 4.2.2. Station data | 37 |
| 4.3. Satellite Data | 37 |
| 5. EXPERIMENT DESIGN AND ANALYSIS | 39 |
| 5.1. Experiment I | 39 |
| 5.1.1. Analysis of experiment I | 40 |
| 5.1.1.1 500 mb level | 40 |
| 5.1.1.2 850 mb level | 43 |
| 5.2. Experiment II | 47 |
| 5.2.1. Analysis of experiment II | 47 |
| 5.2.1.1. 500 mb level | 47 |
| 5.2.1.2. 850 mb level | 50 |
| 5.3. Experiment III | 54 |
| 5.3.1. Analysis of experiment III | 54 |
| 5.3.1.1. 500 mb level | 54 |
| 5.3.1.2. 850 mb level | 58 |
| 5.4. Experiment IV | 62 |
| 5.4.1. Analysis of experiment IV | 62 |
| 5.4.1.1. 500 mb level | 62 |
| 5.4.1.1.1. 36 km domain | 62 |
| 5.4.1.1.2. 12 km nested domain | 66 |
| 5.4.1.2. 850 mb level | 69 |
| 5.4.1.2.1. 36 km coarse domain | 69 |
| 5.4.1.2.2. 12 km nested domain | 72 |
| 5.4.1.2.3. 4 km nested domain | 75 |
| 5.4.1.3. Cross sectional analysis | 78 |
| 5.4.1.3.1. 36 km coarse domain | 78 |
| 5.4.1.3.2. 12 km nested inner domain | 81 |
| 5.4.1.3.3. 4 km nested inner domain | 82 |
| 6. TOTAL ACCUMULATED RAINFALL ANALYSIS | 83 |

| | |
|--|------------|
| 6.1. Experiment I (18 km Resolution Large Domain) | 83 |
| 6.2. Experiment II (18 km Resolution Smaller Domain) | 84 |
| 6.3. Experiment III (9km Resolution Smaller Domain) | 85 |
| 6.4. Experiment IV (Coarse Domain with Nested Approach) | 86 |
| 7. CONCLUSION AND FUTURE WORKS | 91 |
| REFERENCES | 93 |
| APPENDICES | 95 |
| CURRICULUM VITAE | 124 |

ABBREVIATIONS

| | |
|---------------|--|
| ASEM | : Arakawa Schubert Scheme |
| ALPEX | : Alpine Experiment |
| BATS | : Biosphere – Atmosphere Transfer Scheme |
| CCM1 | : Climate Circulation Model |
| ECMWF | : European Center for Medium Range Weather Forecasts |
| EM | : Explicit Moisture scheme |
| FGGE | : First GARP Global Experiment |
| FSU | : Florida State University |
| IR | : Infrared |
| JAXA | : Japan Aerospace Exploration Agency |
| MK | : Modified Kuo scheme |
| MM5 | : Mesoscale Meteorological Model |
| MPA-RT | : Multi-Satellite Precipitation Analysis |
| NASA | : National Aeronautics and Space Administration |
| NCAR | : National Center for Atmospheric Research |
| NCEP | : The National Centers for Environmental Prediction |
| NMC | : National Meteorological Center |
| NPS | : Numerical Point Storm Events |
| PBL | : Planetary Boundary Layer |
| PSU | : The Pennsylvania State University |
| RRTM | : The Rapid Radiative Transfer Model |
| SST | : Sea surface temperature |
| TRMM | : Tropical Rainfall Measuring Mission |
| USGS | : The U.S. Geological Survey |

LIST OF TABLES

| | <u>Page No</u> |
|--|-----------------------|
| Table 2.1. Average precipitation and biases over the domain for different test runs (Giorgi et al., 1991)..... | 11 |
| Table 2.2. Average precipitation and biases over the domain for different test runs including BATS (Giorgi et. al, 1991)..... | 11 |
| Table 4.1. Terrain height data classes according to resolution selected (Dudhia et al., 2004)..... | 34 |
| Table 4.2. Vegetation data classes according to resolution selected (Dudhia et al., 2004)..... | 34 |
| Table 4.3. 25 Category vegetation classes of type 3 vegetation data with physical parameters for northern hemisphere summer and winter... | 35 |

LIST OF FIGURES

| | <u>Page No</u> |
|--|----------------|
| Figure 2.1 : 700 mb wind barb (a, c) and vorticity (b,d) for 48h at 13 July 1981 00 UTC, control experiment (a, b) versus observations (c,d) (Kuo et al., 1988)..... | 4 |
| Figure 2.2 : Vertical cross sections of relative humidity (a), equivalent temperature (b), horizontal wind barbs and vertical velocity (c), and specific humidity and horizontal wind speed (d) for control experiment at 13 July 1981 00 UTC (Kuo et al., 1988)..... | 5 |
| Figure 2.3 : 500 mb wind barb (a, c) and vorticity (b,d) for 48h at 13 July 1981 00 UTC, control experiment (a, b) versus observations (c,d) (Kuo et al., 1988)..... | 6 |
| Figure 2.4 : Control experiment 24 hour accumulated precipitation at 00 UTC 13 July (a), 0000 UTC 14 July (b), 48 hour accumulated precipitation at 00 UTC 14 July (c), and convective and non-convective rate of rainfall integrated over the box at (c) (Kuo et al., 1988)..... | 6 |
| Figure 2.5 : July 1979, thirty day accumulated rainfall obtained by MM4. (Giorgi et. al, 199)..... | 10 |
| Figure 2.6 : Comparison of four horizontal resolutions with ECMWF analysis (Alpert et al., 1996)..... | 12 |
| Figure 2.7 : Different lateral boundary settings (Alpert et al., 1996)..... | 13 |
| Figure 2.8 : Contributions of Initial conditions, lateral boundaries, topography and their synergism to cyclone deepening..... | 13 |
| Figure 2.9 : Model coarse domain with nested domains and terrain heights with a contour interval of 200m (Colle and Mass, 2000)..... | 15 |
| Figure 3.1 : Vertical structure of the model (Chen et al., 1994)..... | 19 |
| Figure 3.2 : Horizontal representation of the dot and cross grid points with the smaller inner box representing a 3:1 coarse-grid distance to fine-grid distance ratio (Dudhia et al., 2004)..... | 20 |
| Figure 3.4 : First time step (Grell et al., 1994)..... | 24 |
| Figure 3.5 : Time step n showing short and long time steps for various parameters (Grell et al., 1994)..... | 24 |
| Figure 3.6 : Time step n+1 showing short and long time steps..... | 25 |
| Figure 3.7 : Dudhai simple ice scheme (Dudhia et al., 2004)..... | 29 |
| Figure 5.1 : Domain of experiment one with terrestrial data shown..... | 39 |
| Figure 5.2 : 500 mb level for experiment 1, geopotential height represented as filled colors, and wind vectors starting at 13 August 00 UTC with 12 hourly interval, ending at 19 August 00 UTC, left column represents the 00 UTC and right column 12 UTC for each forecast day..... | 41-42 |
| Figure 5.3 : Comparison of NCEP Reanalysis map (left column) with experiment I model results (right column)..... | 43 |

| | | |
|--------------------|--|-------|
| Figure 5.4 | : 850 mb level relative humidity represented as filled colors, temperature, and wind vectors starting at 13 August 00 UTC with 12 hourly interval, ending at 19 August 00 UTC, left column represents the 00 UTC and right column 12 UTC for each forecast day..... | 45-46 |
| Figure 5.5 | : Domain of experiment two with terrestrial data shown..... | 47 |
| Figure 5.6 | : 500 mb level for experiment II, geopotential height represented as filled colors, and wind vectors starting at 13 August 00 UTC with 12 hourly interval, ending at 19 August 00 UTC, left column represents the 00 UTC and right column 12 UTC for each forecast day..... | 48-49 |
| Figure 5.7 | : Comparison of NCEP Reanalysis map (left column) with experiment II model results (right column)..... | 51 |
| Figure 5.8 | : 850 Mb Level Relative Humidity Represented As Filled Colors, Temperature, And Wind Vectors Starting At 13 August 00 UTC With 12 Hourly Interval, Ending At 19 August 00 UTC, Left Column Represents The 00 UTC And Right Column 12 UTC For Each Forecast Day..... | 52-53 |
| Figure 5.9 | : Domain of experiment III with terrain heights..... | 54 |
| Figure 5.10 | : Reanalysis (left) and model result (right) for 17 August 00 UTC for experiment III..... | 55 |
| Figure 5.11 | : 500 mb level for experiment 3, geopotential height represented as filled colors, and wind vectors starting at 13 August 00 UTC with 12 hourly intervals, ending at 19 August 00 UTC, and left column represents the 00 UTC and right column 12 UTC for each forecast day..... | 56-57 |
| Figure 5.12 | : Reanalysis (left) and model result for 17 August 2004 00 and 12 UTC for experiment III..... | 59 |
| Figure 5.13 | : 850 mb level relative humidity represented as filled colors, temperature, and wind vectors starting at 13 August 00 UTC with 12 hourly interval, ending at 19 August 00 UTC, left column represents the 00 UTC and right column 12 UTC for each forecast day..... | 60-61 |
| Figure 5.14 | : Coarse and nested domains of the last experiment..... | 62 |
| Figure 5.15 | : Reanalysis (left) and model predicted fields a 500 mb..... | 63 |
| Figure 5.16 | : 500 mb level for the 36km domain of experiment 4, geopotential height represented as filled colors, and wind vectors starting at 13 August 00 UTC with 12 hourly interval, ending at 19 August 00 UTC, left column represents the 00 UTC and right column 12 UTC for each forecast day..... | 64-65 |
| Figure 5.17 | : 500 mb level for the 12 km domain of experiment 4, geopotential height represented as filled colors, and wind vectors starting at 13 August 00 UTC with 12 hourly interval, ending at 19 August 00 UTC, left column represents the 00 UTC and right column 12 UTC for each forecast day..... | 67-68 |
| Figure 5.18 | : Reanalysis (left) and model prediction at 500 mb for 16 August 2004..... | 69 |
| Figure 5.19 | : Reanalysis (left), model results (right) for experiment IV 36km domain..... | 69 |

| | | |
|--------------------|--|-------|
| Figure 5.20 | : Experiment 4, 36 km domain 850 mb level relative humidity represented as filled colors, temperature, and wind vectors starting at 13 August 00 UTC with 12 hourly interval, ending at 19 August 00 UTC, left column represents the 00 UTC and right column 12 UTC for each forecast day..... | 70-71 |
| Figure 5.21 | : Reanalysis (top), and model results for the 12 km inner nest at 850 mb..... | 72 |
| Figure 5.22 | : Experiment 4, 12 km domain 850 mb level relative humidity represented as filled colors, temperature, and wind vectors starting at 13 August 00 UTC with 12 hourly interval, ending at 19 August 00 UTC, left column represents the 00 UTC and right column 12 UTC for each forecast day..... | 73-74 |
| Figure 5.23 | : Reanalysis field (top) and model result (bottom) at 850 mb at 16 August 2004 12 UTC..... | 75 |
| Figure 5.24 | : Experiment 4, 4 km domain 850 mb level relative humidity represented as filled colors, temperature, and wind vectors starting at 13 August 00 UTC with 12 hourly interval, ending at 19 August 00 UTC, left column represents the 00 UTC and right column 12 UTC for each forecast day..... | 76-77 |
| Figure 5.25 | : 36 km coarse domain of experiment four, and the vertical cross section line..... | 78 |
| Figure 5.26 | : Vertical cross sections at 36 km domain of experiment IV..... | 79-80 |
| Figure 5.27 | : 12 km nested domain of experiment four, and the vertical cross section line..... | 81 |
| Figure 5.28 | : Vertical cross section at 16 August 2004 00UTC (left) and 12 UTC(right) for 12 km domain of experiment IV..... | 81 |
| Figure 5.29 | : 4 km nested domain of experiment four, and the vertical cross section line..... | 82 |
| Figure 5.30 | : Vertical cross sections at 16 August 2004 00UTC (left) and 12 UTC(right) for 4 km domain of experiment IV..... | 82 |
| Figure 6.1 | : Multi Satellite data image for 16 August 2004 showing daily total accumulated precipitation for the domain of experiment..... | 83 |
| Figure 6.2 | : Model results for 16 August 2004 showing daily total accumulated precipitation of experiment I..... | 84 |
| Figure 6.3 | : Multi Satellite data image for 16 August 2004 showing daily total accumulated precipitation for the domain of experiment II.... | 84 |
| Figure 6.4 | : Model results for 16 August 2004 showing daily total accumulated precipitation of experiment II..... | 85 |
| Figure 6.5 | : Multi Satellite data image for 16 August 2004 showing daily total accumulated precipitation for the domain of experiment III... | 85 |
| Figure 6.6 | : Model results for 16 August 2004 showing daily total accumulated precipitation of experiment III..... | 86 |
| Figure 6.7 | : Multi Satellite data image for 16 August 2004 showing daily total accumulated precipitation for the coarse domain of experiment IV..... | 87 |
| Figure 6.8 | : Model results for 16 August 2004 showing daily total accumulated precipitation of coarse domain of experiment IV..... | 87 |
| Figure 6.9 | : Multi Satellite data image for 16 August 2004 showing daily total accumulated precipitation for the 12 km domain of experiment IV..... | 88 |

| | | |
|--------------------|---|-----|
| Figure 6.10 | : Model results for 16 August 2004 showing daily total accumulated precipitation of 12 km domain of experiment IV..... | 88 |
| Figure 6.11 | : Multi Satellite data image for 16 August 2004 showing daily total accumulated precipitation for the 4 km domain of experiment IV..... | 89 |
| Figure 6.12 | : Model results for 16 August 2004 showing daily total accumulated precipitation of 4 km domain of experiment IV..... | 89 |
| Figure 6.13 | : Model daily total accumulated results of the last experiment compared with multi satellite data and observations..... | 90 |
| Figure A.1 | : Experiment I, 500 mb NCEP Reanalysis plots..... | 96 |
| Figure A.2 | : Experiment II 500 mb NCEP Reanalysis plots..... | 98 |
| Figure A.3 | : Experiment III 500 mb NCEP Reanalysis plots..... | 100 |
| Figure A.4 | : Experiment IV, 36km coarse domain 500mb NCEP Reanalysis plots..... | 102 |
| Figure A.5 | : Experiment IV, 12km nested inner domain 500mb NCEP Reanalysis plots..... | 104 |
| Figure B.1 | : Experiment I, 850 mb NCEP Reanalysis plots..... | 106 |
| Figure B.2 | : Experiment II, 850 mb NCEP Reanalysis plots..... | 108 |
| Figure B.3 | : Experiment III, 850 mb :NCEP Reanalysis plots..... | 110 |
| Figure B.4 | : Experiment IV, 36 km coarse domain, 850 mb NCEP Reanalysis plots..... | 112 |
| Figure B.5 | : Experiment IV, 12 km inner nested domain, 850 mb NCEP Reanalysis plots..... | 114 |
| Figure B.6 | : Experiment IV, 4 km inner nested domain, 850 mb NCEP Reanalysis plots..... | 116 |
| Figure C.1 | : 36 km domain of experiment IV total accumulated rain in the past 24 hours shown as filled colors, at 13 August 12 UTC with 12 hourly intervals, ending at 19 August 00 UTC, left column represents the 00 UTC, and right column 12 UTC for each forecast day..... | 118 |
| Figure C.2 | : 12 km domain of experiment IV total accumulated rain in the past 24 hours shown as filled colors, at 13 August 12 UTC with 12 hourly intervals, ending at 19 August 00 UTC, left column represents the 00 UTC, and right column 12 UTC for each forecast day..... | 120 |
| Figure C.3 | : 4 km domain of experiment IV total accumulated rain in the past 24 hours shown as filled colors, at 14 August 00 UTC with 12 hourly intervals, ending at 19 August 00 UTC, left column represents the 00 UTC, and right column 12 UTC for each forecast day..... | 122 |

LIST OF SYMBOLS

| | |
|-------------|--|
| B_p | : Model precipitation bias. |
| P_n^0 | : Observed precipitation for a given day at a point |
| P_n^M | : Model precipitation |
| P^O | : Total observed precipitation |
| T^{P_T} | : Daily precipitation threat score |
| $O_n^{P_T}$ | : Number of gridded observed daily precipitation in excess of PT |
| $F_n^{P_T}$ | : Number of model forecasts at excess of observed precipitation |
| $C_n^{P_T}$ | : The number of grid points where both observed and forecast precipitation exceeds PT. |
| σ | : Vertical model coordinate |
| p_s | : Surface pressure |
| p_t | : Top pressure |
| u, v | : Horizontal velocity |
| m | : Mass |
| f | : Coriolis effect |
| T | : Temperature |
| ω | : Tendency |
| D | : Horizontal and vertical diffusion and vertical mixing due to PBL turbulence, or dry convective adjustment. |
| c_p | : Heat capacity for moist air |
| g | : Gravity |
| ρ | : Density |

EFFECTS OF LATERAL BOUNDARIES AND RESOLUTION ON FLOOD PREDICTION: A CASE STUDY FOR ISTANBUL

SUMMARY

Significant amounts of loss of lives and economical problems occur due to flooding events. Recently, it was observed that even without significant amounts of rainfall, flooding could be seen due to the impacts of urbanization. For this reason, it is essential to predict rainfall and flood. In this study, in order to analyze the effects of lateral boundaries and horizontal resolution on flood simulation in Istanbul, four experiments are done using mesoscale model MM5. In the first experiment, a large domain with 18 km horizontal resolution is selected. In the second experiment, a smaller domain with the same horizontal resolution was chosen, to see the impacts of lateral boundaries. Furthermore, a third experiment was employed with 9 km horizontal resolution on the same domain of the second experiment to see the impacts of the horizontal resolution. Finally, a last experiment was done, in order to observe the meteorological pattern better, and provide an accurate flow of information to the inner domains to be constructed, with a much larger domain than all the previous experiments, consisted of a coarse domain with horizontal resolution of 36 km, and inner two domains with horizontal resolutions of 12 and 4 km respectively. Results of experiments were verified with the NCEP Reanalysis fields of 500 and 850 mb and satisfactory results were obtained. Daily total accumulated rainfall amounts and locations were compared in each experiment, leading to the fact that although increased resolution yielded detailed results, overall precipitation pattern obtained was similar in all runs.

SINIR KOŞULLARI VE ÇÖZÜNÜRLÜĞÜN SEL TAHMİNİNDEKİ ETKİLERİ: İSTANBUL ÇALIŞMASI

ÖZET

Sel olayları sonucunda önemli can kayıpları ve ekonomik problemler yaşanmaktadır. Son yıllarda büyük şiddetli bir yağış olmadan da şehirleşme etkisiyle sel oluşabileceği görülmüştür. Bu nedenle yağış ve selin tahmini önem taşımaktadır. Bu çalışmada, sınır şartları ve çözünürlüğün İstanbul'daki sel tahminindeki etkisini araştırmak amacı mezo ölçek model MM5 ile dört deney yapılmıştır. İlk deneyde, 18 km yatay çözünürlükte büyük bir bölge alınmıştır. İkinci deneyde, sınır koşulların etkisini incelemek amacı ile aynı çözünürlükte daha küçük bölge seçilmiştir. Bunun yanında, üçüncü bir deney ile ikinci deneyin alanına çözünürlüğün tahmindeki etkisine bakmak amacıyla 9km yatay çözünürlük uygulanmıştır. Son olarak son bir deney yapılarak, meteorolojik paterni daha iyi görmek ve oluşturulacak iç alanlara bilgi akışını daha doğru sağlamak amacıyla tüm deneylerden daha büyük bir alan seçilmiş 36 km yatay çözünürlükte ve buna, 12 ve 4 km'lik yatay çözünürlükte iç alanlar eklenmiştir. Deney sonuçları NCEP Reanalysis alanları ile 850 ve 500 mb da karşılaştırılmış ve tatmin edici sonuçlar alınmıştır. Günlük toplam yağış miktar ve alanları tüm deneyler için karşılaştırılmış ve düşük çözünürlükte daha detaylı sonuçlar alınmasına rağmen genel pattern tüm deneylerde benzer bulunmuştur.

1. INTRODUCTION

Heavy precipitation and flood are extremely significant meteorological events as they result in lost of lives, and destabilization of the economic conditions of the places in effect. For these reasons, it is very important to be able to accurately predict these events using modeling tools. It is a fact that even without extreme rain flooding events might occur because of urbanization. One of the very respected and important models used in numerical weather prediction is The Pennsylvania State University and The National Center for Atmospheric Research Mesoscale Model of which the fifth version, MM5, is used in this study.

The PSU/NCAR mesoscale modeling system consists of a mesoscale model and several auxiliary programs. These auxiliary programs are performed for the pre-processing and post-processing applications. MM5 model is a fifth-generation mesoscale meteorological model originally developed at Pennsylvania State University (Grell *et al.*, 1994). It is a popular and powerful model that assists to improve forecast of weather. The basic model has been under continuous improvement and testing for more than 20 years (e.g., Anthes and Warner, 1978; Anthes *et al.*, 1987) and has been used world-wide by hundreds of scientists for a variety of meteorological studies including flood simulation.

Meteorological models are used to simulate and forecast short-range meteorological conditions. In addition, operational use of weather prediction models has become widespread in recent years (Mass and Kuo, 1998). Mass *et al.* (2002) studied the effects of increasing horizontal resolution on the forecast skill by examining the results of two years of the University of Washington Real-Time MM5 Modeling and Verification System over the Pacific Northwest. They found that decreasing grid spacing did improve the reliability of the results, but does not necessarily improve significantly the skill accuracy of the forecasts.

Various sensitivity studies were done in the previous years for flood prediction employing different versions of this mesoscale model. These studies are summarized

in the next section and they provide a basis for this study. Alpert *et al.* (1996), for instance, investigates roles of lateral boundaries, initial conditions and topography in flood simulation near Genoa Region, which is of extreme importance for this study. Furthermore, study done by Colle and Mass (2000) employing a large domain of 36 km with nested inner domains of 12, 4, and 1.3 km and analyzing the predictions at each resolution with different model settings is also a key in this study. Main goal of all the analyzed studies on flood prediction was to find the appropriate domain by changing lateral boundaries and grid resolution and to detect the most suitable physics options for the region of influence, in order to obtain an approach in the prediction of future cases.

The main purpose of this study is flood prediction. The case study time chosen is the 16 August 2004 flood of Istanbul, which caused a village to be moved to a newer location. Although at the case study period, rainfall amounts were not extreme, this event is chosen, as it was the most recent phenomenon. Main reason for flood occurrence at this time was therefore, due to urbanization at prior hydrologic areas, and river basins.

In the next chapter, literature review will be done. In chapter 3, general overview of the mesoscale model used in this study (MM5) will be made. Moreover, in chapter 4, data and methodology of the study will be described. What is more, in chapter 5, experiment design and analysis will be explained. In chapter 6, precipitation analysis will be done. Finally, in the last section conclusion and future works will be mentioned.

2. PREVIOUS STUDIES

Studies of flood and precipitation prediction with models are not a recent subject. Over the years, scientists used various models and performed various tests on past events to obtain the best approaches for the prediction of future cases. In this chapter, previous studies focused on flood and precipitation prediction employing developing versions of The Pennsylvania State University / National Center for Atmospheric Research (PSU/NCAR) Mesoscale Model will be reviewed with the most emphasis given to sensitivity studies.

A study done by Kuo *et al.* (1988) examined Sichuan flood of 1981 in China by looking at different aspects of flooding. Since the flood investigated was a result of a long-lived southwest vortex, study concentrated on the prediction of this vortex, its evolution and its structure. PSU/NCAR Mesoscale Model with 13 unevenly spaced vertical sigma layers were used with 121x91 grid points and a grid distance of 80 km. The model used had bulk aerodynamic planetary boundary layer, ground temperature of a surface energy budget and slab model, Kuo and Anthes non-convective precipitation schemes, and Benjamin-Carlson cloud cover parameterization. Moreover, topographical data used in the study were National Center for Atmospheric Research (NCAR) 30-minute terrain data, which were processed by using Cressman objective analysis and smoothed not to have a sharp gradient over edges of the Tibetan Plateau. For initial conditions, National Meteorological Center's (NMC) global analysis data with objectively analyzed rawinsonde observations were used. Various experiments were carried out.

Firstly, the results of the first experiment, which is considered as the control experiment, were compared with the observations. Figures 2.1, 2.2, 2.3 and 2.4 show the observed and model predicted chosen fields. It was revealed through the model results that with simple physical options, smooth initial conditions and the grid size of 80 km, the model was successful at predicting the evolution of two vortices corresponding to the flood. In this way, it was shown that it was not a one vortex

phenomena explained by previous studies. Furthermore, predicted two vortices were leading to the occurrence of another vortex (the plateau vortex over Tibetan plateau) before the occurrence of heavy precipitation. Predicted rainfall was successful, with maximum of 48 hours precipitation and with 213 mm rainfall. Although actual maximum rainfall amount was 320 mm, model simulation should have been found adequate by considering that actual station data were point measurements.

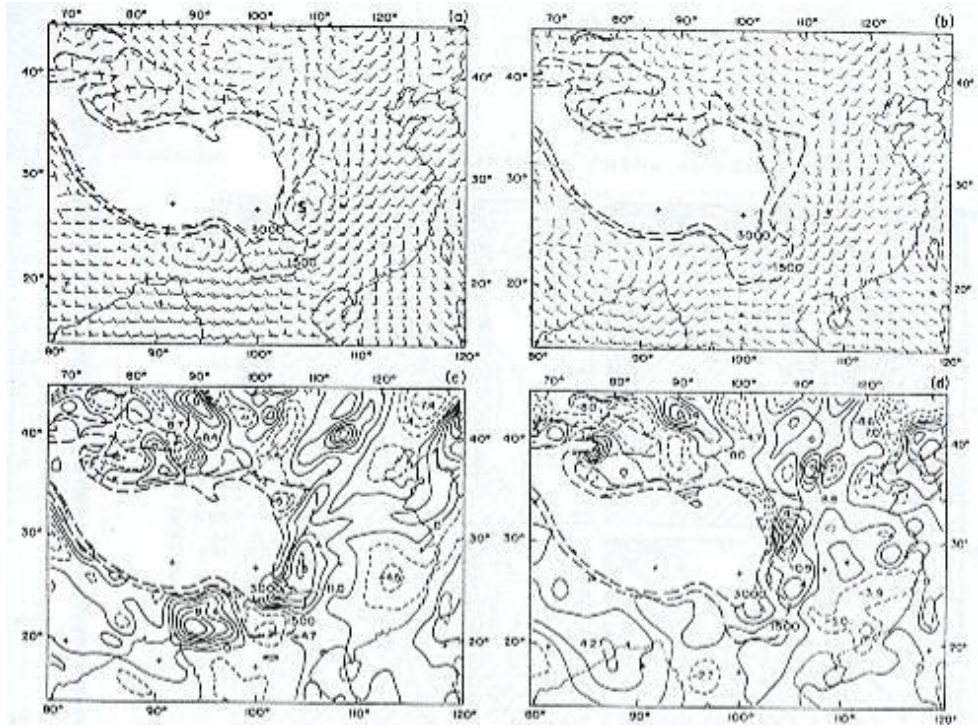


Figure 2.1: 700 mb wind barb (a, c) and vorticity (b,d) for 48h at 13 July 1981 00 UTC, control experiment (a, b) versus observations (c,d) (Kuo *et al.*, 1988)

Secondly, a comparison between control and model run without latent heat experiments was made. Results revealed that it was reasonable to divide the investigation of the southwest vortex into two stages; the formation and the development. Even though formation stage was not affected by the latent heat release, development stage and the evolution of plateau vortex had strong impacts of it. These findings were consistent with the previous studies on the subject. Moreover, another comparison was made between the control run and the run without the impact of surface fluxes. It was shown that surface fluxes did not influence considerably the formation state of the vortex. On the development stage, moderate impacts of surface fluxes were observed, however, the influences of these were mainly seen on mesoscale processes over the plateau. It was evident that without surface fluxes there were weak shear lines and weaker plateau vortex. Another

experiment called adiabatic experiment was done with removed latent heat release and surface energy flux. This was also compared with the control run. It has been shown that without these diabatic parameters, the model was still, although weak, able to capture the flood with vortices. From these results one can conclude that the southwest vortex investigated had a dynamically forced structure other than diabatical, with the impacts of diabatic processes, which seem to be pronounced at the development stage only. Furthermore, impacts of surface friction on model simulation were also examined. This was done with a model run without the impacts of surface friction and other diabatic terms. Simulation predicted a sooner occurred closed southwest vortex, which was observed to be stronger than the adiabatic run. Moreover, low-level kinetic energy of the vortex was observed to be half of the adiabatic run. These indicated that although differential friction did not have an impact on the formation of the vortex, surface friction was a sink of vorticity and kinetic energy.

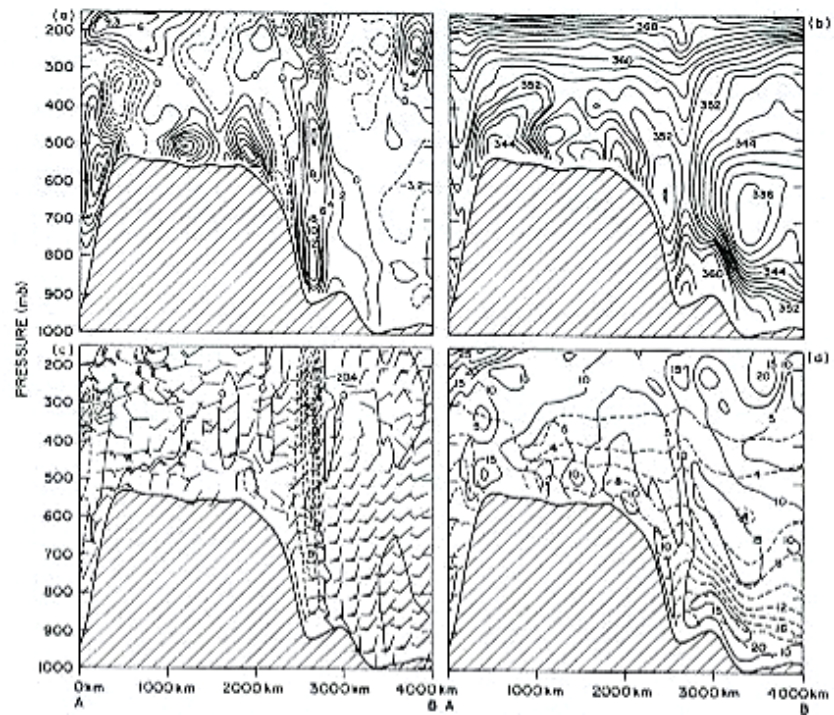


Figure 2.2: Vertical cross sections of relative humidity (a), equivalent temperature (b), horizontal wind barbs and vertical velocity (c), and specific humidity and horizontal wind speed (d) for control experiment at 13 July 1981 00 UTC (Kuo *et al.*, 1988).

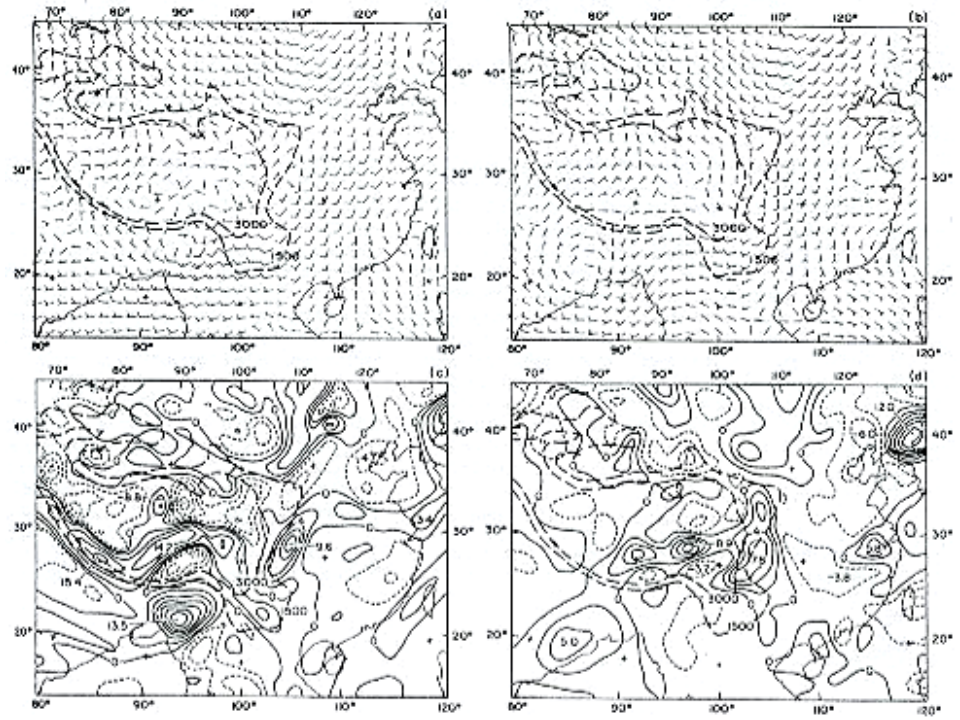


Figure 2.3: 500 mb wind barb (a, c) and vorticity (b,d) for 48h at 13 July 1981 00 UTC, control experiment (a, b) versus observations (c,d) (Kuo *et al.*, 1988).

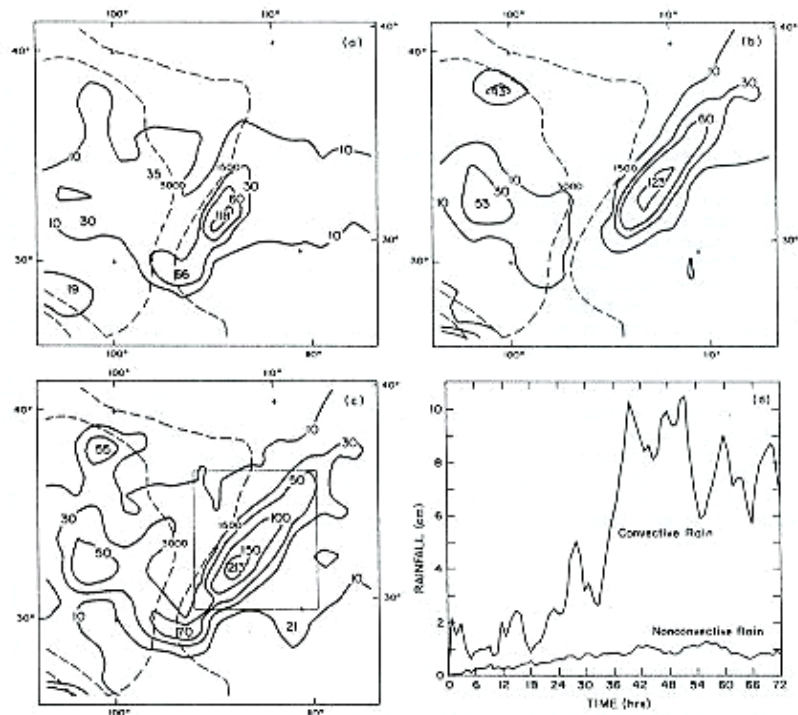


Figure 2.4: Control experiment 24 hour accumulated precipitation at 00 UTC 13 July (a), 0000 UTC 14 July (b), 48 hour accumulated precipitation at 00 UTC 14 July (c), and convective and non-convective rate of rainfall integrated over the box at (c) (Kuo *et al.*, 1988).

Finally, some experiments were done to predict the impacts of the Yun-Gui plateau. The first experiment was a trajectory analysis to determine the blocking effect of the plateau, which revealed a low-level flow blocking effect of the plateau. Moreover, in order to explain the vorticity source of the southwest vortex a back trajectory analysis from the center of vorticity to the southwest vortex was accomplished. This showed that there was no need for a powerful cyclonic vorticity for Yun-Gui plateau to produce a vortex through its associations with the monsoon current. In addition, for a more detailed analysis of the relationship of the Yun-Gui Plateau with the vorticity, a last model run was done without diabatic parameters with removed Yun-Gui Plateau from model topographical data. It was concluded that the plateau was playing a significant role in the blocking of westerly monsoon flows and in turn, promoting the southwest vortex.

Using sensitivity analysis on physical parameters, Giorgi (1991) investigated summer precipitation of Western United States as the next step to the studies on wintertime precipitation of the same region. Time period chosen for this study was July 1979. Since the study aimed to examine the subject climatologically, a one-month period was suitable to obtain the region's climatology. Data used in the study was First GARP Global Experiment (FGGE) data, which was produced by European Center for Medium Range Weather Forecasts (ECMWF) and sea surface temperature (SST) data of observational ECMWF. Model domain grid spacing was chosen to be 60 km. Data of 1436 observation stations were used to verify the model precipitation distribution. Using the observational data, gridded datasets, which had the same grids as MM4 were formed for the purpose of verification. Parameterizations used in this model were as follows, for radiative transfer Anthes radiative heating option, for cumulus Anthes (Kuo type) parameterization, for boundary layer physics Deardorff bulk planetary boundary layer model, and for surface physics Zhang and Anthes parameter. Three precipitation forecast skills were constructed. First of these was model precipitation bias which is represented by B_p and formulated as below:

$$B_p = \frac{100}{N_s P^O} \sum_{n=1}^{N_s} (P_n^M - P_n^O) \quad (2.1)$$

Here, N_s represented total number of daily data for grid points, P_n^O was the observed precipitation for a given day at a point and P_n^M was the model precipitation. Total observed precipitation is defined as :

$$P^O = \frac{1}{N_s} \sum_{n=1}^{N_s} P_n^O \quad (2.2)$$

Second was average daily precipitation threat score represented as T^{P_T} :

$$T^{P_T} = \frac{1}{N_d} \sum_{n=1}^{N_d} T_n^{P_T} \quad (2.3)$$

Here N_d represented total number of days and $T_n^{P_T}$ represented the daily precipitation threat score for a given day.

Third formulation constructed was:

$$T_n^{P_T} = \frac{C_n^{P_T}}{O_n^{P_T} + F_n^{P_T} - C_n^{P_T}} \quad (2.4)$$

$O_n^{P_T}$ is the number of gridded observed daily precipitation in excess of P_T on day n, $F_n^{P_T}$ is the corresponding number of model forecasts, and $C_n^{P_T}$ is the number of grid points where both observed and forecast precipitation exceeds P_T .

Model results of basic flow were compared with the national meteorological center (NMC) analyses; results revealed that model was successful to capture the basic pattern and evolution of the large-scale circulation. Differences are linked to the choices of the physics option and interpolation differences between ECMWF and NMC analysis for parameters like geopotential height. Furthermore, results of the accumulated precipitation show that model was correct predicting the location of maximum precipitation as the Rockies of southeastern Arizona, central New Mexico, Colorado and over Northern Wyoming, eastern Montana and western Washington. However, the model was not successful estimating the magnitude of maximum precipitation. Maximum precipitation was more than 50 cm for most of the regions, whereas observation results showed that values were not more than 15 cm. About 65% of the total precipitation estimated by the MM4 were originated by convective processes and total bias was huge and positive for all regions with maximum

amounts of 125-370 % and minimum of 67 %. Threat scores for light precipitation was than 0.75 for the precipitation thresholds between 0.01-0.1 cm and 0.11 for 5cm heavier precipitation threshold. Average daily precipitation threat scores were between 0.03 and 0.19.

Analyzing the event day by day revealed that the overestimation of precipitation amounts could be linked to numerical point storm (NPS) events. These events are unrealistic occurrence of precipitation at isolated grid points at short times scales. The reason behind these events is feedback between local circulations and release of latent heat of condensation. To remove the effect of NPS from the analysis two test experiments for a five-day run were done by removing surface sensible and latent heat fluxes and condensation heat release. In one of them, there was very little precipitation over land surfaces with accumulated 5 day rainfall not exceeding 0.5 cm. In the second test, daily precipitation amounts were found to be less than 5 cm. These revealed that convection started with surface flux induced instability and strengthened by condensation of latent heat release feed back process. Model physics options also played a role not capturing important stabilizing mechanisms like low level drying by downdrafts and cooling by rain and cloud evaporation. Moreover, surface physics and radiative transfer packages options may also have changed precipitation simulation. In addition, bulk boundary layer selection might not have been enough for close surface circulations over high terrains and the increase of boundary layer level due to summer conditions might also have played a role.

To find out the roles of precipitation parameters on model simulations, three precipitation schemes were tested namely, explicit moisture scheme, Arakawa-Schubert scheme and Kuo scheme. Four simulations carried out. One of them used represented as the explicit moisture (EM) scheme was coupled with the standard Kuo scheme. In second case, modified Kuo (MK) scheme was used with standard stable precipitation scheme. In third simulation, the modified Kuo (MKEM) scheme was coupled with the explicit moisture scheme. In the last case, Arakawa-Schubert (ASEM) scheme was coupled with the explicit moisture scheme. In general the model results were similar to Figure 2.5 showing the impacts of topographical forcing. Modified Kuo scheme and explicit moisture scheme, cases EM, MK, and MKEM tended to reduce precipitation and led to reduction in NPS occurrence. Case

ASEM, however, the location of maxima and NPS occurrence were similar to standard run, but the nature of precipitation evolution was non-convective unlike others even with the run including explicit moisture scheme. Table 2.1 lists the precipitation biases for the corresponding tests.

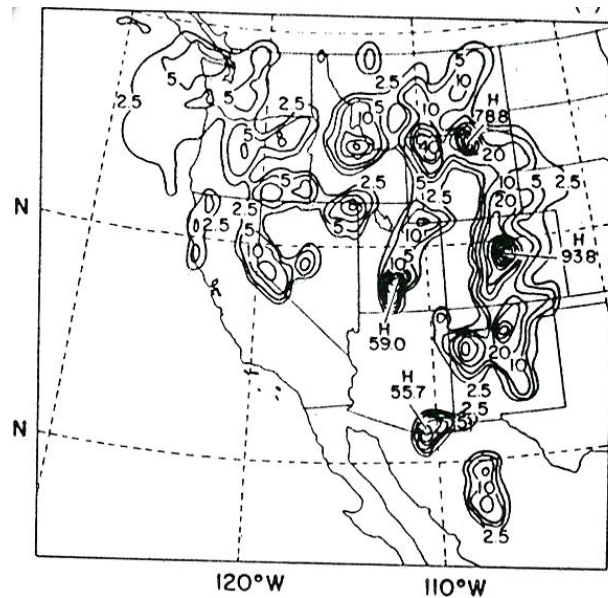


Figure 2.5: July 1979, thirty day accumulated rainfall obtained by MM4. (Giorgi *et. al*, 199)

To test the model sensitivity the addition of the enhanced surface physics and radiative transfer calculations, three simulations were done including Biosphere – Atmosphere Transfer Scheme (BATS), the medium-resolution boundary-layer scheme, and Climate Circulation Model (CCM1) radiation scheme replacing the ground temperature, bulk boundary layer and radiative transfer options of MM4. Case 1 run, BATSEM, included standard Kuo scheme and explicit moisture scheme, whereas Case2 run, BATSMK, had modified Kuo and standard stable precipitation scheme. Third Case, BATSMKEM, included explicit moisture scheme and the modified Kuo scheme. Results revealed that adding BATS to the model affected the precipitation depending on the scheme used and it also caused a drying and in turn, underestimation of precipitation. Analyzing the radiative flux, the study concluded that since both standard MM4 and BATS had same surface albedos, different computations of atmospheric radiation and clouds were the reason for BATS to produce more absorbed solar radiation and outgoing infrared radiation. Furthermore, latent heat and sensible heat fluxes detected by the two models were also different. The higher number of strong precipitation occurrences with BATS can be linked to

the higher surface temperatures and sensible heat flux and in turn enhanced lower instability at daytime. Another test with changed initial soil water content was done namely BATSSW, which showed increased precipitation levels overall. Table 2.2 lists the precipitation biases for the corresponding tests.

The study concludes that the summertime precipitation at the domain of interest is affected by the choice of surface processes in general. In addition, local moisture sources also take an important part in producing precipitation. Occurrence of NPS events were influenced more by the choice of precipitation schemes than BATS. As future work, the study aims to study the impacts of pressure gradient force and horizontal diffusion on sigma surfaces. (Giorgi *et al.*, 1991)

Table 2.1: Average precipitation and biases over the domain for different test runs (Giorgi *et al.*, 1991)

| | Standard MM4 | EM | MK | MKEM | ASEM |
|---|--------------|--------|--------|--------|--------|
| Average precipitation (cm day ⁻¹) | 0.081 | 0.057 | 0.058 | 0.033 | 0.069 |
| Percent of convective precipitation | 66.16 | 94.95 | 51.09 | 91.12 | 30.21 |
| Total bias (%) | 176.05 | 97.61 | 87.41 | 7.12 | 134.21 |
| Pacific Northwest bias (%) | 120.35 | 76.03 | 128.21 | 62.34 | 46.08 |
| Northern Rockies bias (%) | 230.49 | 152.88 | 114.00 | 24.85 | 156.40 |
| Central Rockies bias (%) | 373.52 | 250.91 | 201.33 | 86.04 | 316.79 |
| Southern Rockies bias (%) | 67.48 | 3.15 | -0.39 | -60.11 | 75.82 |
| Great Basin bias (%) | 67.28 | 2.77 | 35.41 | -51.25 | 36.61 |
| California bias (%) | 86.12 | -10.32 | -7.18 | -65.01 | 53.20 |

Table 2.2: Average precipitation and biases over the domain for different test runs including BATS (Giorgi *et al.*, 1991).

| | BATSEM | BATSMK | BATSMKEM (25 days) |
|---|--------|--------|-----------------------|
| Average precipitation (cm day ⁻¹) | 0.060 | 0.041 | 0.026 |
| Percent of convective precipitation | 97.53 | 51.39 | 96.03 |
| Total bias (%) | 85.21 | 29.57 | -23.61 |
| Pacific Northwest bias (%) | 15.29 | 49.81 | 3.25 |
| Northern Rockies bias (%) | 136.27 | 72.53 | -19.49 |
| Central Rockies bias (%) | 327.46 | 127.09 | 68.07 |
| Southern Rockies bias (%) | -33.95 | -37.15 | -70.90 |
| Great Basin bias (%) | -25.41 | -78.89 | -96.92 |
| California bias (%) | -45.58 | -62.42 | -94.61 |

In a study done by Alpert *et al.* (1996) boundary factors named as lateral boundary, initial fields and bottom topography and their impacts were studied for the lee cyclogenetic case during the Alpine Experiment (ALPEX) over the Gulf of Genoa between 3-6 March 1982. In order to distinguish the nonlinear interactions of different parameters, factor separation method was used. As previous studies done on the same case showed that topography did not play a major role, more importance was given in the study to the roles and interactions of lateral boundaries and initial fields. MM4 and for verification purposes Florida State University (FSU) regional

model was used. Four horizontal resolutions of 180, 80, 60, and 40 km were compared with the ECMWF analysis leading to the fact that higher resolution yields better simulations, shown in figure 2.6. Furthermore, the model run with the domain of 80 km grid size and 73x41 grids was repeated with different horizontal boundary conditions to illustrate the impact of lateral boundary conditions in model runs. Comparison between the observations and different domains with the 80 km grid resolution and different lateral boundaries revealed that the one that had closer lateral boundary (A) to Genoa was more consistent with observations. Domains of different lateral boundaries are shown in figure 2.7. A verification run with FSU model was also done, which was in a good agreement with model runs A and C. Since model result A was the best among the ones tested, it was evaluated in more detail, with 2° intervals for 19° - 29° E and with 31x46 grid numbers. Resulting six experiments revealed that the best result was obtained at the 40° N and 25° E, which fits the initial A domain.

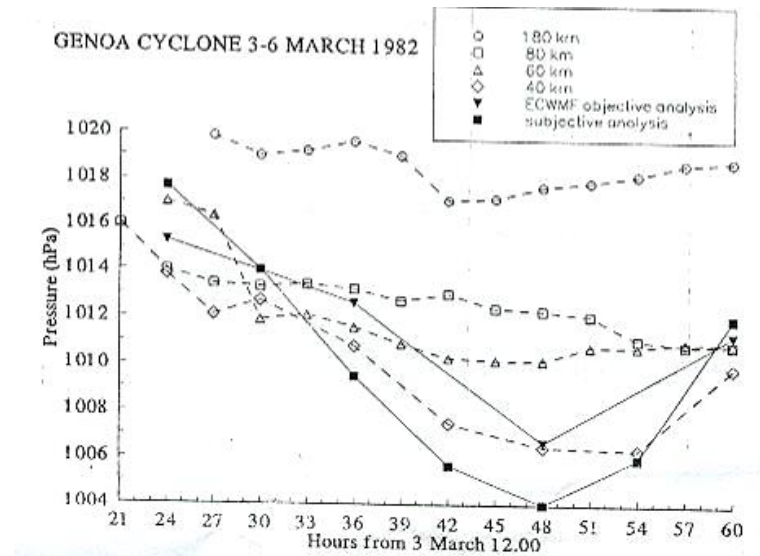


Figure 2.6: Comparison of four horizontal resolutions with ECMWF analysis (Alpert *et al.*, 1996).

Moreover, model runs with worst results had the domain with the boundary located too far away from the development and the one too close to the possible western boundary, revealing that there was an optimal distance for the lateral boundary. Keeping the lateral boundaries constant at 48, 36, 24 h intervals, the relationship between lateral boundaries and lee cyclogenesis was obtained. Results showed that

the lateral boundary conditions after 36 hours of initial time were more important for the cyclone development. In addition, in order to understand the roles of initial boundaries, lateral conditions and topography and their synergistic effects, experiments were done using factor separation method. Results are represented in figure 2.8. It was found out that toward the maximum deepening time, the impact of initial conditions were reduced as the contributions of other conditions were increased and between 30-42 h period, the contributions were as follows: 16% topography, 34 % lateral boundary, 50 % synergistic impacts, in which the lateral boundaries and initial conditions were the most dominant with a factor of about 54%. It was concluded that the contribution of topography was not more than 20% on the evolution of the lee cyclogenesis, which was consistent with the previous studies (Alpert *et al.*, 1996).

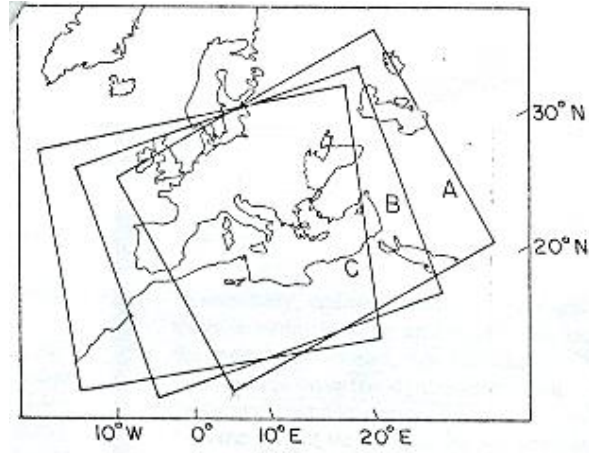


Figure 2.7 Different lateral boundary settings (Alpert *et al.*, 1996).

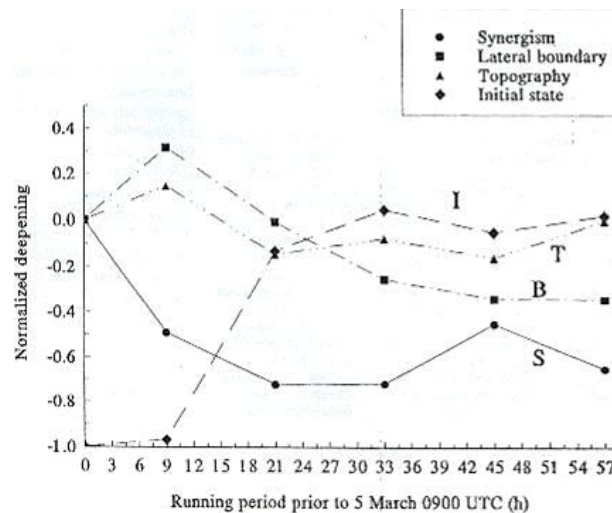


Figure 2.8 Contributions of initial conditions, lateral boundaries, topography and their synergism to cyclone deepening.

Colle and Mass (2000) investigated the flooding event of Pacific Northwest on 5-9 February 1996, which started with heavy rain in many mountain places such as Washington, Oregon and Columbia and led to a damage of 500 million dollars. Because of the heavy rain and snow melting at mountaintop, flood happened at the west of Cascade Mountains. In the study, MM5 model was used to simulate the precipitation corresponding to days of flooding and model variables were altered to obtain the best approach to predict the event. Four domains, of which one way nesting applied to each, were run simultaneously with grid distances of 36, 12, 4 and 1.33 km. For the 4 and 1.33 km resolution domains, the Cascade Mountains and coastal zone is integrated into the model with the 30-second topography by using Cressman type analysis, and smoothed. Figure 2.9 shows the model domain. Then, sea surface temperature (SST), and atmospheric data of National Center for Environmental Prediction (NCEP) were input to the model grids. The data were then improved with the insertion of surface and upper air observations with the same analysis method. The analysis generated this way was at 12-hour intervals and were given to the 36 km domain to generate the lateral boundary conditions. Model vertical layers were thirty-eight unevenly spaced sigma levels with maximum amount of levels in the boundary layer. Physics options used in the model were Kain – Fritsch for cumulus parameterization for the largest two domains, Blackadar planetary boundary layer parameterization, and Klemp and Durran's upper radiative boundary condition for all domains.

Model outputs were compared with surface observations of snow sensors, radar and surface wind profilers. Comparison with the surface observations of two stations revealed that the problem of the model was the timing of the passage of fronts and the strength of the front cooling during nighttime and after. Warm fronts were simulated 2 to 4 hours earlier while cold and occluded fronts were a few hours late. Furthermore, model was right at predicting most of the precipitation associated with fronts, there were times, however, that the model was not successful enough. This failure is linked to the fact that the precipitation was underestimated because prefrontal and subtropical moisture had not been arrived yet. Alternatively, it was statistically shown that prediction of precipitation was increased as the domain grid size decreased. Although 1.33 km resolution generated significant consistent precipitation, it also showed some precipitation, which did not occur. Snow pillow

sensor sites were also compared with the model results and except for the stations located at the rain-shadowed areas the model was accurate. In addition, the comparison with the wind profiler revealed more like the same results in both real time and model time. Although there were some timing errors, model was accurate to capture the most significant wind profile changes. What is more, observed and simulated reflectivities from radar observations were also used for comparison to model results. Model reflectivities were calculated by using the same relations of model physics options of cloud and precipitation mixing ratios. Results showed that 4 and 1.33 km domain results were consistent with the observational radar results, however as the resolution became 12 and 36 km, either because the effects of topography smoothed or/and model microphysics, advection of ice was less. Therefore, estimation of precipitation was reduced over the crest of the Cascades. Furthermore, sensitivity studies were also done changing vertical layers and the microphysics options. Studies on sigma levels revealed that increasing the number of vertical layers lead to increase in precipitation which was associated with the capture of mountain waves by the model. Sensitivity analysis on model physics options led to the fact that it was important to use ice microphysics during the cool season. Another simulation was done to detect the role of coastal range, which omits the coastal range. Results showed that amount of precipitation was decreased along the windward side of the mountain, and the coastal zone precipitation was increased in the lee side of the Cascades. (Colle and Mass, 2000)

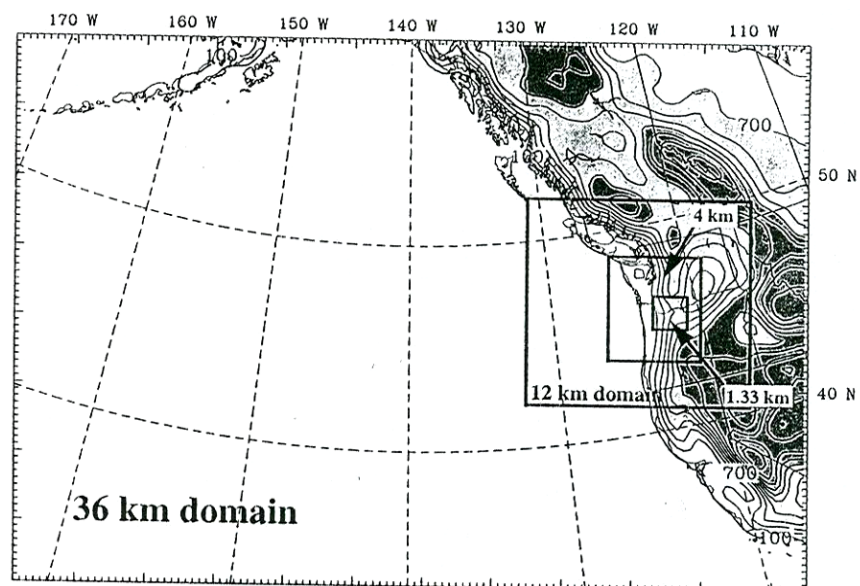


Figure 2.9 Model coarse domain with nested domains and terrain heights with a contour interval of 200m (Colle and Mass, 2000).

In order to determine extreme precipitation events, which were defined in the study as more than 300 mm rainfall per day, relevance with the model resolution Nielsen-Gammon *et al.* (2001) studied four different cases namely, the Southeast Texas flood of October 1994, The Del Rio – Texas flood of August 1998 (2 cases), the South Central Texas flood of October 1998. MM5 V2.11 was used in this study to test the cases with Blackadar planetary boundary layer, Goddard microphysics options. Data used for initial conditions were global NCEP analyses; to increase validation model results rawinsonde observations were also input to the model. Number of model vertical layers was 36. Model runs were than at various parameterized convections of 36, 18, 12, and 9 km; and explicit convections of 9, 6, and 4 km. Various sets of model runs were carried out which revealed the following results. Firstly, 36 km domain was found to be underestimating the amount of precipitation. Moreover, parameterized runs revealed a particular amount of precipitation as the resolution increased. Conversely, explicit runs were the ones producing much more precipitation with the decreased resolution. The individual grids having peak rainfall supported higher resolution simulations with higher peak accumulations. However, 9 km parameterized run revealed lower peak amounts than the 12 km or 18 km at some times. This meant performance of the parameterization reduced with decreasing resolution. Total precipitation was the same as or higher than observed total precipitation for explicit runs. Again, 9 km model run seemed to produce anomalously low peak rainfall totals.

Model result showed that increased resolution runs with Betts-Miller convective parameterization had more detailed, but unchanged patterns from the 36 km run. The explicit runs have narrower bands of precipitation detailed with a tendency for localized areas of high precipitation, which are consistent with the observed precipitation patterns of rain gauge and radar data. The local behavior was linked to the convective environment in the study. High-resolution runs provided useful information on the peak point totals and the small-scale variability of precipitation although distribution of precipitation was not much improved. The study concluded that to forecast the location of extreme rainfall, resolution improvements alone were not adequate; however under some circumstances forecasting peak amounts were possible. Betts-Miller parameterization was not found to be informative below 18

km. Finally, to simulate the events, cumulus parameterization, and grid spacing of 6 km or smaller was found to be consistent (Nielsen-Gammon *et al*,2001).

In the next chapter, general overview of the MM5 model will be done.

3. MM5

The model used in this study is MM5, which is the fifth generation of the mesoscale model generated by The National Center for Atmospheric Research and The Pennsylvania State University. The model was first developed from a mesoscale model used by Anthes, and then in 1978, Anthes and Warner documented the model. MM5 model has the basics of this first and original model but it is more developed with increased options. The changes since the model's first state are a multiple-nest capability, non-hydrostatic dynamics, a four-dimensional data assimilation (Newtonian nudging) capability, an increased number of physics options, and portability to a wider range of computer platforms (Dudhia *et al.*, 2004).

3.1 Model Vertical and Horizontal Grids

Pressure surfaces are generally used in the modeling system. Pressure surfaces are first interpolated to the model's vertical coordinate and then put into the model. The vertical coordinate of the model is represented by σ , and it is terrain following, becomes flat as moved upwards. The value of σ is zero at the model top and 1 at the model bottom. The outline and features of model vertical coordinate can be seen from Figure 3.1. Vertical sigma levels are obtained by the below equation.

$$\sigma = \frac{p - p_t}{p_s - p_t} \quad (3.1)$$

Here p_s and p_t are the surface and top pressures of the model, where p_t is a constant.

The scalar quantities of the horizontal grid are defined at the center of the grid square, which are called as cross points, whereas vector quantities such as eastward (u) and northward (v) velocity components are defined at the corners, which are known as dot points. Schematic of horizontal grids can be seen in Figure 3.2. The

variables other than vertical velocity are defined at half σ levels seen on Figure 3.1, vertical velocity, unlike other variables, is defined at full σ levels (Chen et al., 1994).

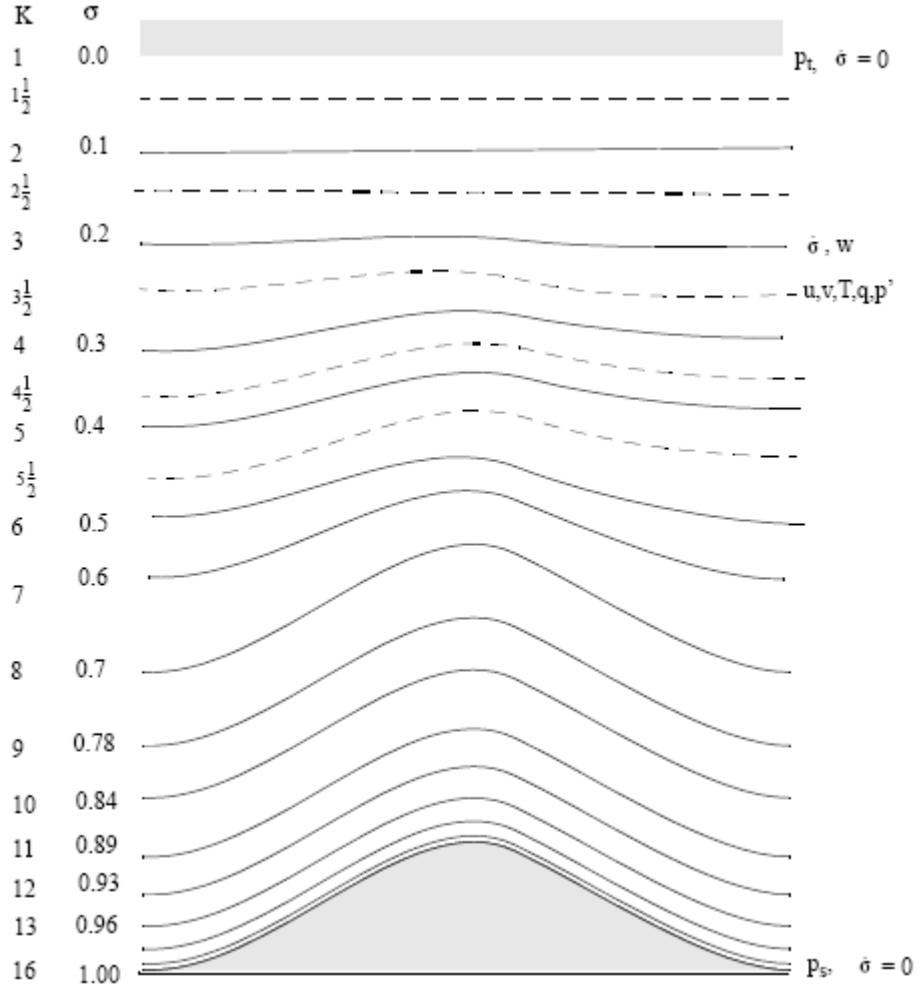


Figure 3.1: Vertical structure of the model (Chen *et al.*, 1994)

3.2. Governing Equations and Numerical Algorithms

3.2.1 Hydrostatic model equations

Hydrostatic model equations are given below under different titles. In these equations the quantity denoted by p^* is given by:

$$p^* = p_s - p_t. \quad (3.2)$$

Furthermore, terms denoted by D in below equations represent vertical and horizontal diffusion, and vertical mixing, which is either caused by the turbulence in the planetary boundary layer (PBL) or dry convective adjustment (Grell *et al.*, 1994).

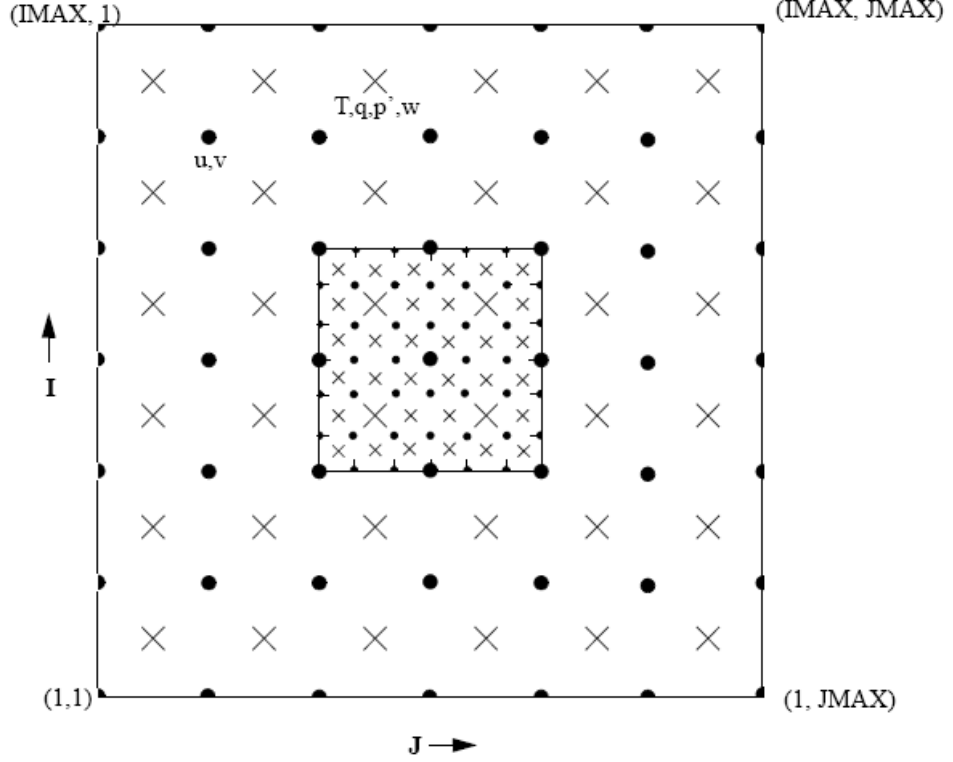


Figure 3.2: Horizontal representation of the dot and cross grid points with the smaller inner box representing a 3:1 coarse-grid distance to fine-grid distance ratio (Dudhia *et al.*, 2004).

3.2.1.1 Horizontal momentum equation

Horizontal momentum equations of the hydrostatic model are given below (Grell *et al.*, 1994).

$$\frac{\partial p^* u}{\partial t} = -m^2 \left[\frac{\partial p^* uu / m}{\partial x} + \frac{\partial p^* vu / m}{\partial y} \right] - \frac{\partial p^* u \sigma}{\partial \sigma} - mp^* \left[\frac{\sigma}{\rho} \frac{\partial p^*}{\partial x} + \frac{\partial \phi}{\partial x} \right] + p^* fv + D_u \quad (3.3)$$

$$\frac{\partial p^* v}{\partial t} = -m^2 \left[\frac{\partial p^* uv / m}{\partial x} + \frac{\partial p^* vv / m}{\partial y} \right] - \frac{\partial p^* v \sigma}{\partial \sigma} - mp^* \left[\frac{\sigma}{\rho} \frac{\partial p^*}{\partial x} + \frac{\partial \phi}{\partial x} \right] + p^* fu + D_v \quad (3.4)$$

3.2.1.2 Temperature

Hydrostatic model temperature equation is given below (Grell *et al.*, 1994).

$$\frac{\partial p^* T}{\partial t} = -m^2 \left[\frac{\partial p^* u T / m}{\partial x} + \frac{\partial p^* v T / m}{\partial y} \right] - \frac{\partial p^* T \sigma}{\partial \sigma} - p^* \frac{\omega}{\rho c_p} + p^* \frac{\dot{Q}}{c_p} + D_T \quad (3.5)$$

Here, ϖ is calculated from the equations below (Grell *et al.*, 1994).

$$\omega = p^* \dot{\sigma} + \sigma \frac{dp^*}{dt} \quad (3.6)$$

$$\frac{dp^*}{dt} = \frac{\partial p}{\partial t} + m \left[u \frac{\partial p^*}{\partial x} + v \frac{\partial p^*}{\partial y} \right] \quad (3.7)$$

3.2.1.3 Surface pressure

Surface pressure is obtained from the below equation.

$$\frac{\partial p^*}{\partial t} = -m^2 \left[\frac{\partial p^* u / m}{\partial x} + \frac{\partial p^* v / m}{\partial y} \right] - \frac{\partial p^* T \sigma}{\partial \sigma} \quad (3.8)$$

This equation is vertically integrated for usage.

$$\frac{\partial p^*}{\partial t} = -m^2 \int_0^1 \left[\frac{\partial p^* u / m}{\partial x} + \frac{\partial p^* v / m}{\partial y} \right] d\sigma \quad (3.9)$$

Pressure at sigma levels are obtained from the below version of (3.8).

$$\dot{\sigma} = \frac{1}{p^*} \int_0^\sigma \left[\frac{\partial p^*}{\partial t} + m^2 \left(\frac{\partial p^* u / m}{\partial x} + \frac{\partial p^* v / m}{\partial y} \right) \right] d\sigma' \quad (3.10)$$

Here σ' is a dummy variable that obtains a zero value at the zero σ level (Grell *et al.*, 1994).

3.2.2 Non-Hydrostatic model equations

For non-hydrostatic conditions, the model equations define a constant reference condition and perturbations from the reference condition (Grell *et al.*, 1994).

$$\begin{aligned}
p(x; y; z; t) &= p_0(z) + p(x; y; z; t) \\
T(x; y; z; t) &= T_0(z) + T_0(x; y; z; t); \\
\rho(x; y; z; t) &= \rho_0(z) + \rho_0(x; y; z; t):
\end{aligned} \tag{3.12}$$

3.2.2.1 Vertical coordinate

Model's vertical coordinate is given by equation (3.1).

3.2.2.2 Momentum

Horizontal momentum equations for non-hydrostatic model are as follows:

$$\begin{aligned}
\frac{\partial p^* u}{\partial t} &= -m^2 \left[\frac{\partial p^* uu / m}{\partial x} + \frac{\partial p^* vu / m}{\partial y} \right] - \frac{\partial p^* u \sigma}{\partial \sigma} + uDIV \\
&- \frac{mp^*}{\rho} \left[\frac{\partial p'}{\partial x} - \frac{\sigma}{p^*} \frac{\partial p^*}{\partial x} \frac{\partial p'}{\partial \sigma} \right] + p^* fv + D_u
\end{aligned} \tag{3.13}$$

$$\begin{aligned}
\frac{\partial p^* v}{\partial t} &= -m^2 \left[\frac{\partial p^* uv / m}{\partial x} + \frac{\partial p^* vv / m}{\partial y} \right] - \frac{\partial p^* v \sigma}{\partial \sigma} + vDIV \\
&- \frac{mp^*}{\rho} \left[\frac{\partial p'}{\partial x} - \frac{\sigma}{p^*} \frac{\partial p^*}{\partial x} \frac{\partial p'}{\partial \sigma} \right] + p^* fu + D_v
\end{aligned} \tag{3.14}$$

Vertical momentum equation for non-hydrostatic model is given below (Grell *et al.*, 1994).

$$\begin{aligned}
\frac{\partial p^* w}{\partial t} &= -m^2 \left[\frac{\partial p^* uw / m}{\partial x} + \frac{\partial p^* vw / m}{\partial y} \right] - \frac{\partial p^* w \sigma}{\partial \sigma} + wDIV \\
&- p^* g \frac{\rho_0}{\rho} \left[\frac{1}{p^*} \frac{\partial p'}{\partial \sigma} + \frac{T_v'}{T} - \frac{T_0 p'}{T p_0} \right] + p^* g [(q_c + q_r)] + D_w
\end{aligned} \tag{3.15}$$

3.2.2.3 Pressure

$$\begin{aligned}
\frac{\partial p^* p'}{\partial t} &= -m^2 \left[\frac{\partial p^* up' / m}{\partial x} + \frac{\partial p^* vp' / m}{\partial y} \right] - \frac{\partial p^* p' \sigma}{\partial \sigma} + p' DIV \\
&- m^2 p^* \gamma p g \frac{\rho_0}{\rho} \left[\frac{\partial u / m}{\partial x} - \frac{\sigma}{mp^*} \frac{\partial p^*}{\partial x} \frac{\partial u}{\partial \sigma} + \frac{\partial v / m}{\partial y} - \frac{\sigma}{mp^*} \frac{\partial p^*}{\partial y} \frac{\partial v}{\partial \sigma} \right] \\
&+ \rho_0 g \gamma p \frac{\partial w}{\partial \sigma} + p^* \rho_0 g w
\end{aligned} \tag{3.16}$$

Pressure equation is given above (Grell *et al.*, 1994).

3.2.2.4 Temperature

Non-hydrostatic model temperature equation is given below (Grell *et al.*, 1994).

$$\begin{aligned} \frac{\partial p^* T}{\partial t} = & -m^2 \left[\frac{\partial p^* u T / m}{\partial x} + \frac{\partial p^* v T / m}{\partial y} \right] - \frac{\partial p^* T \sigma}{\partial \sigma} + T \text{DIV} \\ & + \frac{1}{\rho c_p} \left[p^* \frac{\partial p}{\partial T} - \rho_0 g p^* w - D_p \right] + p^* \frac{\dot{Q}}{c_p} + D_T \end{aligned} \quad (3.17)$$

3.3 Model Dynamics

3.3.1 Finite differencing

3.3.1.1 Spatial finite differencing

In nonhydrostatic finite differencing, horizontal velocity is staggered according to B-grid staggering. Vertical velocity is staggered vertically. Vertical averaging is done as it helps the formation of the non-uniform grid lengths and nonlinear fields like temperature to be suitably weighted. Triple averaging done on horizontal momentum is according to the methods of Anthes (1972).

Hydrostatic finite differencing has specific equations for advection, Coriolis and heating without the involvement of the divergence terms. Furthermore, computation of geopotential height helps the water loading at the usage of explicit moisture scheme (Grell *et al.*, 1994).

3.3.1.2 Temporal finite differencing

For both nonhydrostatic and hydrostatic model, temporal finite differencing involves the usage of leapfrog steps on all variables with an Asselin filter, which helps the solution related to leapfrog remain in the scheme.

A second-order leapfrog time-step scheme is used for these equations, but some terms are handled using a time-splitting scheme. In the leapfrog scheme, the tendencies at time n are used to step the variables from time $n-1$ to $n+1$. This is valid for most of advection, coriolis, and buoyancy terms. For diffusion and microphysics where the tendencies are calculated at time $n-1$, a forward step is used to step the

variables from $n-1$ to $n+1$. Some of the radiation and cumulus options use a constant tendency over periods of many model time steps and are only recalculated every 30 minutes or so, on contrary for certain terms such as sound waves, precipitation fall, and PBL tendencies terms, required model time step for prediction is shorter step due to stability conservation. Figures 3.4, 3.5 and 3.6 show the short and long time steps for the initialization, n and $n+1$ time steps.

For numerical stability, some processes are handled implicitly. An implicit time scheme is one in which the tendencies of variables depend not only on the present and the past values, but also the future values. These require a matrix inversion to put into operation. In 1-d column calculations for vertical sound waves and vertical diffusion, the implicit schemes are used in MM5 (Grell *et al.*, 1994).

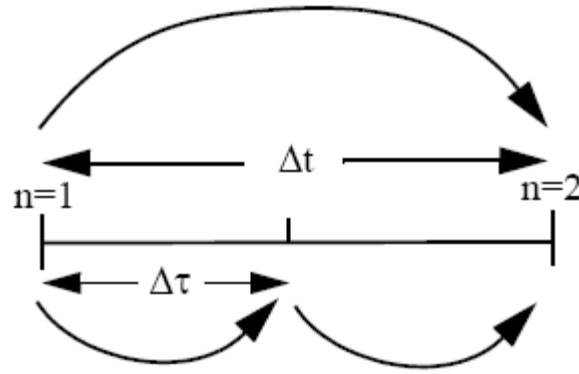


Figure 3.4: First time step (Grell *et al.*, 1994)

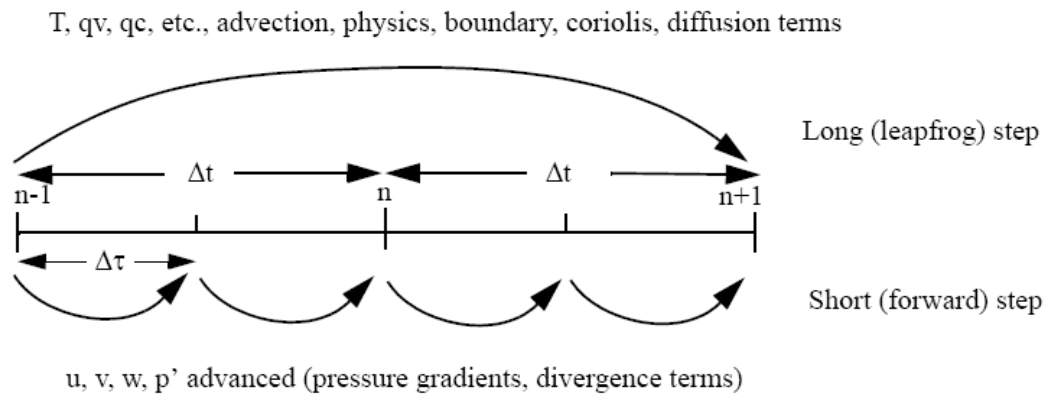


Figure 3.5: Time step n showing short and long time steps for various parameters (Grell *et al.*, 1994).

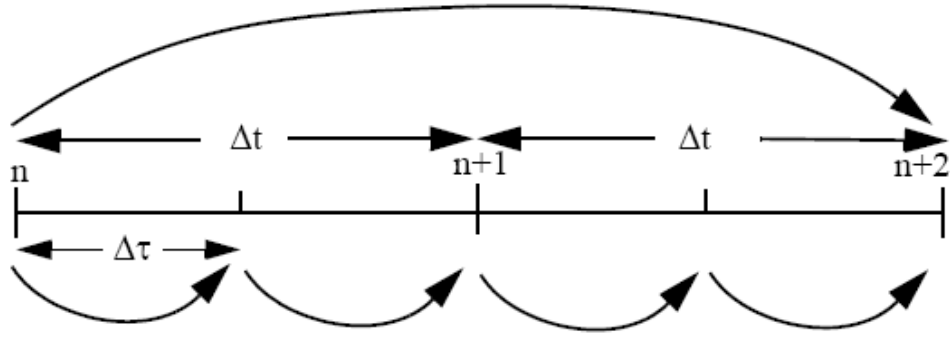


Figure 3.6: Time step $n+1$ showing short and long time steps

3.3.2 Time splitting

The non-hydrostatic equations of the model permit sound waves, which are fast and require short time steps for numerical stability, and the hydrostatic model equations in the same manner permit the fast external gravity waves. Therefore, in order to split the impacts of these on model results and in order to increase the efficiency of the model results, a time splitting scheme is applied (Grell *et al.*, 1994).

3.3.2.1 Nonhydrostatic time splitting

Splitting the terms associated with acoustic waves directly from the equations is possible. Terms associated with these waves can be handled in shorter time steps as required to make the model more efficient and the other terms can be handled in less frequent times. Time splitting solution used in the nonhydrostatic equations is the semi-implicit scheme of Klemp and Wilhelmson (1978) for the short time step. Furthermore, another key step in time splitting to increase efficiency is the implicitly handling of the vertical propagation of sound waves, which allows the short time step to be independent of the vertical resolution of the model. In addition, horizontal propagation of sound waves is controlled by the divergence dumping technique of Skamarock and Klemp (1992). In this technique, as the temperature and moisture do not contain no high-frequency terms contributing to acoustic waves, leapfrog step is used to predict them. The slow terms for momentum and pressure are also treated using the leapfrog steps, however this time transition from $t-\Delta t$ to $t+\Delta t$ is split into typically four steps at which momentum and pressure are updated continuously (Grell *et al.*, 1994).

3.3.2.2 Hydrostatic time splitting

External gravity waves, which are quick, small in intensity, and have little energy, affect the stability criterion of these equations. As the rate of change of these waves in time is slow compared to Rossby wave time scale, splitting these from the solutions is possible. Splitting method chosen for these equations is the Madala (1981) method, which is a scheme extracting the terms dominated by gravity modes from the terms dominated by Rossby modes. Extraction is done separating the motion as eigenmodes. Unlike the splitting method described for the nonhydrostatic model, the method here calculates correction terms for the hydrostatic equations. Time step of the fast modes are dependent on the modes, for this reason to effectively separate of modes, a vertical normal mode initialization mode developed by Errico (1986) is used, which computes the vertical modes at the model start. On the latest versions of the model, the external and the most quick internal mode is handled with varying time steps, which leads for the slow tendencies to be twice larger than the values on previous algorithms used and to be comparable to the nonhydrostatic ones (Grell *et al.*, 1994).

3.3.3 Lateral boundary conditions

Sponge boundary conditions are obtained by an equation not involving the Newtonian terms, and these conditions are not in use for the nonhydrostatic model parts. Unlike sponge boundary conditions, the nudging boundary conditions are used in nonhydrostatic parts of the model to nudge pressure perturbation to the observations or large-scale simulations and involve the addition of Newtonian and diffusion terms. In nonhydrostatic model solutions, vertical velocity is not nudged and can differ independently for the zero gradient places, which are latter rows and columns. The values at the inflow points for vertical velocity components, which are needed to calculate the nonlinear horizontal momentum flux divergence terms, are attained from interior points. Moisture variables such as cloud water, rainwater, snow and ice are zero on inflow and zero gradient on outflow (Grell *et al.*, 1994).

3.3.4 Upper radiative boundary condition

This is an option of the nonhydrostatic model developed by Klemp and Durran (1983) and Bougeault (1983), which creates a boundary condition for the wave energy to pass without being reflected. The calculation involves the wave numbers and Fourier components. It is combined with the implicit pressure/vertical momentum calculation and used involving Klemp and Durran's suggestion that the finite differencing of pressure gradients and divergences are needed to define the effective wave numbers. When B-grid staggering is used, the effective wave numbers can be expressed in terms of the dimensionless wave numbers (Grell *et al.*, 1994).

3.3.5 Mesh refinement scheme and feedback

Grids of the model have to be in parallel with the coordinates of the model. The mesh refinement scheme used is an interactive two-way scheme that promotes the usage of overlapping and translating grids with refinement levels. In order to obtain numerical stability, the solution in the overlap region must be the same. For this reason after each time-step of the overlapping grids, the boundary conditions in the region are given by the overlapping mesh. The ratio between refinement levels, which is a temporal, and spatial grid augmentations, is taken as three.

Interpolation to the domains is done on the basis of the studies of Smolarkiewicz and Grell (1992). This method not only is used on the beginning of the new nests, but also on defining the boundaries of fine meshes. The approach used consists of a class of schemes obtained from the monotone advection algorithms of Smolarkiewicz and Grell (1992), which state that when distance vector replaces the velocity vector, interpolation problem is the same as advection problem. Interpolation problem of MM5 involves both shape preservation and monotonicity, so the Flux Corrected Transport (FCT) scheme. This scheme employs high-order accurate constant-grid-flux dissipative algorithms developed by Tremback et al. (1987). Limiters of the equations are the ones that are defining the monotonicity of the scheme and are specified by Zalesak (1979). High and low order fluxes are calculated from the advection schemes of the Tremback et al. (1987). The order of accuracy used to interpolate boundary conditions to finer meshes is four, however, to start new nests, the order of accuracy is six. Boundary interpolation is done on the remotest two

rows and columns of the nest, unlike nest starting on which interpolation is on the whole domain.

When there is a 2-way interaction between the mother domain and its finer domain, the finer domain feed back of meteorological fields to the mother domain leads noise on the coarser domain. In order to stop this, the smoother method of Shapiro (1970) is used in the current versions. In addition, the nine point averager method of (Zhang et al. 1986 also stays as an option, which can be chosen to work with one coarse domain and one finer domain. Furthermore, a smoother-desmoother is also applied in the model to the coarse domain where the coarse values are replaced by the nested values. . This method filters the short waves not touching the long ones in two steps. Firstly, fields are smoothened by the removal of short waves and secondly, remaining waves are brought back to their prior amplitudes (Grell *et al.*, 1994).

3.3.6 Map projection

There are three projection types available for the modeling system, Polar stereographic, Lambert conformal, and Mercator. Lambert Conformal projection is suitable for mid latitudes. In this projection the shapes of geographic features are conserved (Grell *et al.*, 1994).

3.4 Model Physics

3.4.1 Horizontal diffusion

Horizontal diffusion equations of the model are of second order for the border grids of the lateral boundaries of the coarsest domain and fourth order at the grids inside the coarse domain and at the whole finer meshes (Grell *et al.*, 1994).

3.4.2 Dry convective adjustment

When in the model atmosphere there are super adiabatic layers created, a simple dry convective adjustment scheme, which works for one time on the whole sounding

preserving the vertical integral of internal and potential energy, is used to cancel them (Grell *et al.*, 1994).

3.4.3 Precipitation physics

Precipitation schemes used in MM5 is of two types namely, explicit and implicit schemes. The differences between these two are as follows, the explicit schemes handle the resolved precipitation physics whereas the implicit schemes handle the non-resolved precipitation physics. What is more, the two schemes mentioned can operate at a grid at the same time. Additionally, for finer grid resolutions for the times of highly resolved convective precipitation, it is not possible to make the distinction and to define the contrast between convective and stable precipitation. For this reason, the important terms in MM5 precipitation schemes will be resolved, non-resolved, and explicit, implicit. On contrary, the model can also make dry runs, or fake dry runs. In the first one, moisture is taken as passive and in the second one the latent heat release options are eliminated (Grell *et al.*, 1994).

3.4.3.1 Simple ice moisture scheme

Simple ice moisture scheme adds ice phase processes, does not include supercooled water and immediate melting of snow below freezing level. This scheme involves ice phase processes below 0°C and treats cloud water as cloud ice and rain as snow. Size distributions are assumed to be of Marshall Palmer type for all the processes Figure 3.3 simplifies the simple ice scheme with an illustration (Grell *et al.*, 1994), (Dudhia *et al.*, 2004).

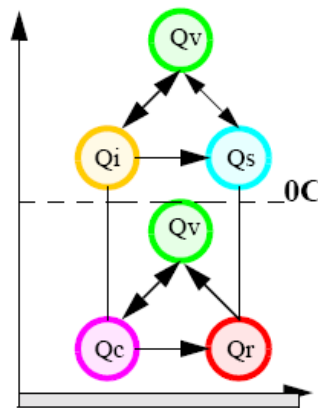


Figure 3.7: Dudhia simple ice scheme (Dudhia *et al.*, 2004).

3.4.3.2 Kain Fritsch 2 cumulus scheme

The original Kain Fritsch scheme is a mass flux parameterization, which predicts the upward, downward features, cloud and precipitation, entrainment, detrainment, removing all available buoyant energy in the relaxation time. Method used to predict the existence of instability and in case of existence to choose the correct features of the convective clouds to be formed, is the Lagrangian method of Simson and Wiggert (1969) and Kreitzberg and Perkey (1976) and the vertical momentum dynamics of Donner (1983). The original scheme was investigated in three components as convective trigger function, mass flux formulation, and closure assumptions. The new Kain Fritsch 2 scheme, however, has changes in the components such as updraft formulation in terms of minimum entrainment rate, variable cloud radius, variable minimum cloud depth threshold, downdraft and the convective assumption and has the inclusion of shallow convection. For instance, changes in updraft are inclusion of a minimum entrainment rate, cloud radius varies as a function of subcloud layer convergence, and minimum cloud depth becomes a function of cloud base temperature, shallow convective clouds, which do not generate precipitation, are active. Similarly, the changes in downdraft parameterization are introduction of a new algorithm and mass flux. Finally, change in the closure approximation is summarized as change in the calculation of CAPE. (Kain *et.al.*, 2002), (Dudhia, *et. al.*, 2004)

3.4.4 Planetary boundary layer parameterizations

Surface Energy Equation used in the model has the basis of the Blackadar (Zhang and Anthes 1982) force-restore method. Net radiative fluxes depend on the basis of Benjamin (1983). Sensible heat flux and surface moisture flux used is dependent on the PBL scheme chosen. Bulk aerodynamic physics is defined by the methods of Deardorff (1972). Vertical diffusion uses the K theory and moist vertical diffusion involves the impacts of moist adiabatic processes defined by Durran and Klemp (1982) in cloudy air. (Grell *et. al.*, 1994).

3.4.4.1 MRF Planetary boundary layer (PBL)

This scheme is known also as Hong-Pan PBL, which is suitable to obtain high-resolution in PBL. The method used in this scheme is Troen-Mahrt representation of countergradient term and K profile in the well-mixed PBL. An implicit scheme is used for vertical diffusion in order to tolerate longer time steps (Dudhia, *et al.*, 2004).

3.4.5 Atmospheric radiation parameterization scheme

There is a longwave and a shortwave radiation scheme. These have relations with the cloud and precipitation fields, surface and the atmosphere. For long wave absorption the method applied is Stephens' (1984) method with the emissivity equations of Rodgers (1967). For shortwave radiation, the cloud back-scattering and absorption is again obtained from the works of Stephens and the function of absorption is obtained from Lacis and Hansen (1974) (Grell *et al.*, 1994).

3.4.5.1 Rapid radiative transfer model (RRTM)

This is a longwave radiation scheme, but is combined with the cloud radiation shortwave scheme when used in the model. The method used is an extremely accurate method obtained by Mlawer *et al.* 1997. This is a rapid radiative transfer model including the impacts created by the detailed absorption of CO₂, water vapour, and O₃ with the help of a correlated-k model. It works with the cloud and precipitation schemes of the model (Dudhia, *et al.*, 2004).

3.4.6 Surface scheme

Five layer soil model includes the temperatures predicted in 1,2,4,8,16 cm layers. Using the vertical diffusion equation. Thermal inertia used vertically resolves diurnal temperature variation helping to have more rapid response of surface temperature (Dudhia, *et al.*, 2004).

3.5 Model Components

MM5 consists of programs that work individually to provide the transition for each other. The first program in the modelling system is TERRAIN, which creates grids

and rectangular domains of interest, according to user specifications and interpolates terrestrial data to the chosen domain. The interpolation is done according to various map projections, either Mercator, Lambert Conformal, or Polar Stereographic projection. The next program REGRID, which involves two programs called pregrid and regridder, chooses the meteorological data corresponding to the specified time period among the data file and interpolates them to the TERRAIN output. The third program, which is either LITTLE_R or RAWINS, is optional, it increases the variety of data with the addition of the observational data from either surface or rawinsonde observations, and strengthens the detail. The next program is INTERPF. This program functions to do the vertical interpolation from pressure levels to the σ -coordinate. Then the last program MM5 is executed according to the chosen physics options to do the numerical weather prediction process. After this part, another program called INTERPB is available and optional to back-integrate the data from sigma to pressure levels or NESTDOWN is available and optional to integrate to have a better grid interpolating model data again. Furthermore, the modelling system can be processed in the TERRAIN, REGRID, and INTERPF sequence with an additional program called 3DVAR to put the satellite data into the model. The outputs from individual programs can be viewed with graphical packages such as RIP or GRAPH. MM5 requires terrain and landuse data, and gridded atmospheric data in order to work.

4. DATA

There are three types of data used in this study, terrestrial data and meteorological data, and for verification purposes the satellite data. Terrestrial data as terrain height and land use types are obtained from the United States Geological Survey's (USGS) data. The meteorological data used in model runs is obtained from the National Center for Environmental Prediction (NCEP) and the National Center for Atmospheric Research (NCAR) Reanalysis Data. Satellite data used in this study are obtained from Tropical Rainfall Measuring Mission (TRMM) of the NASA, Goddard Institute of Earth Sciences, Data and Information Services Center.

4.1 Terrestrial Data

These data are used in the first step of the MM5 modelling system, the TERRAIN program. In order to construct the domains, terrain program requires terrain elevation, and vegetation data.

4.1.1 Terrain height data

Terrain height data used in this study United States Geological Survey's (USGS) terrain height data. It consists of six resolutions namely 1-degree, 30-, 10-, 5-, 2-minutes and 30-second United States Geological Survey's (USGS) data. Lower resolution data are created from the 30 seconds USGS data. Details on data are given in Table 1. The relevant dataset from the list is chosen for the selected grid distance of the model run.

Table 4.1: Terrain height data classes according to resolution selected (Dudhia *et al.*, 2004)

| Resolution | Data source* | Coverage | Size(bytes) |
|-------------------------------|---|--|--|
| 1 deg. (111.0 km) | USGS | Global | 129,600 |
| 30 min. (55.0 km) | USGS | Global | 518,400 |
| 10 min. (18.5 km) | USGS | Global | 4,665,600 |
| 5 min. (9.25 km) | USGS | Global | 18,662,400 |
| 2 min. (3.70 km) | USGS | Global | 116,640,000 |
| Tiled 30 sec. (0.925 km)** | GTOPO30 by U.S. Geological Survey's EROS Data Center in late 1996 | Global (33 tiles: 40° lon. x 50° lat. or 60° lon. x 30° lat.) | 57,600,000 or 51,840,000 for each of tiles |
| 30 sec. (0.925 km) | USGS | Global*** | 1,866,240,000 |

4.1.2. Vegetation data

There are three types of vegetation data that can be used for the MM5 program TERRAIN, one is a 13 category global coverage vegetation data with resolutions of 1 degree, 30 and 10 minute, the other is a 17 category, North-American coverage vegetation data with resolutions of 1 degree, 30, 10, 5, 2 minutes and 30 seconds, and the last one is a 25 category, global coverage vegetation data with the resolution of 1 degree, 30, 10, 5, 2 minutes and 30 seconds. In this study the 25 category vegetation data is chosen, as its coverage is wider and more detailed. Details of the third type vegetation data can be seen from Table 4.2, and from Table 4.3, the 25 categories and associated physical parameters of third type vegetation can be seen.

Table 4.2: Vegetation data classes according to resolution selected (Dudhia *et al.*, 2004)

| Resolution | Data source | Coverage | Size(bytes) |
|--------------------|-------------|----------|---------------|
| 1 deg. (111.0 km) | USGS | Global | 1,620,000 |
| 30 min. (55.0 km) | USGS | Global | 6,480,000 |
| 10 min. (18.5 km) | USGS | Global | 58,320,000 |
| 5 min. (9.25 km) | USGS | Global | 233,280,000 |
| 2 min. (3.70 km) | USGS | Global | 1,458,000,000 |
| 30 sec. (0.925 km) | USGS | Global | 933,120,000 |

Table 4.3: 25 Category vegetation classes of type 3 vegetation data with physical parameters for northern hemisphere summer and winter.

| Vegetation Integer Identification | Vegetation Description | Albedo(%) | | Moisture Avail. (%) | | Emissivity (% at 9 μ m) | | Roughness Length (cm) | | Thermal Inertia (cal cm ⁻² k ⁻¹ s ^{-1/2}) | |
|-----------------------------------|------------------------|-----------|-----|---------------------|-----|-----------------------------|-----|-----------------------|------|---|------|
| | | Sum | Win | Sum | Win | Sum | Win | Sum | Win | Sum | Win |
| 1 | Urban | 18 | 18 | 10 | 10 | 88 | 88 | 50 | 50 | 0.03 | 0.03 |
| 2 | Drylnd Crop. Past. | 17 | 23 | 30 | 60 | 92 | 92 | 15 | 5 | 0.04 | 0.04 |
| 3 | Irrg. Crop. Past. | 18 | 23 | 50 | 50 | 92 | 92 | 15 | 5 | 0.04 | 0.04 |
| 4 | Mix. Dry/Irrg.C.P. | 18 | 23 | 25 | 50 | 92 | 92 | 15 | 5 | 0.04 | 0.04 |
| 5 | Crop./Grs. Mosaic | 18 | 23 | 25 | 40 | 92 | 92 | 14 | 5 | 0.04 | 0.04 |
| 6 | Crop./Wood Mosaic | 16 | 20 | 35 | 60 | 93 | 93 | 20 | 20 | 0.04 | 0.04 |
| 7 | Grassland | 19 | 23 | 15 | 30 | 92 | 92 | 12 | 10 | 0.03 | 0.04 |
| 8 | Shrubland | 22 | 25 | 10 | 20 | 88 | 88 | 10 | 10 | 0.03 | 0.04 |
| 9 | Mix Shrb./Grs. | 20 | 24 | 15 | 25 | 90 | 90 | 11 | 10 | 0.03 | 0.04 |
| 10 | Savanna | 20 | 20 | 15 | 15 | 92 | 92 | 15 | 15 | 0.03 | 0.03 |
| 11 | Decids. Broadlf. | 16 | 17 | 30 | 60 | 93 | 93 | 50 | 50 | 0.04 | 0.05 |
| 12 | Decids. Needlf. | 14 | 15 | 30 | 60 | 94 | 93 | 50 | 50 | 0.04 | 0.05 |
| 13 | Evergm. Broadlf. | 12 | 12 | 50 | 50 | 95 | 95 | 50 | 50 | 0.05 | 0.05 |
| 14 | Evergm. Needlf. | 12 | 12 | 30 | 60 | 95 | 95 | 50 | 50 | 0.04 | 0.05 |
| 15 | Mixed Forest | 13 | 14 | 30 | 60 | 94 | 94 | 50 | 50 | 0.04 | 0.06 |
| 16 | Water Bodies | 8 | 8 | 100 | 100 | 98 | 98 | .01 | .01 | 0.06 | 0.06 |
| 17 | Herb. Wetland | 14 | 14 | 60 | 75 | 95 | 95 | 20 | 20 | 0.06 | 0.06 |
| 18 | Wooded wetland | 14 | 14 | 35 | 70 | 95 | 95 | 40 | 40 | 0.05 | 0.06 |
| 19 | Bar. Sparse Veg. | 25 | 25 | 2 | 5 | 85 | 85 | 10 | 10 | 0.02 | 0.02 |
| 20 | Herb. Tundra | 15 | 60 | 50 | 90 | 92 | 92 | 10 | 10 | 0.05 | 0.05 |
| 21 | Wooden Tundra | 15 | 50 | 50 | 90 | 93 | 93 | 30 | 30 | 0.05 | 0.05 |
| 22 | Mixed Tundra | 15 | 55 | 50 | 90 | 92 | 92 | 15 | 15 | 0.05 | 0.05 |
| 23 | Bare Grnd. Tundra | 25 | 70 | 2 | 95 | 85 | 95 | .10 | 5 | 0.02 | 0.05 |
| 24 | Snow or Ice | 80 | 82 | 95 | 95 | 95 | 95 | 0.01 | 0.01 | 0.05 | 0.05 |
| 25 | No data | | | | | | | | | | |

4.2 Meteorological Data

Meteorological data used are the NCEP/NCAR Reanalysis Data and Station Data.

4.2.1 NCEP/NCAR Reanalysis data

NCEP and NCAR cooperated on the Reanalysis Data project, which first began in 1991 as a branch of the Climate Data Assimilation System (CDAS) project. The NCEP/NCAR Reanalysis Project includes the recovery of land surface, ship,

rawinsonde, pibal, aircraft, satellite, The Comprehensive Ocean Atmosphere Data Set (COADS) and other data. Moreover, in the project the quality of the data is being checked and a data assimilation system is being used to assimilate the data. The project uses a frozen state-of-the-art analysis/forecast system and does data assimilation. The system used is able to execute one month's analysis in one day and consists of data decoder and quality control preprocessor, data assimilation module with an automatic monitoring system and archive module. The reanalysis is done using T62 global spectral model with a resolution of 209 km and 28 vertical levels. 5 levels of boundary layer and nearly 7 levels above 100 hPa are included in the model. About 5 hPa is the lowest model level from the surface and about 3 hPa is the highest level. In order to let the boundary layer well resolved and to make the 10hPa analysis less influenced by the outer boundary conditions, the vertical structure was preferred in this way.

The output of the Reanalysis project is divided four classes depending on the relative impact of the data and the model on the gridded variable. Class A means the most reliable data as the observed data has more impact on it. Upper air temperature and wind are in this class. On the other hand, class B points out that, observational data has an effect on the value of the variable, but the analysis value is well influenced by the model. Humidity and surface temperature are in Class B. Moreover, class C mentions that the variable is found by the model fields using data assimilation and there is not any observation directly influencing the variable. Class C includes clouds, precipitation, and surface fluxes. In Class D, the field is obtained from observations. Plant resistance and land-sea mask are the described Class D variables. (Kalnay *et al.*, 1995)

What is more, The NCEP/NCAR Reanalysis data consist of the atmospheric data from 1948 to today. These data are analyzed and forecasted to obtain information in the reanalysis project. 0Z, 6Z, 12Z, and 18Z forecasts are used to calculate the daily and monthly average values. For the period between 1948 and 1957, data are generated 8 times daily because the forecasts were done at 3Z, 9Z, 15Z, and 21Z besides at 0Z 6Z, 12Z and 18Z. Therefore, the original forecast values of 0Z, 6Z, 12Z, and 18Z were forecasted and added to the forecasts of 3Z, 9Z, 15Z, and 21Z.

The data set used in this study is the Pressure level data which has a coverage of 144x73 grids of 2.5 degrees of latitude and longitude from 90°N to 90°S and 0°E to 357.5°E. For some variables data starts from the year 1958 other than 1948. Data are available at the pressure levels of 1000, 925, 850, 700, 600, 500, 400, 300, 250, 200, 150, 100, 70, 50, 30, 20, 10 hPa. Not all variables are obtained at all levels and there is no missing data (Data Management Group NOAA-CIRES Climate Diagnosis Center, 2003, <http://www.cdc.noaa.gov/cdc/data.ncep.reanalysis.html/>).

4.2.2 Station data

Total accumulated rain data from two stations are obtained, one of which is Gözpete Station of State Meteorological Service of Turkey, and the other is Kandilli Station of the Bogazici University Institute of Earthquake Researches Center.

4.3 Satellite Data

Satellite data used in this study are obtained from Goddard Earth Sciences, Data and Information Services Center, Distributed Active Archive Center. These data are multi satellite data including data from the The Tropical Rainfall Measuring Mission (TRMM) Project and other satellites. TRMM is an associated project between NASA and the Japan Aerospace Exploration Agency (JAXA) aiming to monitor and analyze the tropical rainfall. Furthermore, the most important aspects that are enlightened with the start of TRMM are frequency distributions of rainfall intensity and areal coverage, partitioning of rainfall into convective and stratiform categories, vertical distribution of hydrometeors, variation of the timing of heaviest rainfall, and diurnal intensification of orographically and sea-breezed forced systems over land.

Maps used are obtained as designed for visualization and analysis of the near-real-time Multi-Satellite Precipitation Analysis (MPA-RT) precipitation estimates, using data from TRMM and other satellites. The aim of this multi data project is to have increased number of input datasets in near real time and to improve quasi-global precipitation predictions. Data production started in December 2001. Data products are experimental and are still in development. There are three types of products this

multi project yield namely, 3B40RT, 3B41RT, and 3B42RT, which is the one used in this study. The first data are a combination of microwave precipitation estimates; second one is precipitation estimates from geostationary infrared (IR) observations and the last one is a combination of the first two datasets. Furthermore, data have a temporal resolution of three hours and a spatial resolution of $0.25^{\circ} \times 0.25^{\circ}$. Spatial coverage of data is from 60°S to 60°N , with no rain data beyond 50°N and 50°S (Huffman, 2005).

In this study four experiments with different lateral boundary conditions and horizontal resolution were done and visually compared to the precipitation estimates of MPA-RT in order to obtain an approach for the prediction of flood in Istanbul. In the next section analysis will be made.

5. EXPERIMENT DESIGN AND ANALYSIS

In this study, four experiments are designed in order to analyze the sensitivity of flood prediction in Istanbul to different settings such as lateral boundaries and horizontal resolution. In all experiments, vertical resolution is kept constant at 23 sigma levels. Options used for model runs are the same for each experiment. Planetary boundary layer scheme is MRF PBL, radiation scheme is RRTM, moisture scheme is simple ice, and cumulus scheme is Kain Fritsch 2.

5.1 Experiment I

Domain of the first experiment is seen on Figure 5.1 drawn with the terrain heights of the region. In this case, horizontal resolution is 18 km with 135x205 grid points.

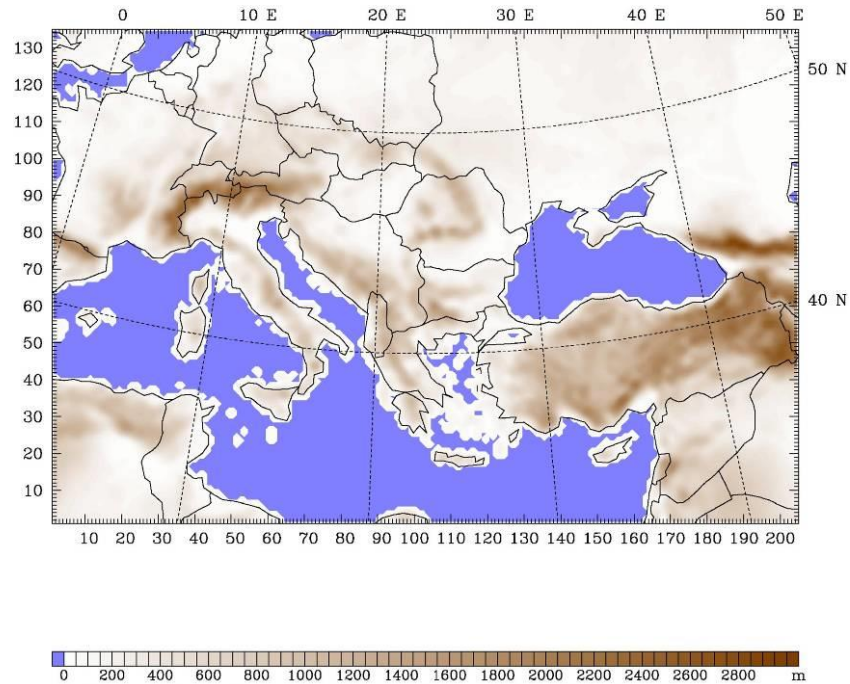


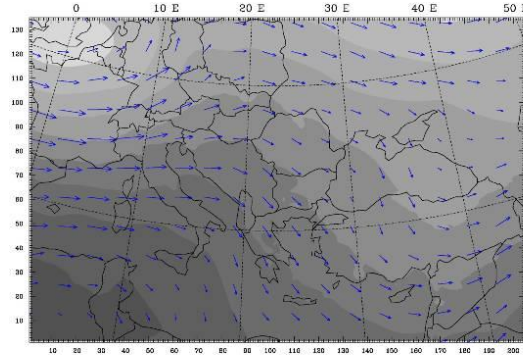
Figure 5.1: Domain of Experiment I with terrestrial data shown.

5.1.1 Analysis Of experiment I

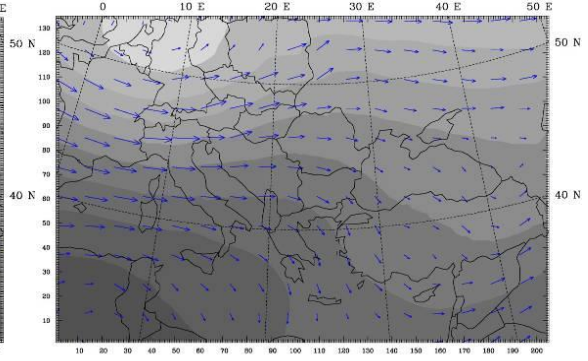
5.1.1.1 500 mb level

Model results for 500 mb level are given in Figure 5.2 in a 12 hourly display starting with 13 August 00 UTC, and ending at 19 August 00 UTC. For comparison, NCEP NCAR 2.5x2.5 Reanalysis data is used, corresponding fields same as the above dates are shown in Appendix A. 500 mb fields reveal the following: At 13 August 00 UTC, there is a low centered at 0° , this is also confirmed with the circulation of wind fields and decrease in height levels. After 12 hours, the low center moves towards 10°E . At 14 August 00 UTC, the center is located near the 20°E , without any deepening in the system. Comparing this with Reanalysis, it can be seen that the general structure of geopotential height levels, and wind speeds and directions are quite the same as Reanalysis and location of the low center is similar. However, there is one very slight difference that is model low center is effective at a wider area than Reanalysis. At these times, on Turkey, prevailing winds are low in magnitude. Since 14 August 12 UTC, the low center coming toward the Black Sea region has started to deepen, and become more distinguished. At this time, the trough can clearly be seen. Furthermore, similar structures are seen at the reanalysis (NCEP) map. Differences are that lowest region of the trough is wider at model prediction than Reanalysis, and the movement of trough is a little more quick at model predictions yielding slight geopotential height differences when compared. At 15 August 00 UTC, the system has moved toward $30\text{--}40^{\circ}\text{E}$ and increased its region of influence. Especially, wind speeds over Turkey have become increased. 12 hours later, wind circulations are quite concrete and system has cut off. At 16 August 00 UTC, there are two cut off centers of low, one of which is located at the $40\text{--}50^{\circ}\text{E}$ and the other located at the western Turkey. In addition, westerly wind circulations over Turkey since 14 August 00 UTC, have changed their direction and become southwesterly. After 12 hours, the system located at the western Turkey has deepened. This reduction, meaning more closely spaced contours, yields more powerful southwesterly winds over Turkey. During these times, patterns are extremely similar on both reanalysis and model predicted fields. At 17 August 00 UTC, western Turkey is under the influence of the system. Moreover, the system is located at Marmara and Aegean Region and system is cut off more quickly in model run remaining at western Turkey at 12 UTC.

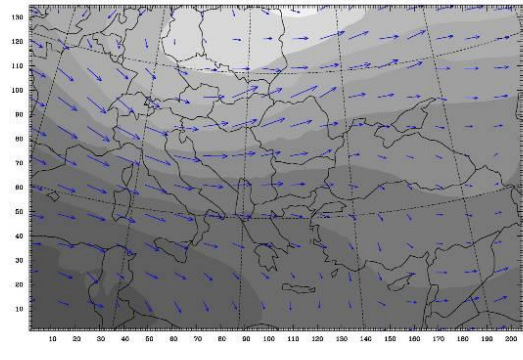
a.) 13 August 2004 00 UTC



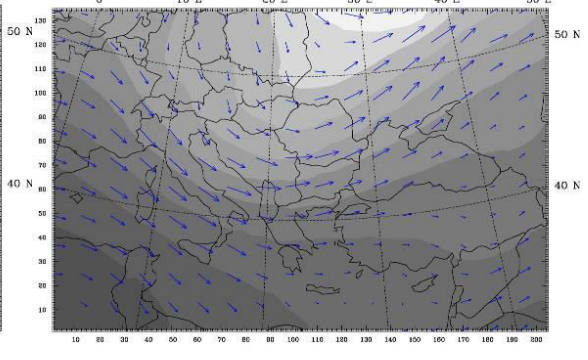
b.) 13 August 2004 12 UTC



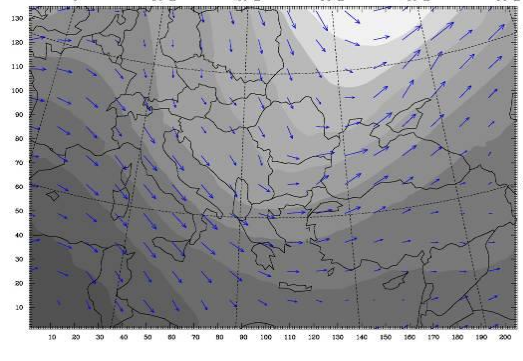
c.) 14 August 2004 00 UTC



d.) 14 August 2004 12 UTC



e.) 15 August 2004 00 UTC

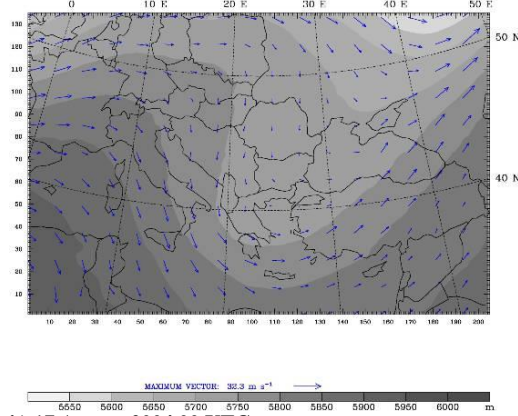


f.) 15 August 2004 12 UTC

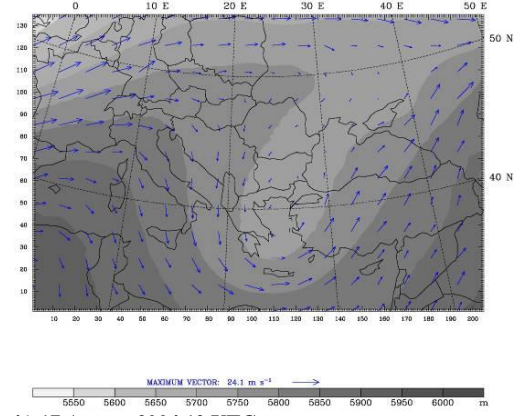


Figure 5.2: 500 mb level for experiment 1, geopotential height represented as filled colors, and wind vectors starting at 13 August 00 UTC with 12 hourly interval, ending at 19 August 00 UTC, left column represents the 00 UTC and right column 12 UTC for each forecast day. Panels a-f representing the period between 13-15 August 2004.

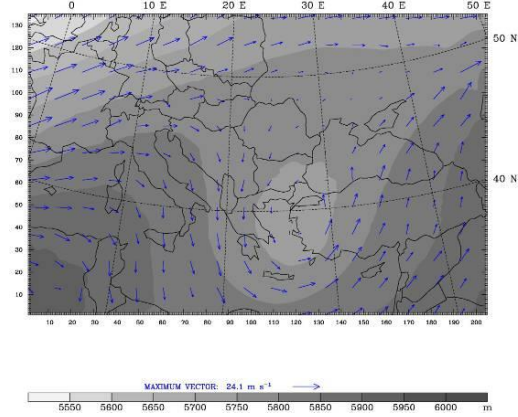
g.) 16 August 2004 00 UTC



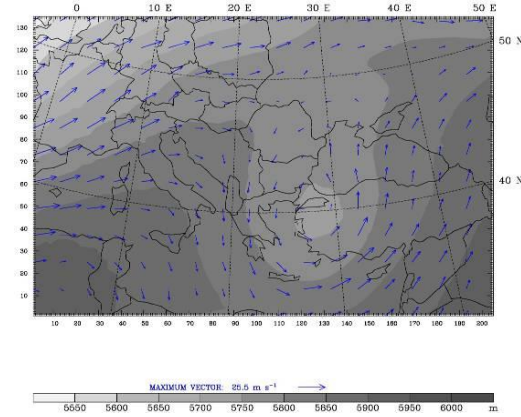
h.) 16 August 2004 12 UTC



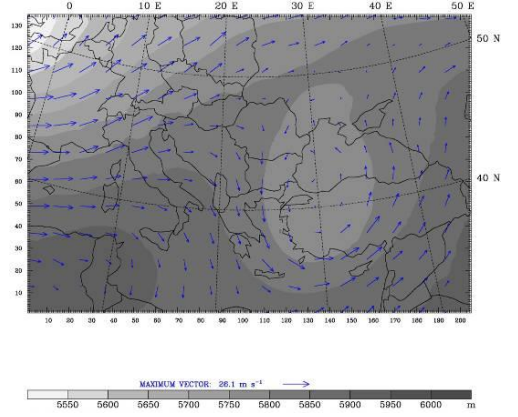
i.) 17 August 2004 00 UTC



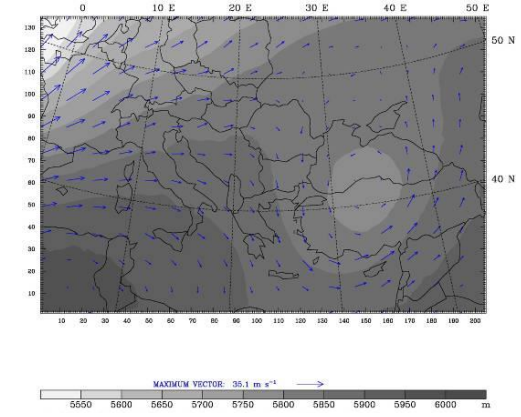
j.) 17 August 2004 12 UTC



k.) 18 August 2004 00 UTC



l.) 18 August 2004 12 UTC



m.) 19 August 2004 00 UTC

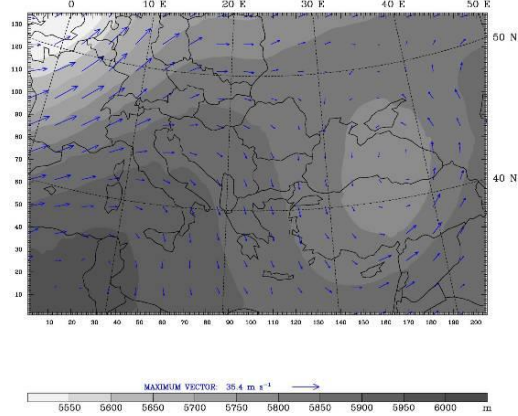


Figure 5.2 (Cont.): Panels g to m representing the period between 16 and 19 August 2004.

At 18 August 00 UTC it has started to leave the region with deepening itself again. Furthermore, it has more regions influenced around low center on model result at this time, and at 12 UTC, it has moved east with less region of influence than Reanalysis. Finally at 19 August 00 UTC, system is at northern Turkey centered at the vicinity of the mid Black Sea Region, in model prediction it is still cut off, however in Reanalysis map, it is attached to the system that it was previously detached from. Generally over viewing the comparison between Reanalysis and model predicted 500 mb fields, it can be concluded that the general pattern is effectively captured with same magnitudes of wind speeds, and directions and geopotential height values.

5.1.1.2 850 mb Level

For comparison, figure 5.3 gives Reanalysis and model prediction maps of 850 mb at 14 August 00 UTC. It can be seen from these dates that at 14 August 00 UTC, on both NCEP Reanalysis and model predicted field, winds are southwesterly, low in magnitude and the isotherm passing through Istanbul is 18°C.

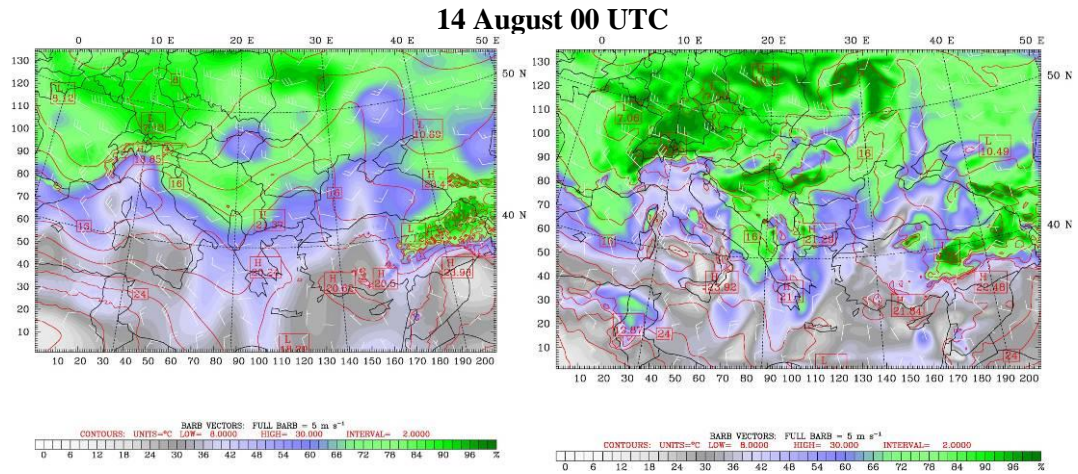


Figure 5.3: Comparison of NCEP Reanalysis map (left column) with experiment I model results (right column).

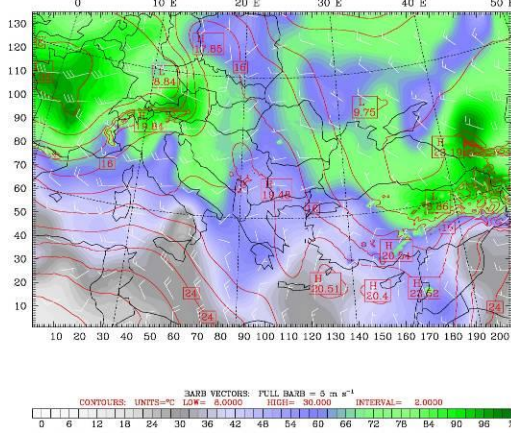
General situation in model results seen in figure 5.4 are as follows. At 13 August 00 UTC, around the low centered at northwest air is quite saturated. It has the 8°C isotherm passing through it. Wind speeds at the center are about 15 m/s. After 12 hours, the system is starting to increase its humidity to about 96% and move toward east. At this time temperatures the low center are reduced. During this period, over Turkey relative humidity is about 30 % at 12 UTC and a little more at 00 UTC. In addition, as there are not any systems effecting Turkey at these times, prevailing wind directions over Turkey are low in magnitude and vary in direction. Although

the wind directions and magnitudes are similar in both Reanalysis and model results, the low located at northwest has about 80 % relative humidity in Reanalysis whereas the model predicts higher values of about 90 %. In addition, pumping of relative humidity from the low located at the northwest is much wider at spatial effectivity in model results. Furthermore, impacts of topography are seen on model predictions creating more moisture near mountainous regions of the northeastern border of Turkey because of orographic uplift. Relatively high humidity field is carried toward Black Sea coasts of Turkey in model prediction. At 14 August 00 UTC, the system has shifted east, preserving its humidity and temperature it previously had. During these times, the reason for the eastern Turkey to have high humidity values is not due to any present systems, but due to the effects of topography. At 14 August 12 UTC, the wind circulations have become more westerly. The system moving toward has increased its region of influence with increase in humidity value and wind speeds and has constructed four low centers in it. After 12 hours, the low center located at the northwestern Black Sea Region has 7C value with 96% humidity. Circulating wind directions at the region are consistent with the mentioned system. At 15 August 12 UTC, the system has moved toward western Turkey. The system that has increased values of humidity at Trakya Region at 14 August 12 UTC, has started to become effective at this time all through western Turkey. Therefore, Marmara Region, Western Black Sea Region and Trakya Region have quite increased humid conditions. At 16 August 00 UTC, humid conditions are completely effective at western Turkey and relative humidity reaches almost 100 % values of relative humidity. After 12 hours and at 17 August 00 UTC, system has a limited area of movement and western Turkey remains to have high humidity conditions with the pattern moving restricted around itself. Furthermore, at 12 UTC, This system has high wind speeds same as 18 August 00 UTC with 15 m/s at center. At 12 UTC, the humidity is reduced and system has moved toward east. Finally, at 19 August 00, system is again moving easterly and the relative humidity conditions at Marmara Region is about 30 %.

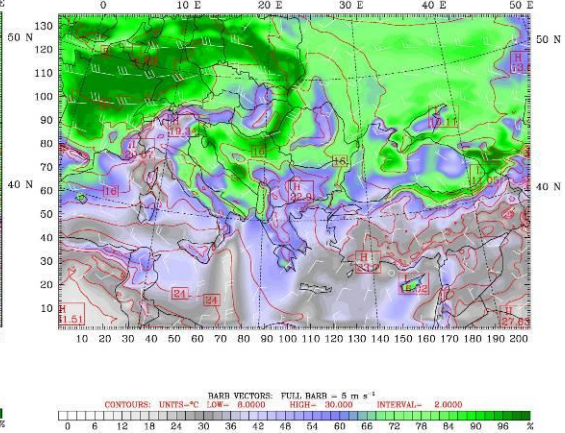
Briefly, when compared with the NCEP Reanalysis fields, general patterns and movements of temperature, relative humidity and wind speeds and directions are quite similar with the model prediction, but model predicted relative humidity values are higher than Reanalysis. These higher values are normal since the 18 km is more

detailed than the $2.5^\circ \times 2.5^\circ$ NCEP Reanalysis. For comparison purposes, all the NCEP Reanalysis 850 mb maps corresponding to the case study period of 13-19 August 2004 can be found in the Appendix B.

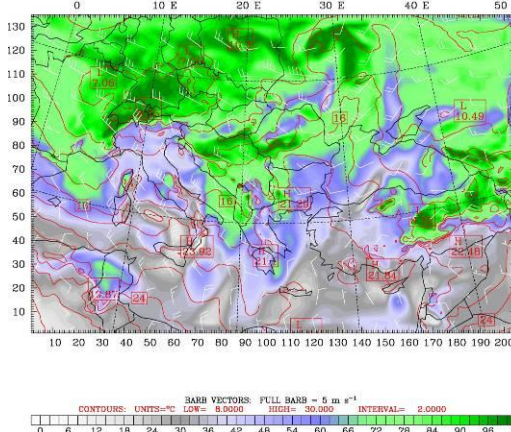
a.) 13 August 2004 00 UTC



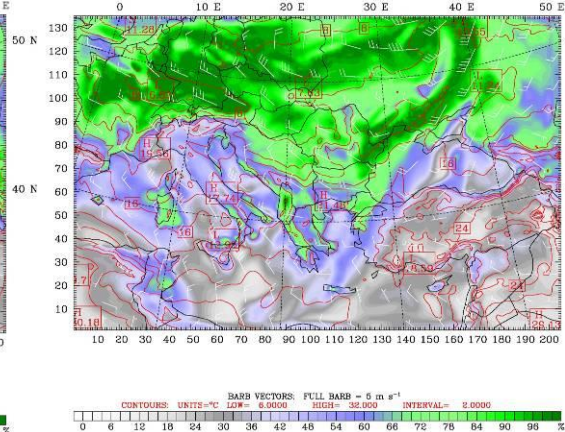
b.) 13 August 2004 12 UTC



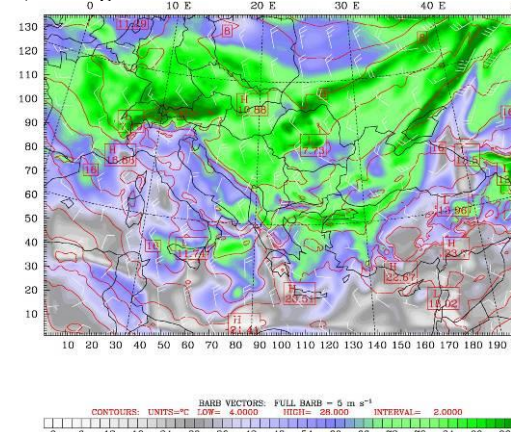
c.) 14 August 2004 00 UTC



d.) 14 August 2004 12 UTC



e.) 15 August 2004 00 UTC



f.) 15 August 2004 12 UTC

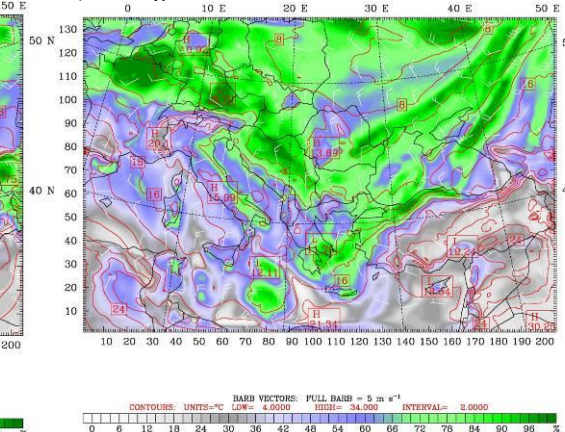
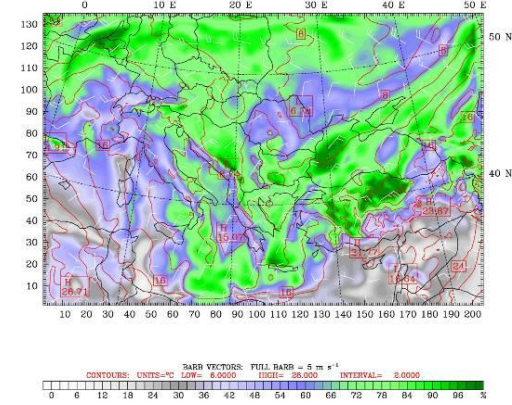
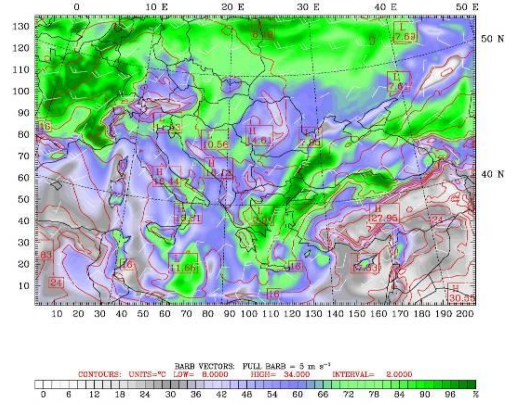


Figure 5.4: 850 mb level relative humidity represented as filled colors, temperature, and wind vectors starting at 13 August 00 UTC with 12 hourly interval, ending at 19 August 00 UTC, left column represents the 00 UTC and right column 12 UTC for each forecast day. Panels a to f representing 13 to 15 August 2004.

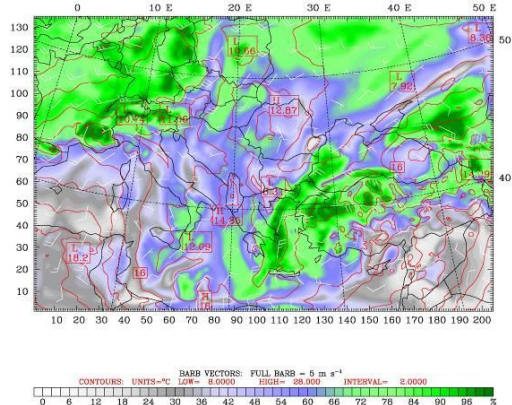
g.) 16 August 2004 00 UTC



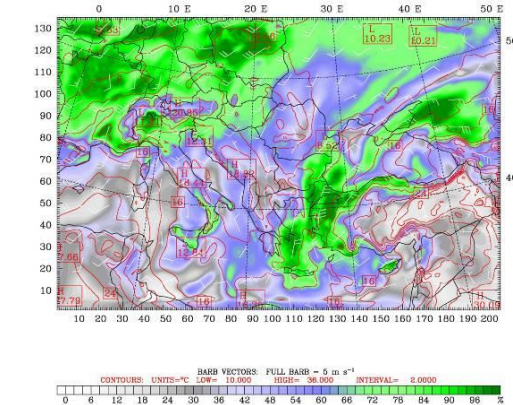
h.) 16 August 2004 12 UTC



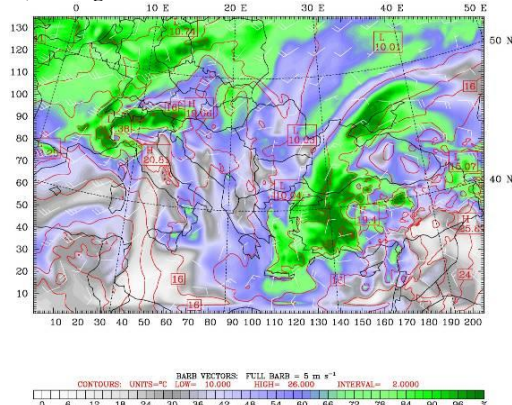
i.) 17 August 2004 00 UTC



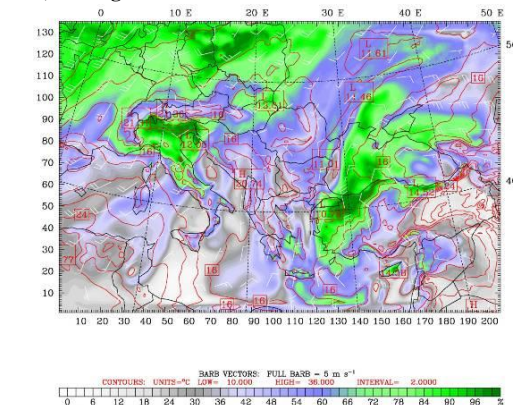
j.) 17 August 2004 12 UTC



k.) 18 August 2004 00 UTC



l.) 18 August 2004 12 UTC



m.) 19 August 2004 00 UTC

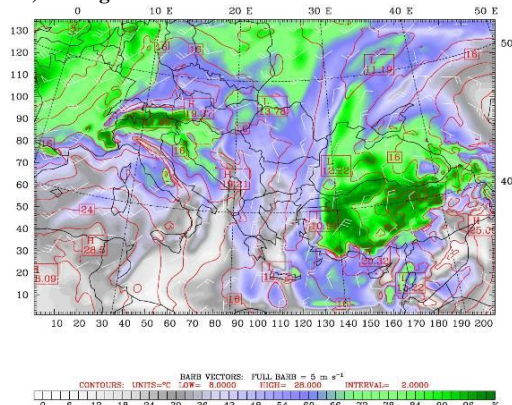


Figure 5.4 (Cont.): Panels g to m representing the period between 16 and 19 August 2004.

5.2 Experiment II

In order to analyze and emphasize the impact of lateral boundaries, a smaller domain with the same resolution as experiment one (18 km) is selected. Domain of this experiment is seen on figure 5.5 drawn with elevation of the domain region. This case has 110x160 grids.

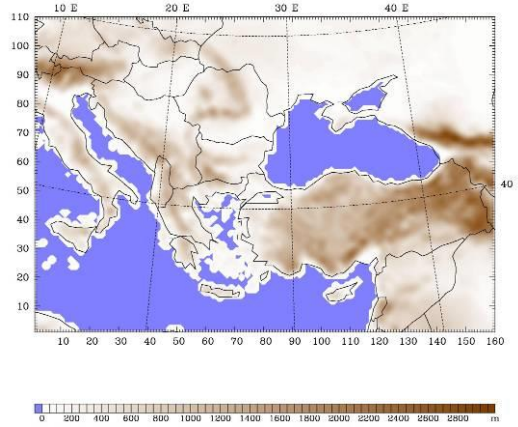


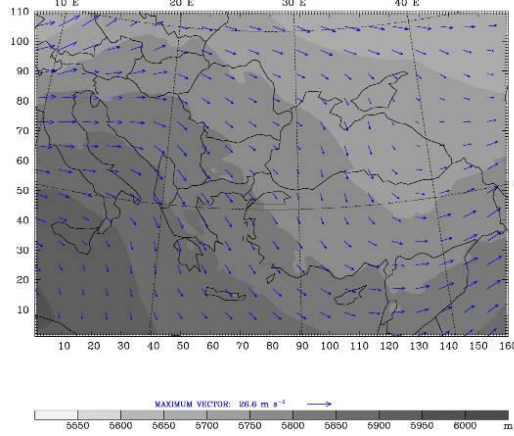
Figure 5.5 Domain of Experiment II with terrestrial data shown

5.2.1 Analysis of Experiment II

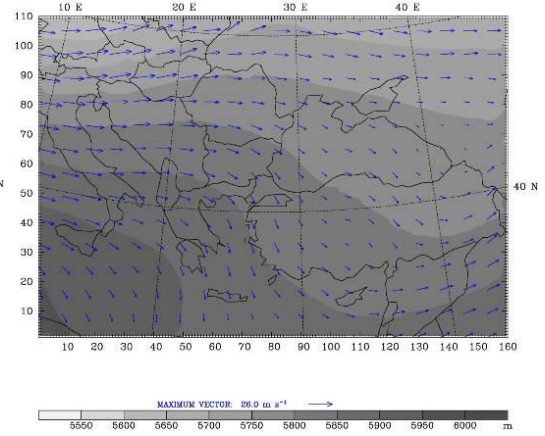
5.2.1.1 500 mb Level

General structure of the meteorological fields is well captured by the model in this experiment seen in figure 5.6. Some differences between Reanalysis and model results occur. For instance at 17 August 00 UTC, cut off center of flow located west of Turkey is wider at Reanalysis than model. At 17 August 12 UTC, this situation is again present. In addition, at 18 August 00 UTC, the cut off center of low is not seen on 18 km model run. Conversely, in the first experiment, this cut off can be seen. Moreover, the deeper values of center of low, are not seen in the results of experiment 2. At 18 August 12 UTC, the center of low is cut off and is wider in area of influence at NCEP Reanalysis field, unlike model prediction. Finally, at 18 August 00, and 12 UTC, and 19 August 00 UTC, wind speeds are lower in model prediction, at 19 August, the center of low located on Black Sea on NCEP map is not seen on model simulation, therefore winds are more powerful at NCEP map. Although center is still cut off at prediction it is attached to the system it originated from in model run.

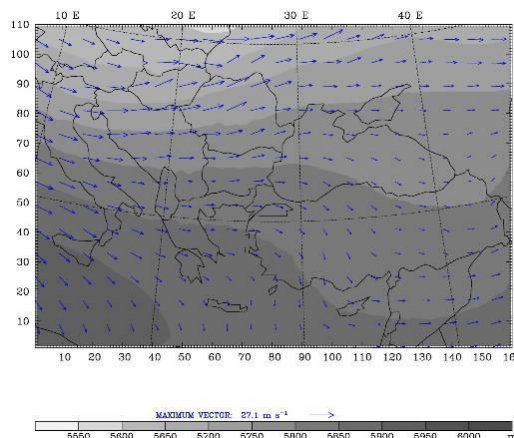
a.) 13 August 2004 00 UTC



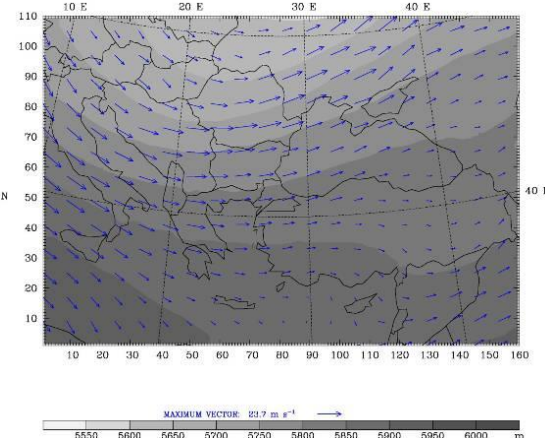
b.) 13 August 2004 12 UTC



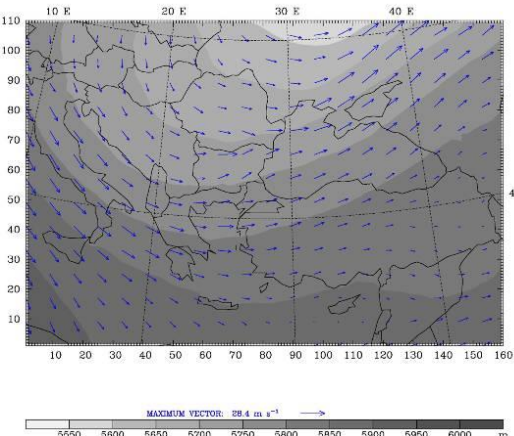
c.) 14 August 2004 00 UTC



d.) 14 August 2004 12 UTC



e.) 15 August 2004 00 UTC



f.) 15 August 2004 12 UTC

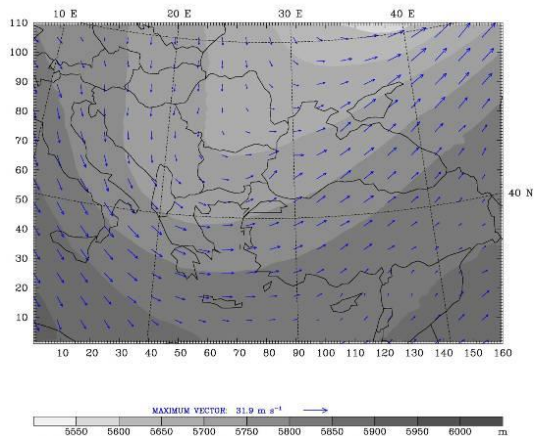
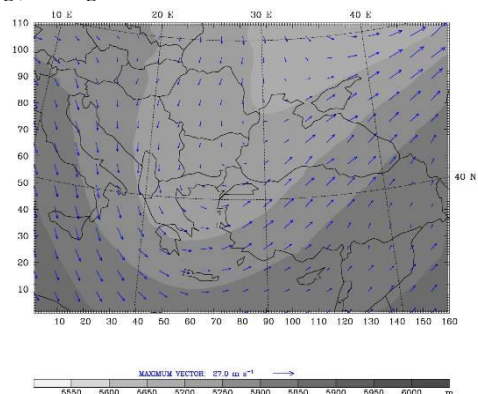
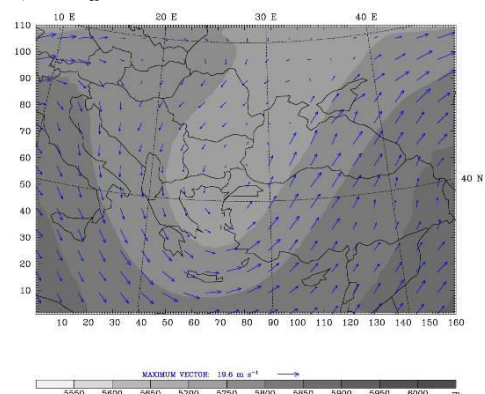


Figure 5.6: 500 mb level for experiment II, geopotential height represented as filled colors, and wind vectors starting at 13 August 00 UTC with 12 hourly interval, ending at 19 August 00 UTC, left column represents the 00 UTC and right column 12 UTC for each forecast day. Panels a to f representing the 13-15 August 2004 period.

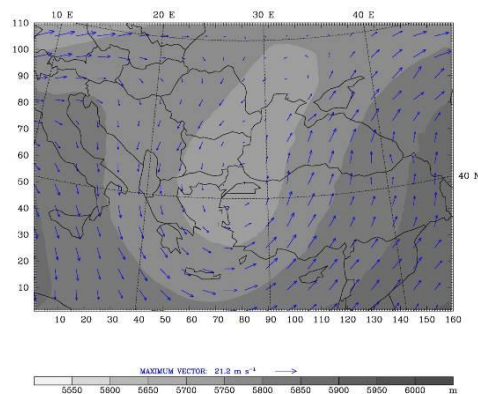
g.) 16 August 2004 00 UTC



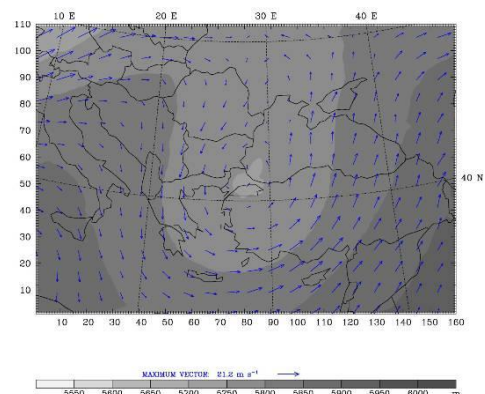
h.) 16 August 2004 12 UTC



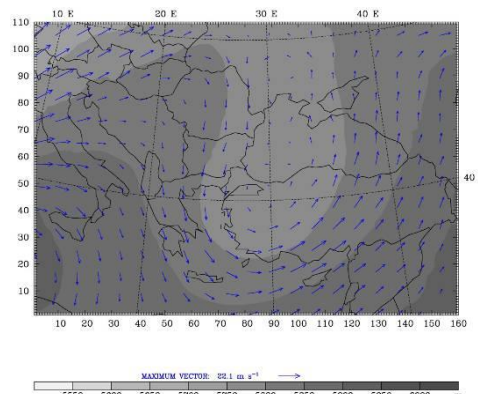
i.) 17 August 2004 00 UTC



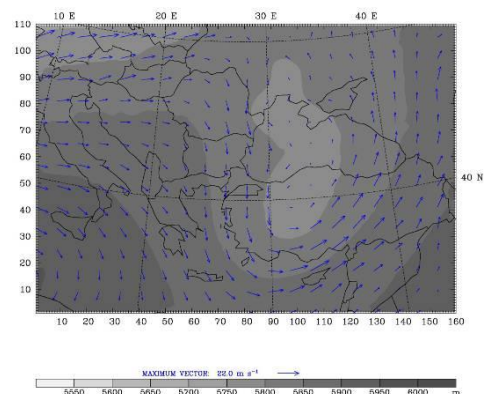
j.) 17 August 2004 12 UTC



k.) 18 August 2004 00 UTC



l.) 18 August 2004 12 UTC



m.) 19 August 2004 00 UTC

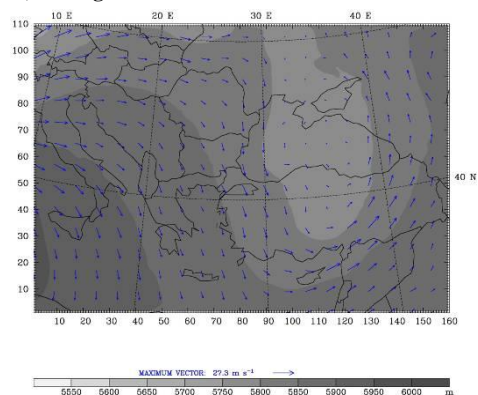


Figure 5.6 (Cont.): Panels g to m representing the 16-19 August 2004 period.

Moreover, analyzing the 500 mb level model predicted fields reveals that similar fields are obtained as in experiment one. Some slight differences occur which are as follows. At 13 August 12 UTC, center of low located on northwest is less deep than it is in experiment one. In general, wind speeds obtained are a little less than they were in experiment one. In addition, at 17 August 00 UTC, the center of cut off low is located around Trakya, and has a larger area of influence unlike experiment I, where the cut off center of low has a center located around the Aegean coasts and has a less area of influence. Furthermore, at 12 UTC, center of low is located over Istanbul, whereas it was south of Istanbul at experiment one. After these times, there are again slight differences on the location and areal extent of the flow of the center of low. These differences are arising since the domain of experiment one is larger than the domain of experiment two. Larger domain of experiment one captures more flows than smaller domain leading to slight changes in obtained fields.

5.2.1.2 850 mb Level

Comparison of model results of 850 mb level with NCEP Reanalysis yields very successful results, with similar wind, wind directions, temperature values, and general relative humidity fields. Figure 5.7 compares the reanalysis and model result at 850 mb. It is seen that overall quality of obtaining meteorological fields is satisfactory. At 14 August 00 UTC, model shows similar values as of Reanalysis, temperature over Istanbul is 16⁰C in Reanalysis and 18⁰C in model prediction. Relative humidity is generally same, but above the northern coasts of Black Sea, model predicts higher values. At 12 UTC, temperatures and in general relative humidity fields are same in both maps. In addition, relatively more moist air is located over Istanbul, southern Greece and northeastern coasts of Black Sea. Slight differences between Reanalysis and model, in the fields of the 850 mb may be related to the resolution of the NCEP Reanalysis, which is of 2.5⁰x2.5⁰, and therefore does not reflect detail as of the model run having 18 km grid resolution. The model results of 850 mb are given in figure 5.8. For comparison, Reanalysis fields are given in Appendix 2. The difference is that and it is not only limited to this model run, the model relative humidity field, although show the similar pattern as Reanalysis, has higher values than Reanalysis.

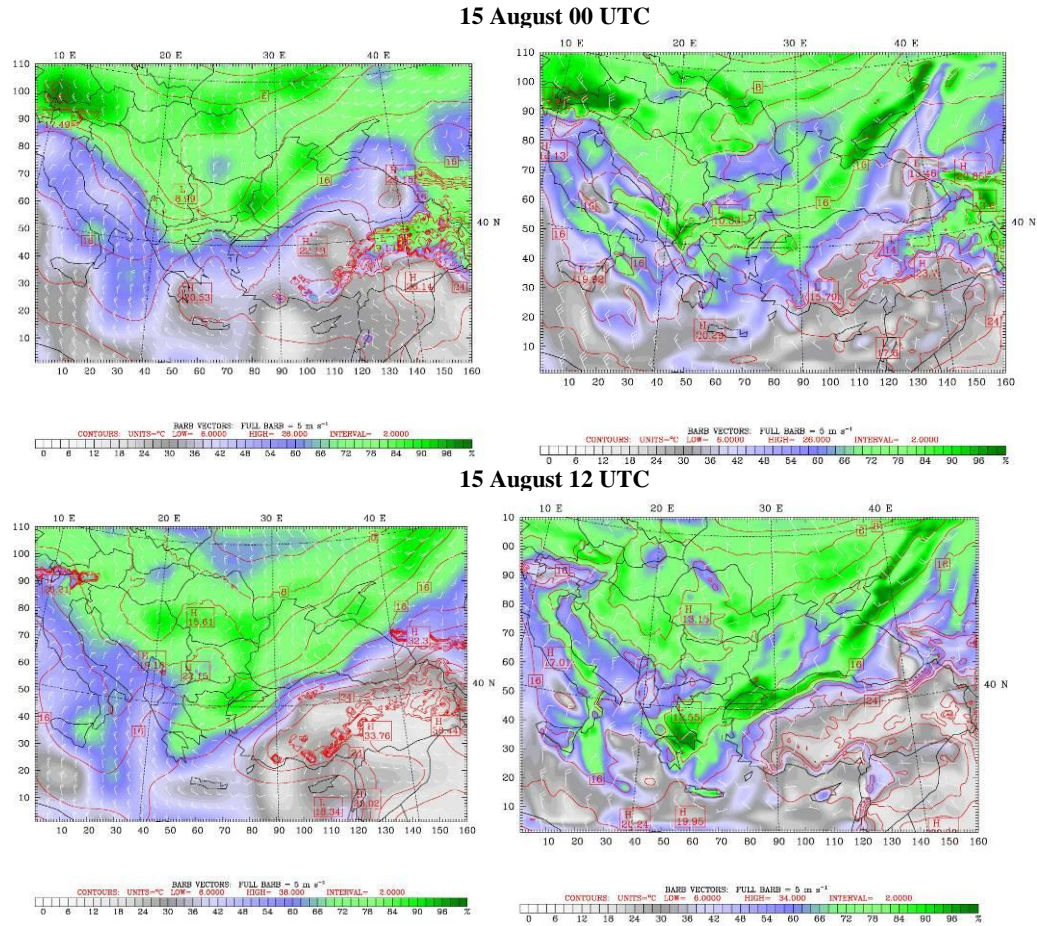
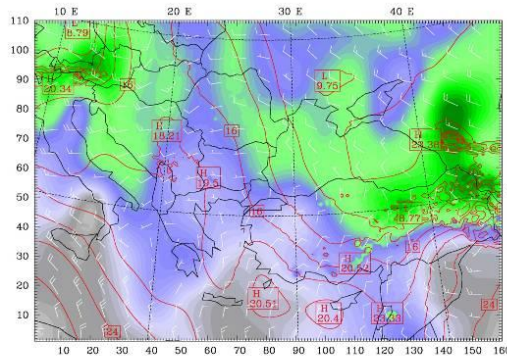


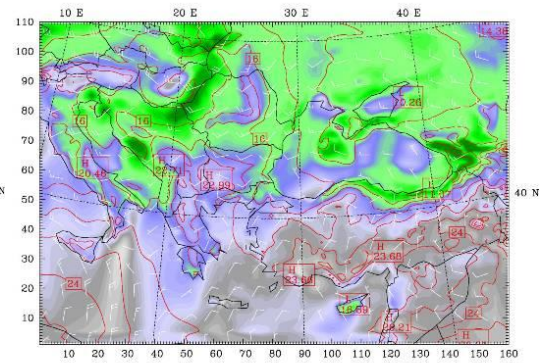
Figure 5.7 Comparison of NCEP Reanalysis map (left column) with experiment II model results (right column).

Furthermore, obtained fields at 850mb level are very similar to the larger 18 km domain of experiment one. General location of relative humidity fields, wind patterns and magnitudes, and temperatures are similar. Overall, the larger domain of experiment one generates more moisture than the domain of experiment two, which is associated with its ability to capture and pump in more flow patterns due to its spatial extent. However, at 15 August 12 UTC, relative humidity obtained on Istanbul is more at prediction of the experiment two. Furthermore, at 18 August 00 UTC, at the southwest of Greece, relative humidity of about 80% is obtained, however it was not obtained at experiment one.

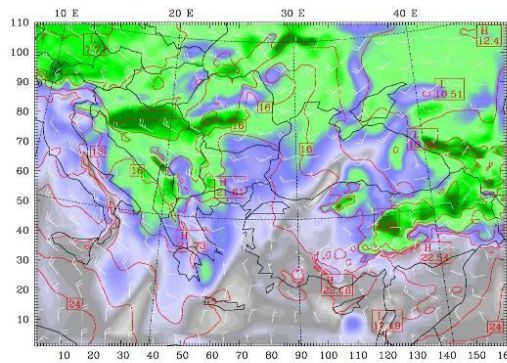
a.) 13 August 2004 00 UTC



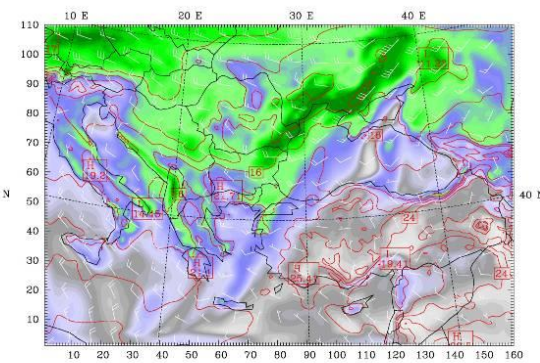
b.) 13 August 2004 12 UTC



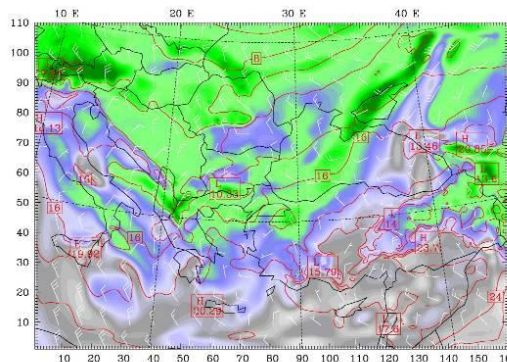
c.) 14 August 2004 00 UTC



b.) 14 August 2004 12 UTC



e.) 15 August 2004 00 UTC



f.) 15 August 2004 12 UTC

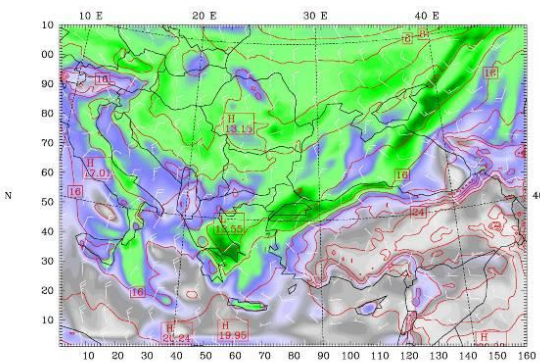
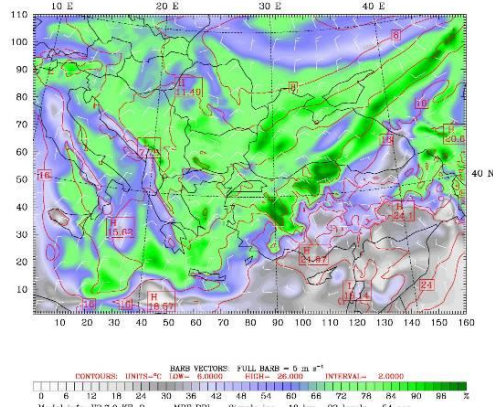
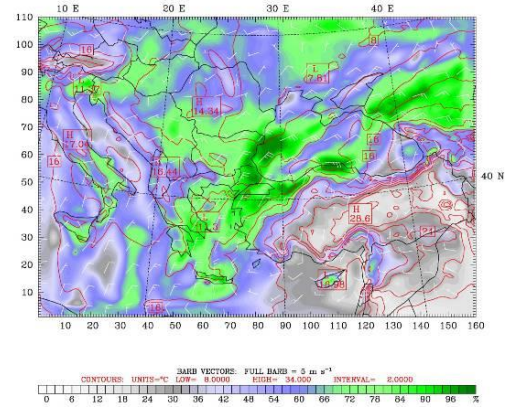


Figure 5.8: 850 mb Level Relative Humidity Represented As Filled Colors, Temperature, And Wind Vectors Starting At 13 August 00 UTC With 12 Hourly Interval, Ending At 19 August 00 UTC, Left Column Represents The 00 UTC And Right Column 12 UTC For Each Forecast Day. Panels a to f representing the 13-15 August 2004 period.

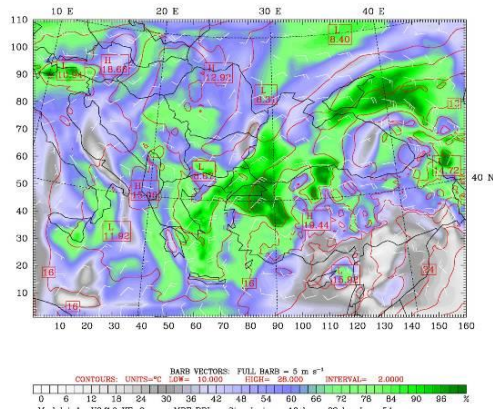
g.) 16 August 2004 00 UTC



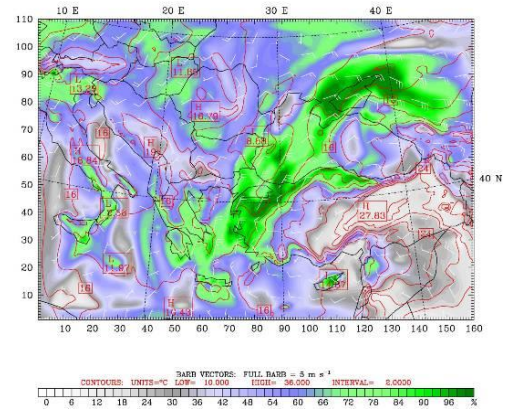
h.) 16 August 2004 12 UTC



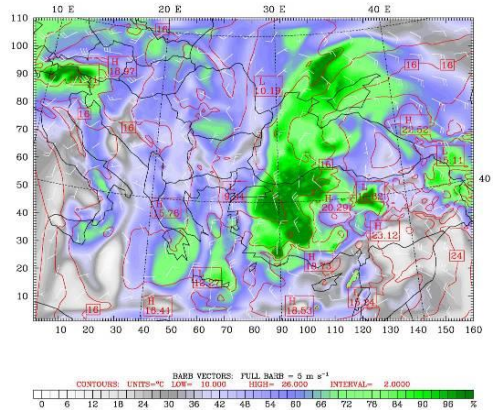
i.) 17 August 2004 00 UTC



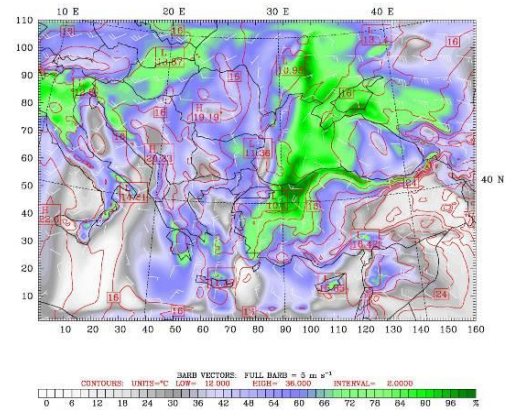
j.) 17 August 2004 12 UTC



k.) 18 August 2004 00 UTC



l.) 18 August 2004 12 UTC



m.) 19 August 2004 00 UTC

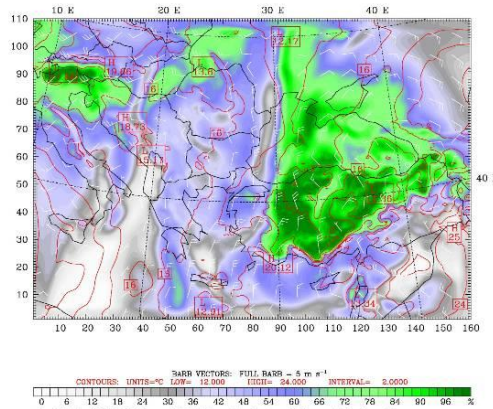


Figure 5.8 (Cont.): Panels g to m representing the 16-19 August 2004 of the case study period.

5.3 Experiment III

In order to detect the impacts of horizontal resolution on flood prediction, the domain of experiment two is repeated with 9km horizontal resolution with 220x320 grids. Domain and terrain elevation of the third experiment can be seen on Figure 5.9.

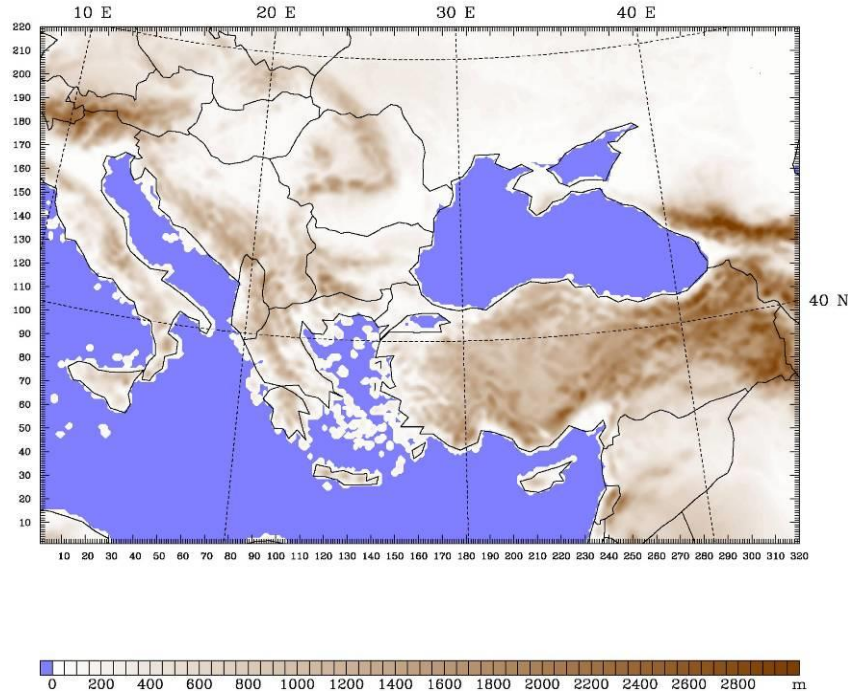


Figure 5.9: Domain of Experiment III with terrain heights.

5.3.1 Analysis Of Experiment Three

5.3.1.1 500 mb Level

500 mb level fields of experiment III are consistent with the 500 mb fields of NCEP Reanalysis. Figure 5.10 shows the comparison for the Reanalysis and model prediction at 500mb level at 17 August 00 UTC. It is seen that pattern is similar having similar wind directions, magnitudes, and geopotential height values. On contrary, model prediction shows that the low system is cut off, on Reanalysis, however, it is seen that the system is not cut off yet.

17 August 2004 00 UTC

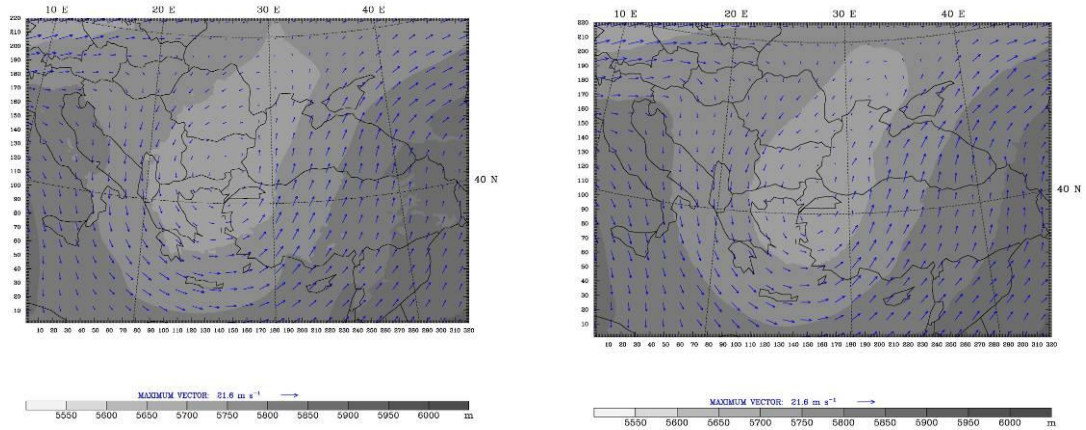
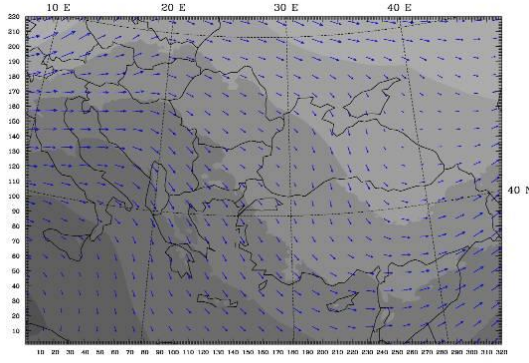


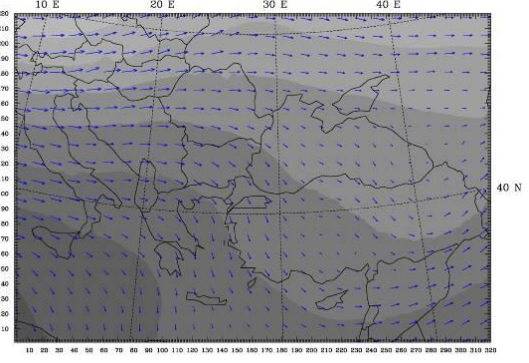
Figure 5.10 Reanalysis (left) and model result (right) for 17 August 00 UTC for experiment III.

Another difference between Reanalysis and model results, is that model predicted field at 17 August 12 UTC, there is a very small area at the north of Istanbul having deeper geopotential height values, but in Reanalysis, this area is covering not only the European side of Istanbul, but also extending towards west, north and South of Istanbul. In addition, at 18 August 00 UTC, a similar condition occurs, the deeper cut off region of the trough is not captured by the model. Furthermore, at 19 August, center of low is seen as a cut off region, however, it is not in model prediction and deepest region is not seen in model prediction. Despite the slight differences, model results are quite satisfactory. Furthermore, differences in location, extent and whether the centers are cut off or not, could be linked to the fact that the NCEP Reanalysis is not as detailed as model prediction of 9 km horizontal resolution. For this reason, it is normal to have differences in predicted fields. Reanalysis fields for this experiment can be found in Appendix A and model results are seen in figure 5.11. General picture obtained with this model prediction is similar to the pattern of the first and second experiments. Some slight differences are as follows: At 17 August 00 UTC, the system is cut off and its central area of influence is wider at both 9km resolution model prediction and Reanalysis, unlike experiment one, where the system is cut off more quickly with less area of influence than Reanalysis and 9km resolution.

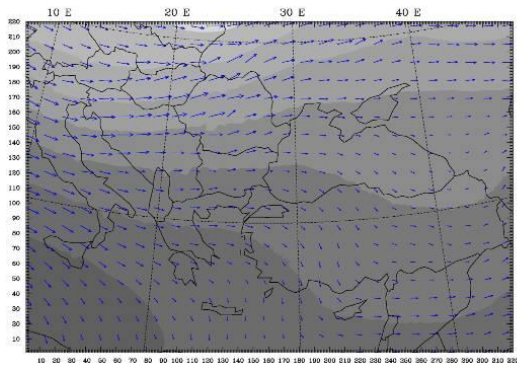
a.) 13 August 2004 00 UTC



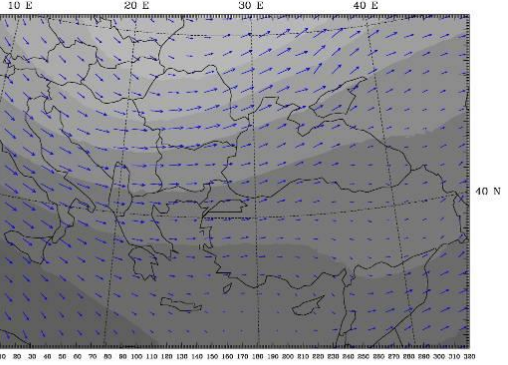
b.) 13 August 2004 12 UTC



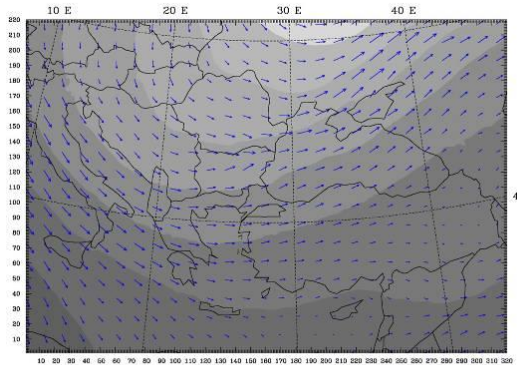
c.) 14 August 2004 00 UTC



d.) 14 August 2004 12 UTC



e.) 15 August 2004 00 UTC



f.) 15 August 2004 12 UTC

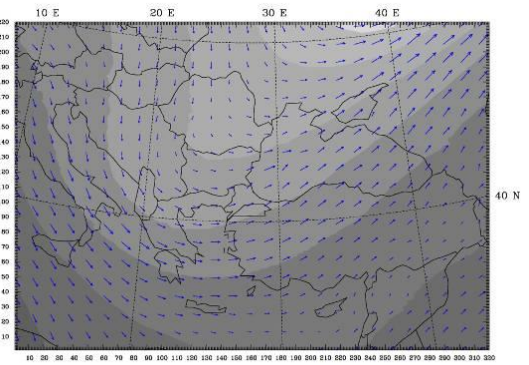
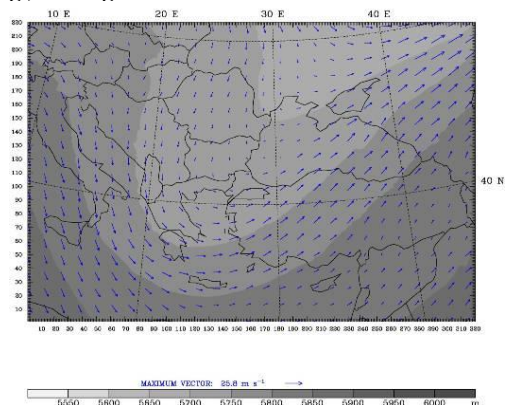
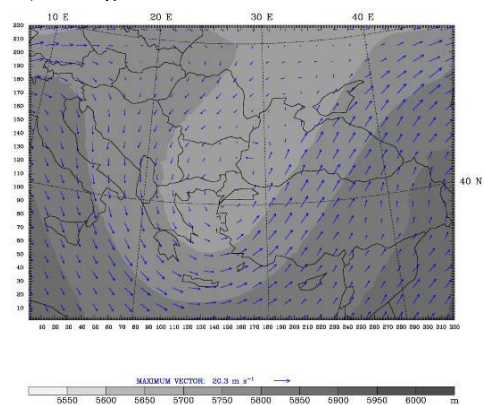


Figure 5.11 500 mb level for experiment 3, geopotential height represented as filled colors, and wind vectors starting at 13 August 00 UTC with 12 hourly intervals, ending at 19 August 00 UTC, and left column represents the 00 UTC and right column 12 UTC for each forecast day. Panels a to f represents the period from 13 August to 15 August 2004.

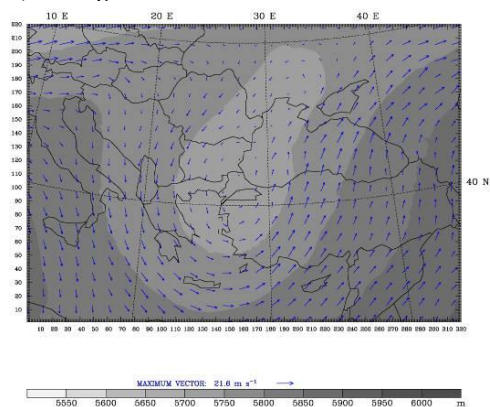
g.) 16 August 2004 00 UTC



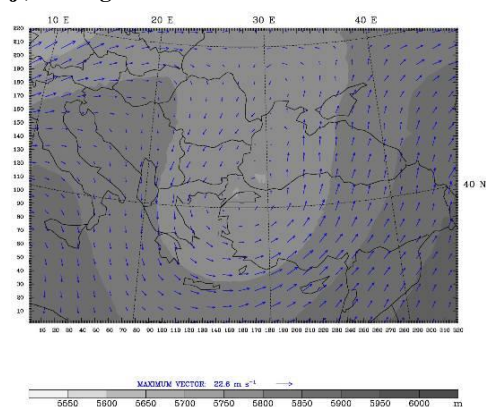
h.) 16 August 2004 12 UTC



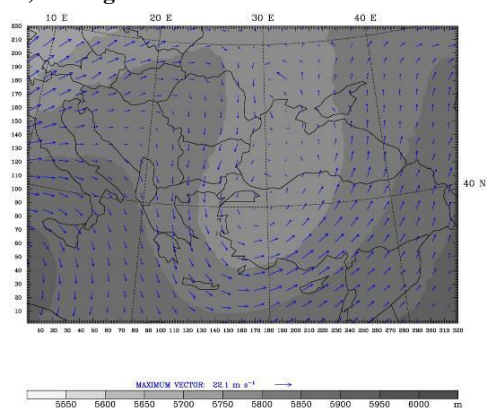
i.) 17 August 2004 00 UTC



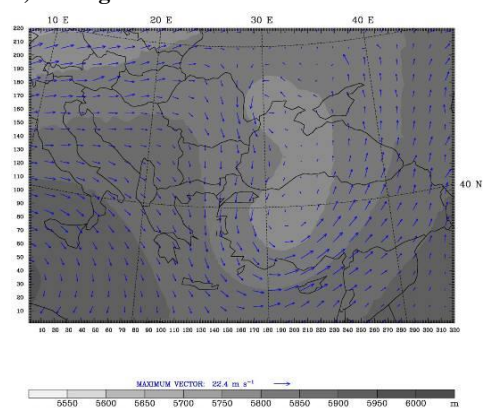
j.) 17 August 2004 12 UTC



k.) 18 August 2004 00 UTC



l.) 18 August 2004 12 UTC



m.) 19 August 2004 00 UTC

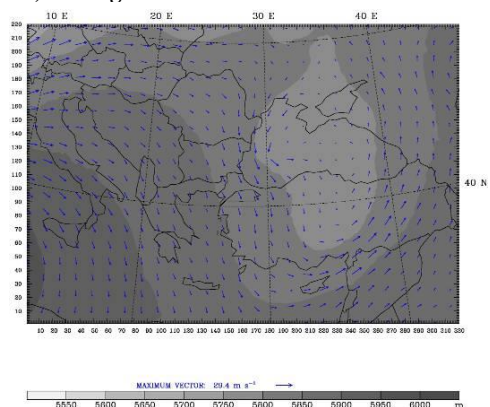


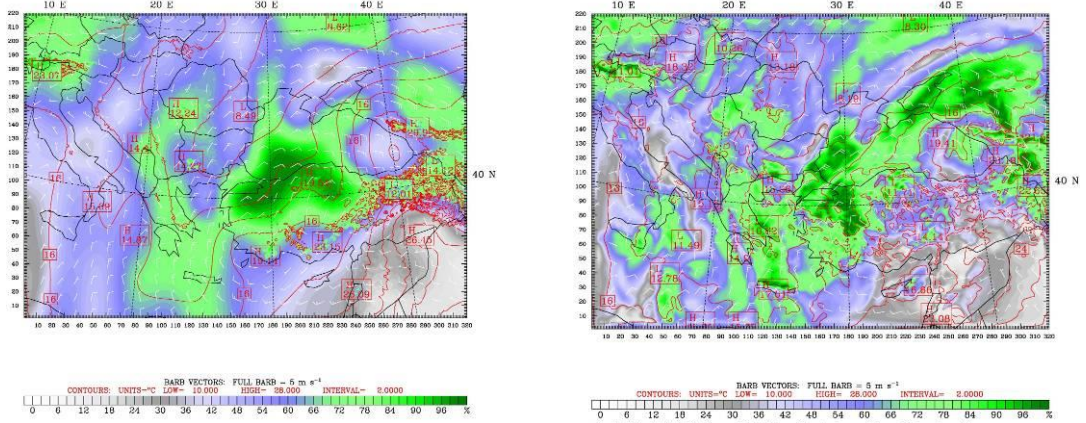
Figure 5.11 (Cont.) Panels g to m represents the period from 16 August to 19 August 2004.

What is more, at 12 UTC, the center of trough has deeper values at experiment one compared with experiment III. In addition, after 12 hours, the restriction of flow by southwesterly and westerly flows is more evident in experiment one. After this time, system is leaving as a cut off system, later at 18 August 12 UTC at 9 km resolution than at experiment one where the system is cut off since 17 August 00 UTC without combining to the flow at the northwest it originated from. Comparing the results of this experiment with experiment two, it can be said that similar but more detailed fields are obtained at this increased resolution experiment. For instance the center of low at 15 August 12 UTC is located on 32E, whereas at experiment two, location was about 37E. However, it is also seen that increased resolution does not always yield detailed fields, the center of low at 17 August 12 UTC is on Istanbul at experiment two, unlike experiment three, where it can hardly be seen. There are differences at the location and extent of center of low between experiment three and two on and after 18 August. At 18km horizontal resolution, the southerly flows are carrying and increasing the area of extent of the center of low more quickly than with 9 km resolution. Therefore there are some differences at the location, its shape and areal extent of the low center.

5.3.1.2 850 mb Level

850 mb model results of experiment III are compared with Reanalysis fields and are found out to be satisfactory. Some differences arise due to the more detailed nature of the 9km domain experiment than the Reanalysis fields. In general, fields are quite the same, in terms of wind fields and speeds, temperatures and relative humidity. Model results give more relative humidity than Reanalysis, which is expected as mentioned before due to the detailed resolution of the model. Model results of 17 August 00 UTC are compared with Reanalysis in figure 5.12. As seen in below, a 00 UTC, model prediction and Reanalysis both show 14°C in Istanbul, and wind speeds and directions are similar. Reanalysis shows the general structure with about 90 % humidity east of Istanbul, model gives more detailed representation of this relative humidity field. What is more, at 12 UTC, Istanbul has 12°C temperature value, and other fields are similar. Relative humidity is shown in more detail at experiment results with location of the field same as Reanalysis.

17 August 2004 00 UTC



17 August 2004 12 UTC

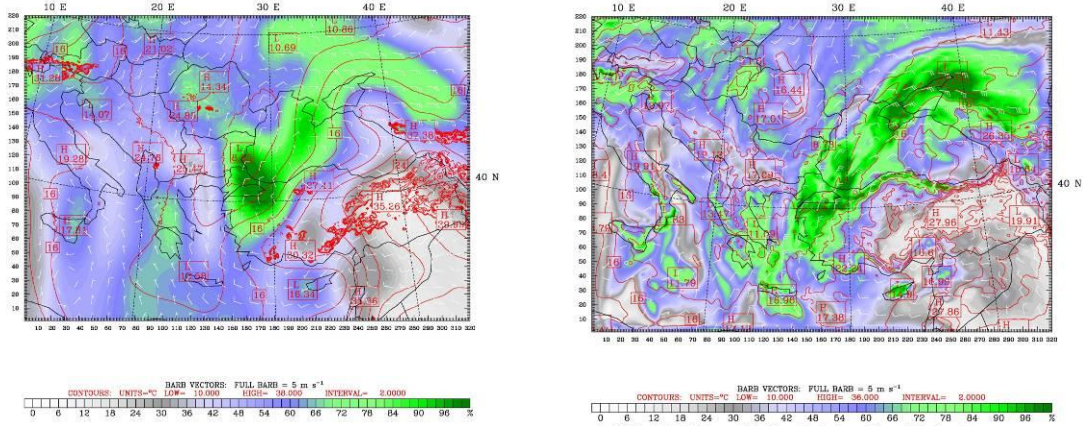
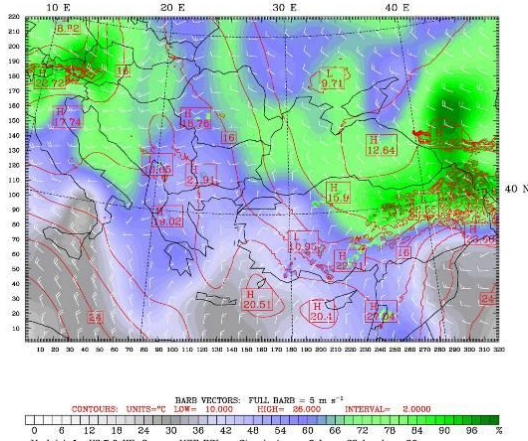


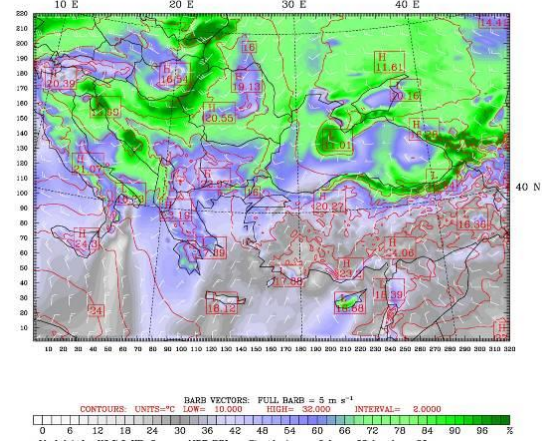
Figure 5.12: Reanalysis (left) and model result for 17 August 2004 00 and 12 UTC for experiment III.

All results of experiment III 850 mb fields are seen in figure 5.13, and for comparison, model predicted fields are given in Appendix B. The patterns obtained are nearly the same as the patterns of the previous experiment that employed decreased resolution on the same domain. The only difference is that 9 km gives more detailed representation of fields. The isotherms are becoming closer as the resolution is increased, and surface topographical impacts are represented in more detail by the model.

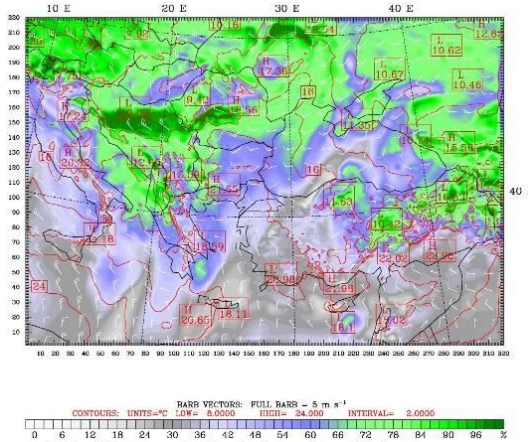
a.) 13 August 2004 00 UTC



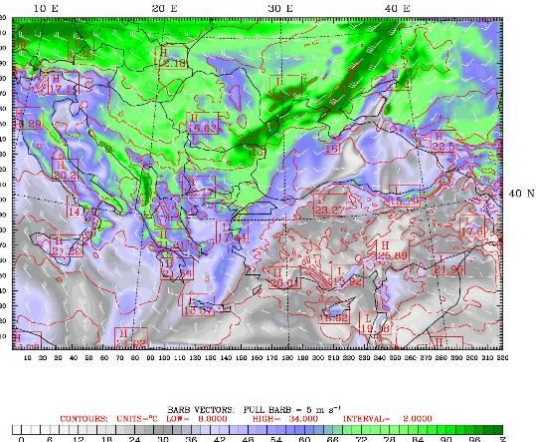
b.) 13 August 2004 12 UTC



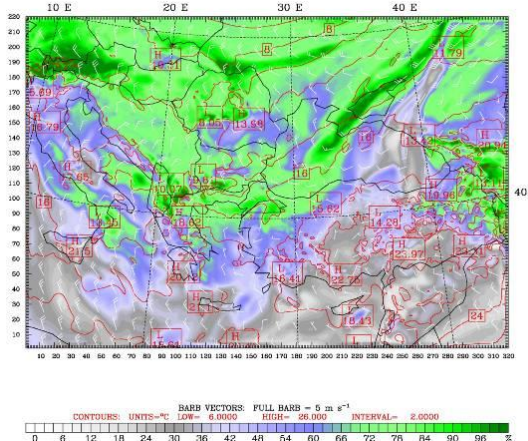
c.) 14 August 2004 00 UTC



d.) 14 August 2004 12 UTC



e.) 15 August 2004 00 UTC



f.) 15 August 2004 12 UTC

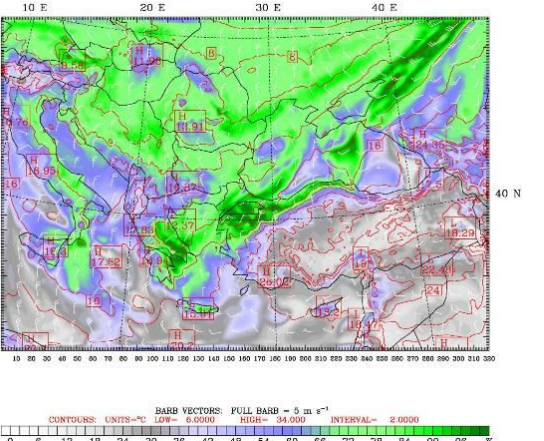
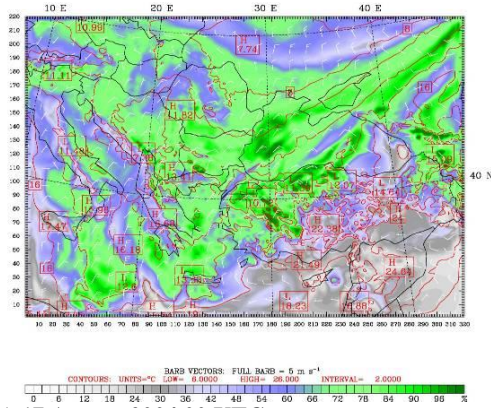
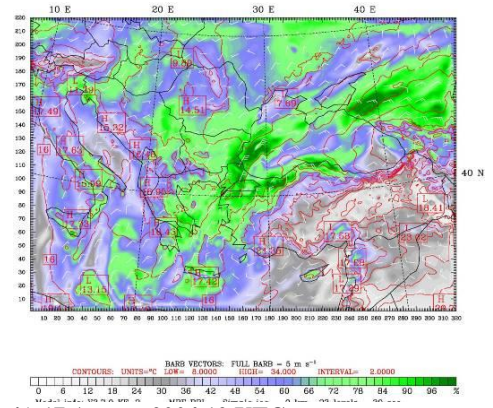


Figure 5.13 850 mb level relative humidity represented as filled colors, temperature, and wind vectors starting at 13 August 00 UTC with 12 hourly interval, ending at 19 August 00 UTC, left column represents the 00 UTC and right column 12 UTC for each forecast day. Panels a to f represent the 13-15 August 2004 of the case study period.

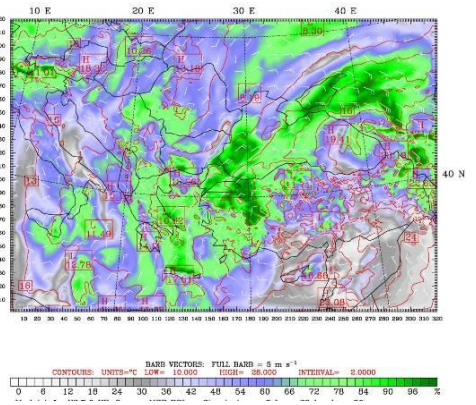
g.) 16 August 2004 00 UTC



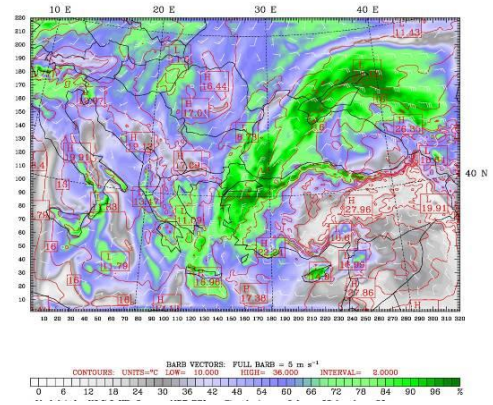
h.) 16 August 2004 12 UTC



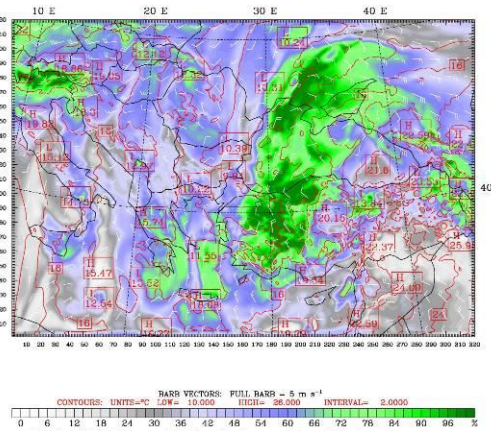
i.) 17 August 2004 00 UTC



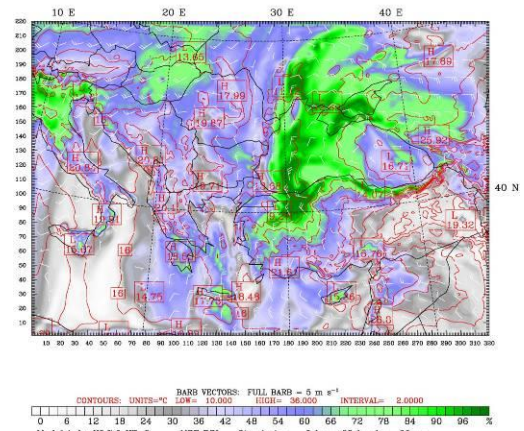
j.) 17 August 2004 12 UTC



k.) 18 August 2004 00 UTC



l.) 18 August 2004 12 UTC



m.) 19 August 2004 00 UTC

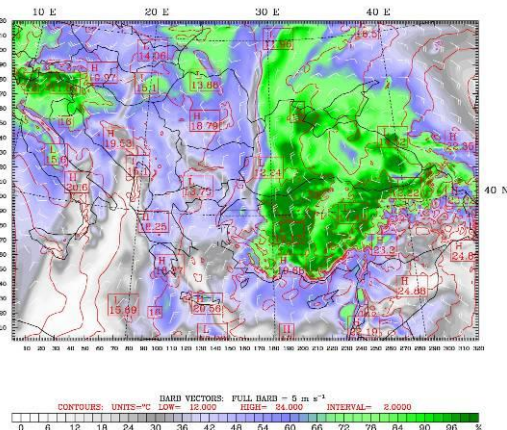


Figure 5.13 (Cont.) Panels g to m represents the 16-19 August 2004 of the case study period.

5.4 Experiment IV

In this last experiment, a much larger domain than the previous experiments is chosen and one way nesting is applied to the two inner domains constructed. This is done in order to compare the results of the prior narrow lateral boundary experiments with a larger domain experiment having finer domains that are fed from the mother domain. Domains have horizontal resolutions of 36 km, 12 km and 4 km. The grid sizes are 95x121 for the coarse domain, 151x181 for the 12 km nested domain, and 70x100 for the 4 km nested domain.

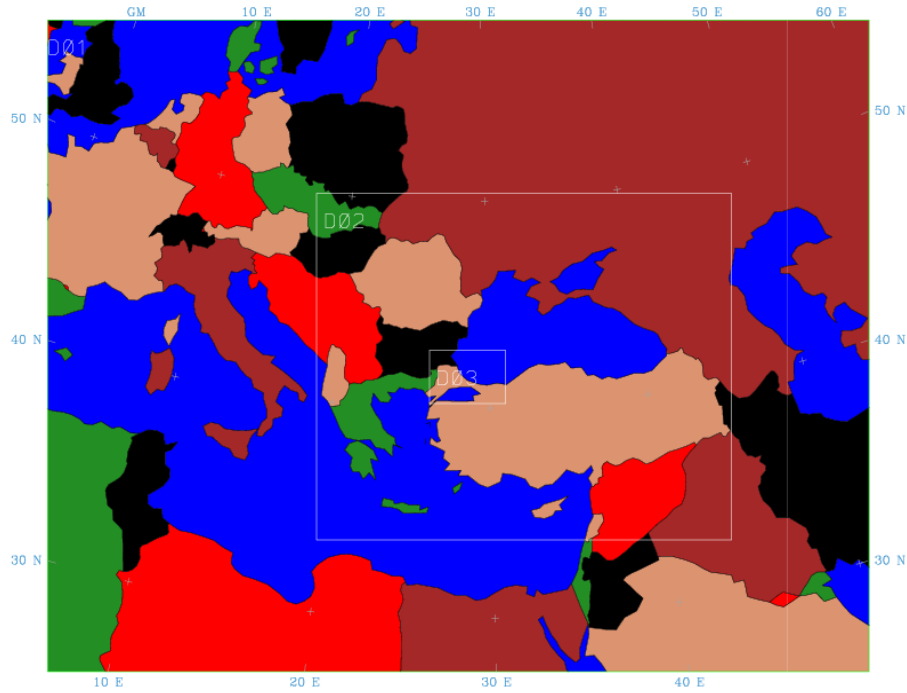


Figure 5.14: Coarse and nested domains of the last experiment.

5.4.1 Analysis of experiment IV

5.4.1.1 500 mb fields

5.4.1.1.1 36 km domain

With the 36 km coarse domain, the synoptic picture of the case is more clearly seen. It can be distinguished that there are two centers of low at the start; one located at 0E and the other at 40⁰E and in the first 12 hours, these two low centers combine. Comparing 36 km coarse domain results with Reanalysis we find out the following. Deeper regions of the central trough axis are wider in model predicted fields after 14

August 12 UTC. Furthermore, at 17 August 00 UTC, model representation of the 500 mb field reveals that there is a cut off low, however, this flow is not cut off yet and has wider area of influence in Reanalysis. Moreover, at 17 August 12 UTC, and 18 August 00 UTC, deeper field on Istanbul is not captured by the model. At 18 August 12 UTC, the location of low is shifted a little east and south in model. Finally, at 19 August 00 UTC, the center of low on Black Sea is connected to the system in Reanalysis, whereas in model prediction it is centered on mid and eastern Turkey. Figure 5.15 shows a comparison for Reanalysis and model results at 15 August 00 UTC. The center of low is clearly seen in both maps, 500 mb geopotential height pattern, wind speeds and directions are quite similar pointing to the satisfactory model results.

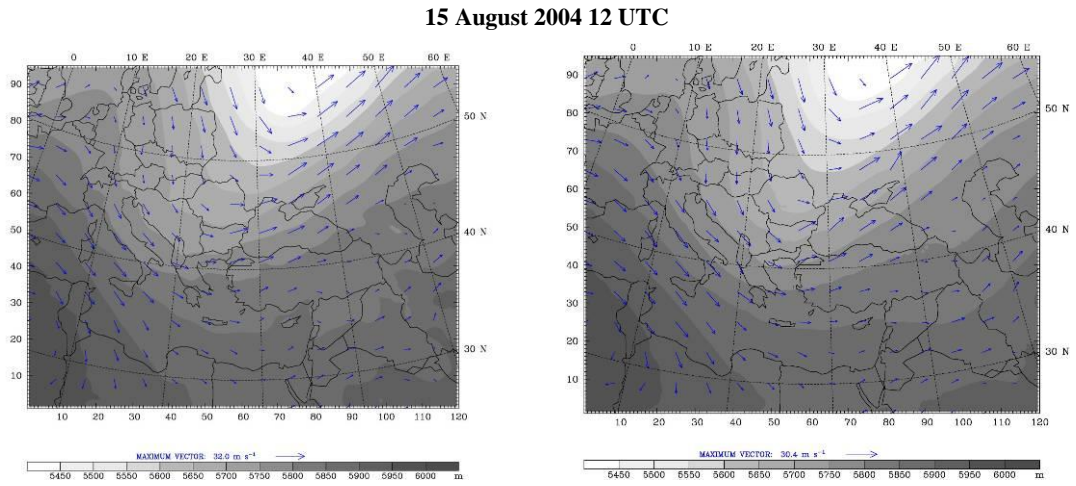
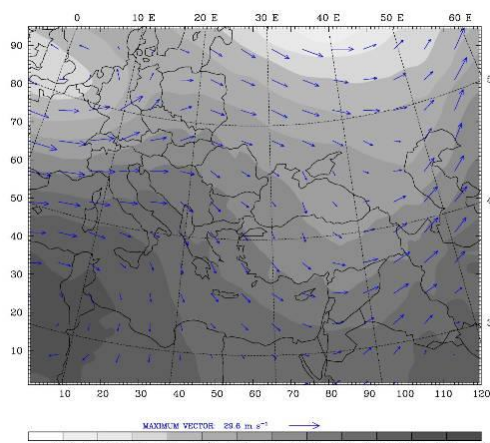


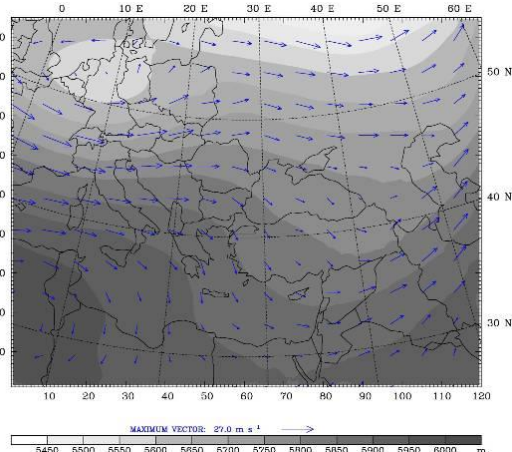
Figure 5.15: Reanalysis (left) and model predicted fields a 500 mb.

The synoptic pattern obtained with this model run showing the existence of two centers of low and their adjointment, was not obtained in the large domain of experiment I that had 18 km horizontal resolution, thus, the movements of the systems are effectively seen at this low-resolution large domain. With 36 km resolution and large domain area, the results include much more large amplitude weather patterns and give better representation of the general situation. It is therefore essential to test a large domain with feedback inner nests to obtain a good approach in precipitation prediction. Figure 5.16 shows the 500 mb level model predictions for the coarse domain. NCEP Reanalysis for the corresponding days can be found in Appendix A for comparison.

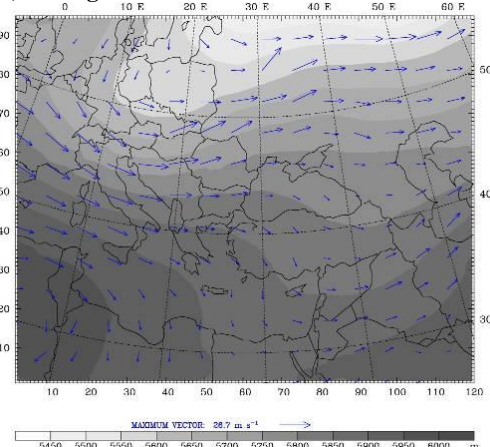
a.) 13 August 2004 00 UTC



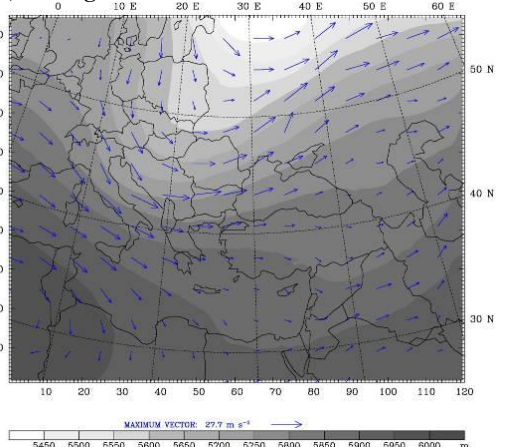
b.) 13 August 2004 12 UTC



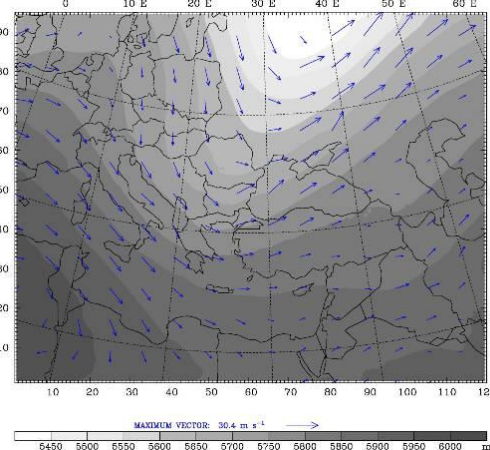
c.) 14 August 2004 00 UTC



d.) 14 August 2004 12 UTC



e.) 15 August 2004 00 UTC



f.) 15 August 2004 12 UTC

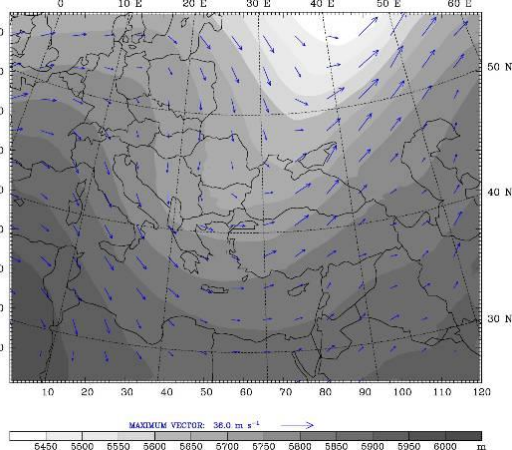
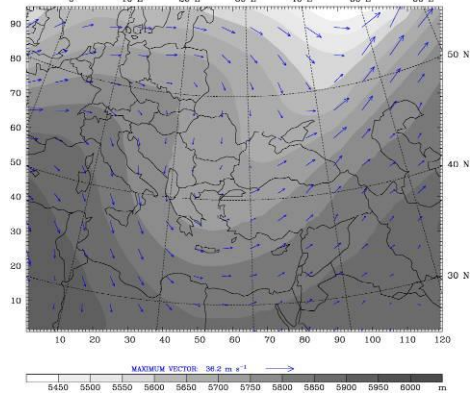
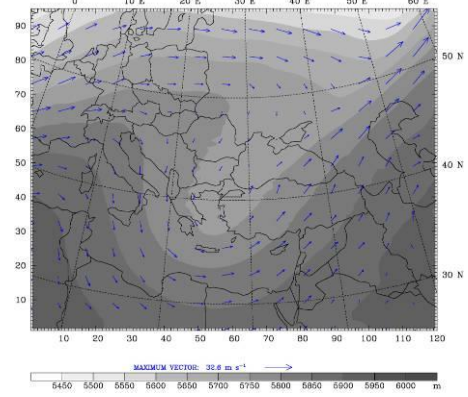


Figure 5.16: 500 mb level for the 36km domain of experiment 4, geopotential height represented as filled colors, and wind vectors starting at 13 August 00 UTC with 12 hourly interval, ending at 19 August 00 UTC, left column represents the 00 UTC and right column 12 UTC for each forecast day. Panels a to f represents the 13-15 August 2004 of the case study period. Panels a to f represent the 13-15 August 2004 of the case study period.

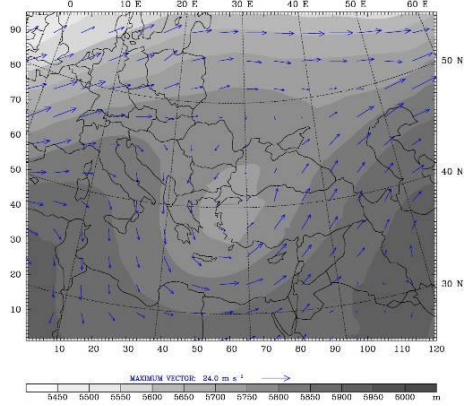
g.) 16 August 2004 00 UTC



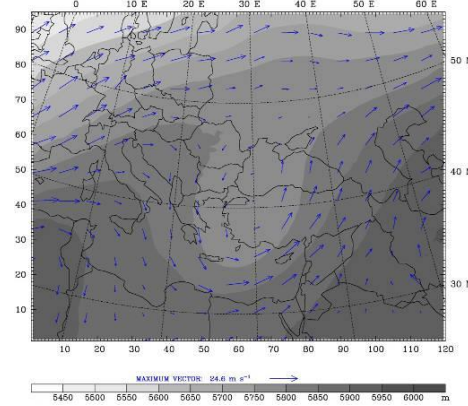
h.) 16 August 2004 12 UTC



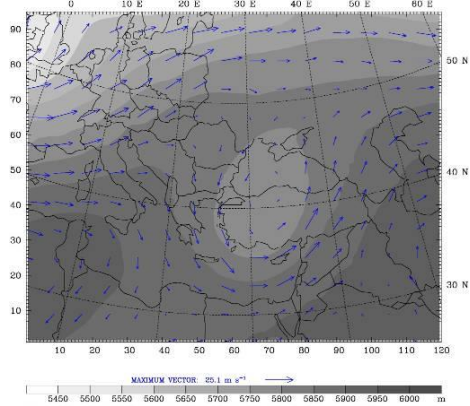
i.) 17 August 2004 00 UTC



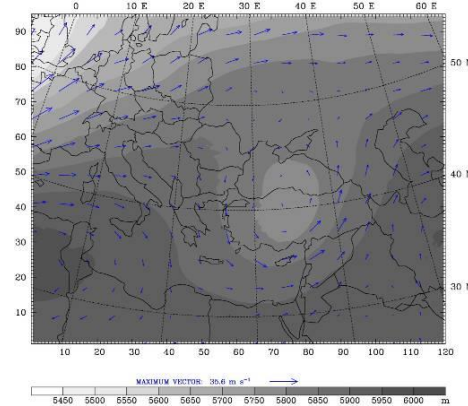
j.) 17 August 2004 12 UTC



k.) 18 August 2004 00 UTC



l.) 18 August 2004 12 UTC



m.) 19 August 2004 00 UTC

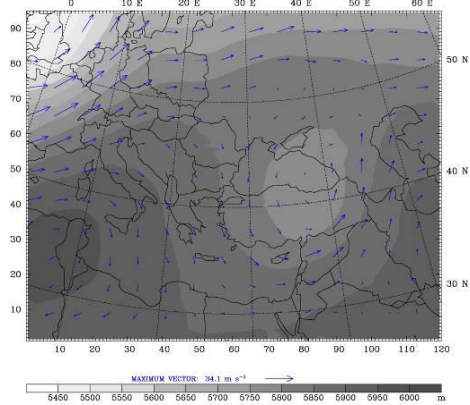


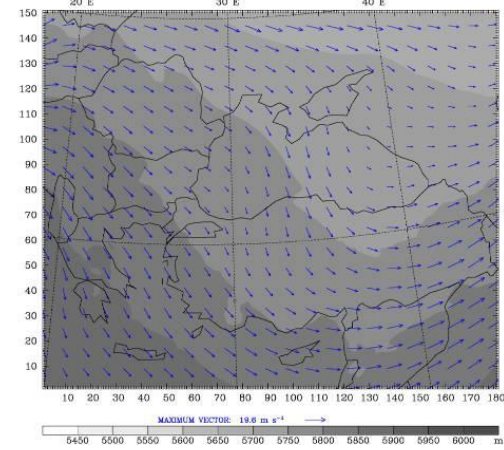
Figure 5.16 (Cont.): Panels g to m represent the 16-19 August 2004 of the case study period.

5.4.1.1.2 12 km nested domain

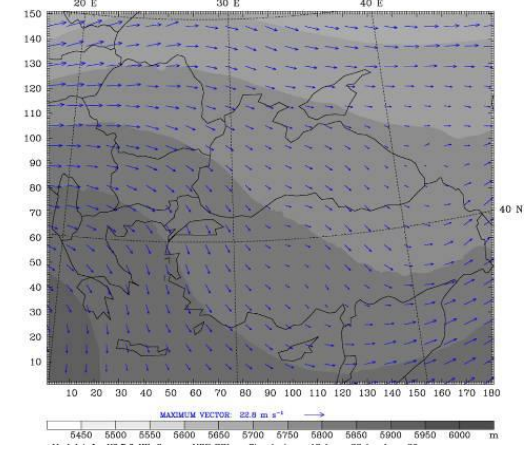
The overall pattern of the 500 mb field of the nested 12 km domain is similar to NCEP Reanalysis maps, which are shown in Appendix A. Some differences occur such as at 14 August 00 UTC, and 15 August 00 and 12 UTC, the center of low is deeper in model prediction, which is consistent with the 36 km mother domain showing larger regions of deeper geopotential. Furthermore, the 16 August 00 UTC, 12 UTC and 17 August 12 UTC, the trough movement toward east is a little more quickly in model prediction. Moreover, at 17 August 00 UTC, center of low is smaller in extent in 12 km model domain than in Reanalysis field. At 18 August 00 UTC, the cut of center of low seen over western Turkey is deeper in circulation over a region including Istanbul and extending toward north. After 12 hours, the location of trough is shifted southeast at the model. Finally at 19 August 00 UTC, it is deepened and reconnected to its origin in NCEP Reanalysis unlike model prediction.

Results of 500mb model predictions of nested 12km domain are seen in Figure 5.1. General structure of synoptic pattern obtained in 12 km is also similar to previous model runs. Like in the first experiment with a large domain of 18 km horizontal resolution, the 12 km domain, as it is feedback from the 36 km coarse domain, is showing the similar differences with 9km domain. Most important of all, since 12 km domain is fed from the coarse domain of 36 km, which is larger than all other domains of previous experiments, the values of geopotential height is more detailed than the other experiments. For instance, at experiment I, the deepest value of geopotential height is 5550m, same as experiment 2 and 3, however in this last experiment, we see more deeper values of 5450mb in 36km domain and 5500mb in 12 km domain. After 18 August, location and areal extent of the center of low is difference, for instance similar to experiment one, center of low is cut off more quickly than experiment three and two.

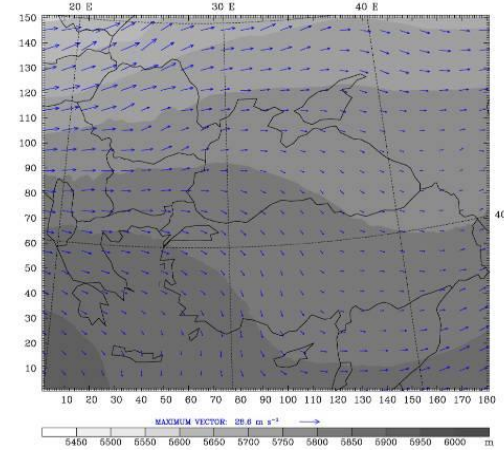
a.) 13 August 2004 00 UTC



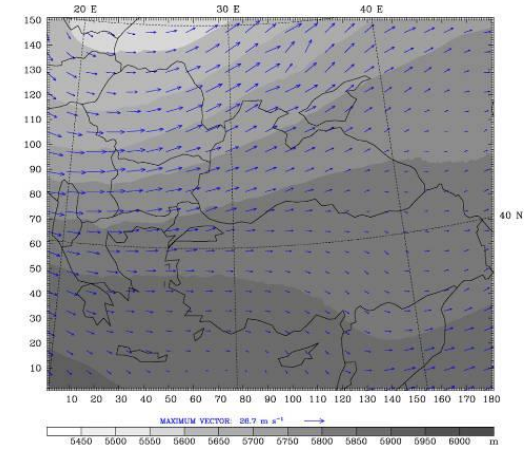
b.) 13 August 2004 12 UTC



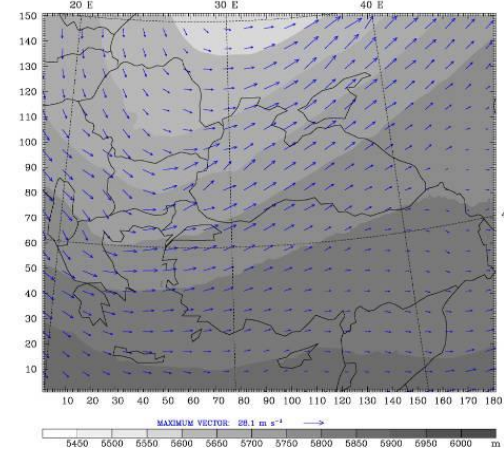
c.) 14 August 2004 00 UTC



d.) 14 August 2004 12 UTC



e.) 15 August 2004 00 UTC



f.) 15 August 2004 12 UTC

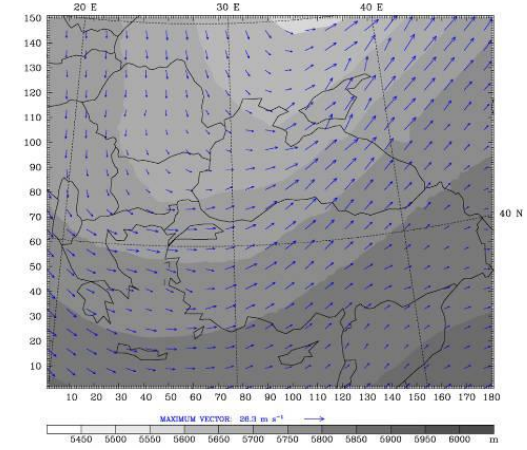
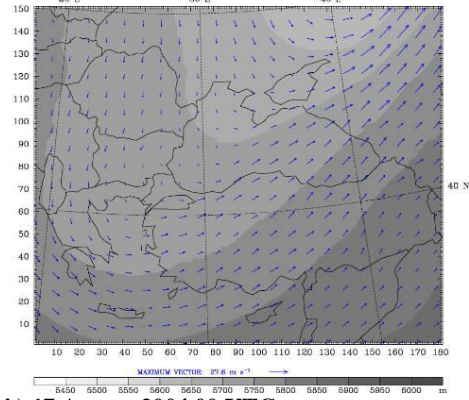
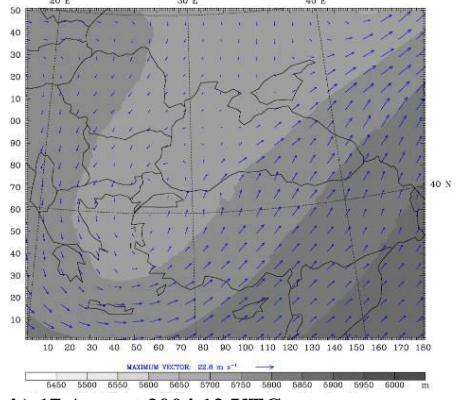


Figure 5.17: 500 mb level for the 12 km domain of experiment 4, geopotential height represented as filled colors, and wind vectors starting at 13 August 00 UTC with 12 hourly interval, ending at 19 August 00 UTC, left column represents the 00 UTC and right column 12 UTC for each forecast day. Panels a to f represent the 13-15 August 2004 of the case study period.

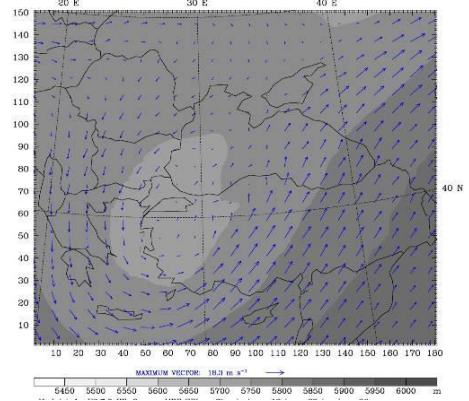
g.) 16 August 2004 00 UTC



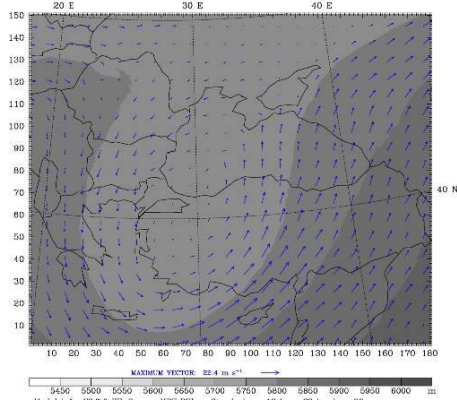
h.) 16 August 2004 12 UTC



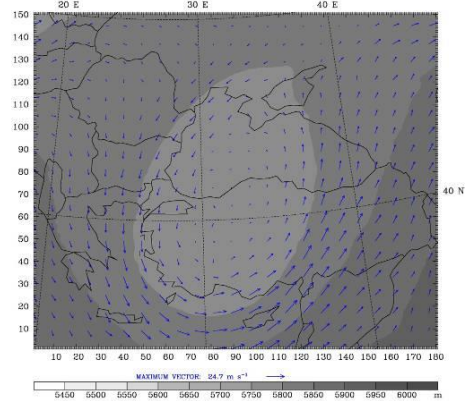
i.) 17 August 2004 00 UTC



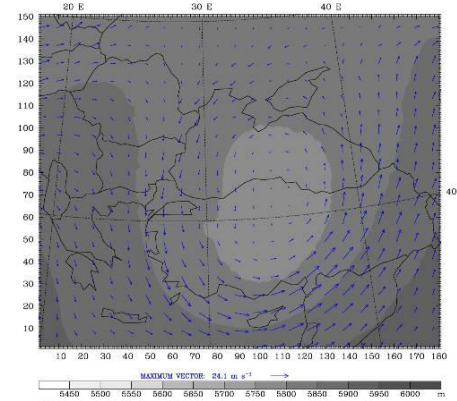
j.) 17 August 2004 12 UTC



k.) 18 August 2004 00 UTC



l.) 18 August 2004 12 UTC



m.) 19 August 2004 00 UTC

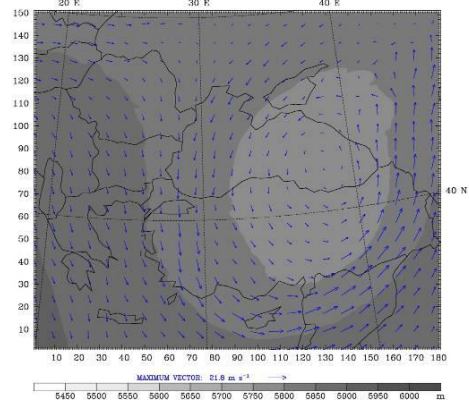


Figure 5.17 (Cont.): Panels g to m represent the 16-19 August 2004 of the case study period.

Figure 5.18 shows the comparison of Reanalysis with model results at 16 August 00 UTC. It is seen that similar patterns are observed, model as fed from mother domain representing more detail than the Reanalysis. Wind speeds are a little less in Istanbul than Reanalysis, and model results show a little shifted geopotential height influence areas.

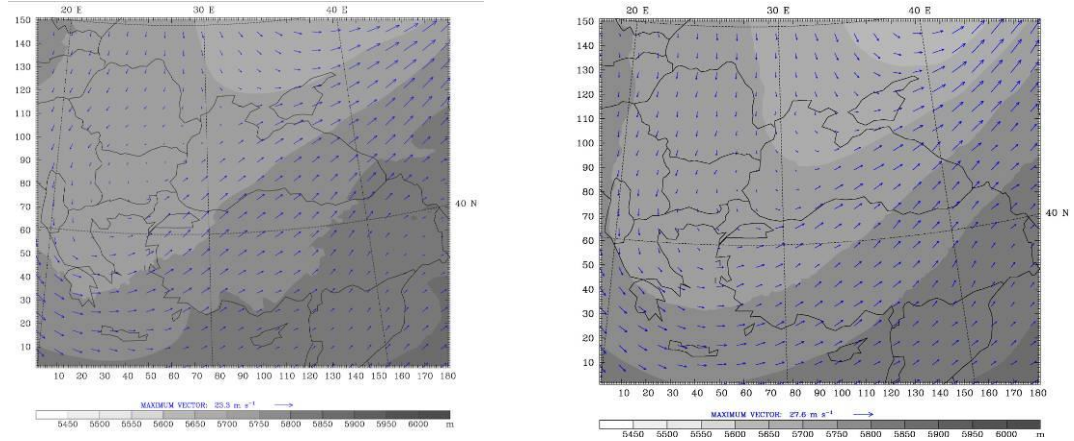


Figure 5.18: Reanalysis (left) and model prediction at 500 mb for 16 August 2004

5.4.1.2 850 mb field

5.4.1.2.1 36 km coarse domain

Patterns of the 850 mb fields reveal similar fields in all model predictions and these are consistent with NCEP Reanalysis. For comparison in figure 5.19 Reanalysis and model results are seen for 16 August 00 UTC.

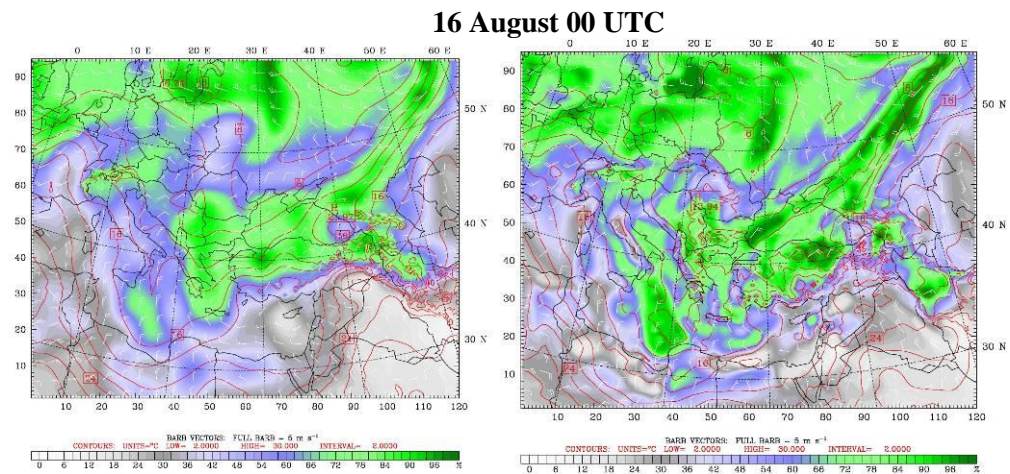


Figure 5.19: Reanalysis (left), model results (right) for experiment IV 36km domain.

It can be seen that model and Reanalysis fields are quite similar. Model as in higher resolution predicts more relative humidity than Reanalysis. NCEP reanalysis fields for other days are seen in Appendix B and model results are seen in figure 5.20. The relative humidity values are greater on larger domains with lower horizontal resolution as they are generating the impacts of larger flows more than the other domains, and as they are closer to the two centers of low. Thus, the 36 km model run is predicting same fields as of the 9km run but with higher relative humidity.

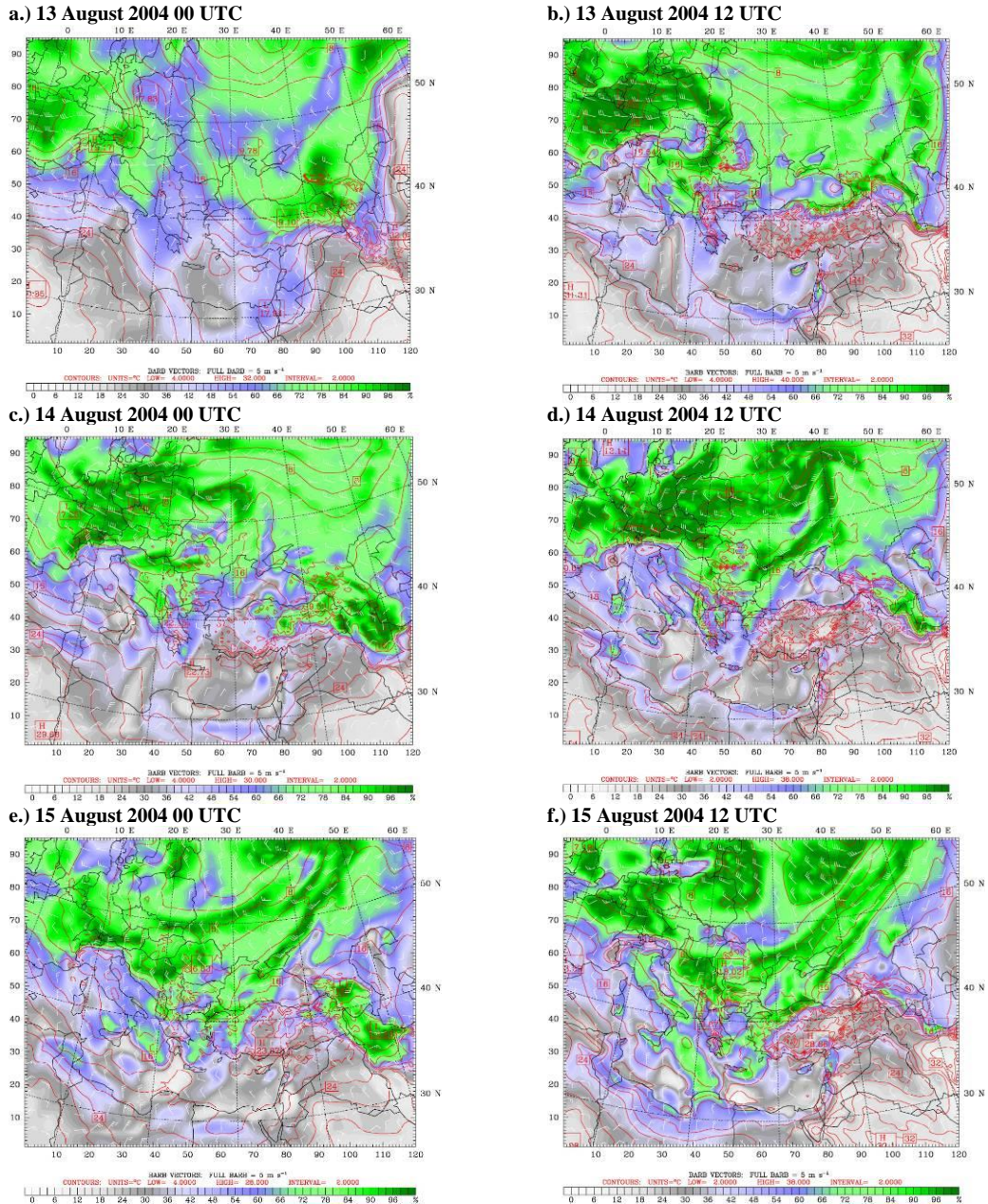
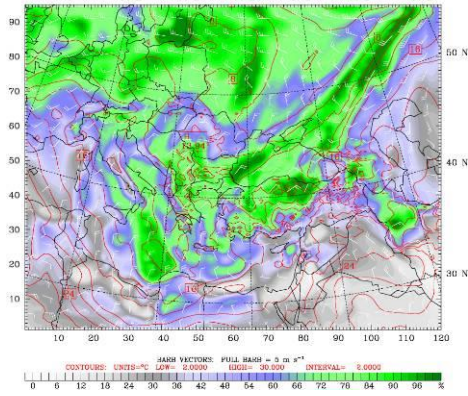
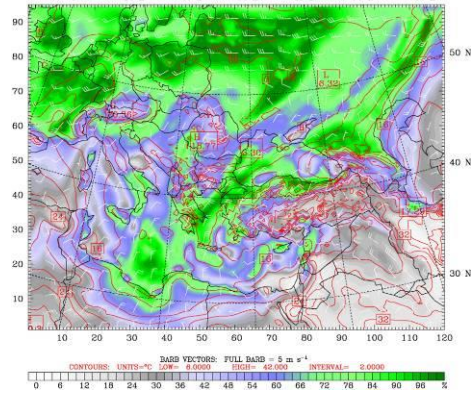


Figure 5.20 Experiment 4, 36 km domain 850 mb level relative humidity represented as filled colors, temperature, and wind vectors starting at 13 August 00 UTC with 12 hourly interval, ending at 19 August 00 UTC, left column represents the 00 UTC and right column 12 UTC for each forecast day. Panels a to f represent the 13-15 August 2004 of the case study period.

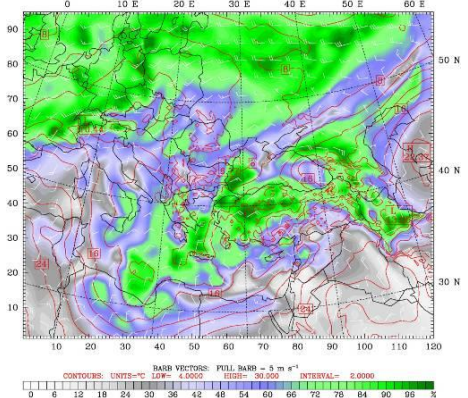
g.) 16 August 2004 00 UTC



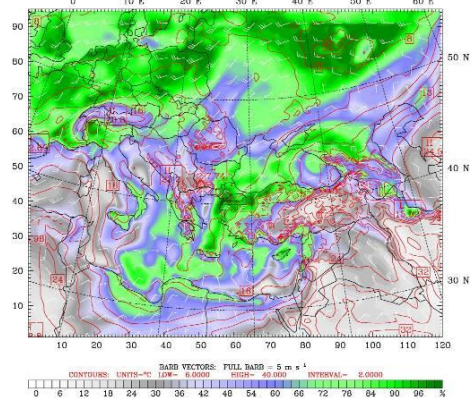
h.) 16 August 2004 12 UTC



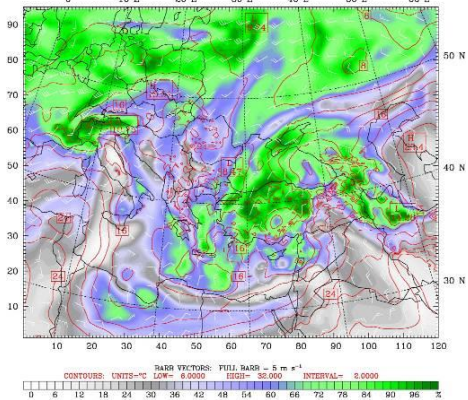
i.) 17 August 2004 00 UTC



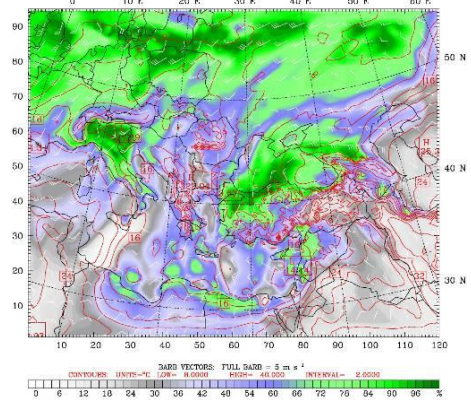
j.) 17 August 2004 12 UTC



k.) 18 August 2004 00 UTC



l.) 18 August 2004 12 UTC



m.) 19 August 2004 00 UTC

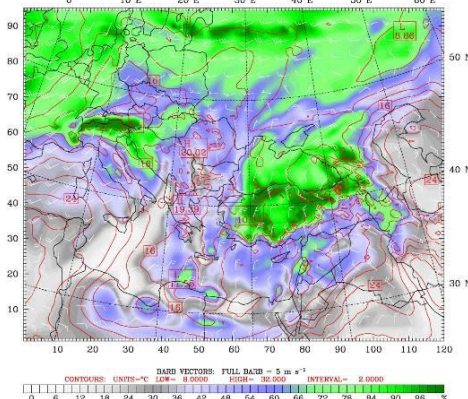


Figure 5.20 (Cont.): Panels g to m represent the 16-19 August 2004 of the case study period.

5.4.1.2.2 12 km nested domain

Similar conditions apply to the 850 mb fields of the 12 km inner nest. When compared with Reanalysis fields given in the Appendix B, it can be seen that wind directions, magnitudes, temperature fields are well captured as well as relative humidity fields. In relative humidity fields, detailed images are seen in model results since model resolution is higher than the Reanalysis resolution and since this domain is fed from the mother domain of 36 km.

As an illustration, a comparison with NCEP Reanalysis is seen in figure 5.21 for 16 August 00 UTC.

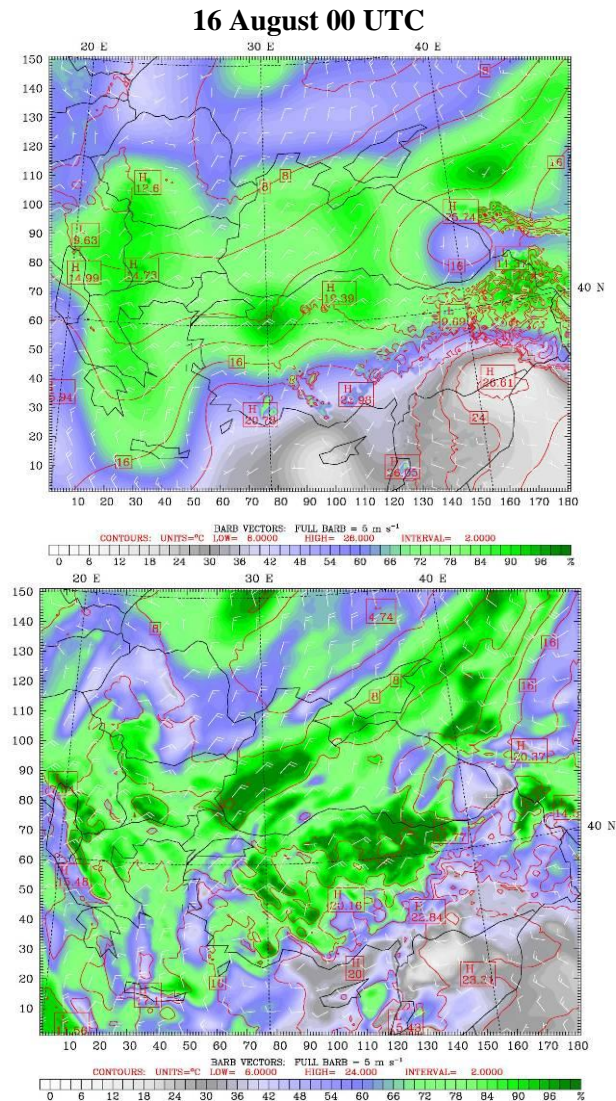
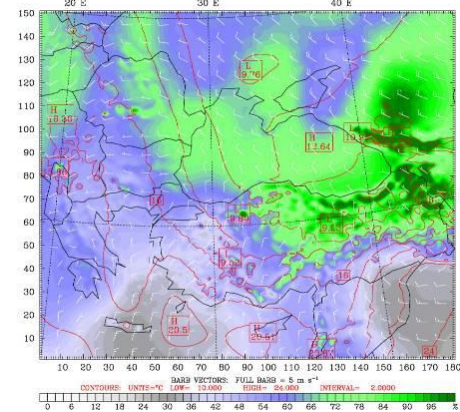


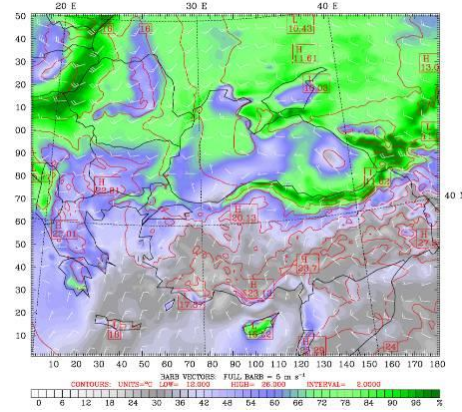
Figure 5.21: Reanalysis (top), and model results for the 12 km inner nest at 850 mb.

It is seen from these figures again that model results for 16 August 00 UTC are consistent with Reanalysis, more detailed fields are seen in model predicted fields. Analyzing this date and the others, it can be concluded that model verification is quite satisfactory. Figure 5.22 shows the 850 mb results of the inner 12 km domain.

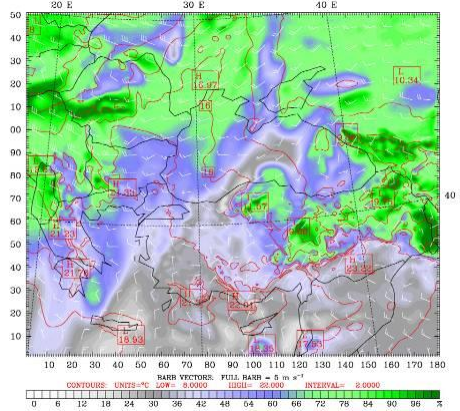
a.) 13 August 2004 00 UTC



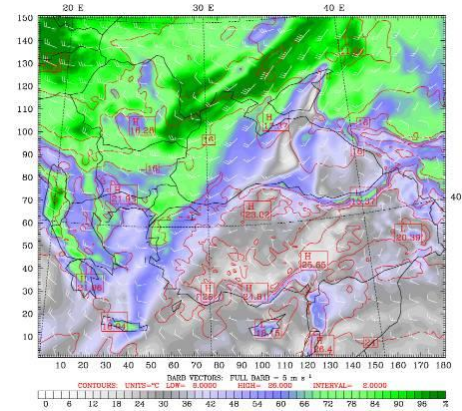
b.) 13 August 2004 12 UTC



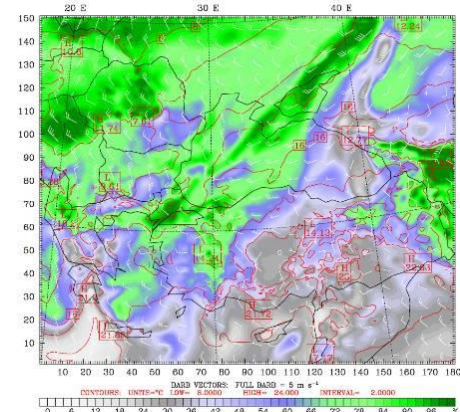
c.) 14 August 2004 00 UTC



d.) 14 August 2004 12 UTC



e.) 15 August 2004 00 UTC



f.) 15 August 2004 12 UTC

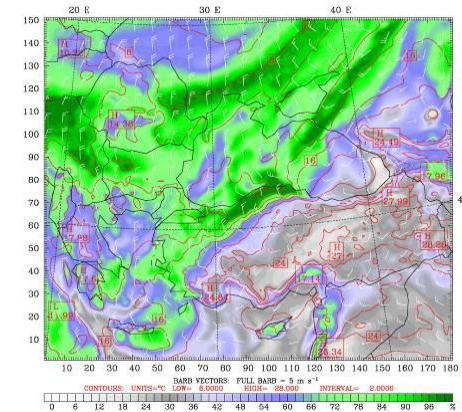
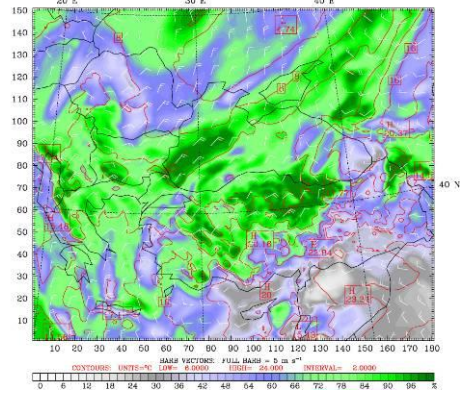
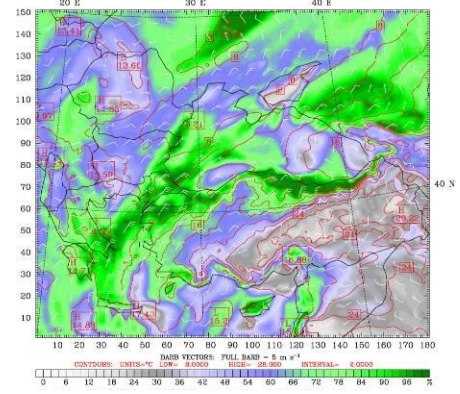


Figure 5.22: Experiment 4, 12 km domain 850 mb level relative humidity represented as filled colors, temperature, and wind vectors starting at 13 August 00 UTC with 12 hourly interval, ending at 19 August 00 UTC, left column represents the 00 UTC and right column 12 UTC for each forecast day. Panels a to f represent the 13-15 August 2004 of the case study period.

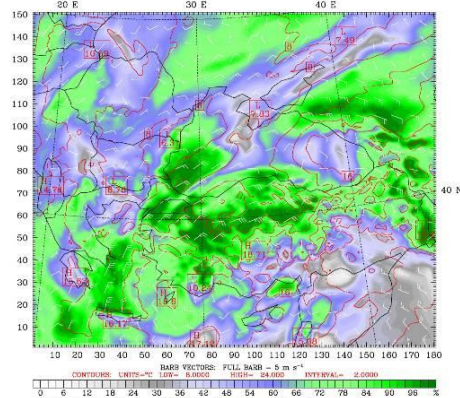
g.) 16 August 2004 00 UTC



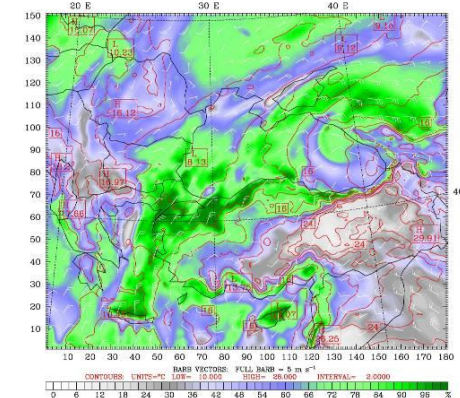
h.) 16 August 2004 12 UTC



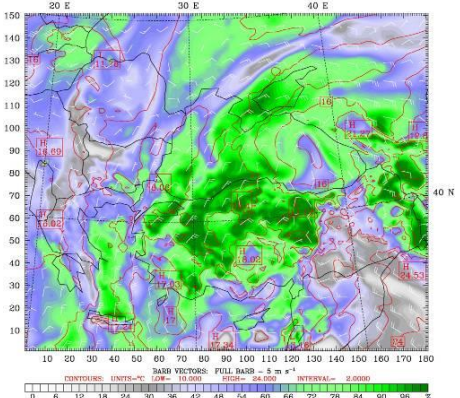
i.) 17 August 2004 00 UTC



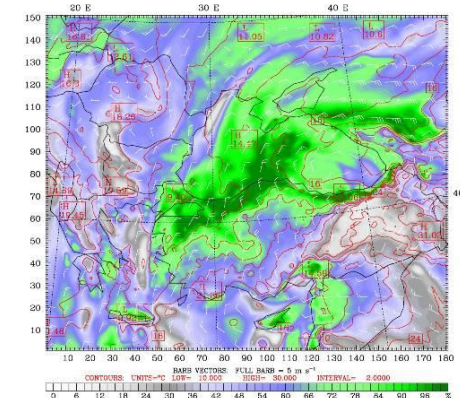
j.) 17 August 2004 12 UTC



k.) 18 August 2004 00 UTC



l.) 18 August 2004 12 UTC



m.) 19 August 2004 00 UTC

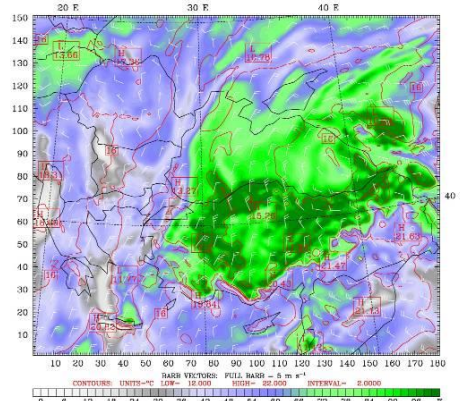


Figure 5.22 (Cont.): Panels g to m represent the 16-19 August 2004 of the case study period.

5.4.1.2.3 4 km nested domain

At 4 km model domain, conditions over Istanbul are seen more remarkably. For comparison figure 5.23 shows NCEP Reanalysis fields and model output at 850 mb for August 16, 2004 at 12 UTC. Reanalysis, since it is of lower resolution shows relative humidity of 80% all over the domain with higher values located on Marmara Sea and northward. Model prediction however, distributes these humidity fields as it has higher resolution and more impacts of surface. Wind speeds and directions are same, and temperature field is given in more at model result with 12⁰C over Istanbul in both maps.

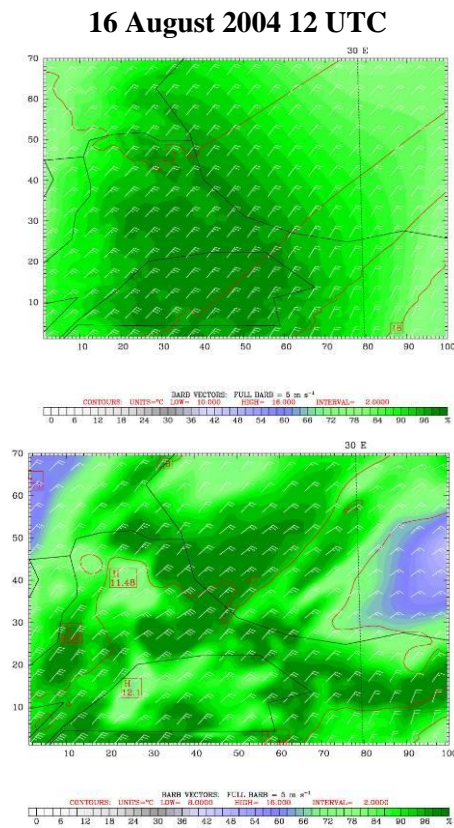
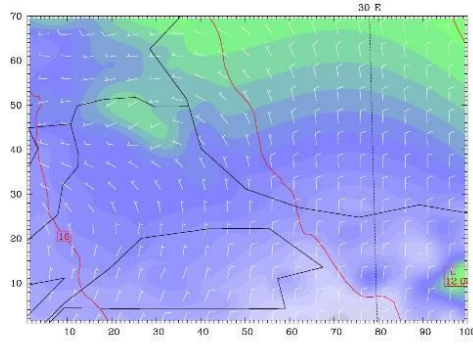


Figure 5.23: Reanalysis field (top) and model result (bottom) at 850 mb at 16 August 2004 12 UTC

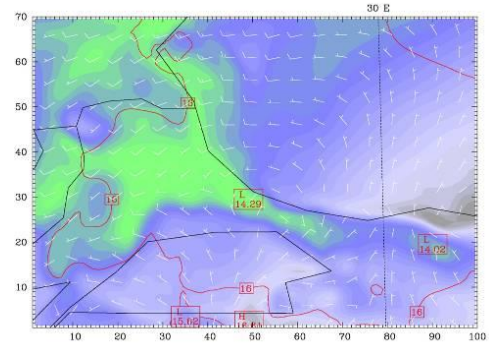
Analysis of the 850 mb fields of the inner nested 4km resolution domain of experiment IV, shown in figure 5.24, reveals the following. At 13 August 12 UTC, model is predicting moisture on western side of the Istanbul which is not consistent with Reanalysis. Furthermore, at 14 August 12 UTC, the model prediction on the western side is greater in areal extent than Reanalysis. From 15 August 00 UTC to 18 August 00 UTC, the model as it is in a very increased resolution, gives more

detailed fields, with similar amounts of relative humidity. Finally, from 18 August 00 UTC to the end of the case study period, the model is predicting more moisture than Reanalysis. Although the model predicted relative humidity fields are higher with detailed location, as a result of increase resolution, and the general picture obtained is more detailed, it is consistent with the Reanalysis fields.

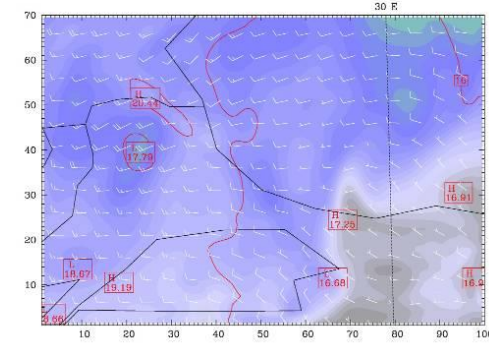
a.) 13 August 2004 00 UTC



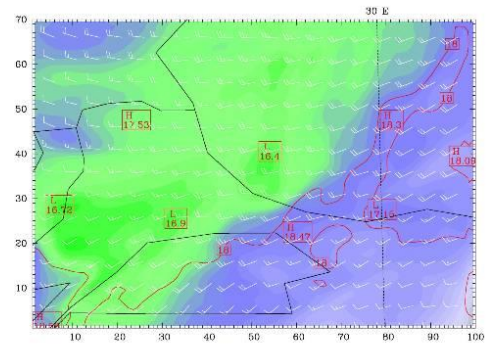
b.) 13 August 2004 12 UTC



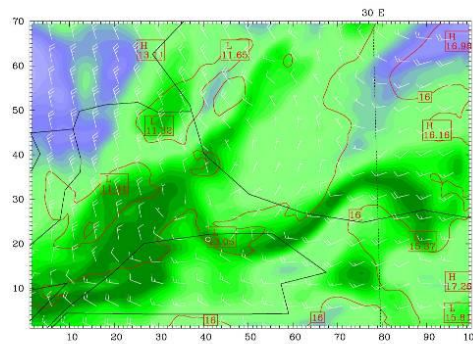
c.) 14 August 2004 00 UTC



d.) 14 August 2004 12 UTC



e.) 15 August 2004 00 UTC



f.) 15 August 2004 12 UTC

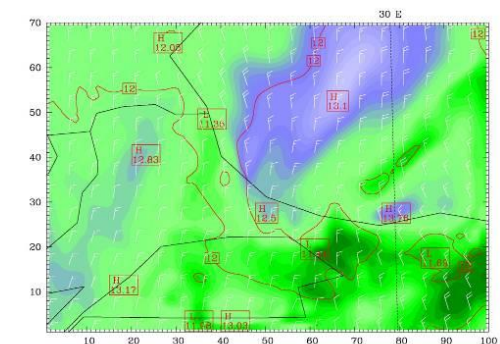
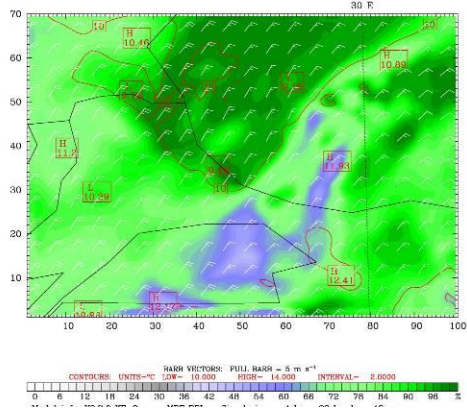
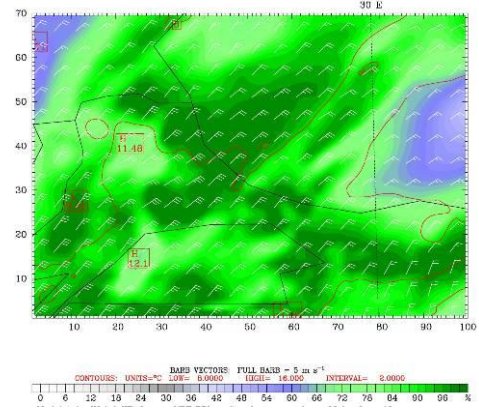


Figure 5. 24: Experiment 4, 4 km domain 850 mb level relative humidity represented as filled colors, temperature, and wind vectors starting at 13 August 00 UTC with 12 hourly interval, ending at 19 August 00 UTC, left column represents the 00 UTC and right column 12 UTC for each forecast day. Panels a to f represent the 13-15 August 2004 of the case study period.

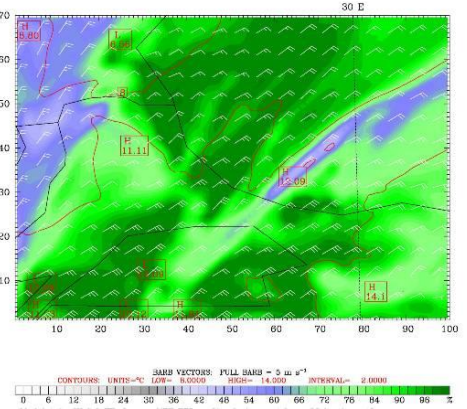
g.) 16 August 2004 00 UTC



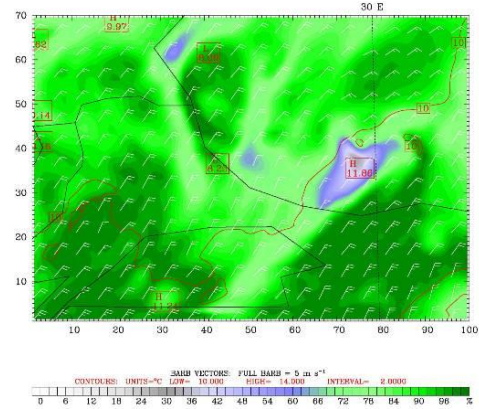
h.) 16 August 2004 12 UTC



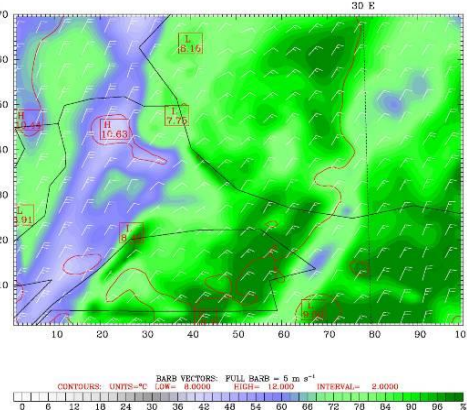
i.) 17 August 2004 00 UTC



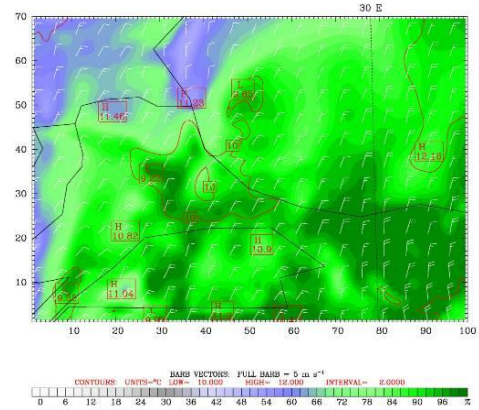
j.) 17 August 2004 12 UTC



k.) 18 August 2004 00 UTC



l.) 18 August 2004 12 UTC



m.) 19 August 2004 00 UTC

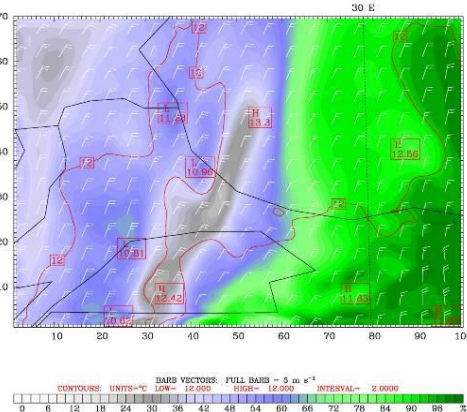


Figure 5. 24 (Cont.): Panels g to m represent the 16-19 August 2004 of the case study period.

5.4.1.3 Cross sectional analysis

5.4.1.3.1 36 km coarse domain

In order to analyze the meteorological situation, a line is selected and vertical cross section at this line is investigated. The position of line is chosen according to the direction of flow at the day of flood 16 August. Figure 5.25 shows the position of flood on the 36 km coarse domain and figure 5.26 shows the vertical cross section fields for this domain.

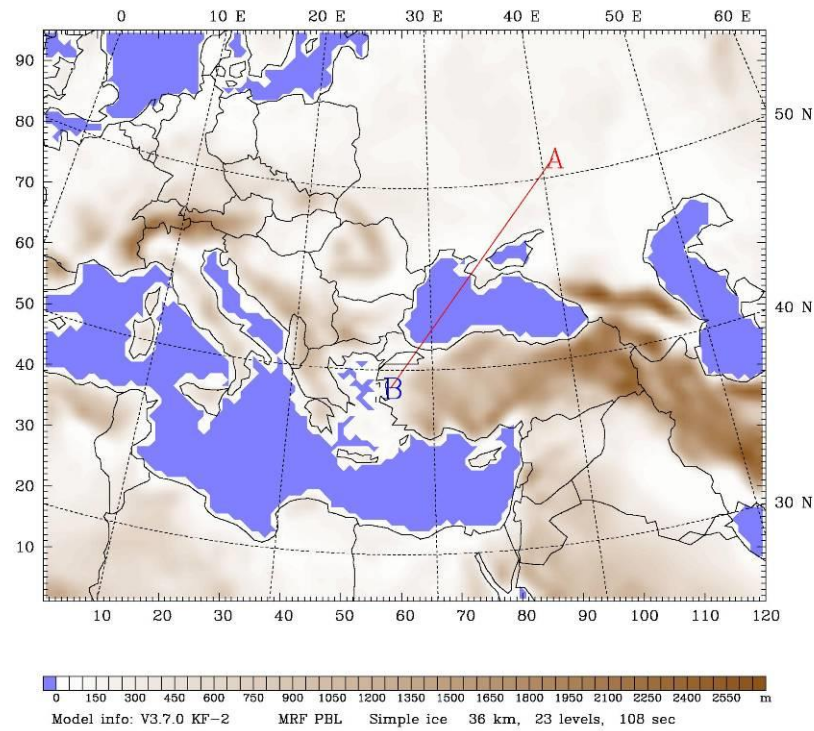
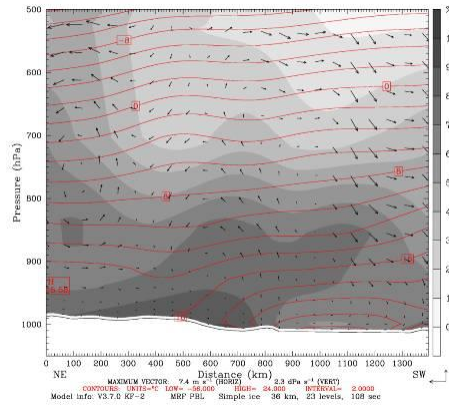


Figure 5.25: 36 km coarse domain of experiment four, and the vertical cross section line.

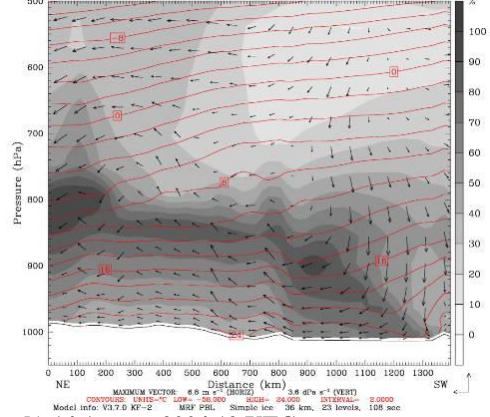
At 13 August there are subsiding motions over Istanbul and temperatures are 24°C , at 12 UTC subsiding motions are more powerful. At 14 August 12 UTC, winds start to be calmer and there is not a distinct downward motion. Conversely at 15 August 00 UTC, the winds are changing direction and relative humidity field is being carried from Black Sea Region to Istanbul, temperatures are greater than 24°C in Istanbul and convective activity starts. Furthermore, at this time carried relative humidity is combined with the upward motions and feeds the created convective motions from Black Sea region as mentioned. At 16 August 00 UTC, the upward motions are very strong and there are high amounts of relative humidity about 90-100% over Istanbul,

temperatures are decreased to 22°C over Istanbul. At 16 August 12 UTC, the upward motions are suppressed but there is still maximum amounts of relative humidity over Istanbul and relative humidity is still being transported from Black Sea towards Istanbul. After this time convective motions do not exist, although relative humidity is still carried toward Istanbul with prevailing surface winds. At 17 August 00 UTC, maximum relative humidity is leaving Istanbul, temperatures are about 22.5°C , at 12 UTC, very tiny upward motion is present at the south of Istanbul.

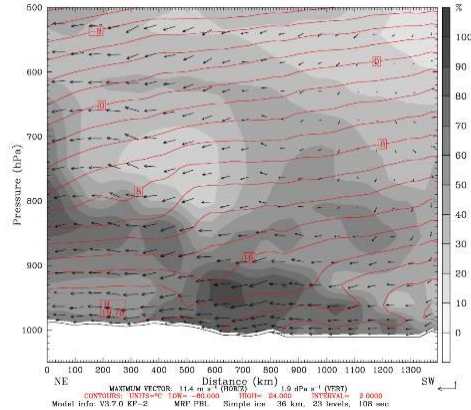
a.) 13 August 2004 00 UTC



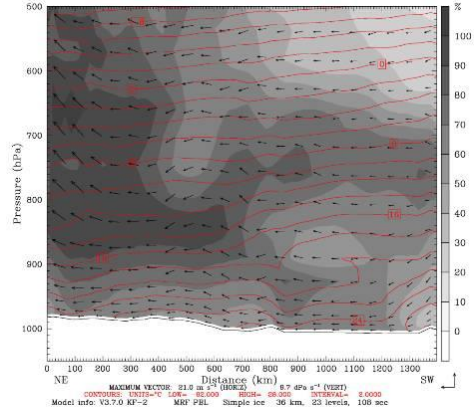
b.) 13 August 2004 12 UTC



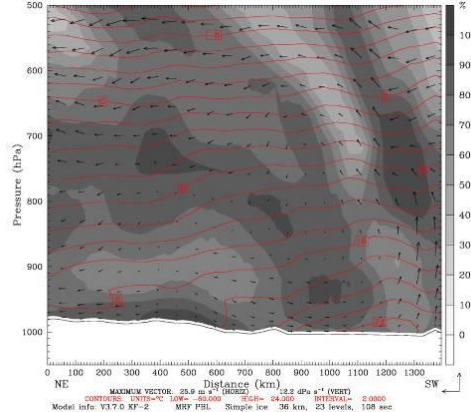
c.) 14 August 2004 00 UTC



d.) 14 August 2004 12 UTC



e.) 15 August 2004 00 UTC



f.) 15 August 2004 12 UTC

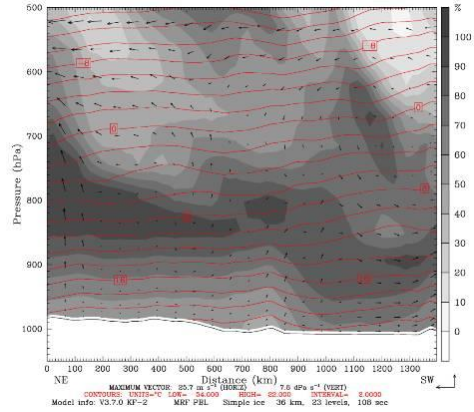
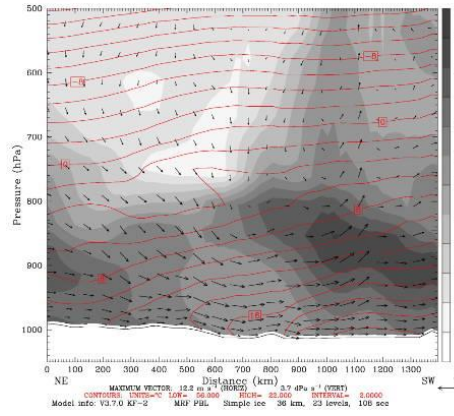
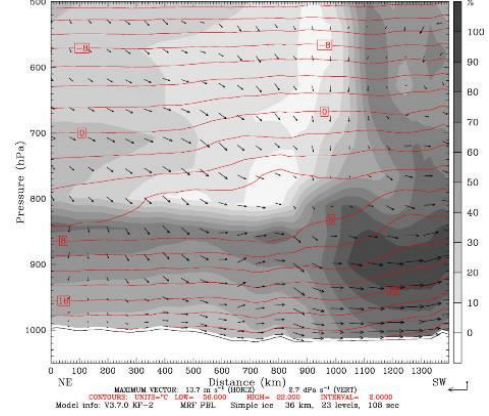


Figure 5.26: Vertical cross sections at 36 km domain of experiment IV. Panels a to f represent the 13-15 August 2004 of the case study period.

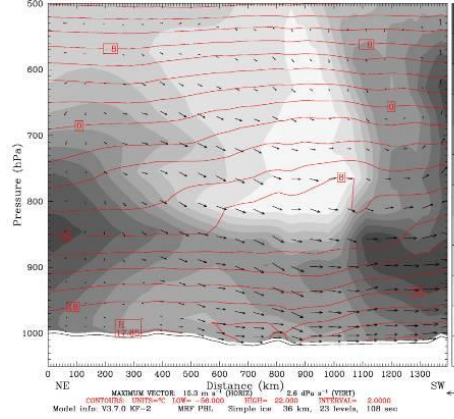
g.) 16 August 2004 00 UTC



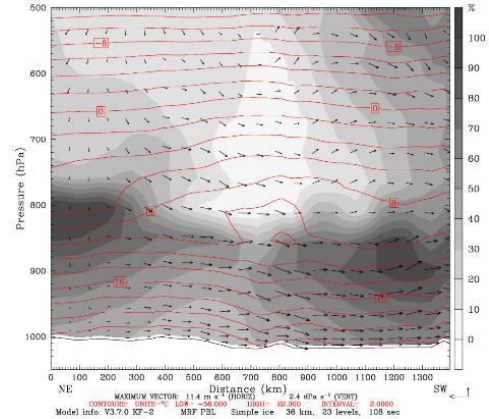
h.) 16 August 2004 12 UTC



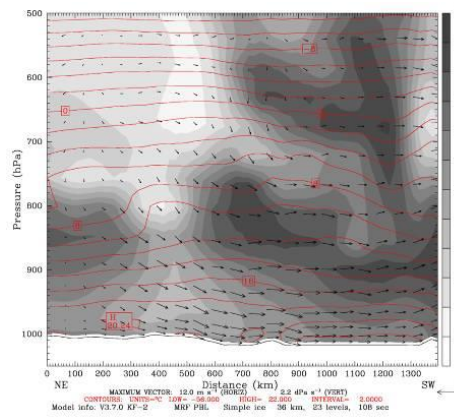
i.) 17 August 2004 00 UTC



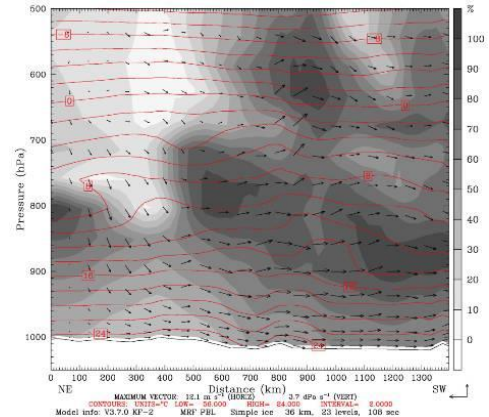
j.) 17 August 2004 12 UTC



k.) 18 August 2004 00 UTC



l.) 18 August 2004 12 UTC



m.) 19 August 2004 00 UTC

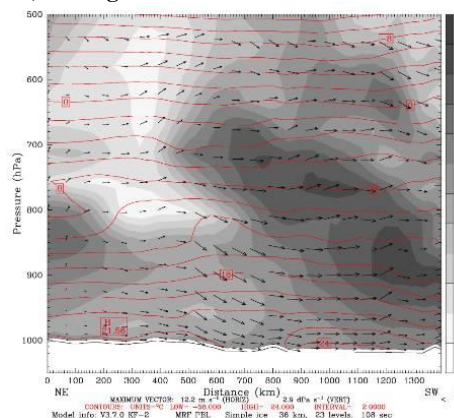


Figure 5.26 (Cont.): Panels g to m represent the 16-19 August 2004 of the case study period.

5.4.1.3.2 12 km nested inner domain

Figure 5.27 shows the location of the vertical cross section chosen on this domain and figure 5.28 shows the vertical cross sections at 16 August 00 and 12 UTC.

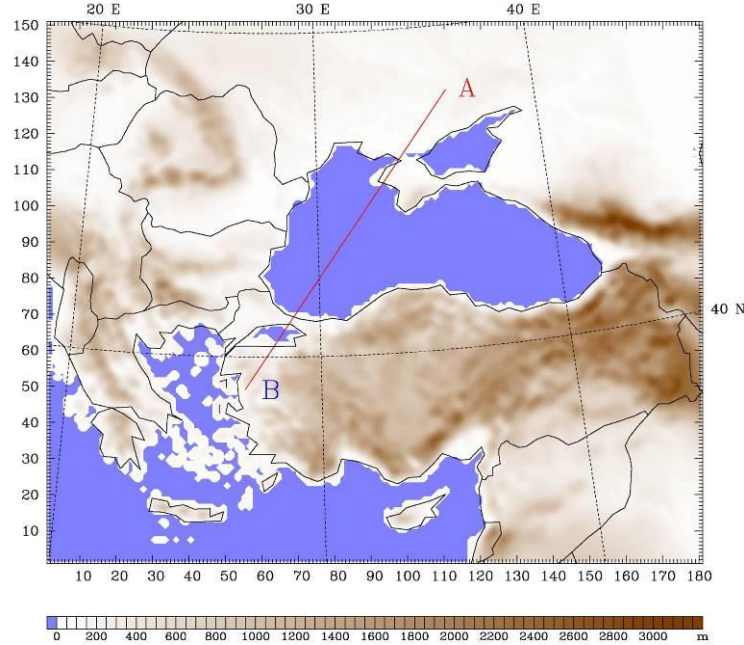


Figure 5.27: 12 km nested domain of experiment four, and the vertical cross section line.

At 12 km horizontal resolution, vertical movements of air are seen in more detail. The downward motions over Istanbul are more distinct than in 36 km coarse domain, and similar patterns are observed as expected. Moreover, relative humidity carried from the Black Sea region and the aforementioned upward motions and convective movements are seen more effectively. Figure shows the vertical cross section for 16 August 00 and 12 UTC. Convective motions at the vicinity of Istanbul are seen clearly.

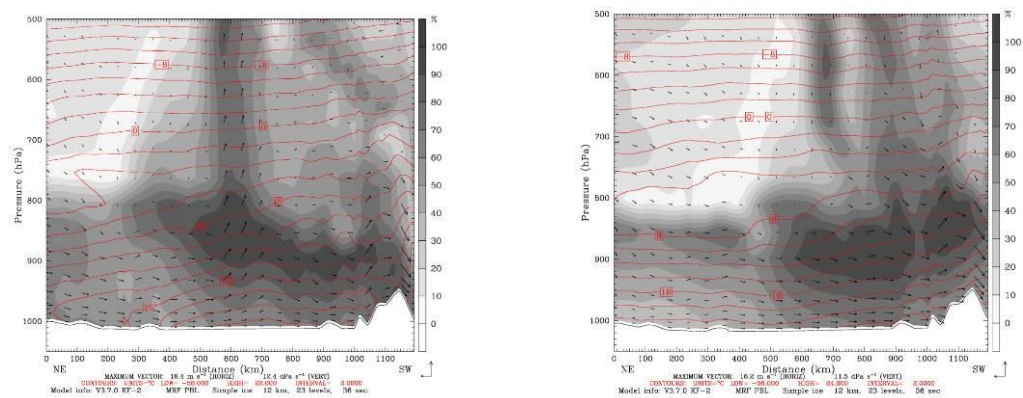


Figure 5.28: Vertical cross section at 16 August 2004 00UTC (left) and 12 UTC(right) for 12 km domain of experiment IV.

5.4.1.3.3 4 km nested inner domain

Figure 5.29 shows the location of the vertical cross section chosen on this domain and figure 5.30 shows the vertical cross section for 16 August 00 and 12 UTC.

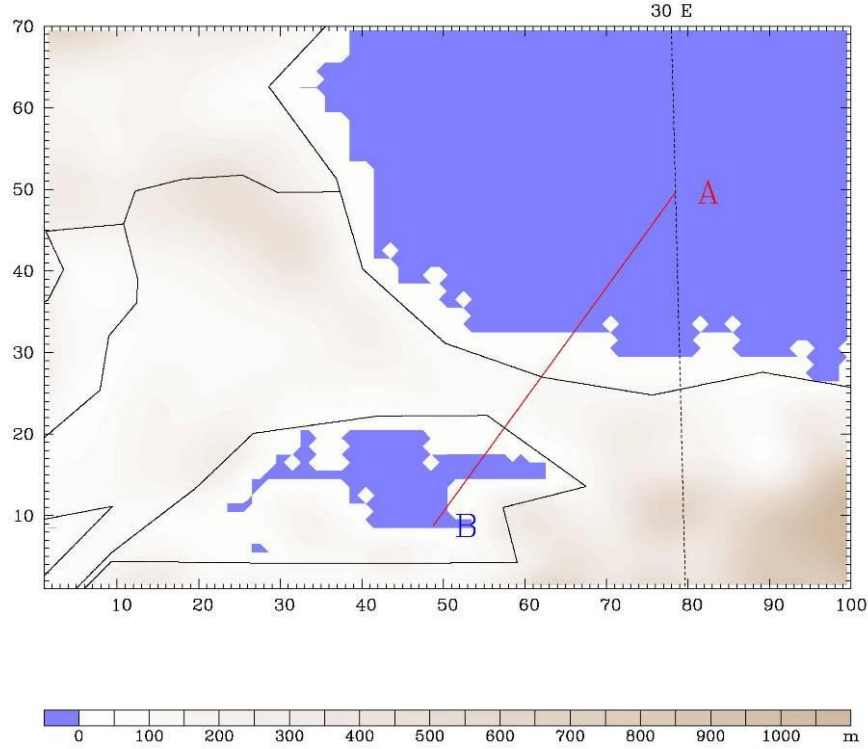


Figure 5.29: 4 km nested domain of experiment four, and the vertical cross section line.

At 4 km resolution, relative humidity fields carried toward Istanbul are again observed. Furthermore, convective motions are seen, and there is about 90-100 % relative humidity over Istanbul with surface temperatures of about 22°C

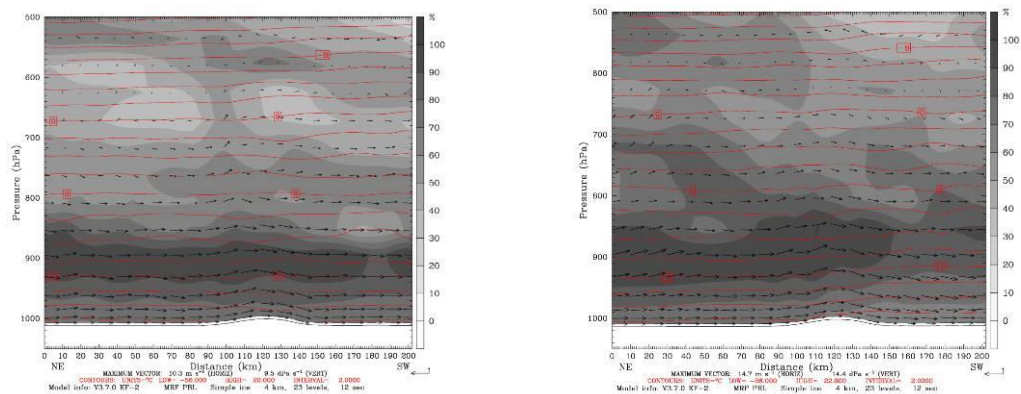


Figure 5.30: Vertical cross sections at 16 August 2004 00UTC (left) and 12 UTC(right) for 4 km domain of experiment IV.

In the next chapter, daily total accumulated rainfall analysis will be made.

6. TOTAL ACCUMULATED RAIN ANALYSIS

In this part, total accumulated rain amounts of each experiment results are compared with the multi satellite data, and finally for the last experiment a detailed comparison is done involving observations.

6.1 Experiment I (18 km Resolution Large Domain)

Model results for experiment one and the multi satellite data image are seen in Figure 6.1 and 6.2 respectively. It can be seen that model is able to capture the total accumulated precipitation fields of the multi satellite data image. Location of precipitation over Italy is simulated well with a little shift to east, but amounts are less than the satellite data. In addition, over mountainous regions of Georgia, model results are giving more precipitation. Moreover, rainfall area over Istanbul is shifted towards north. Rainfall area over mid Black Sea region in satellite is not seen or is shifted and combined with the precipitation area at the southeast of Istanbul. Finally, precipitation area southeast of Istanbul is seen more detailed due to the higher resolution of the experiment domain compared to the satellite data.

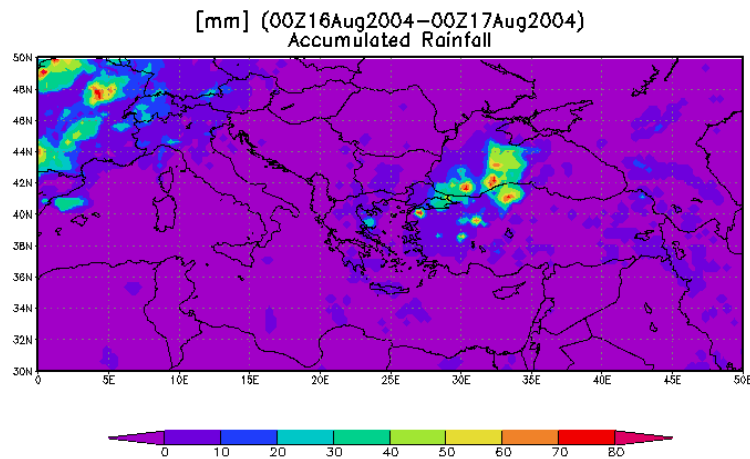


Figure 6.1: Multi Satellite data image for 16 August 2004 showing daily total accumulated precipitation for the domain of experiment I.

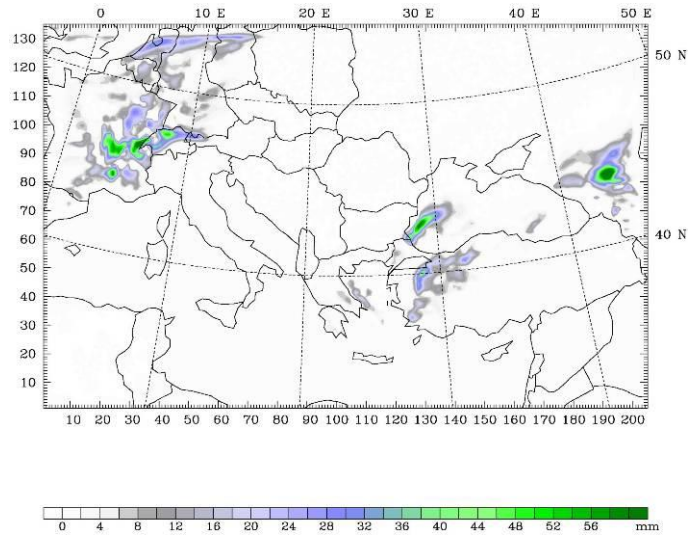


Figure 6.2: Model results for 16 August 2004 showing daily total accumulated precipitation of experiment I.

6.2 Experiment II (18 km Resolution Smaller Domain)

Model results for experiment two and the multi satellite data image are seen in Figure 6.3 and 6.4. In this experiment, while the model is able to demonstrate the rain fields over northwestern Turkey, due to the lateral boundary conditions, it cannot show the precipitation over northern Italy. However, this precipitation pattern can clearly be seen on the larger domain of experiment one. Both mid Black Sea precipitation area and the precipitation area southeast of Istanbul are seen.

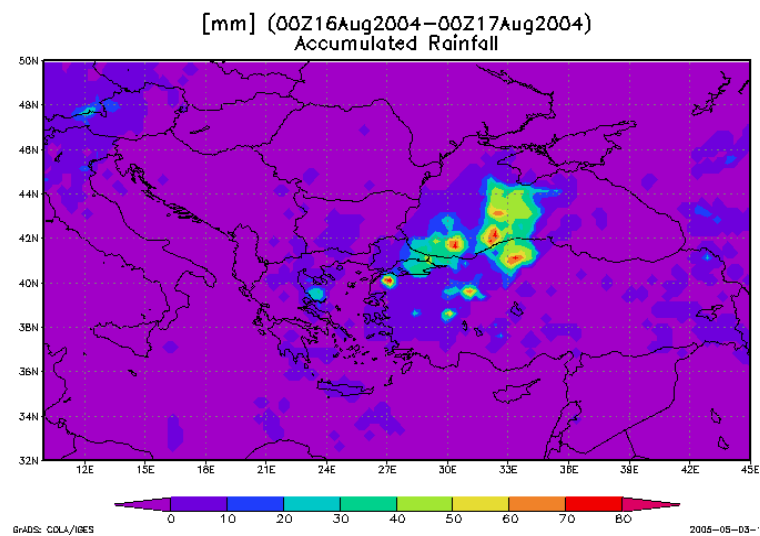


Figure 6.3: Multi Satellite data image for 16 August 2004 showing daily total accumulated precipitation for the domain of experiment II.

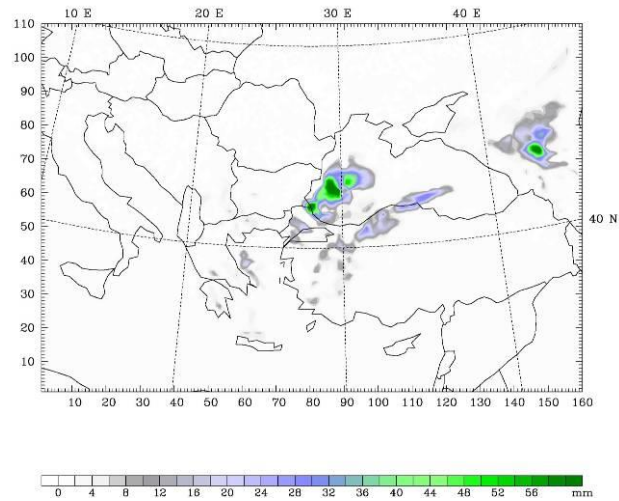


Figure 6.4: Model results for 16 August 2004 showing daily total accumulated precipitation of experiment II.

6.3 Experiment III (9 km Resolution Smaller Domain)

Model results for the experiment and the multi satellite data image are seen in Figure 6.5 and 6.6. In this experiment, the impacts of lateral boundary conditions as in experiment II are also seen and precipitation field over Italy is not predicted. Location of the other fields are similar to experiment II, however, in experiment III, model shows the precipitation fields over Turkey in more detail as a result of smaller grid resolution. For instance a detailed precipitation band connecting cities Zonguldak and Muğla is predicted. Even though results are consistent with satellite over Istanbul, the field is shifted towards west, and generally precipitation amounts are underestimated. Although detailed, this experiment is not correctly simulating the whole field.

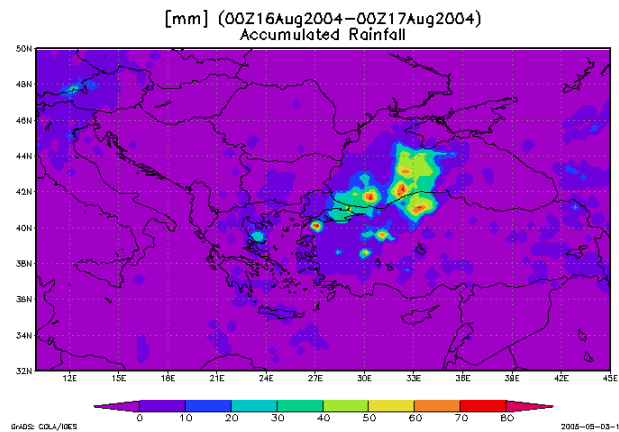


Figure 6.5: Multi Satellite data image for 16 August 2004 showing daily total accumulated precipitation for the domain of experiment III.

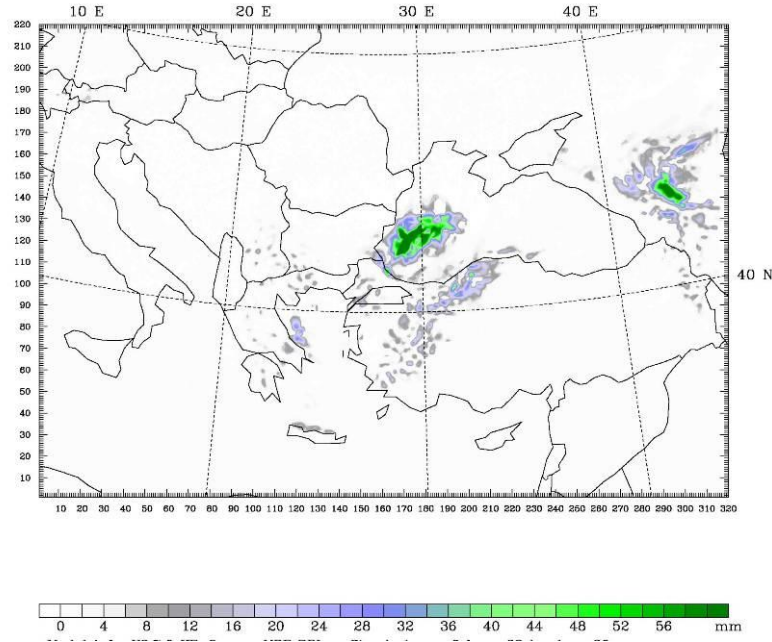


Figure 6.6: Model results for 16 August 2004 showing daily total accumulated precipitation of experiment III.

6.4 Experiment IV (Coarse Domain with Nested Approach)

In the previous experiments, reduced lateral boundaries led to the result that precipitation fields close to lateral boundaries were not captured. For this reason in this experiment, a much larger domain is selected unlike the previous experiments and downscaling approach has been employed for the whole simulation period. Here, coarse domain helps us to see the overall synoptic pattern and finer domains help us to see the details of the systems. Results can be seen from the following figures. Figures 6.7, 6.9 and 6.11 show the multi satellite data image for 16 August 2004 corresponding to each domain. In figure 6.8, as mentioned before, the coarse model domain could determine each precipitation area of the domain, which will provide correct flow of information to finer domains. Furthermore, location of the precipitation field on Istanbul is better simulated than the previous experiments.

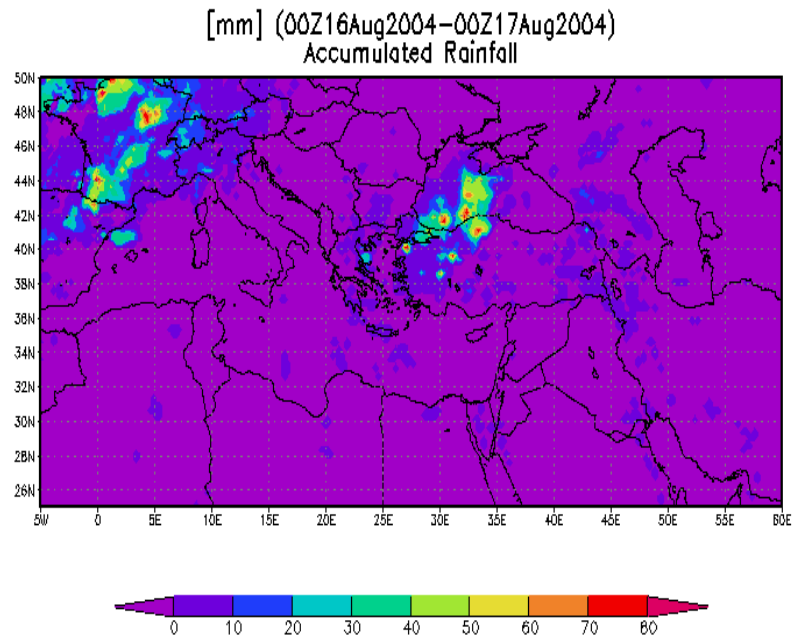


Figure 6.7: Multi Satellite data image for 16 August 2004 showing daily total accumulated precipitation for the coarse domain of experiment IV.

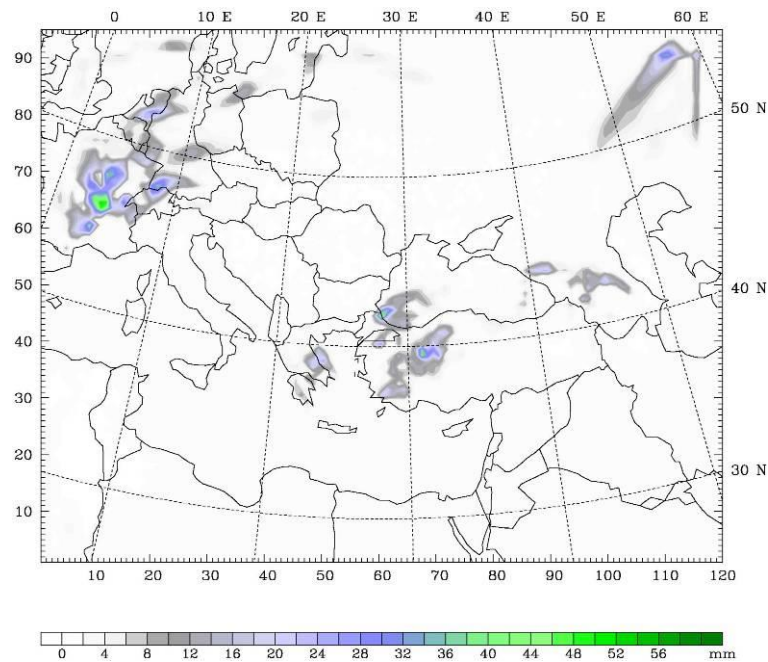


Figure 6.8: Model results for 16 August 2004 showing daily total accumulated precipitation of coarse domain of experiment IV.

With the feedback of the coarse domain, the 12 km domain results, figure 6.10, are quite good when compared with satellite data. Precipitation area over Istanbul is better seen with more detail. In addition, precipitation field over southeast of Istanbul, central Turkey, is accurately captured and given in more detail.

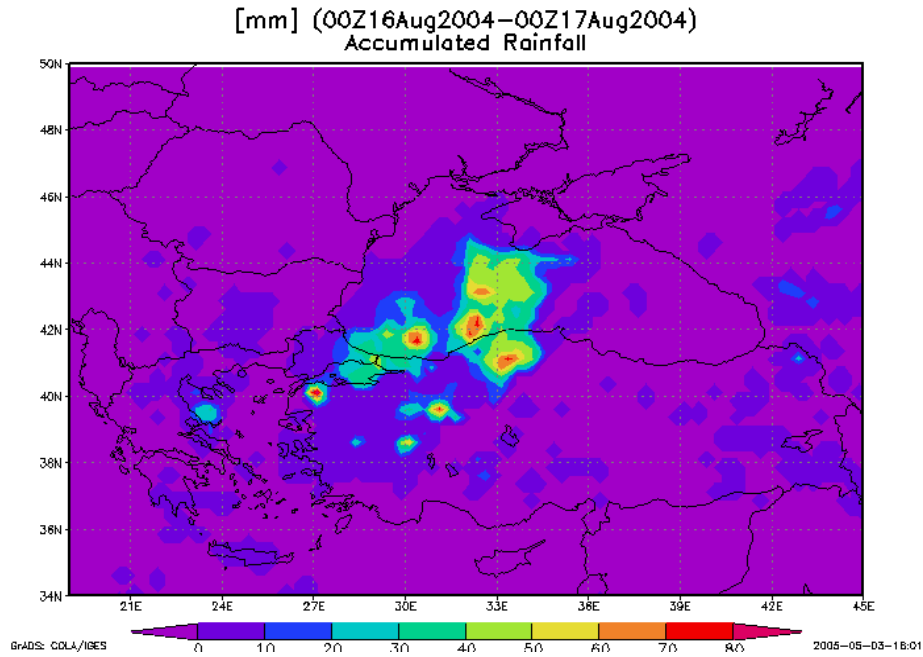


Figure 6.9: Multi Satellite data image for 16 August 2004 showing daily total accumulated precipitation for the 12 km domain of experiment IV.

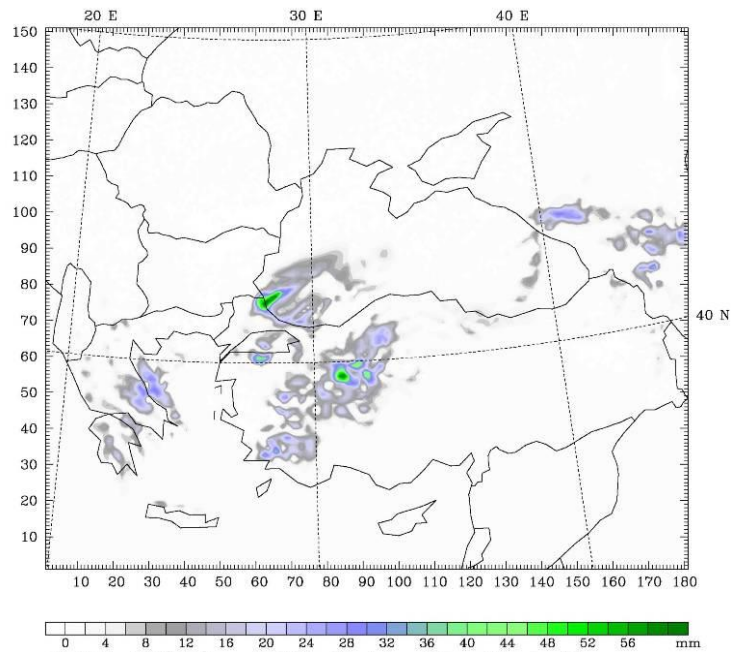


Figure 6.10: Model results for 16 August 2004 showing daily total accumulated precipitation of 12 km domain of experiment IV.

Finally, in figure 6.11, the smallest model domain (4 km) gives the most comprehensive results. According to the multi satellite data, the model can capture the area of influence of precipitation, but there are some discrepancies between the two plots. Southeastern side of the map gives similar amount of precipitation in both model and satellite data image. Central precipitation location is predicted north of

Istanbul, compared with satellite, it is shifted west. It is essential to mention here that the multi satellite data is of $0.25^\circ \times 0.25^\circ$ resolution, which is much lower than this high-resolution domain, and is also an estimation experiment data that is still being tested. Therefore, for verification purposes model results are also compared with station data.

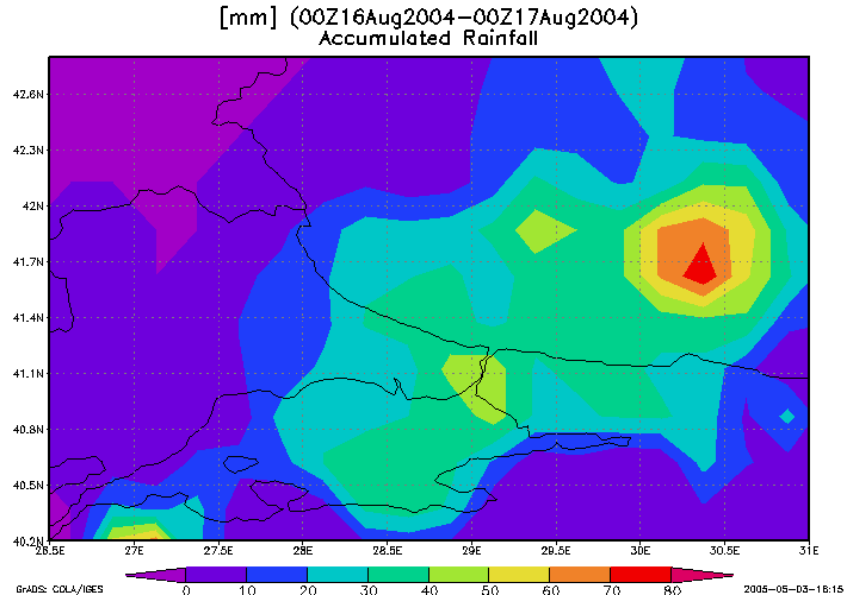


Figure 6.11: Multi Satellite data image for 16 August 2004 showing daily total accumulated precipitation for the 4 km domain of experiment IV.

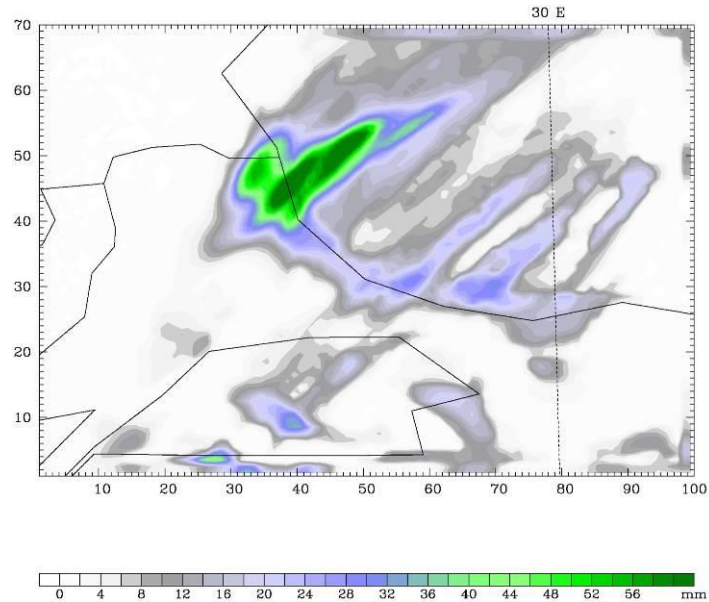


Figure 6.12: Model results for 16 August 2004 showing daily total accumulated precipitation of 4 km domain of experiment IV.

Comparison is done with the observations of Goztepe and Kandilli Station. Figure 6.13 gives the comparison for 36, 12, and 4 km domains with observations and estimate multi satellite data.

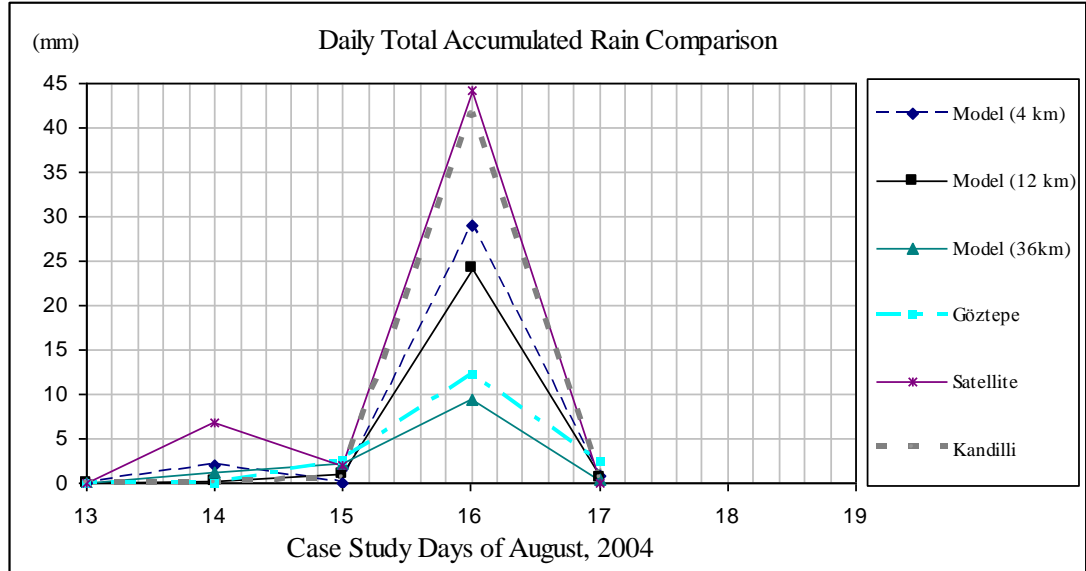


Figure 6.13: Model daily total accumulated results of the last experiment compared with multi satellite data and observations.

As the model domain became smaller, and grid resolution increased, estimated precipitation amounts increased for the associated grid that the station is located. Although precipitation amounts of the Goztepe Station are less than the multi satellite data, at the regions of flood it is known that amounts of total accumulated precipitation were closer to the satellite data. As a result, inner domain is more accurate in predicting precipitation than the outer domains.

7. CONCLUSION AND FUTURE WORKS

Flood is an extremely hazardous event giving harm not only to humans, and nature but also to the economy of the affected regions and people. In this study, a sensitivity analysis was done for flood prediction in Istanbul for the 16 August 2004 case. The analysis included tests of lateral boundaries and horizontal resolution. Four experiments were done at this basis. In the first experiment, a larger domain with 18 km horizontal resolution was selected. As a next step, a second experiment was done in a smaller domain with the same horizontal resolution of 18 km to see the impacts of lateral boundaries on flood prediction. Furthermore, a third experiment was employed with 9 km horizontal resolution on the same domain of the second experiment. This experiment was done in order to see the impacts of the horizontal resolution. Finally, a last experiment was done with a much larger domain than all the previous experiments and consisted of 3 domains of which, one was the coarse domain with horizontal resolution of 36 km, and the other two were inner domains with horizontal resolutions of 12 and 4 km respectively.

In all model runs, model verification of 850 and 500 mb fields were done with NCEP Reanalysis maps, and satisfactory results were obtained. Analyzing these maps and model predictions, it was found out that in order to see the overall synoptic pattern more effectively, it was significant and essential to have a large domain with low horizontal resolution and have inner domains of increased resolution to obtain accurate flow of information to the inner nests. This was the reason the last experiment was done. As a result, with large lateral boundaries, synoptic systems are more successfully predicted and flow of information input to the system of nests is more accurately done minimizing the noise in the area of interest.

Furthermore, analyzing model predicted fields of daily total accumulated precipitation; it was found out that narrow lateral boundaries were failing to produce precipitation fields close to the lateral boundaries. In all model domains, Istanbul was not close to the lateral boundaries, and all experiments were predicting almost similar fields with higher resolution yielding more detailed patterns. However, even with the downscaling approach, there was the problem of accurately detecting the location of the rainfall. In addition, comparison for this location problem was done with the multi satellite data, which is of $0.25^{\circ} \times 0.25^{\circ}$ and is experimental that is still being

tested. Considering these and the very simple moisture parameterization used in all model runs, it would be more better to employ different physics settings to further improve the model results. Moreover, initial condition start in all model runs could be given as 14 August other than 13 August, this may change the precipitation fields obtained, and may give better results in terms of location and amounts.

Additionally, another comparison was also done for the last experiment with daily total accumulated rainfall observations of Göztepe Station. Results revealed that at higher resolution, results were more consistent with observations. The domain with higher resolution was able to capture the relatively heavy rain. However, as the horizontal resolution of the model increased, model was underestimating precipitation over Istanbul for this case. At this point, if there were data available, a regional comparison between model and observations would be better for the verification of model predicted precipitation results.

Moreover, since the model is predicting more precipitation near high altitude areas such as the Alpine and Georgia regions, it would be essential to have high altitude precipitation observations for comparison purposes. Besides, model input sea surface temperatures of The Black Sea would improve observations. Especially for predictions of northern Turkey, model would yield better results if these observations were also used in the model.

It is important to note that precipitation amounts were not extreme in Istanbul at this flood time. The reason for flood to take place was mostly due to urbanization and more importantly urbanization at prior hydrologic fields and river basins. For this reason, since even normal amount of precipitation is able to create flood in Istanbul, it is extremely significant to establish a good approach for the prediction of precipitation in Istanbul.

REFERENCES

- Alpert, P., Krichak, S.O., Krishnamurti, T.N., Stein, U., Tsidulko, M.,** 1996. The Relative Roles of Lateral Boundaries, Initial Conditions and Topography in Mesoscale Simulations of Lee Cyclogenesis, *Journal of Applied Meteorology*, **35**, 1091-1099.
- Anthes, R., A. and T. T. Warner,** 1978. The Development of Mesoscale Models Suitable for Air Pollution and Other Mesometeorological Studies, *Monthly Weather Review*, **106**, 1045-1078.
- Anthes, R. A. Hsie, E. Y. and Kuo, Y. H.,** 1987. Description of the Penn State/NCAR mesoscale model version 4 (MM4). NCAR Tech Note NCAR/TN-282+STR, 66 p.
- Chen S., Guo, Y. R.,** 1994. Terrain and Land Use for the Fifth-Generation Penn State/NCAR Mesoscale Modeling System (MM5): Program TERRAIN. NCAR Tech Note NCAR/TN-397+IA.
- Data Management Group NOAA-CIRES Climate Diagnosis Center,** 2003, available: <http://www.cdc.noaa.gov/cdc/data.ncep.reanalysis.html/>
- Dudhia, J.,** 2004, PSU/NCAR Mesoscale Modeling System Tutorial Class Notes and User's Guide:MM5 Modeling System Version 3.
- Giorgi, F. ,** 1991, Sensitivity of Simulated Summertime Precipitation over the Western United States to Different Physics Parameterizations, *Monthly Weather Review*, **119**, 2870-2888.
- Grell, G. A., Dudhia, J., Stauffer, D. R.,** 1994. A Description of the Fifth-Generation Penn State/NCAR Mesoscale Model (MM5). National Center for Atmospheric Research, Boulder, CO, NCAR/TN-389+STR.
- Huffman, G. J.,** 2005. Readme for Accessing Experimental TRMM Real-Time Multi-Satellite Precipitation Analysis (MPA-RT) Data Set. Available: ftp://aeolus.nacsom.nasa.gov/pub/merged/3B4XRT_README/
- Kain, J. S.,** 2002. The Kain-Fritsch Convective Parameterization: An Update, Cooperative Institute for Mesoscale Meteorological Studies, *Journal of Applied Meteorology*, in press.
- Kalnay, E., and Coauthors,** 1996, The NCEP/NCAR 40-Year Reanalysis Project. *Bull. Amer. Meteor. Soc.*, **77**, 437-471.

- Kuo, Y. H., Cheng, L., Bao, J. W.,** 1988. Numerical Simulation of 1981 Sichuan Flood. Part I: Evolution of a Mesoscale Southwest Vortex, **116**, 2481-2504.
- Mass, C. F., and Y.-H. Kuo,** 1998. Regional Real-Time Numerical Weather Prediction. Current Status and Future Potential, *Bull. Amer. Meteor. Soc.*, **79**, 253-263.
- Mass, C., Colle, B. A.,** 2000. The 5-9 February 1996 Flooding Event over the Pacific Northwest: Sensitivity Studies and Evaluation of the MM5 Precipitation Forecasts, *Monthly Weather Review*, **128**, 593-617.
- Mass, C., Ovens, D., Grimit, E. and Albright, M.,** 2002. (Dept. of Atmospheric Sciences, University of Washington). Issues in Mesoscale Verification: Implications of the Verification of High Resolution MM5 Forecasts over the Northwest Pacific Papers Presented at the Twelfth PSU/NCAR Mesoscale Model Users' Workshop NCAR, Colorado, USA, June 24 – 25.
- Nielsen-Gammon, J. and Strack J.,** 2001, Model resolution dependence of simulations of extreme rainfall events, The Tenth Penn State/NCAR MM5 Users' Workshop, Mesa Laboratory, NCAR, Colorado, USA, June 21-23, 2000.

APPENDICES

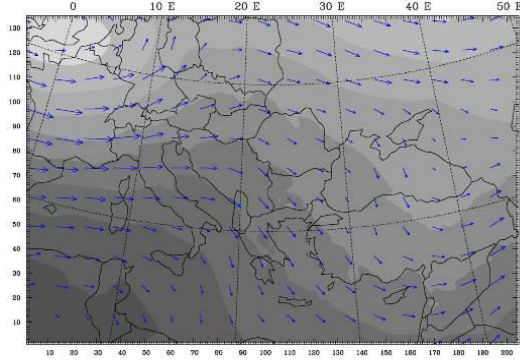
Appendix A: 500 mb NCEP Reanalysis Fields For Experiments

Appendix B: 850 mb NCEP Reanalysis Fields For Experiments

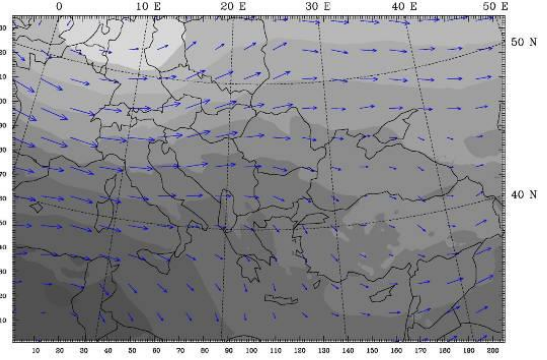
Appendix C: Total Accumulated Rain Fields For Experiment IV

Appendix A. 500 mb NCEP Reanalysis Fields For Experiments

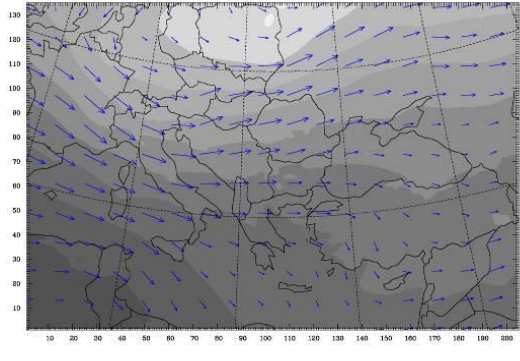
a.) 13 August 2004 00 UTC



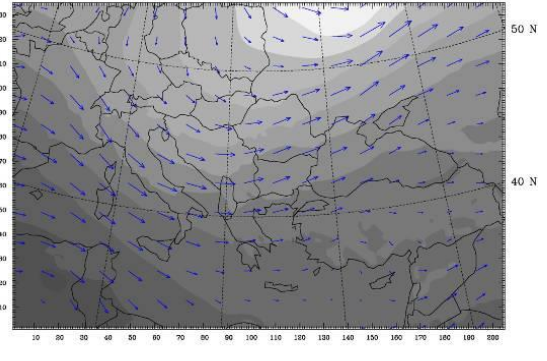
b.) 13 August 2004 12 UTC



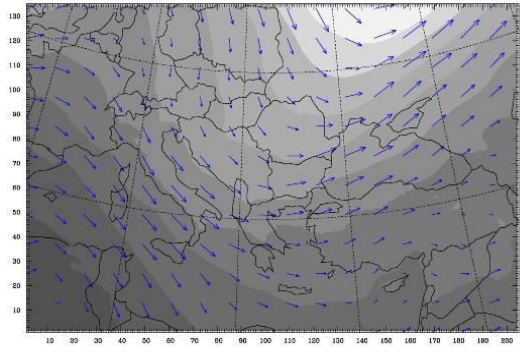
c.) 14 August 2004 00 UTC



d.) 14 August 2004 12 UTC



e.) 15 August 2004 00 UTC



f.) 15 August 2004 12 UTC

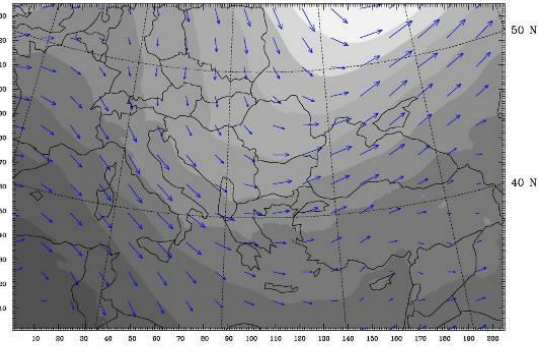
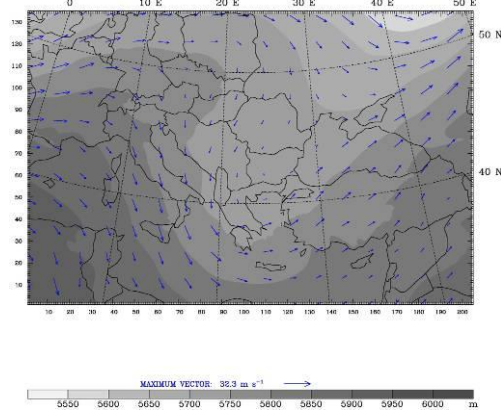
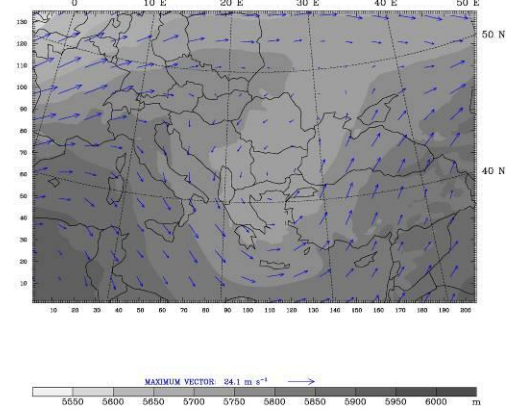


Figure A.1: Experiment I, 500 mb NCEP Reanalysis plots. Panels a to f represent the 13-15 August 2004 of the case study period.

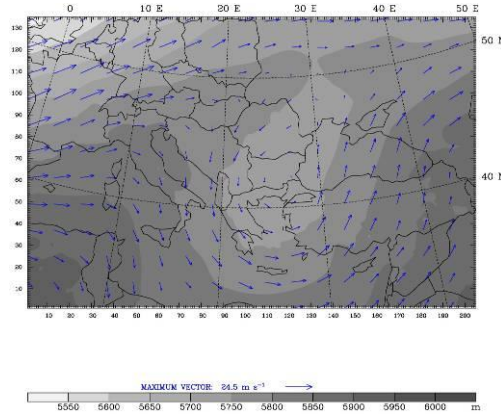
g.) 16 August 2004 00 UTC



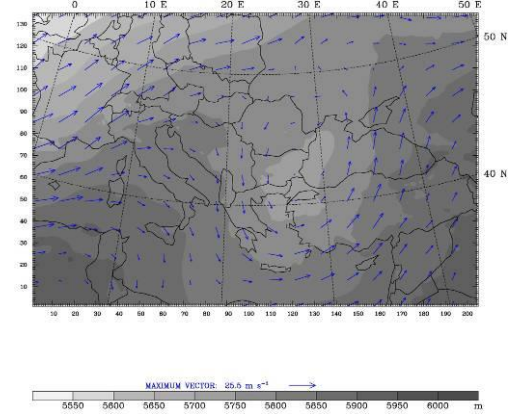
h.) 16 August 2004 12 UTC



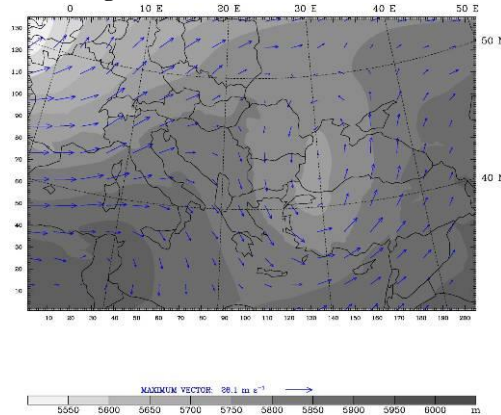
i.) 17 August 2004 00 UTC



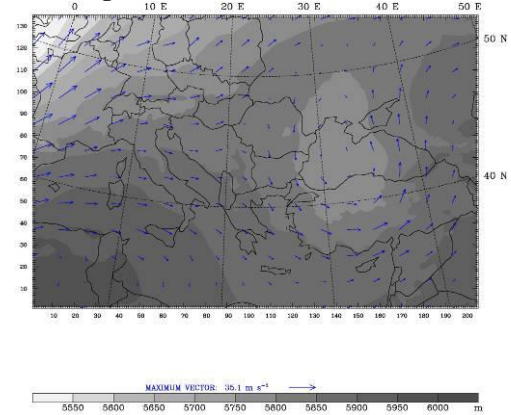
j.) 17 August 2004 12 UTC



k.) 18 August 2004 00 UTC



l.) 18 August 2004 12 UTC



m.) 19 August 2004 00 UTC

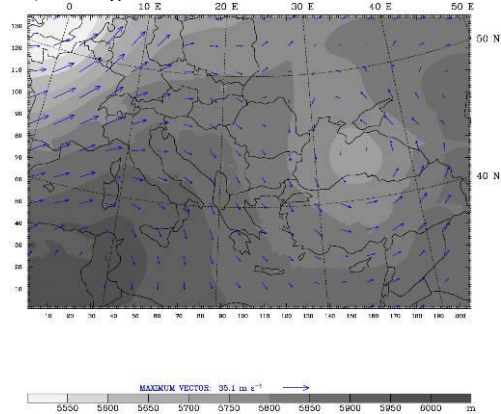
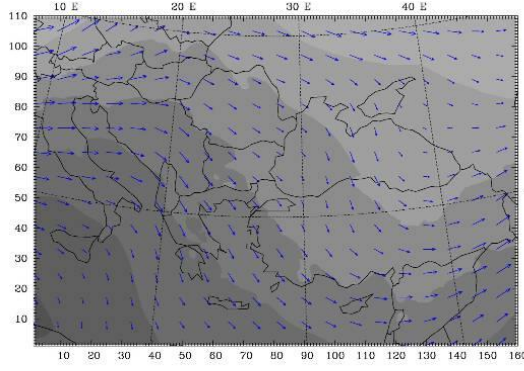
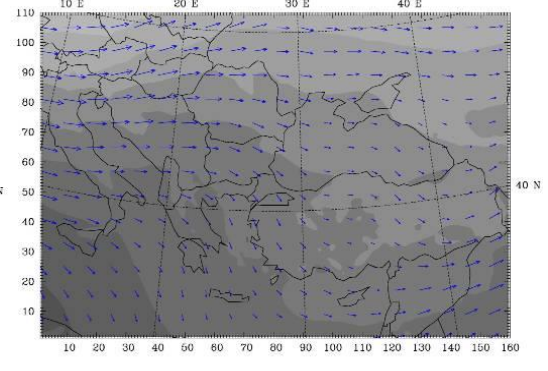


Figure A.1 (Cont.): Experiment I, 500 mb NCEP Reanalysis plots. Panels g to m represent the 16-19 August 2004 of the case study period.

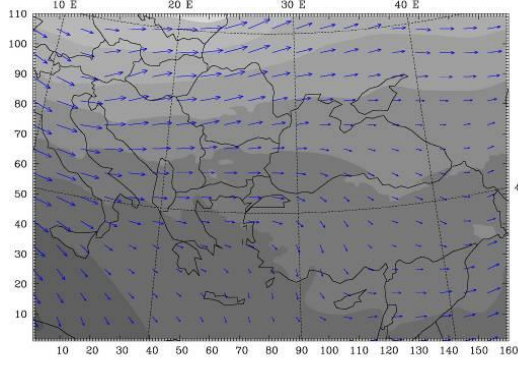
a.) 13 August 2004 00 UTC



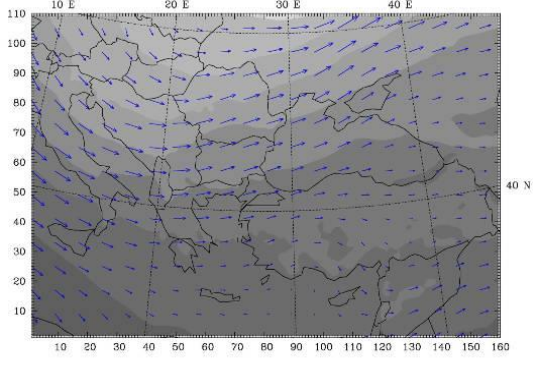
b.) 13 August 2004 12 UTC



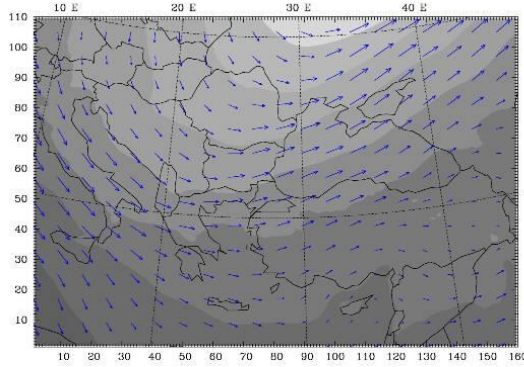
c.) 14 August 2004 00 UTC



d.) 14 August 2004 12 UTC



e.) 15 August 2004 00 UTC



f.) 15 August 2004 12 UTC

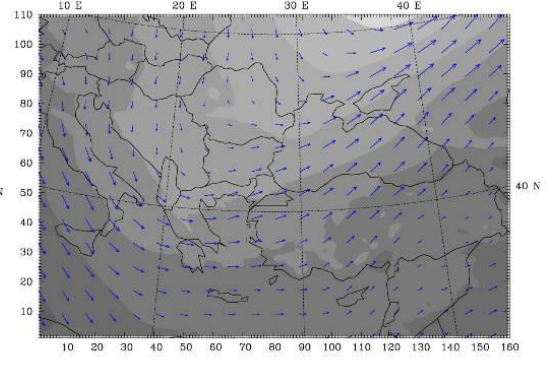
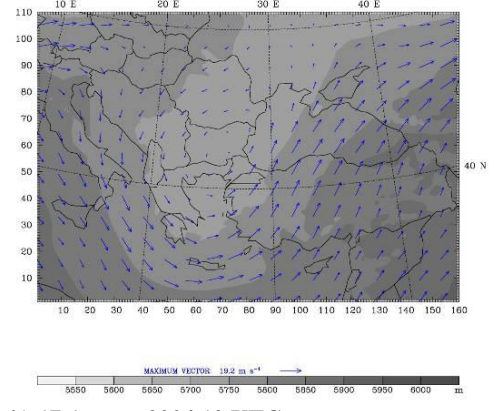


Figure A.2: Experiment II, 500 mb NCEP Reanalysis plots. Panels a to f represent the 13-15 August 2004 of the case study period.

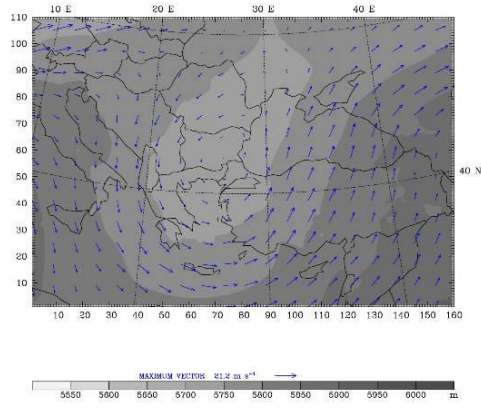
g.) 16 August 2004 00 UTC



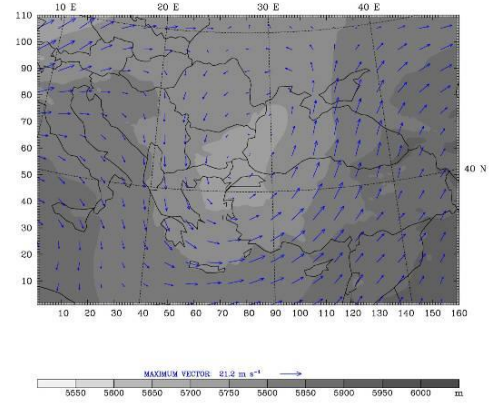
h.) 16 August 2004 12 UTC



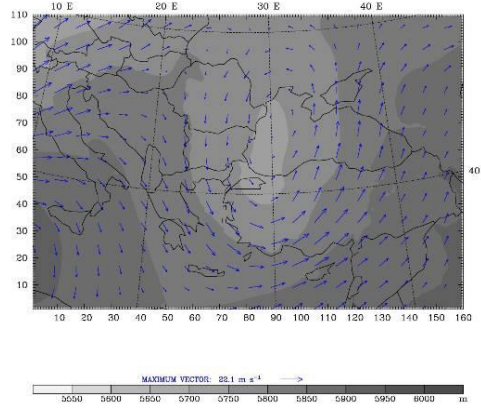
i.) 17 August 2004 00 UTC



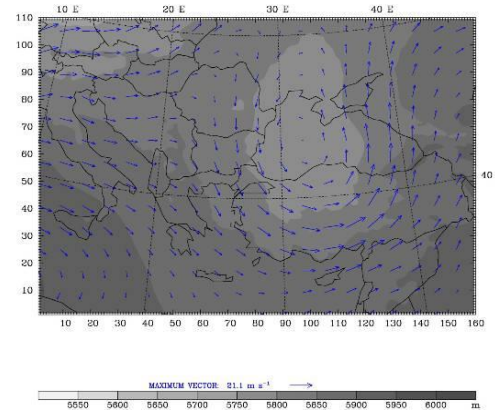
j.) 17 August 2004 12 UTC



k.) 18 August 2004 00 UTC



l.) 18 August 2004 12 UTC



m.) 19 August 2004 00 UTC

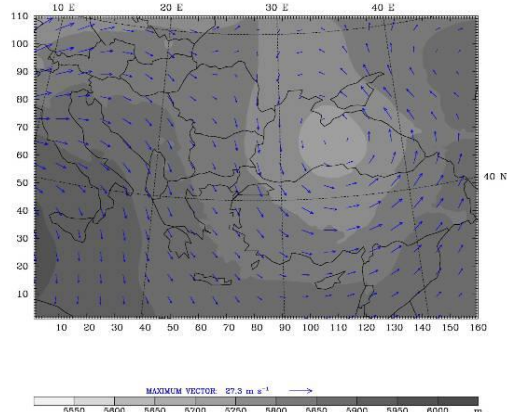
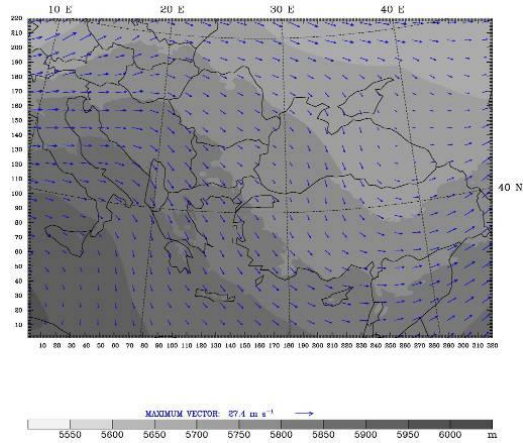
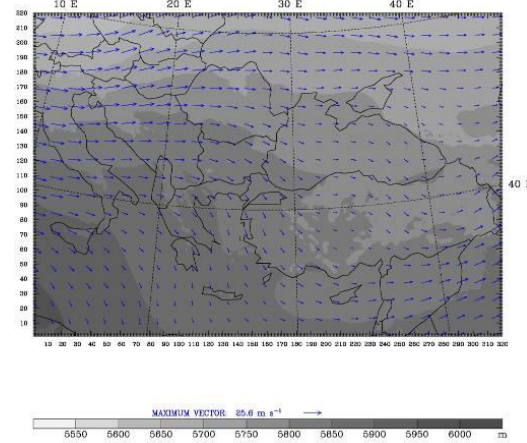


Figure A.2 (Cont.) Experiment II, 500 mb NCEP Reanalysis plots. Panels g to m represent the 16-19 August 2004 of the case study period.

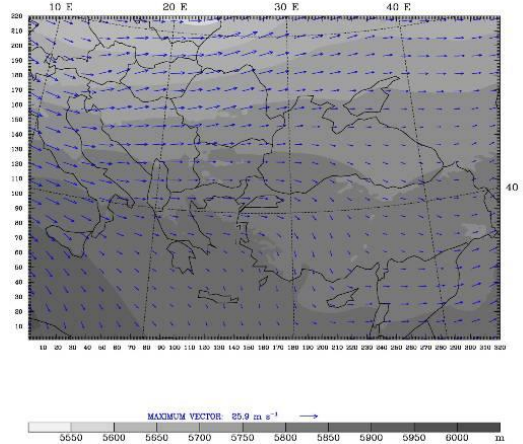
a.) 13 August 2004 00 UTC



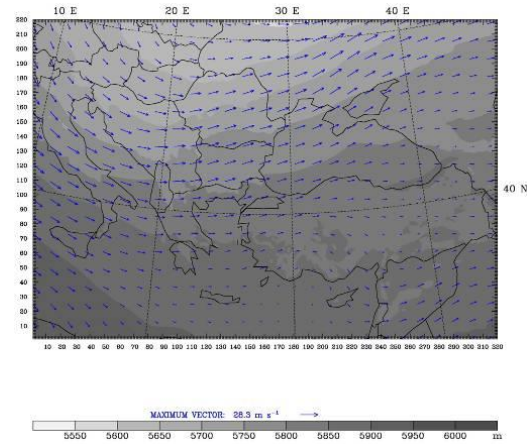
b.) 13 August 2004 12 UTC



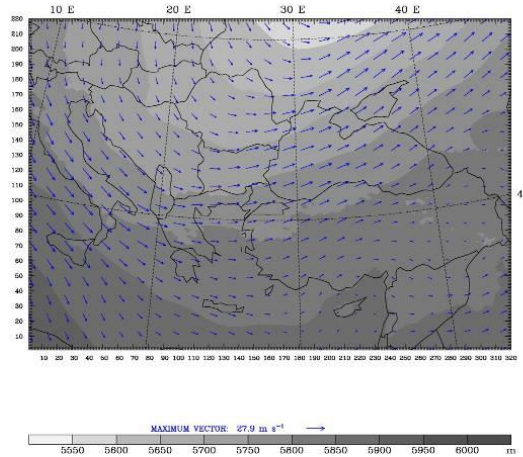
c.) 14 August 2004 00 UTC



d.) 14 August 2004 12 UTC



e.) 15 August 2004 00 UTC



f.) 15 August 2004 12 UTC

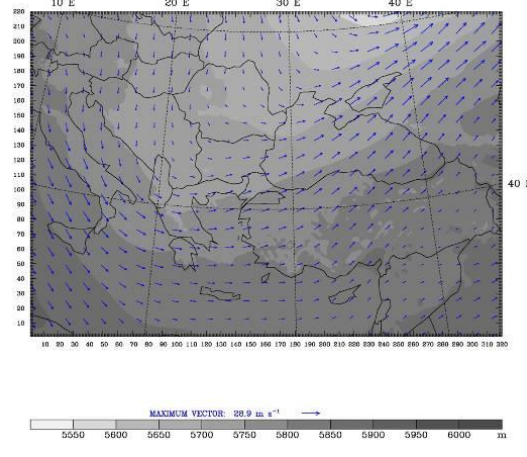
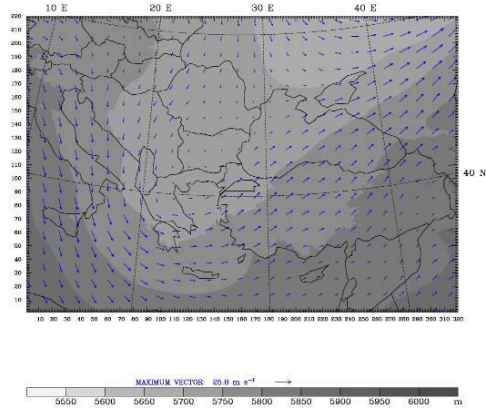
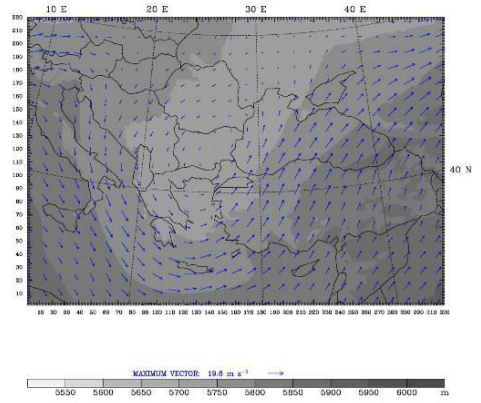


Figure A.3: Experiment III, 500 mb NCEP Reanalysis plots. Panels a to f represent the 13-15 August 2004 of the case study period.

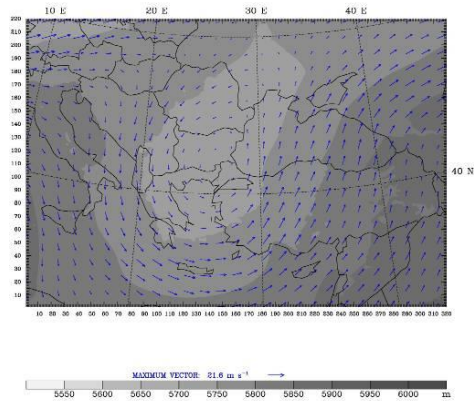
g.) 16 August 2004 00 UTC



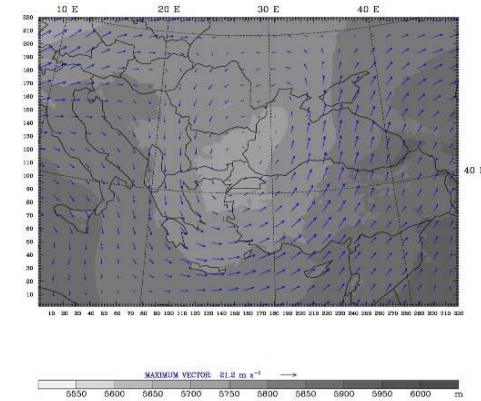
h.) 16 August 2004 12 UTC



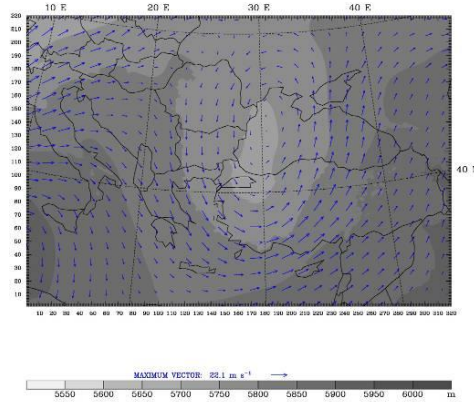
i.) 17 August 2004 00 UTC



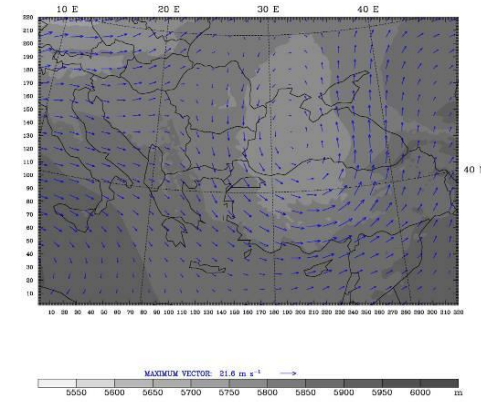
j.) 17 August 2004 12 UTC



k.) 18 August 2004 00 UTC



l.) 18 August 2004 12 UTC



m.) 19 August 2004 00 UTC

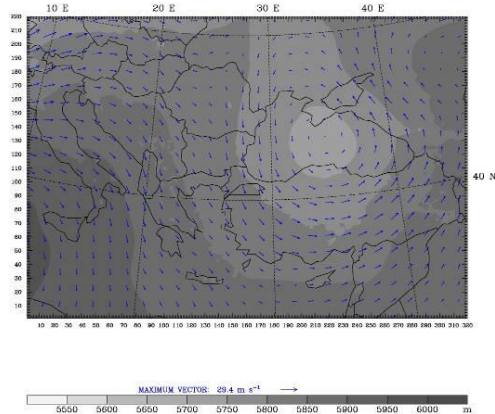
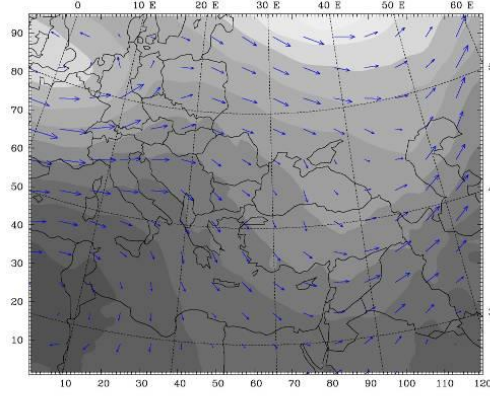
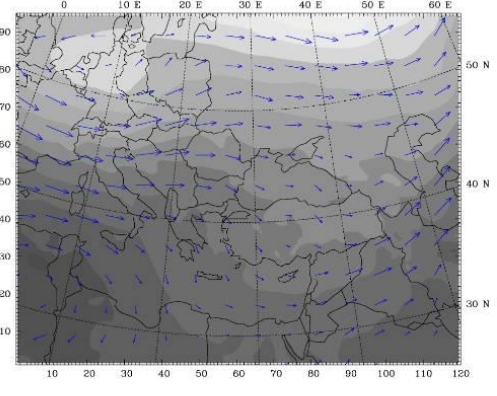


Figure A.3 (Cont.): Experiment III, 500 mb NCEP Reanalysis plots. Panels g to m represent the 16-19 August 2004 of the case study period.

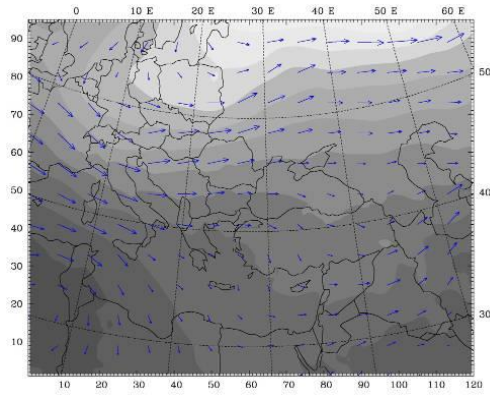
a.) 13 August 2004 00 UTC



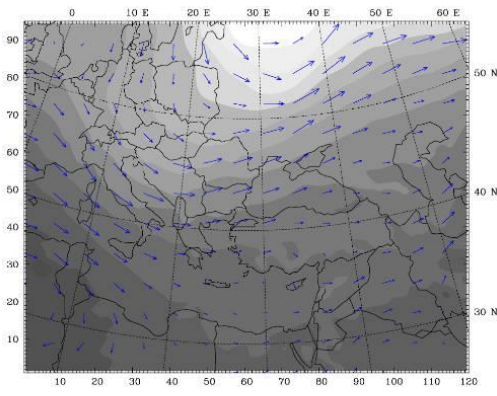
b.) 13 August 2004 12 UTC



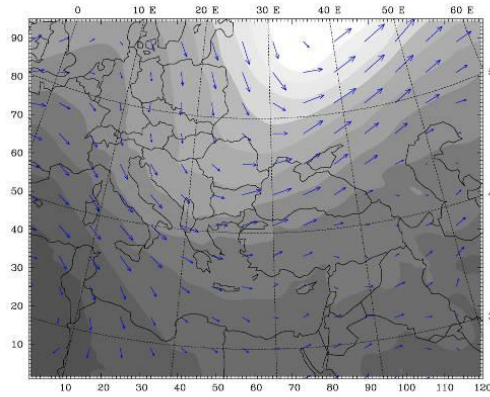
c.) 14 August 2004 00 UTC



d.) 14 August 2004 12 UTC



e.) 15 August 2004 00 UTC



f.) 15 August 2004 12 UTC

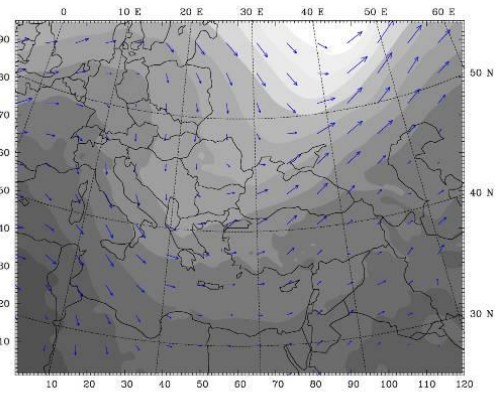
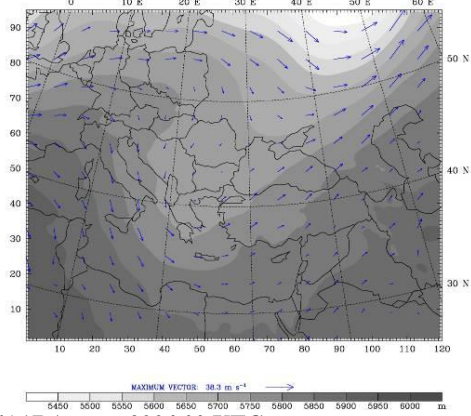
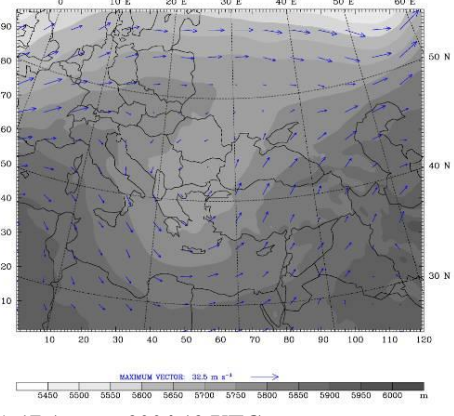


Figure A.4: Experiment IV, 36 km coarse domain 500 mb NCEP Reanalysis plots. Panels a to f represent the 13-15 August 2004 of the case study period.

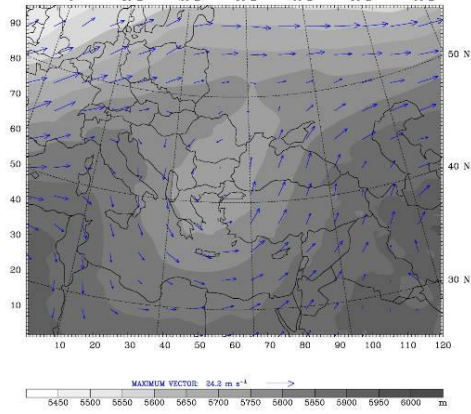
g.) 16 August 2004 00 UTC



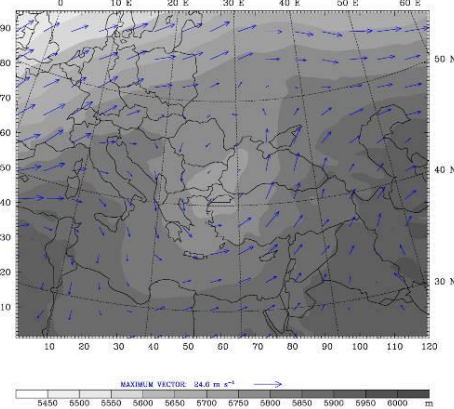
h.) 16 August 2004 12 UTC



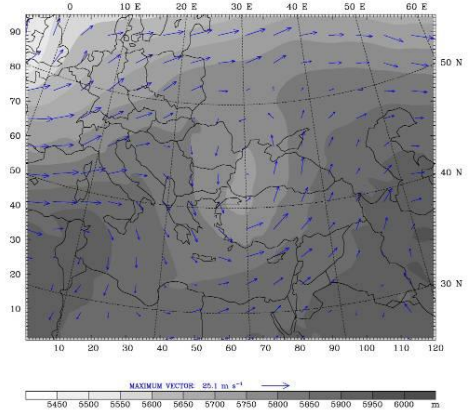
i.) 17 August 2004 00 UTC



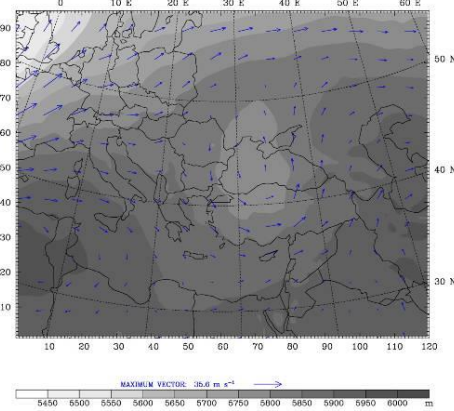
j.) 17 August 2004 12 UTC



k.) 18 August 2004 00 UTC



l.) 18 August 2004 12 UTC



m.) 19 August 2004 00 UTC

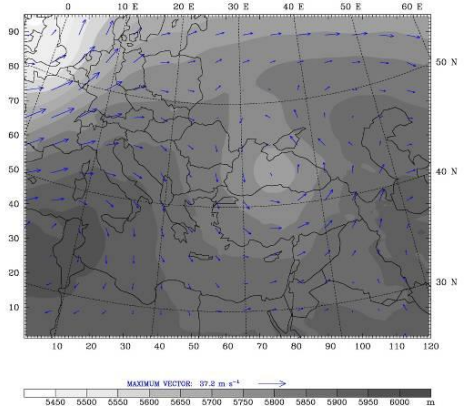
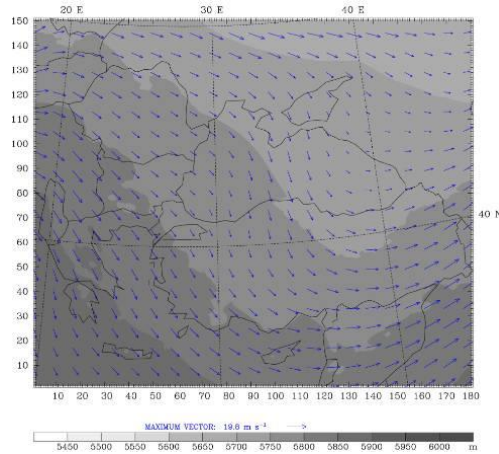
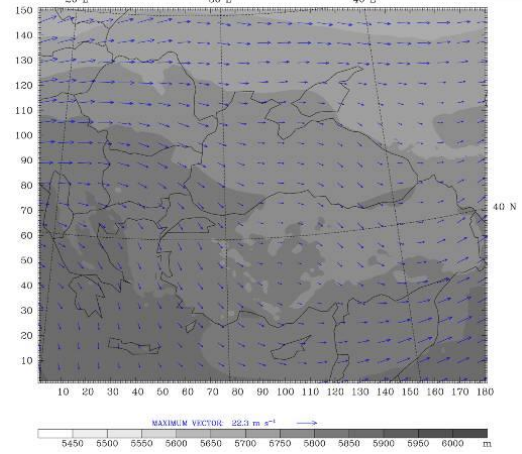


Figure A.4 (Cont.): Experiment IV, 36 km coarse domain 500 mb NCEP Reanalysis plots. Panels g to m represent the 16-19 August 2004 of the case study period.

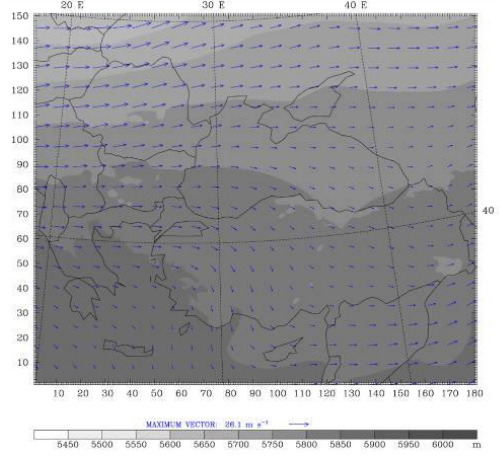
a.) 13 August 2004 00 UTC



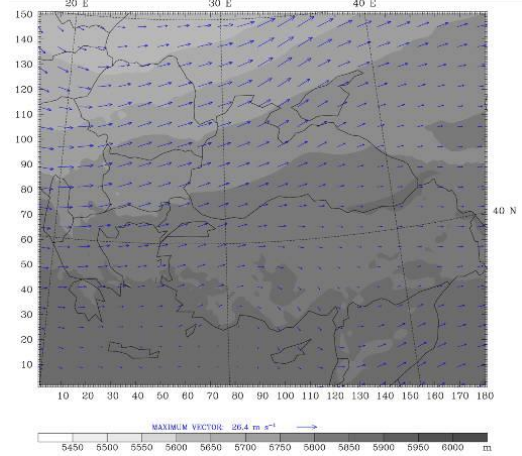
b.) 13 August 2004 12 UTC



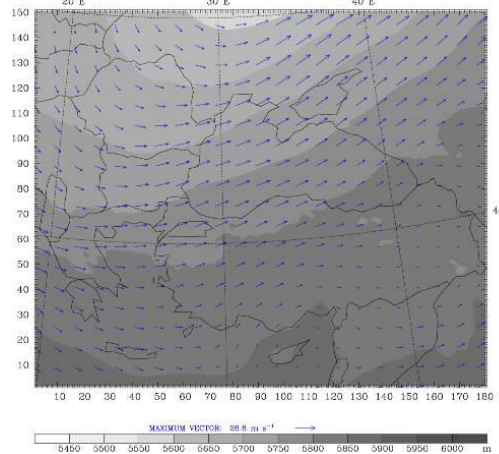
c.) 14 August 2004 00 UTC



d.) 14 August 2004 12 UTC



e.) 15 August 2004 00 UTC



f.) 15 August 2004 12 UTC

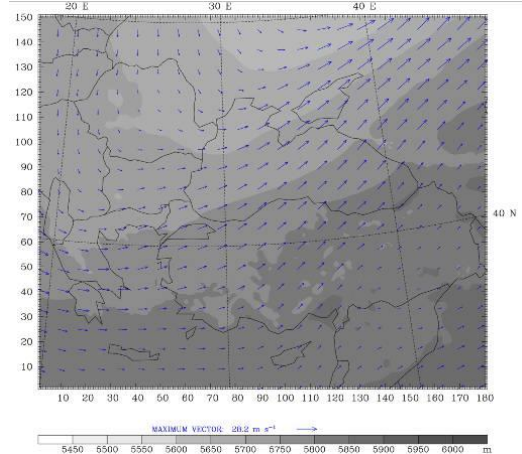
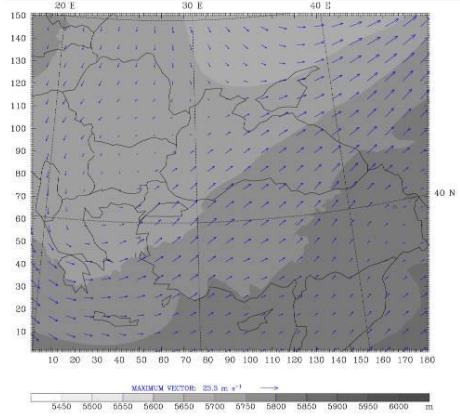
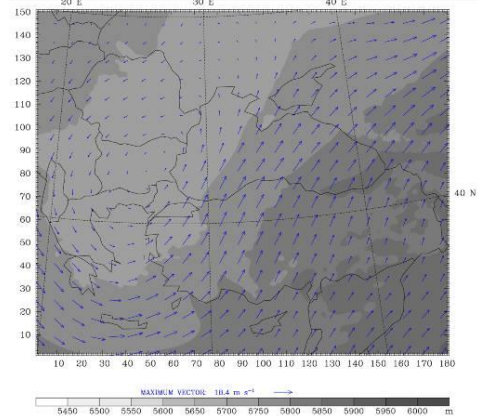


Figure A.5: Experiment IV, 12 km nested inner domain 500 mb NCEP Reanalysis plots. Panels a to f represent the 13-15 August 2004 of the case study period.

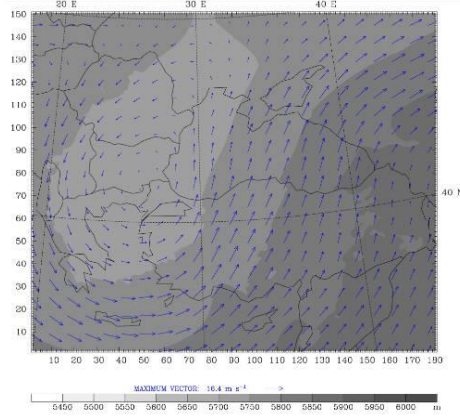
g.) 16 August 2004 00 UTC



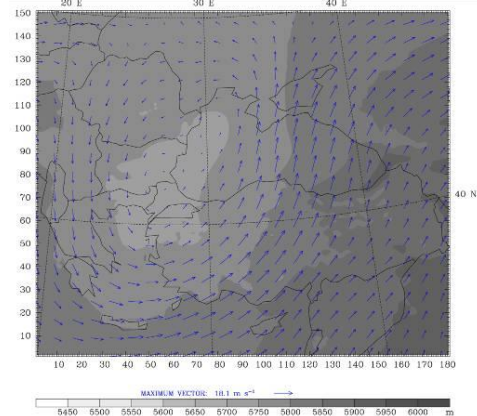
h.) 16 August 2004 12 UTC



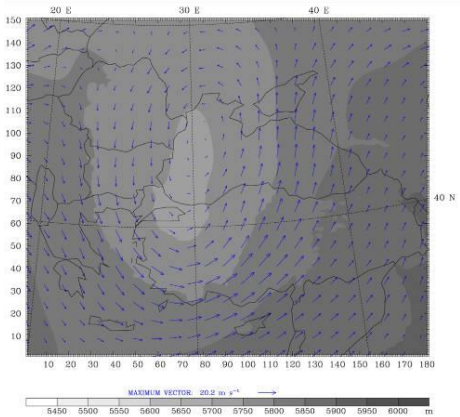
i.) 17 August 2004 00 UTC



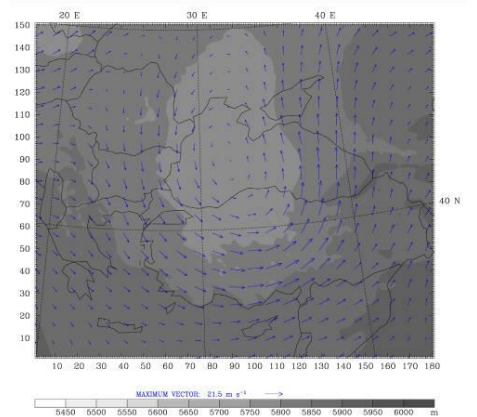
j.) 17 August 2004 12 UTC



k.) 18 August 2004 00 UTC



l.) 18 August 2004 12 UTC



m.) 19 August 2004 00 UTC

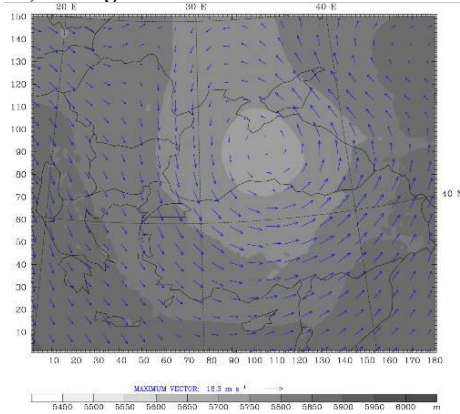
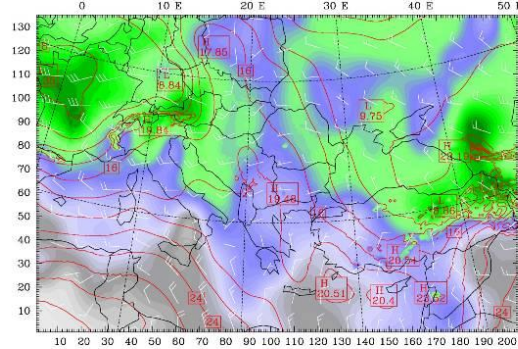


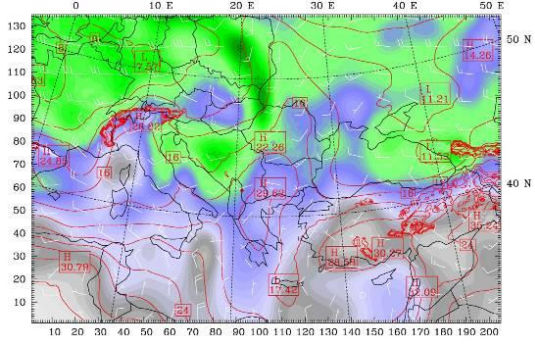
Figure A.5 (Cont.): Experiment IV, 12 km nested inner domain 500 mb NCEP Reanalysis plots. Panels g to m represent the 16-19 August 2004 of the case study period.

Appendix B. 850 mb NCEP Reanalysis Fields For Experiments

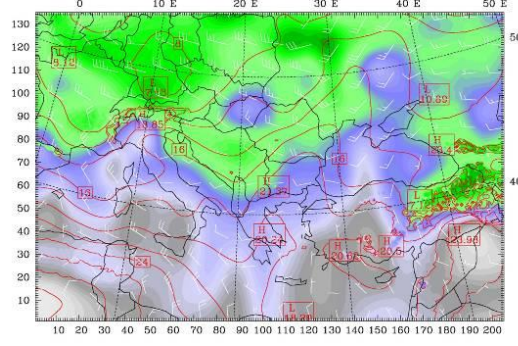
a.) 13 August 2004 00 UTC



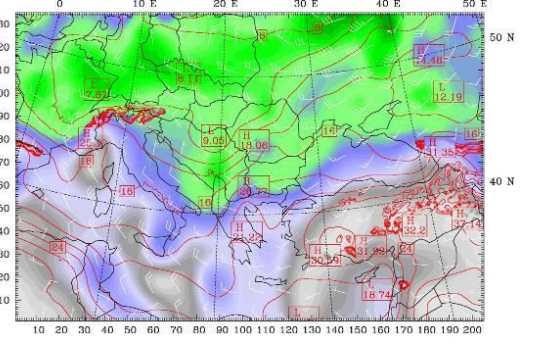
b.) 13 August 2004 12 UTC



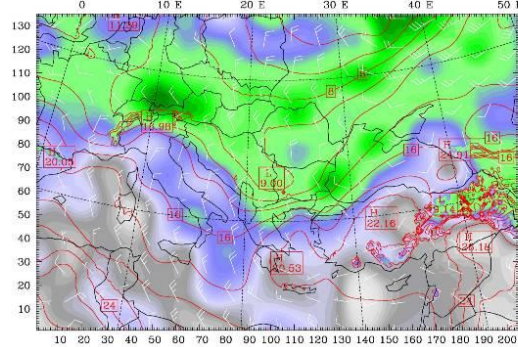
c.) 14 August 2004 00 UTC



d.) 14 August 2004 12 UTC



e.) 15 August 2004 00 UTC



f.) 15 August 2004 12 UTC

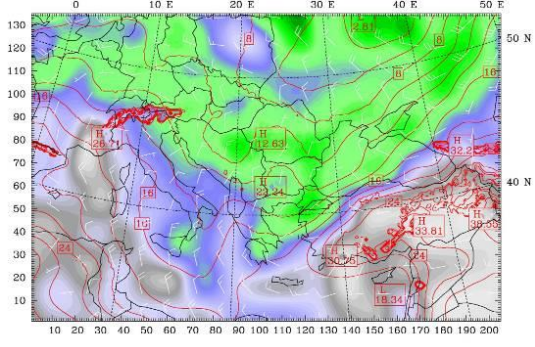
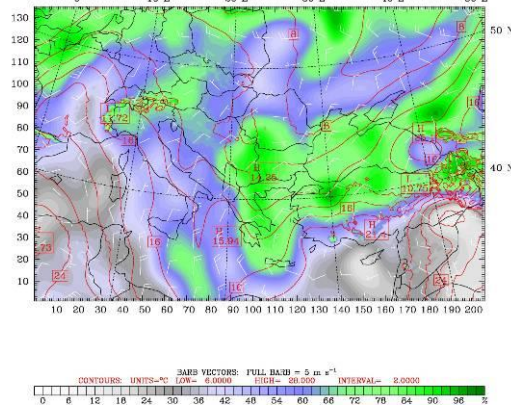
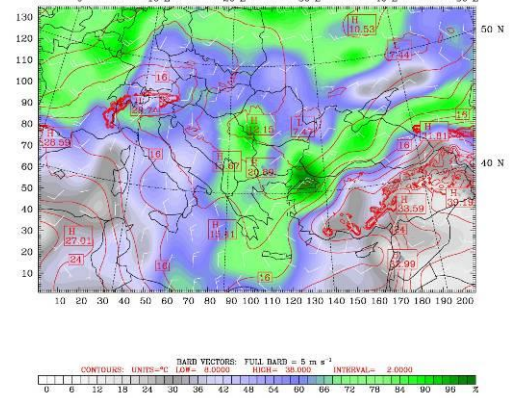


Figure B.1: Experiment I, 850 mb NCEP Reanalysis plots. Panels a to f represent the 13-15 August 2004 of the case study period.

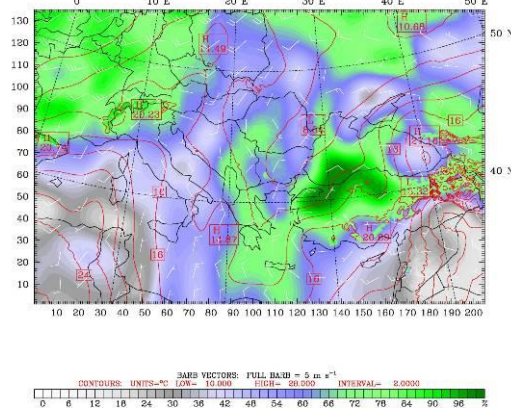
g.) 16 August 2004 00 UTC



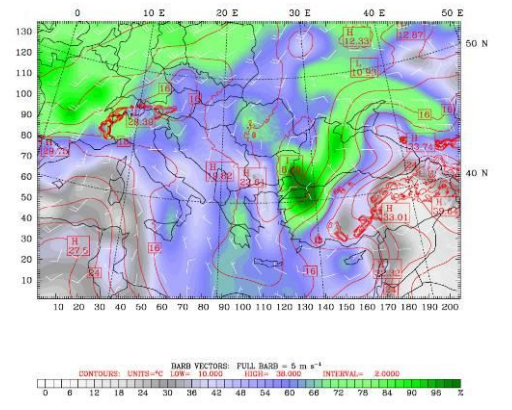
h.) 16 August 2004 12 UTC



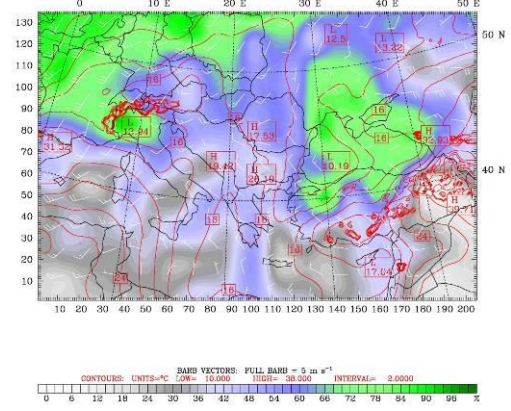
i.) 17 August 2004 00 UTC



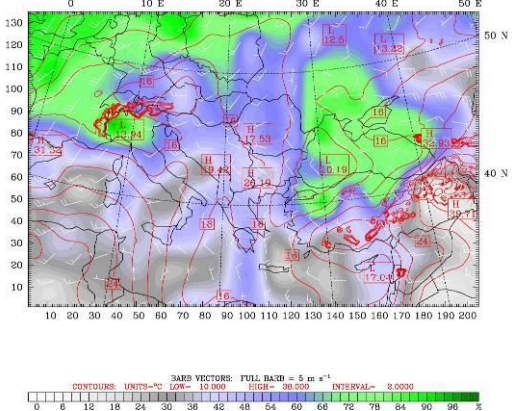
j.) 17 August 2004 12 UTC



k.) 18 August 2004 00 UTC



l.) 18 August 2004 12 UTC



m.) 19 August 2004 00 UTC

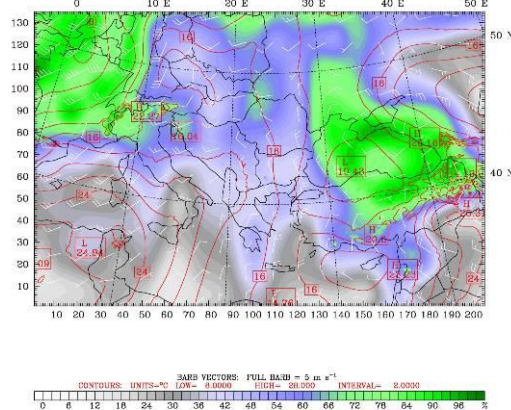
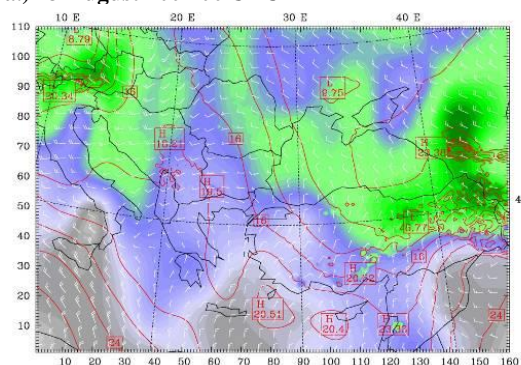
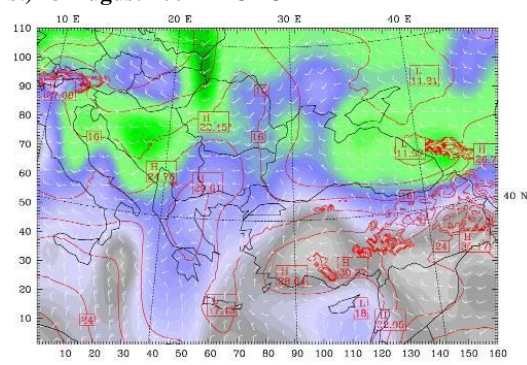


Figure B.1 (Cont.): Experiment I, 850 mb NCEP Reanalysis plots. Panels g to m represent the 16-19 August 2004 of the case study period.

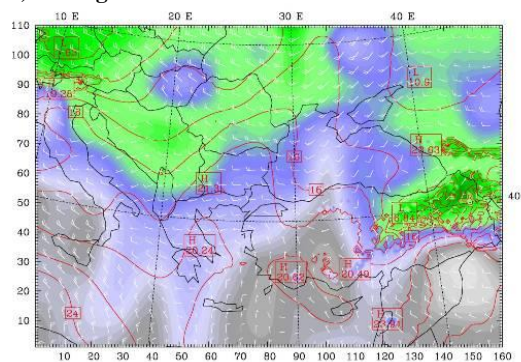
a.) 13 August 2004 00 UTC



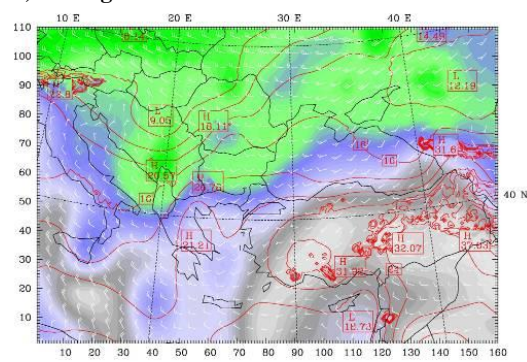
b.) 13 August 2004 12 UTC



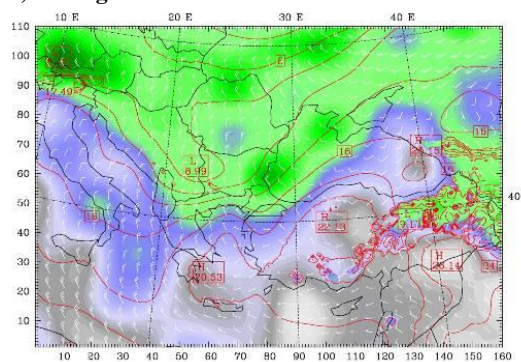
c.) 14 August 2004 00 UTC



d.) 14 August 2004 12 UTC



e.) 15 August 2004 00 UTC



f.) 15 August 2004 12 UTC

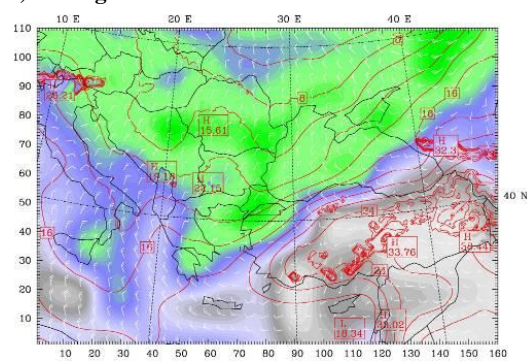
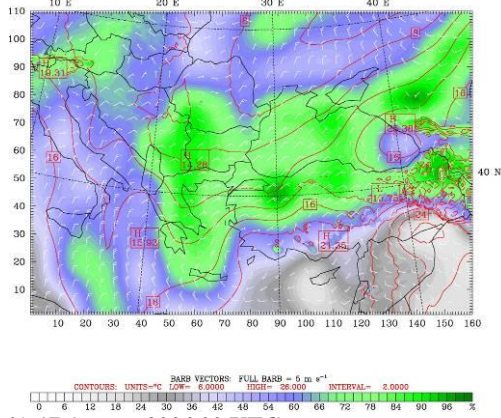
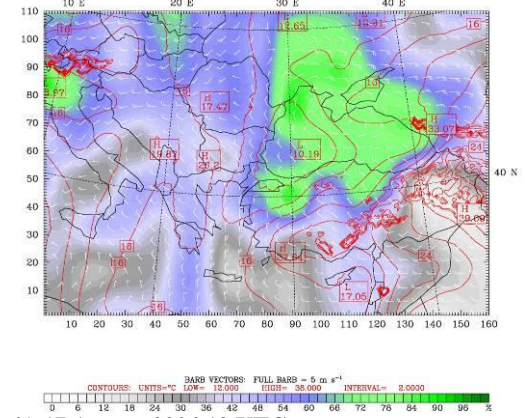


Figure B.2: Experiment II, 850 mb NCEP Reanalysis plots. Panels a to f represent the 13-16 August 2004 of the case study period.

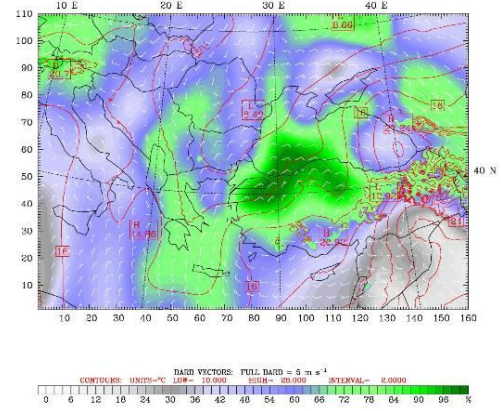
g.) 16 August 2004 00 UTC



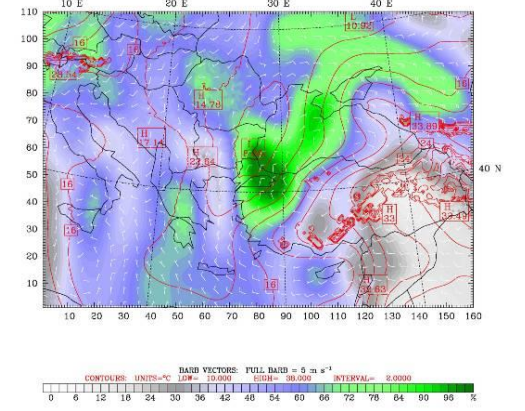
h.) 16 August 2004 12 UTC



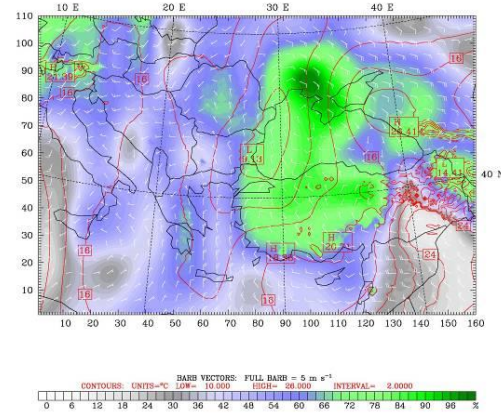
i.) 17 August 2004 00 UTC



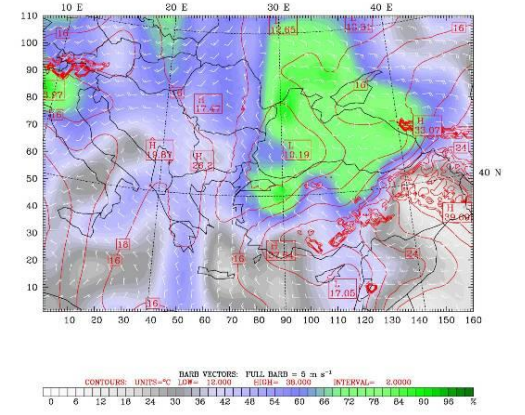
j.) 17 August 2004 12 UTC



k.) 18 August 2004 00 UTC



l.) 18 August 2004 12 UTC



m.) 19 August 2004 00 UTC

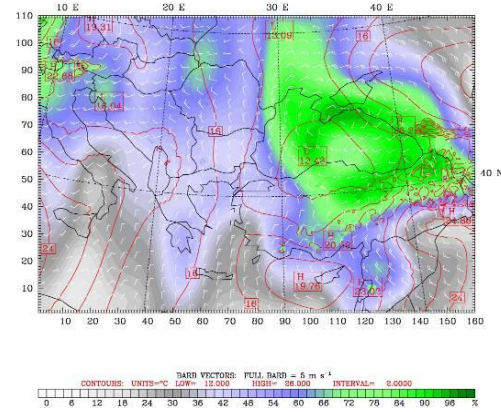
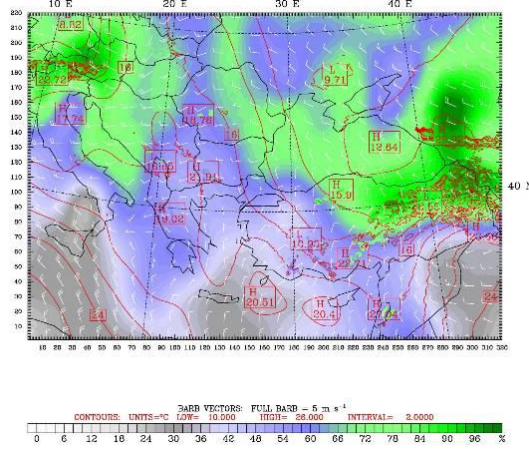
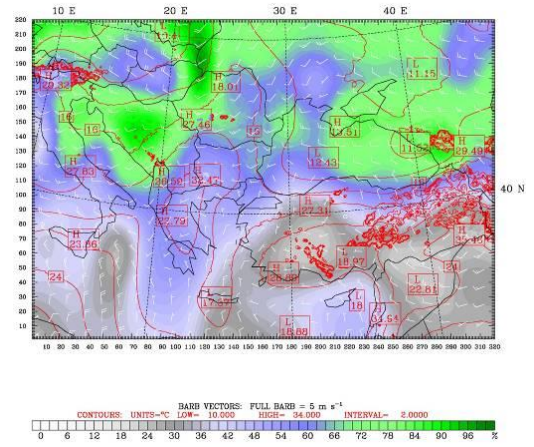


Figure B.2 (Cont.): Experiment II, 850 mb NCEP Reanalysis plots. Panels g to m represent the 16-19 August 2004 of the case study period.

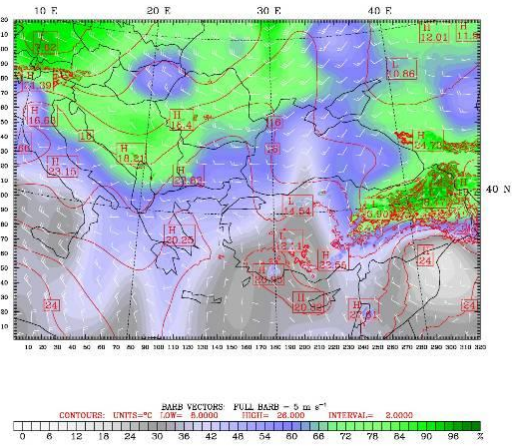
a.) 13 August 2004 00 UTC



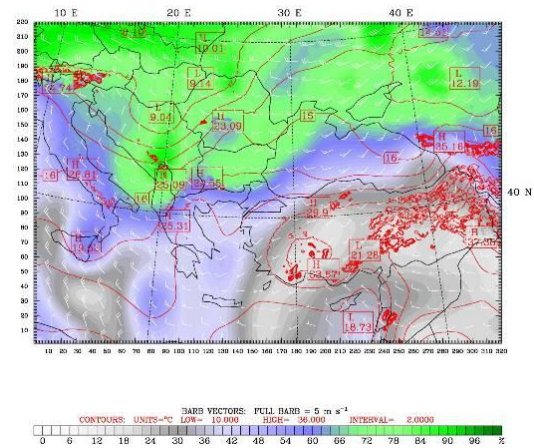
b.) 13 August 2004 12 UTC



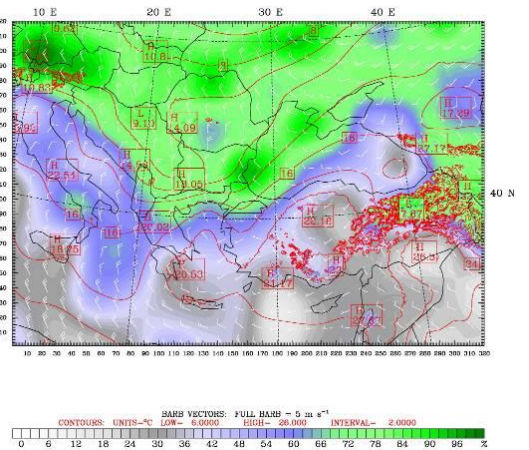
c.) 14 August 2004 00 UTC



d.) 14 August 2004 12 UTC



e.) 15 August 2004 00 UTC



f.) 15 August 2004 12 UTC

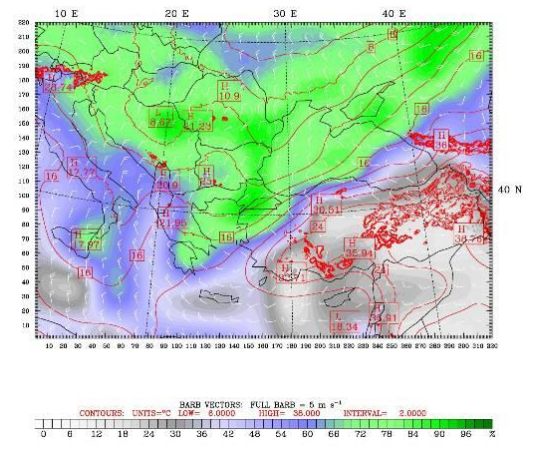
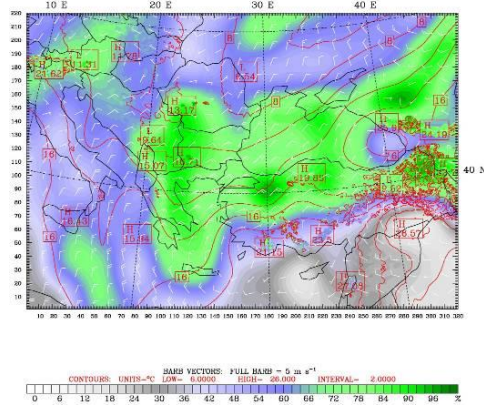
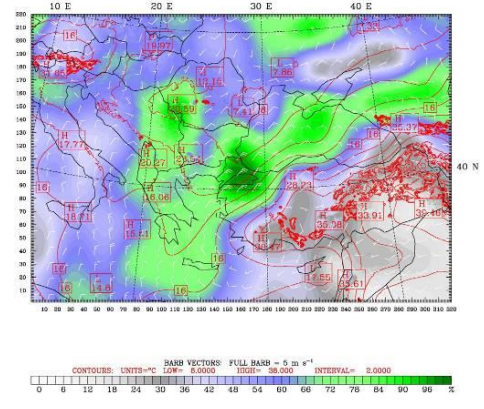


Figure B.3: Experiment III, 850 mb NCEP Reanalysis plots Panels a to f represent the 13-15 August 2004 of the case study period.

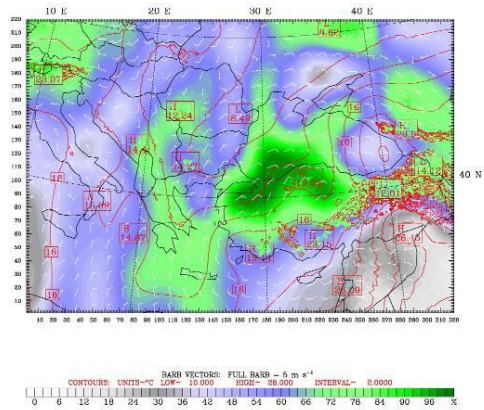
g.) 16 August 2004 00 UTC



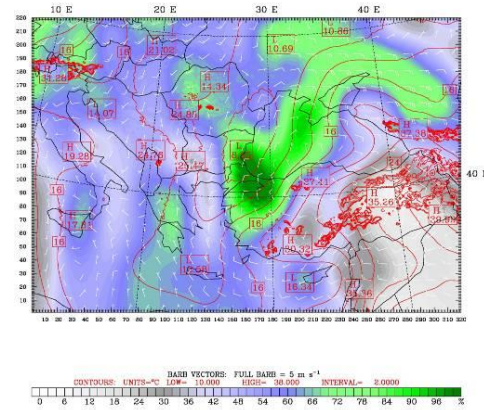
h.) 16 August 2004 12 UTC



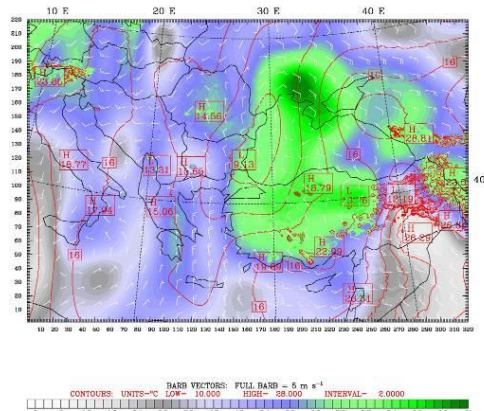
i.) 17 August 2004 00 UTC



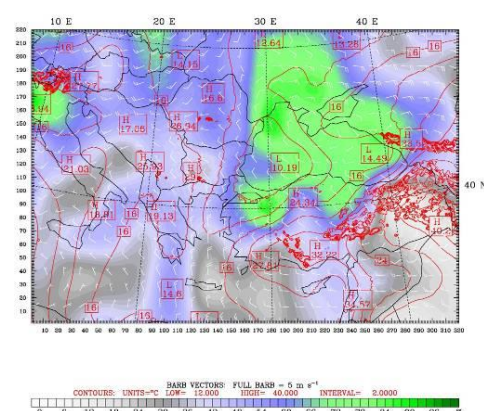
j.) 17 August 2004 12 UTC



k.) 18 August 2004 00 UTC



l.) 18 August 2004 12 UTC



m.) 19 August 2004 00 UTC

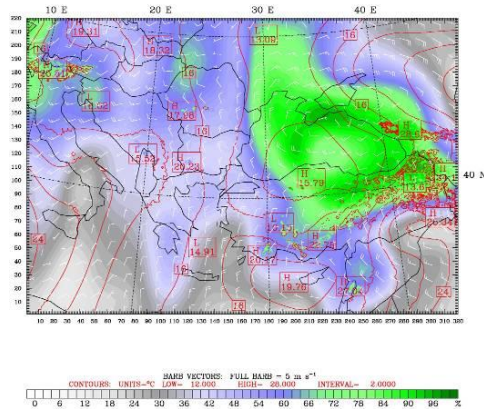
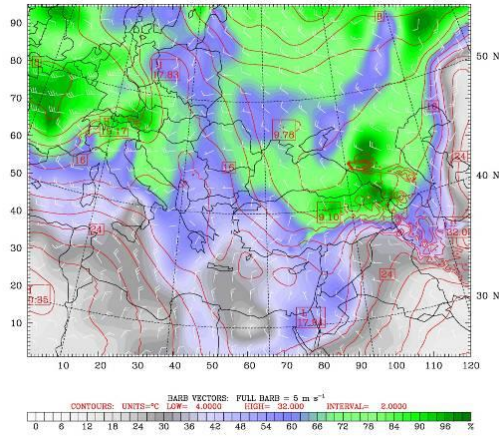
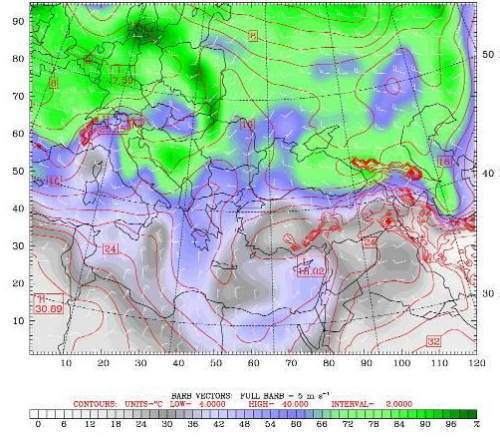


Figure B.3 (Cont.): Experiment III, 850 mb NCEP Reanalysis plots Panels g to m represent the 16-19 August 2004 of the case study period.

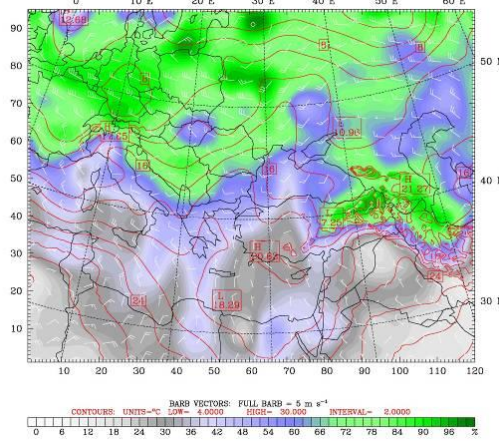
a.) 13 August 2004 00 UTC



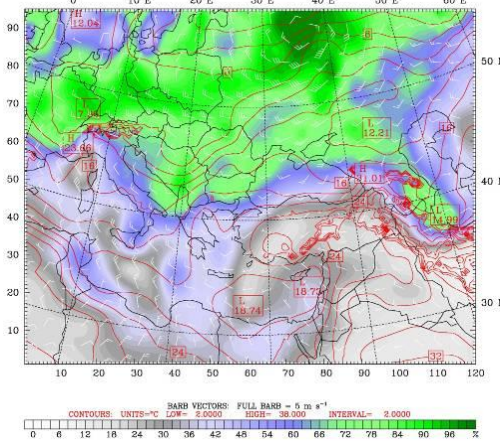
b.) 13 August 2004 12 UTC



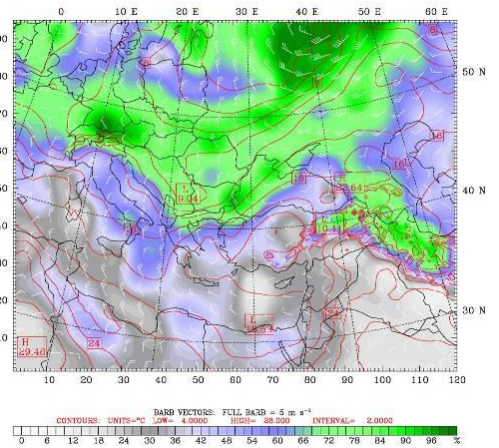
c.) 14 August 2004 00 UTC



d.) 14 August 2004 12 UTC



e.) 15 August 2004 00 UTC



f.) 15 August 2004 12 UTC

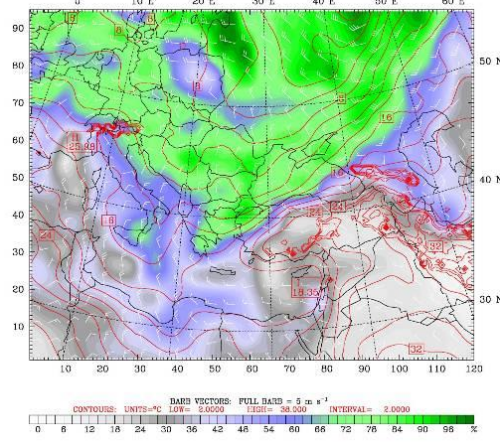
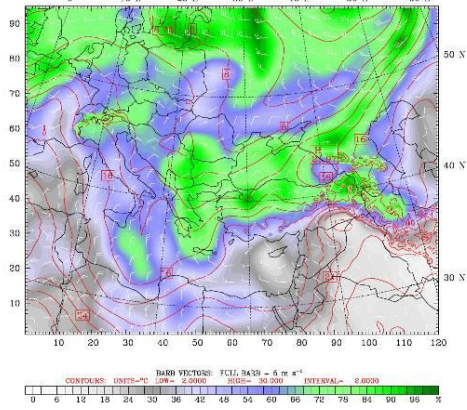
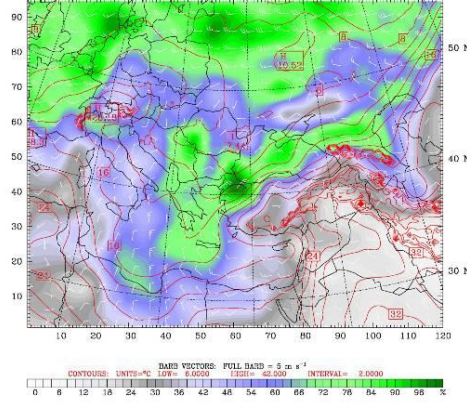


Figure B.4: Experiment IV 36 km coarse domain, 850 mb NCEP Reanalysis plots. Panels a to f represent the 13-15 August 2004 of the case study period.

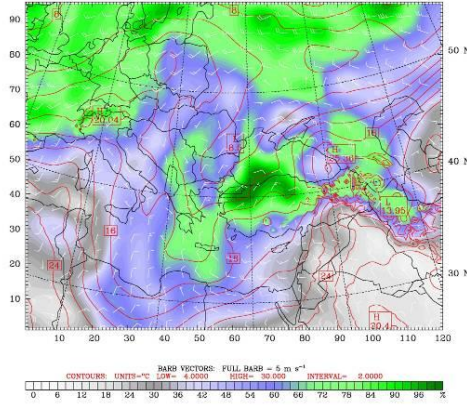
g.) 16 August 2004 00 UTC



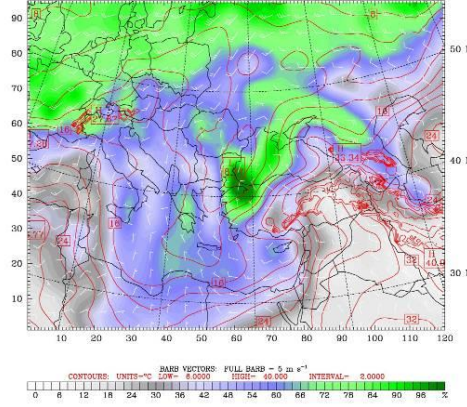
h.) 16 August 2004 12 UTC



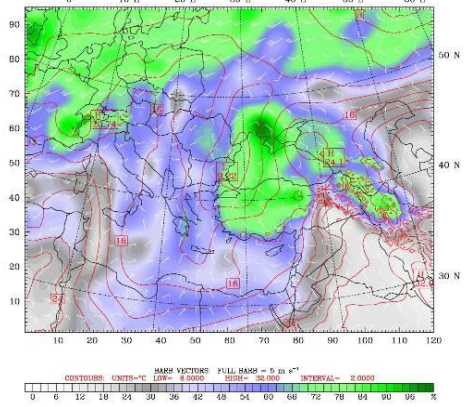
i.) 17 August 2004 00 UTC



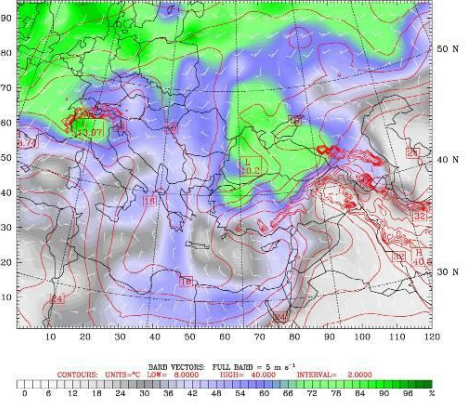
j.) 17 August 2004 12 UTC



k.) 18 August 2004 00 UTC



l.) 18 August 2004 12 UTC



m.) 19 August 2004 00 UTC

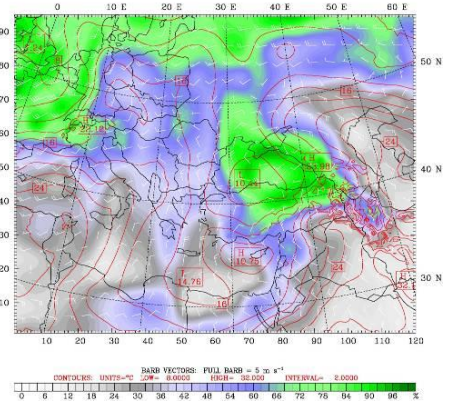
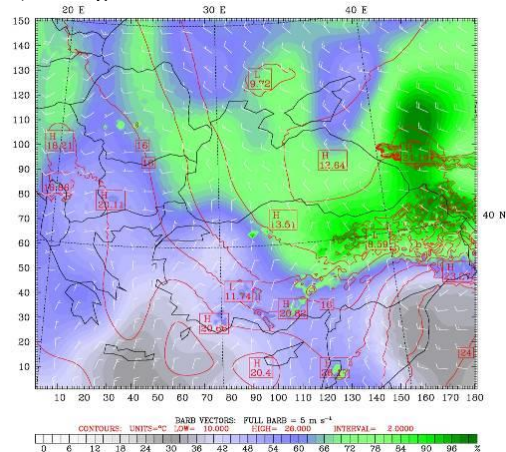
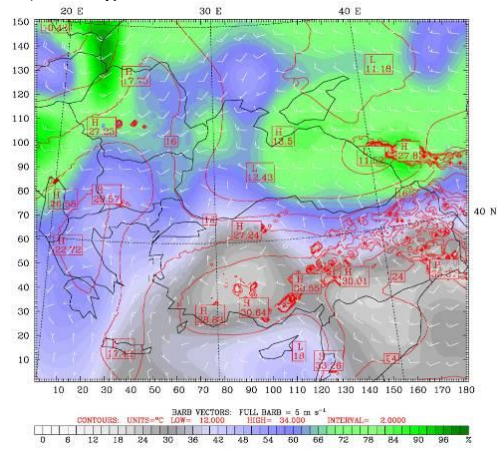


Figure B.4 (Cont.): Experiment IV 36 km coarse domain, 850 mb NCEP Reanalysis plots. Panels g to m represent the 16-19 August 2004 of the case study period.

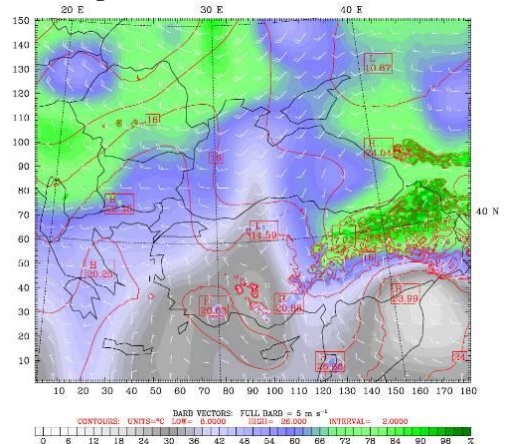
a.) 13 August 2004 00 UTC



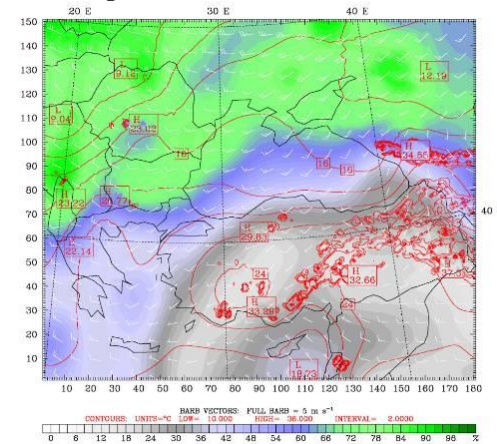
b.) 13 August 2004 12 UTC



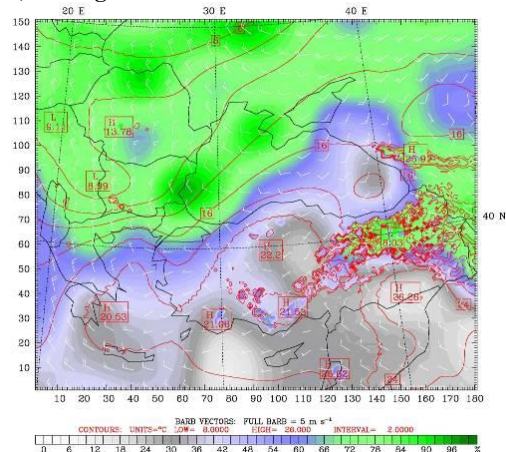
c.) 14 August 2004 00 UTC



d.) 14 August 2004 12 UTC



e.) 15 August 2004 00 UTC



f.) 15 August 2004 12 UTC

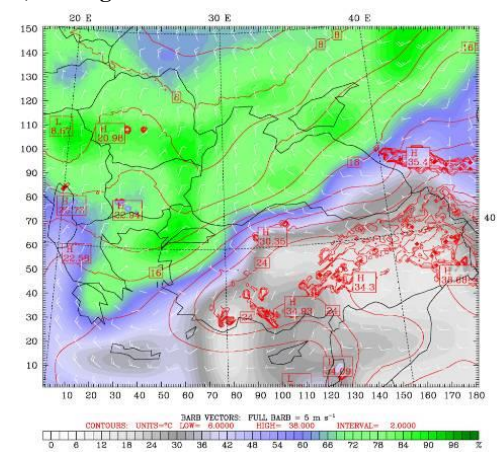
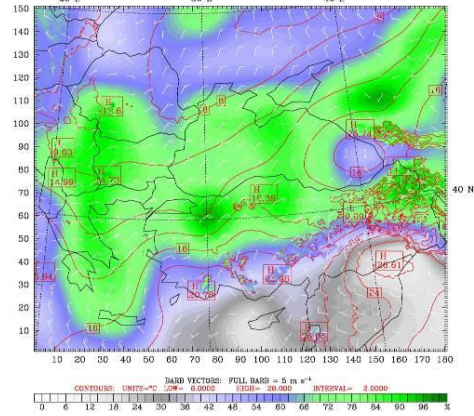
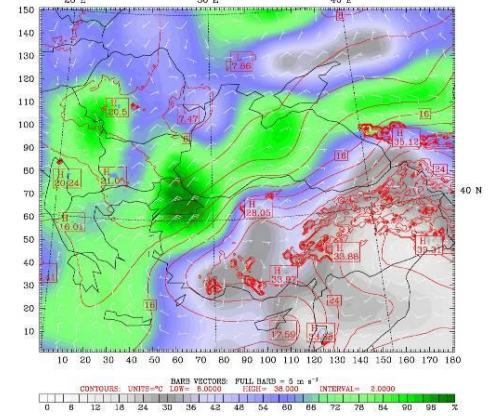


Figure B.5: Experiment IV 12 km inner nested domain, 850 mb NCEP Reanalysis plots. Panels a to f represent the 13-15 August 2004 of the case study period.

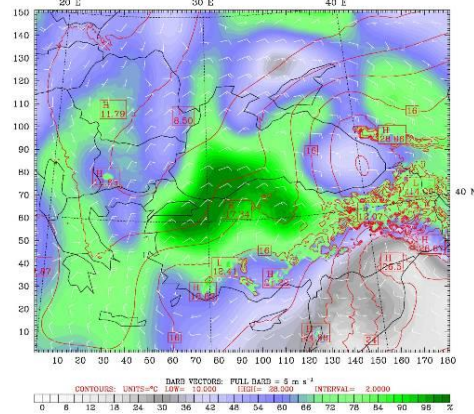
g.) 16 August 2004 00 UTC



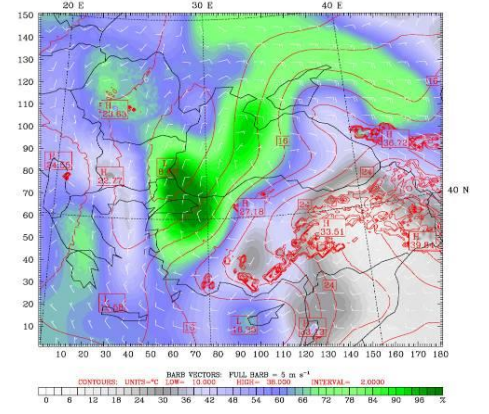
h.) 16 August 2004 12 UTC



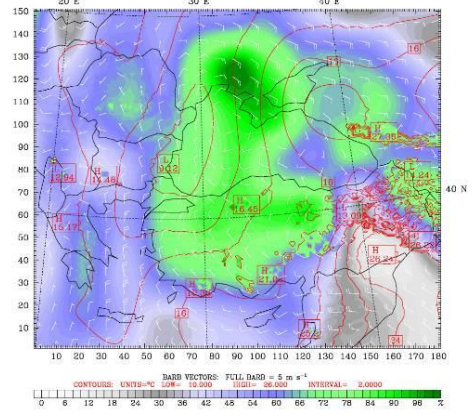
i.) 17 August 2004 00 UTC



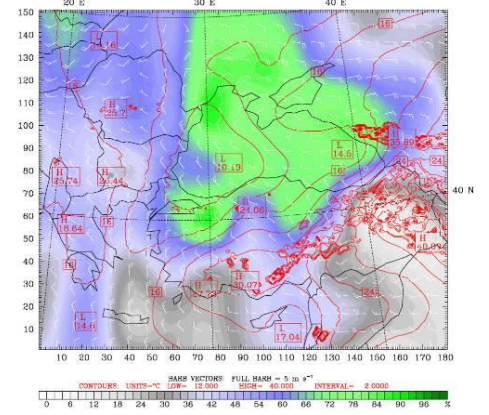
j.) 17 August 2004 12 UTC



k.) 18 August 2004 00 UTC



l.) 18 August 2004 12 UTC



m.) 19 August 2004 00 UTC

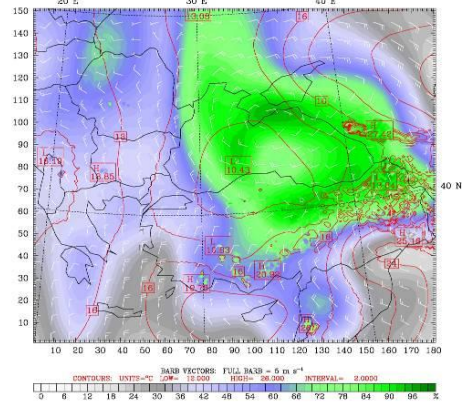
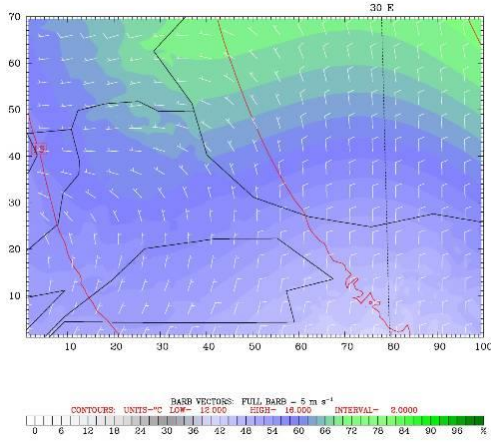
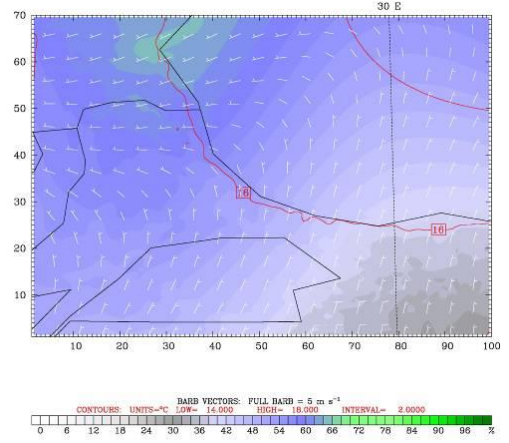


Figure B.5 (Cont.): Experiment IV 12 km inner nested domain, 850 mb NCEP Reanalysis plots. Panels g to m represent the 16-19 August 2004 of the case study period.

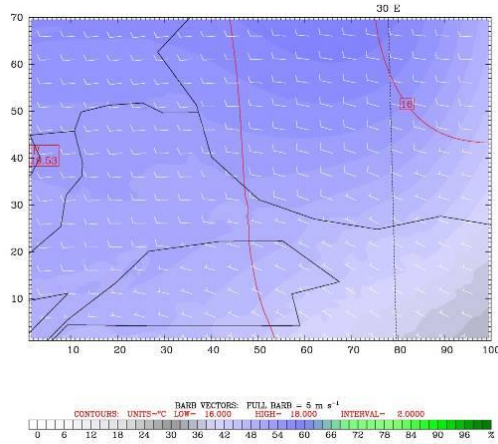
a.) 13 August 2004 00 UTC



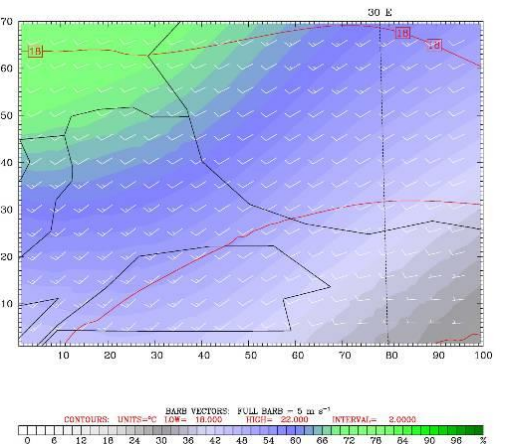
b.) 13 August 2004 12 UTC



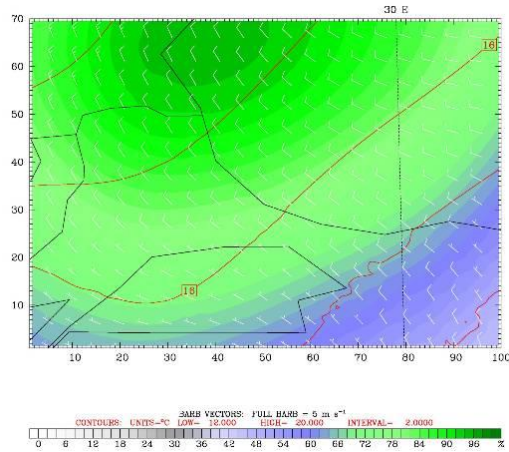
c.) 14 August 2004 00 UTC



d.) 14 August 2004 12 UTC



e.) 15 August 2004 00 UTC



f.) 15 August 2004 12 UTC

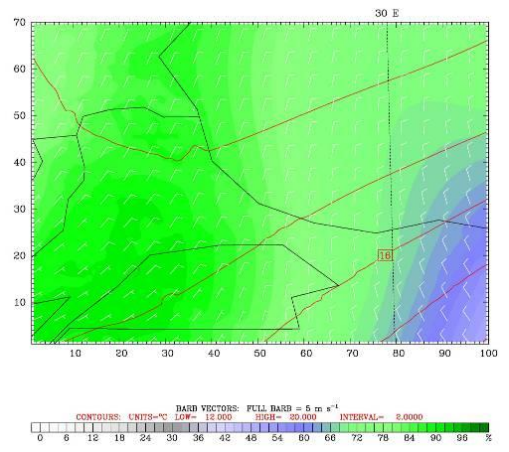
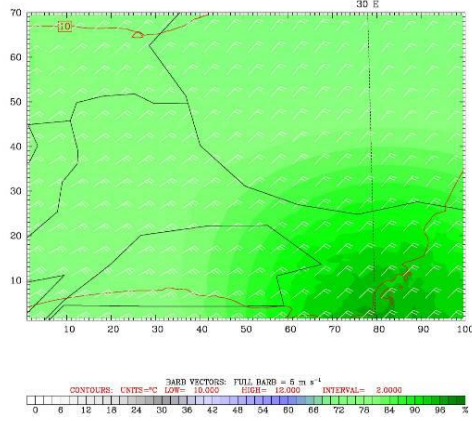
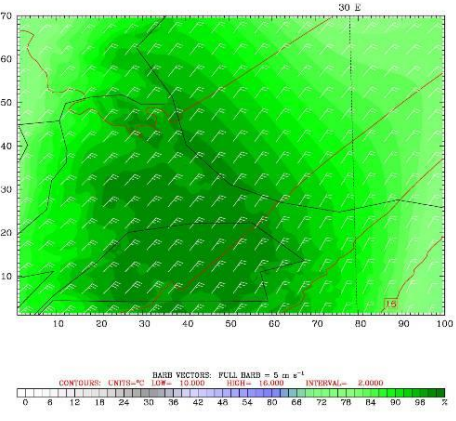


Figure B.6: Experiment IV 4 km inner nested domain, 850 mb NCEP Reanalysis plots. Panels a to f represent the 13-15 August 2004 of the case study period.

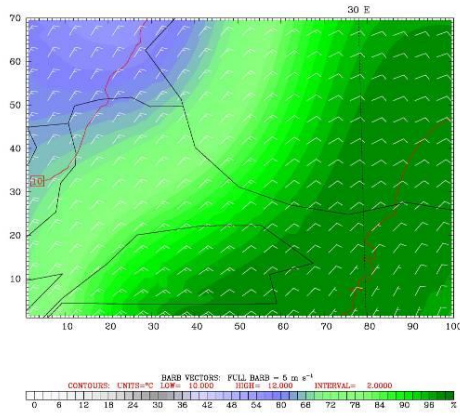
g.) 16 August 2004 00 UTC



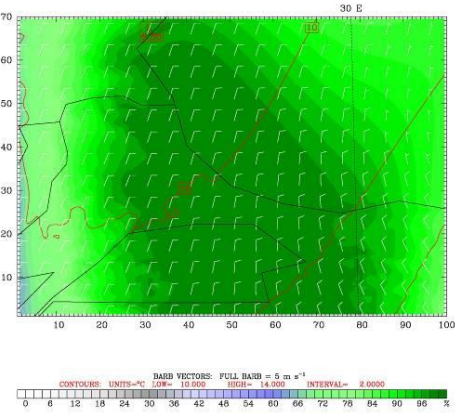
h.) 16 August 2004 12 UTC



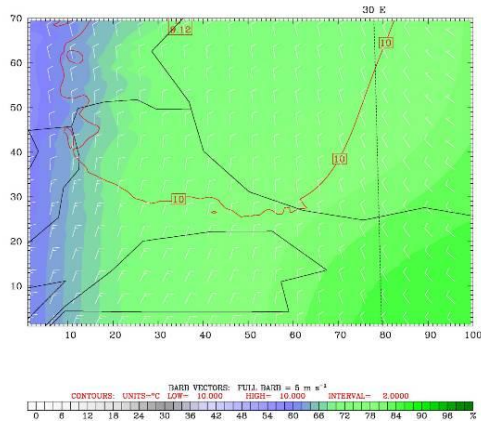
i.) 17 August 2004 00 UTC



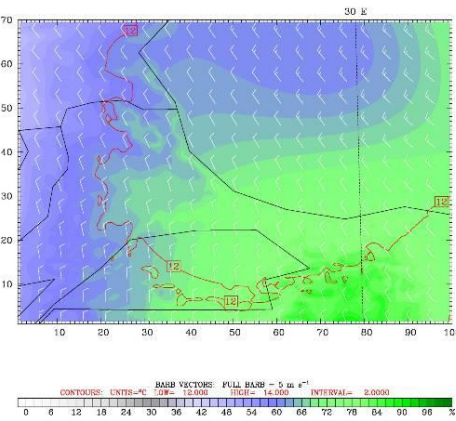
j.) 17 August 2004 12 UTC



k.) 18 August 2004 00 UTC



l.) 18 August 2004 12 UTC



m.) 19 August 2004 00 UTC

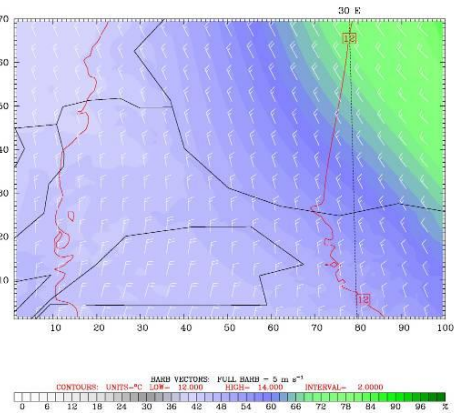


Figure B.6 (Cont.): Experiment IV 4 km inner nested domain, 850 mb NCEP Reanalysis plots. Panels g to m represent the 16-19 August 2004 of the case study period.

Appendix C. Total Accumulated Rain Fields of Experiment IV

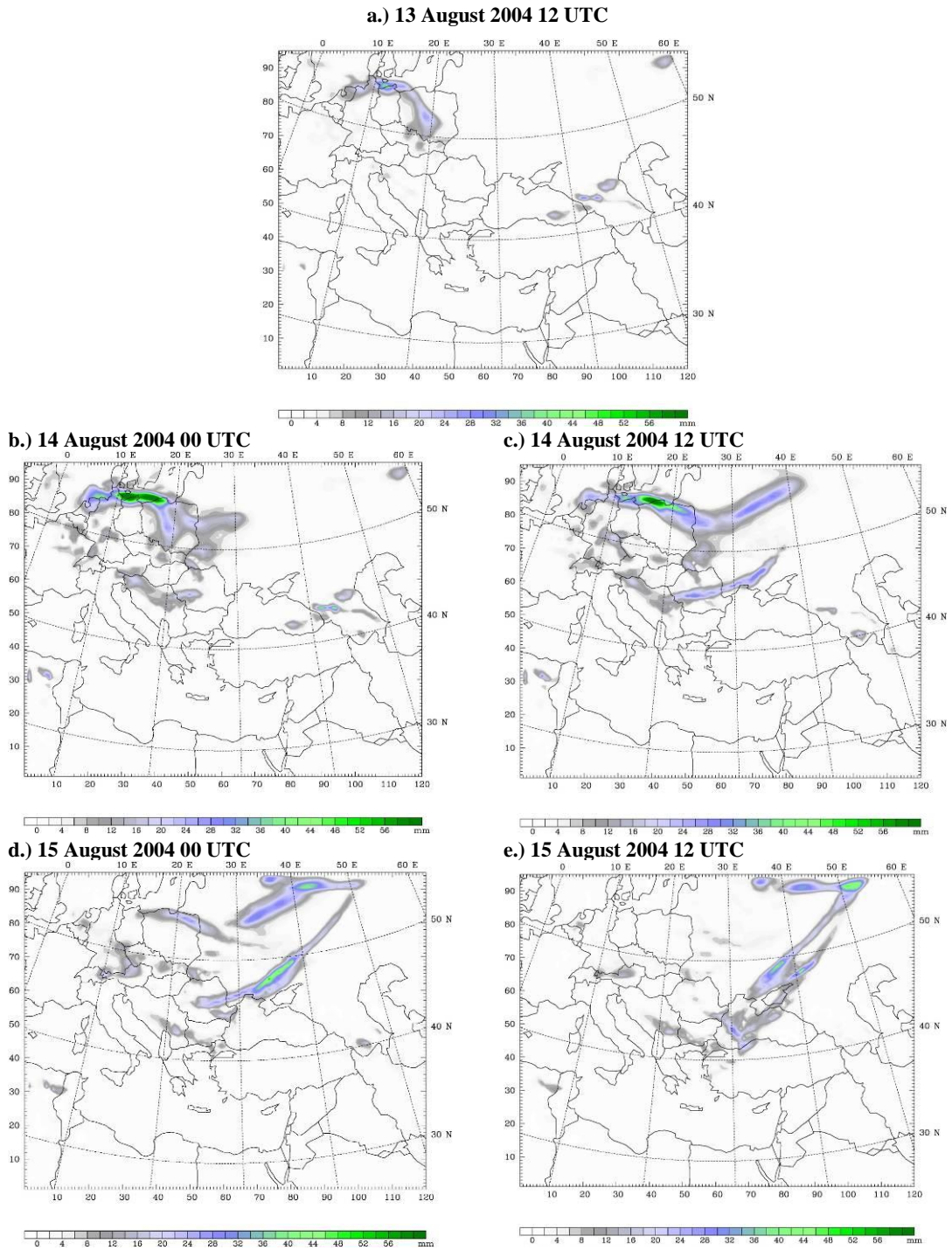
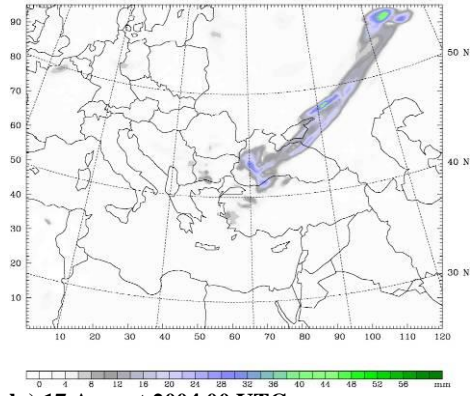
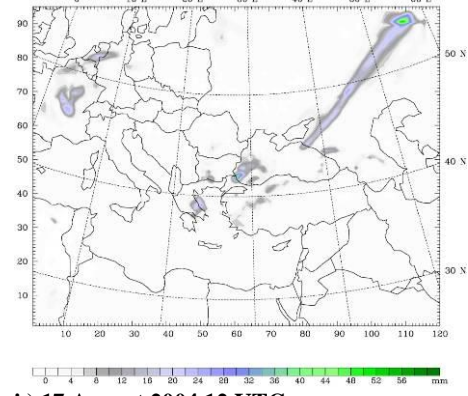


Figure C.1: 36 km domain of experiment IV total accumulated rain in the past 24 hours shown as filled colors, at 13 August 12 UTC with 12 hourly interval, ending at 19 August 00 UTC, left column represents the 00 UTC and right column 12 UTC for each forecast day. Panels a to e represent the 13-15 August 2004 of the case study period.

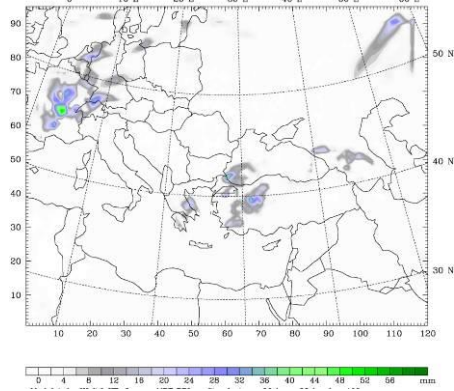
f.) 16 August 2004 00 UTC



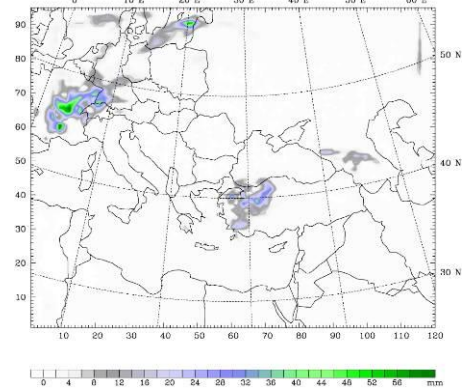
g.) 16 August 2004 12 UTC



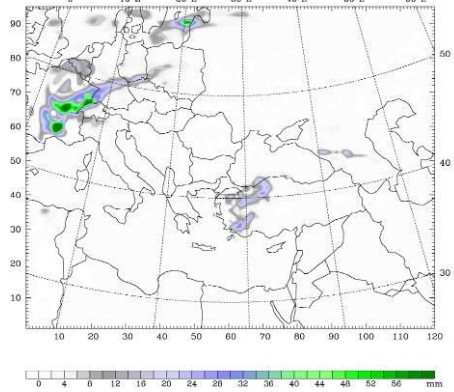
h.) 17 August 2004 00 UTC



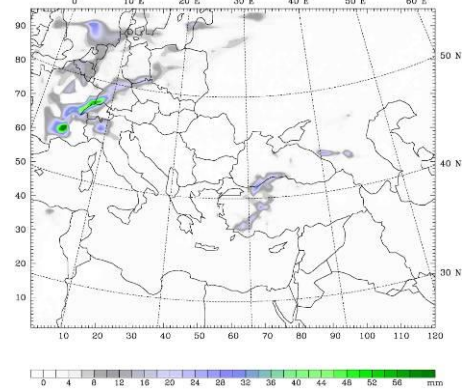
i.) 17 August 2004 12 UTC



j.) 18 August 2004 00 UTC



k.) 18 August 2004 12 UTC



l.) 19 August 2004 00 UTC

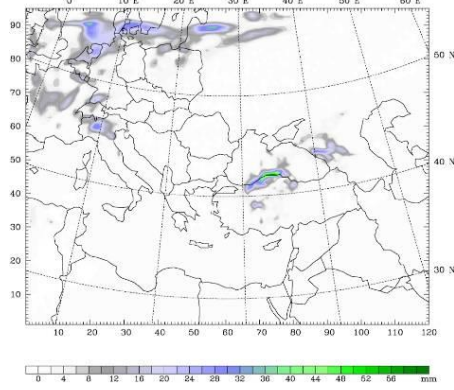


Figure C.1 (Cont.): 36 km domain of experiment IV total accumulated rain in the past 24 hours shown as filled colors, at 13 August 12 UTC with 12 hourly interval, ending at 19 August 00 UTC, left column represents the 00 UTC and right column 12 UTC for each forecast day. Panels f to m represent the 16-19 August 2004 of the case study period.

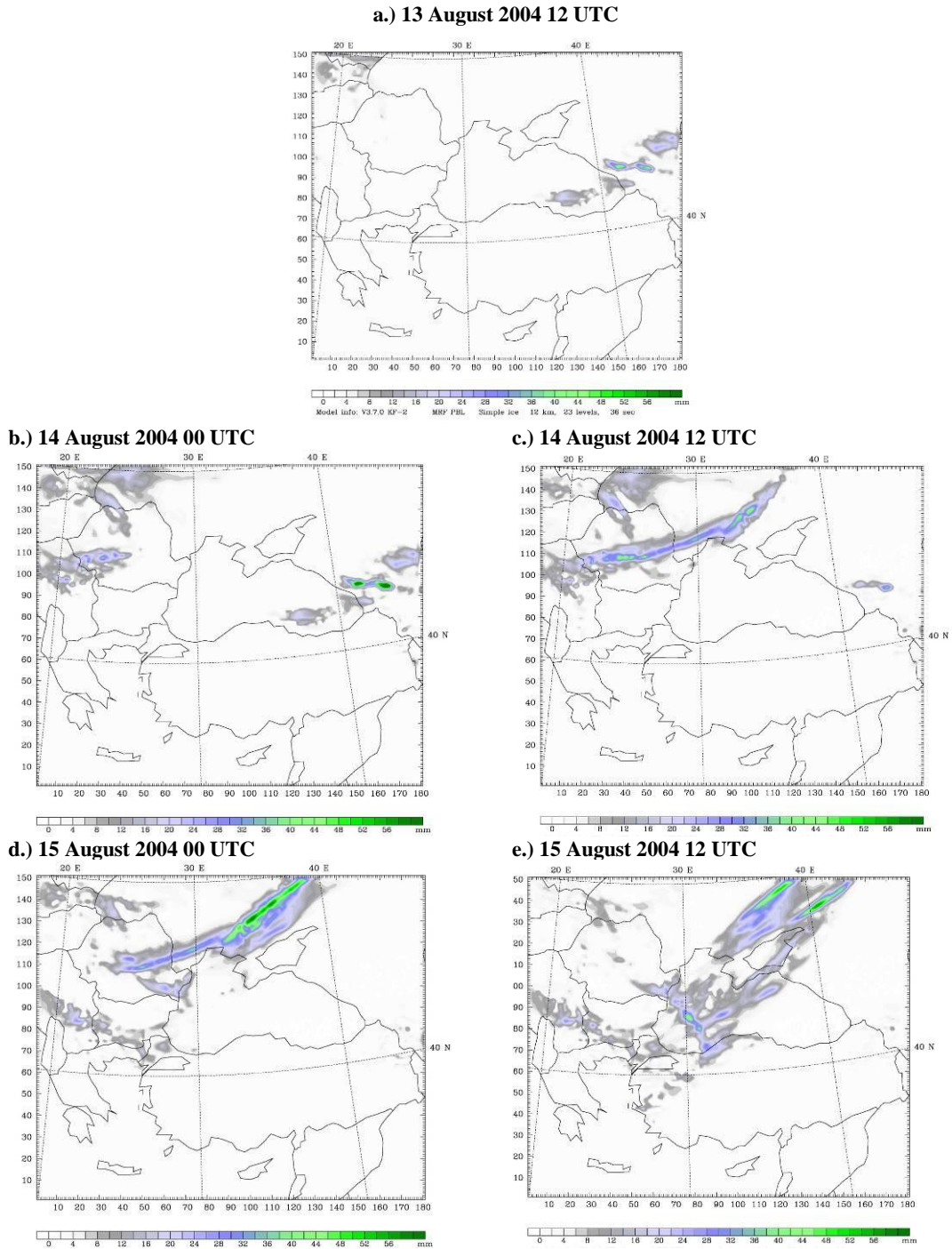
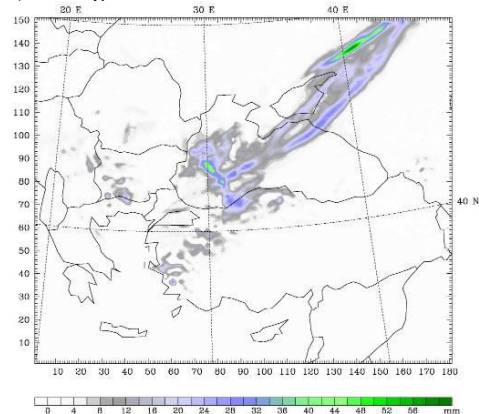
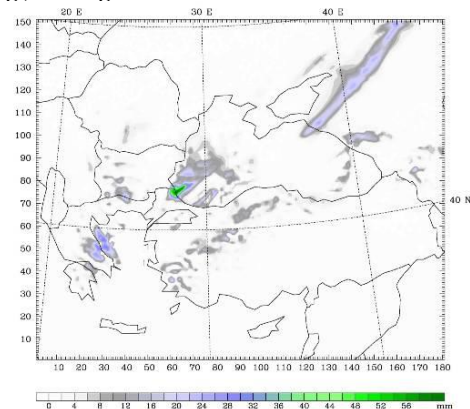


Figure C.2: 12 km domain of experiment IV total accumulated rain in the past 24 hours shown as filled colors, at 13 August 12 UTC with 12 hourly interval, ending at 19 August 00 UTC, left column represents the 00 UTC and right column 12 UTC for each forecast day. Panels a to e represent the 13-15 August 2004 of the case study period.

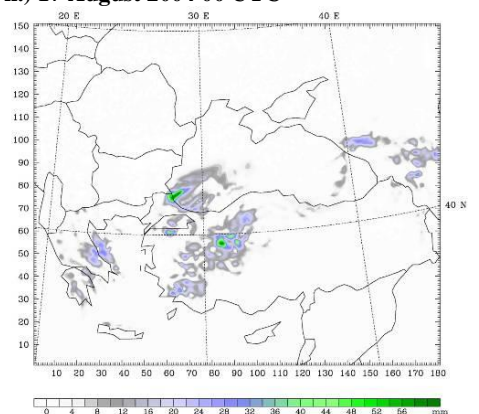
f.) 16 August 2004 00 UTC



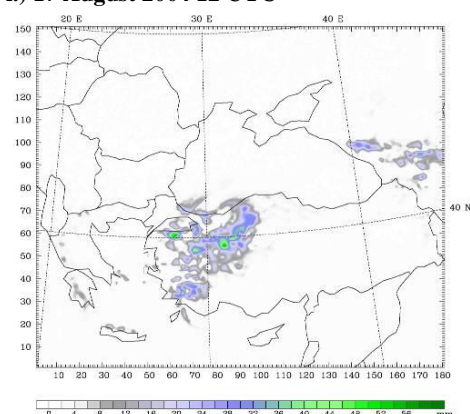
g.) 16 August 2004 12 UTC



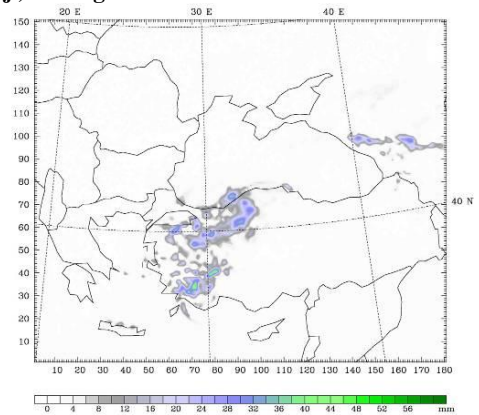
h.) 17 August 2004 00 UTC



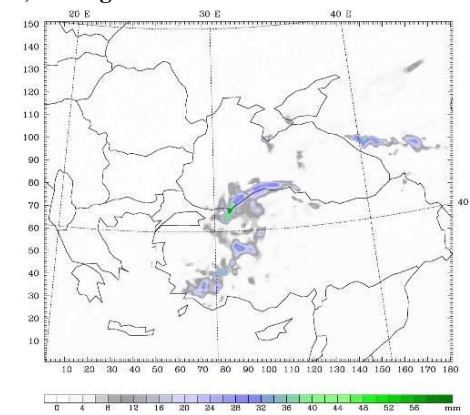
i.) 17 August 2004 12 UTC



j.) 18 August 2004 00 UTC



k.) 18 August 2004 12 UTC



l.) 19 August 2004 00 UTC

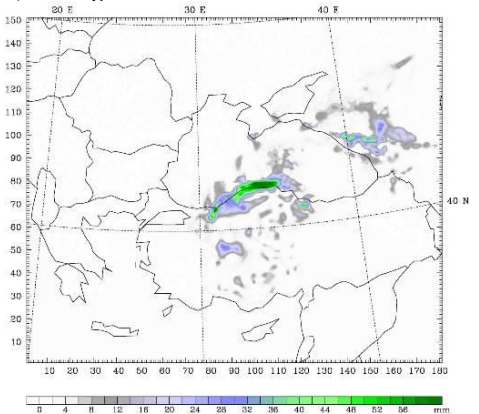
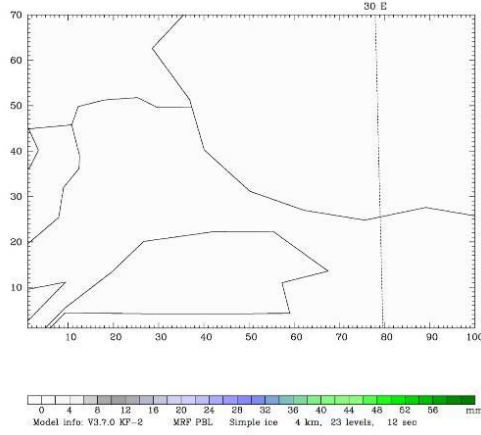
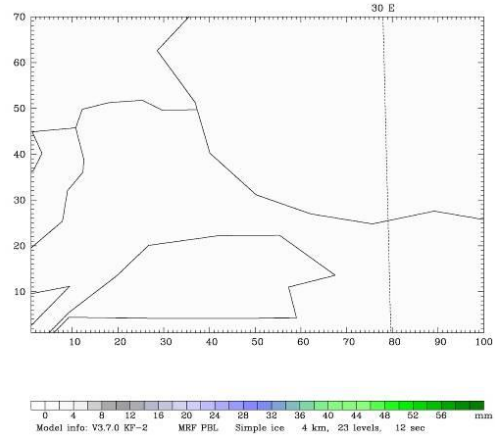


Figure C.2 (Cont.): Panels f to l represent the 16-19 August 2004 of the case study period.

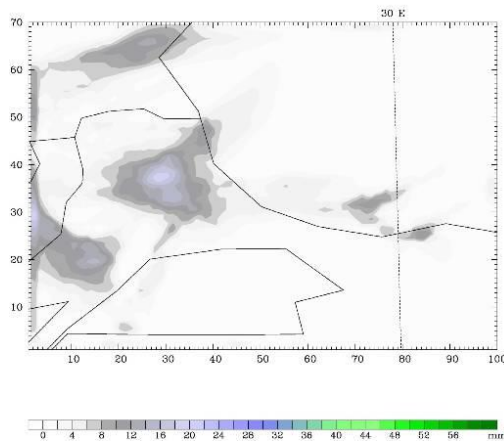
a.) 14 August 00 UTC



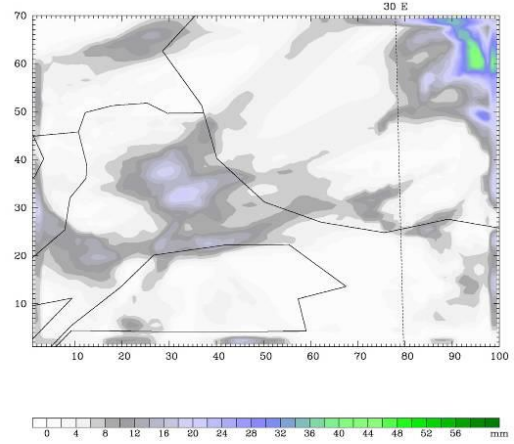
b.) 14 August 12 UTC



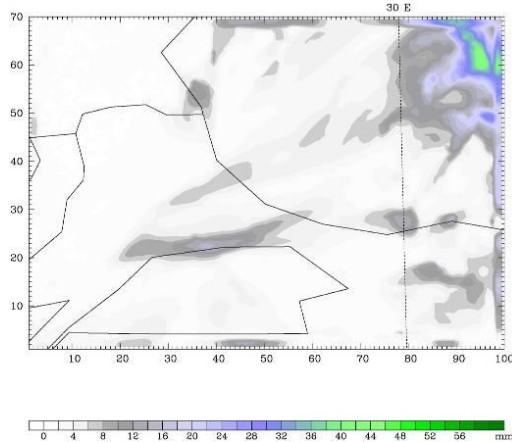
c.) 15 August 00 UTC



d.) 15 August 12 UTC



e.) 16 August 00 UTC



f.) 16 August 12 UTC

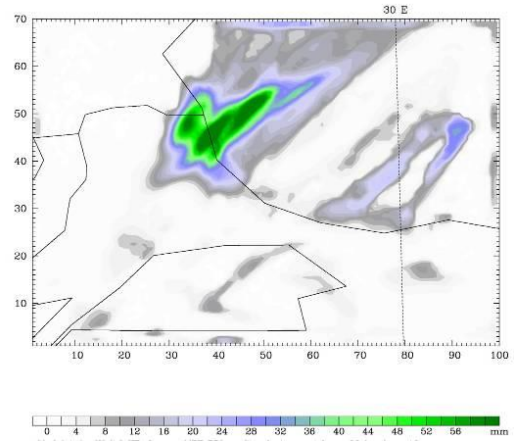
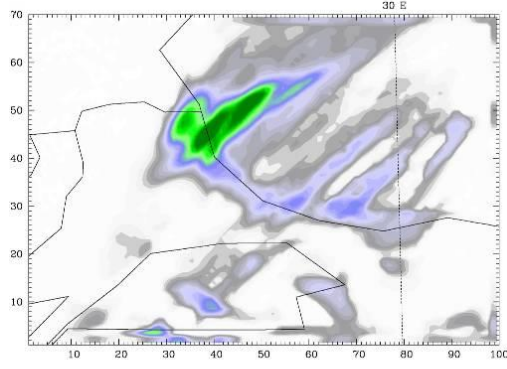
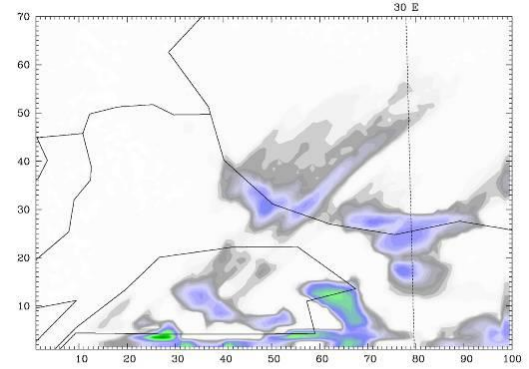


Figure C.3: 4 km domain of experiment IV total accumulated rain in the past 24 hours shown as filled colors, at 14 August 12 UTC with 12 hourly interval, ending at 19 August 00 UTC, left column represents the 00 UTC and right column 12 UTC for each forecast day. Panels a to f represent the 14-16 August 2004 of the case study period. (13 August 2004 not given as no precipitation is predicted by the model on that day.)

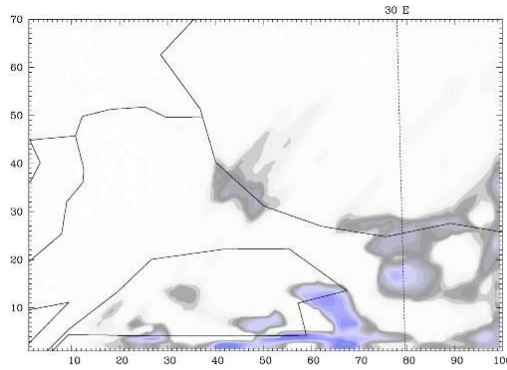
g) 17 August 00 UTC



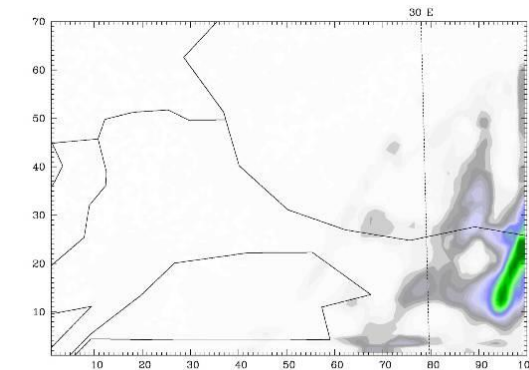
h.) 17 August 00 UTC



f.) 18 August 00 UTC



g.) 18 August 12 UTC



h.) 19 August 00 UTC

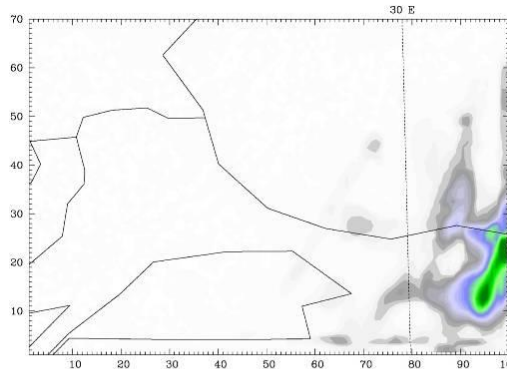


Figure C.3 (Cont.): 4 km domain of experiment IV total accumulated rain in the past 24 hours shown as filled colors, at 14 August 12 UTC with 12 hourly interval, ending at 19 August 00 UTC, left column represents the 00 UTC and right column 12 UTC for each forecast day. Panels g to h represent the 17-19 August 2004 of the case study period.

CURRICULUM VITAE

Müge Kömürcü was born in Istanbul on 15th February 1981. She graduated from Mehmet Karamancı İlkokulu (Primary School) in 1992, Mustafa Mihriban Boysan Orta Okulu (Secondary School) in 1995 and in 1999 from Kabataş Erkek Lisesi (High school). She started to study BSc. on meteorological engineering at the Faculty of Aeronautics and Aerospace at Istanbul Technical University in 1999 and in 2001 she also started to study BSc. on environmental engineering at the Faculty of Civil Engineering at Istanbul Technical University as a double major student. She received her BSc. degree on meteorological engineering in June 2003, graduated as top student of class of meteorology, and on environmental engineering in August 2004. She started masters' degree program of meteorological engineering at Istanbul Technical University in July 2003 and is supposed to receive her masters' degree in June 2005.